UNIVERSITY OF OKLAHOMA

GRADUATE COLLEGE

EVOLUTION OF SPECIFIC DIFFERENTIAL PHASE IN SQUALL LINES AND CORRESPONDING LIGHTNING CHANNELS

A THESIS

SUBMITTED TO THE GRADUATE FACULTY

in partial fulfillment of the requirements for the

Degree of

MASTER OF SCIENCE IN METEOROLOGY

By

ZACKERY THOMAS ZOUNES
Norman, Oklahoma
2016

EVOLUTION OF SPECIFIC DIFFERENTIAL PHASE IN SQUALL LINES AND CORRESPONDING LIGHTNING CHANNELS

A THESIS APPROVED FOR THE
SCHOOL OF METEOROLOGY

BY

_____
Dr. Michael Biggerstaff, Chair

_____
Dr. Donald MacGorman

_____
Dr. Guifu Zhang

Acknowledgements

To the advisor who went to bat every time, to the wizard of the office who knows everything, to the fake tough guy who would never say no, to the electrician who never gets enough rest, to the polarimetry master who pointed out the flaws, to the hiccuper who shared love of floofs, to the larper who taught charge, to the girl who kept me grounded and stable, to the scotch master who kept the computers running, to the academic expert who had all the paperwork, to the enthusiastic director who gave me a shot, to the camp counselor who taught me how to read people, to the warrior who led by example, to the cloudmaster who listened, to the frat boy who empathized, to the robbin who ran, to the roommate who analyzed…I am draped across your shoulders as you lift me up, for you all are the reason I made it, even just barely, to the stage.

Table of Contents

List of Tables

List of Figures

Abstract

Dual-polarimetric radar products have been used in observing changes and persistence of thunderstorm electric fields in relation to lightning discharges. One such product, specific differential phase (K_{DP}), is valuable for its ability to detect the change in particle orientation. Negative K_{DP} values above the freezing level indicate ice crystals are oriented vertically beyond 45^{o} in response to an electric field. The relationship between negative K_{DP} to electric fields and the evolution of negative K_{DP} values through the life cycle of thunderstorms has not been previously well documented.

In this study, one of the Shared Mobile Atmospheric Research and Teaching (SMART) radars was used to sample a small Florida squall line (2012) and a large Oklahoma squall line (2016). Data collected from the Florida event was overlaid with local lightning mapping array (LMA) data. The resulting composites were used to compare lightning channel positions to polarimetric signatures, and to study the evolution of those signatures through the life cycle of the squall line. A charge analysis was performed to examine the locations of charge regions in relation to the polarimetric ice-alignment signatures for the Florida squall line. Polarimetric signatures from the Oklahoma squall line were compared to those found in the Florida squall line.

In both cases, a persistent, strongly-negative K_{DP} region was observed above the freezing level on the stratiform side of the reflectivity maximum. This negative K_{DP} region was elongated and sloped downward from the convective region into the stratiform region during later stages of the stratiform region development. A second

region of negative K_{DP} also existed on the forward side of the reflectivity maximum associated with mature convective cells, but fluctuated in strength frequently. In the Florida case, LMA radiation points for a given flash tended to follow contours of zero-K_{DP} and would initiate around one of the negative K_{DP} regions. A charge analysis of the flashes found that the negative K_{DP} region tended to be below the positive charge region and above the negative charge region.

Given that the location of the negative K_{DP} region in relation to the lightning channels, it can be concluded that radar could be used to monitor the electrification of thunderstorms. However, the application is limited by the scan speed. The use of phased-array technology would be necessary to attempt to predict individual intracloud flashes.

Chapter 1: Introduction

A Mesoscale Convective System (MCS) is defined as a cluster of thunderstorms producing a contiguous area of precipitation at least 100 km wide in at least one horizontal direction (American Meteorological Society 2017). MCSs are important, as they provide up to 30-70% of warm season (April-September) rainfall across the Central Plains in the United States (Fritsch et al. 1986, Nesbitt et al. 2006). MCSs also negatively impact lives by causing dangerous weather phenomena including floods (c.f. Schumacher and Johnson 2005), windstorms (c.f., Johns and Hirt 1987), damaging hail (Wakimoto et al. 2006), tornadoes (Thompson et al. 2012) and lightning (Makowski et al. 2013). Improving scientific understanding and monitoring of lightning could save lives, since lightning strikes are responsible for 50 deaths each year in the U.S. (Lopez and Holle 1998).

Until recently, lightning has been difficult to study quantitatively since flashes are often short-lived, sometimes as short as tenths of seconds. Moreover flash rates are often greater than one per minute (e.g. Markowski et al. 2013). Recently developed instruments such as a lightning mapping array (LMA) (Rison et al. 1999, Krehbiel et al. 2000, Thomas et al. 2004, Edens et al. 2012) can record locations of radiation bursts from the leader tips of lightning channels on the order of microseconds or less. But LMA networks are limited in number and have limited range (~100 km) for mapping the vertical component of the radiation source. An alternative to monitoring lightning directly is to indirectly monitor the electric fields that lead to

lightning by using radar to detect the effects of the electric fields on ice crystals in the cloud (Carey et al. 2009).

1.1 Ice Crystal Orientation Induced by Electric Fields

The effects of electric fields on ice crystals were first studied by Vonnegut (1965) to verify a theory by Lacy (1950) that ice crystals rotate in thunderstorm electric fields. This idea was prompted by observations by Ludlam (1950) and Hale (1950) who witnessed a "streamer" of light that grew and then disappeared following a lightning discharge in an isolated cumulonimbus cloud. Vonnegut tested this theory by exposing ice crystals to a charged rod using a Schaefer cold box (Schaefer 1946). Vonnegut shined a light at the crystals and found they reflected light in different directions depending on the location of charged rod, suggesting the crystals were rotating in response to the changing electric field associated with the charged rod. However, unlike in Vonnegut's experiments, the electric fields in thunderstorms are not controlled, air flow is often turbulent, and there are often many different types of ice crystals. Thus, to be able to use ice crystal orientation as a parameter for detecting strong electric fields, the factors that affect ice crystal orientation have to be established.

Several studies following Vonnegut's work assessed the steady state orientation of different crystals in labs. It was found that hexagonal plates and other types of crystals, including columns (Jayaweera and Mason 1965) and six types of snow platelets (List and Schemenauer 1971) fall horizontally in laminar flow and stagnant air when unexposed to electric fields. Zikmunda and Vali (1972) found that

majority of ice crystals had little deviations from horizontal orientation as they fell in steady flows, with the exception of conical graupel and some types of capped columns; however, larger crystals in more unsteady flows are more susceptible to oscillations. Unsteady flows are determined to have Reynold's Number (Re) > 100, where

$$Re = \frac{\rho v L}{\mu} \quad \text{(Eq. 1)}$$

and ρ is the fluid density, v is the fluid's characteristic velocity, L is the fluid's characteristic length (or depth) and μ is the fluid's viscosity. The Reynold's number represents the relative importance of inertial to viscous forces in a fluid and is used to describe flow steadiness. Typically, Re in the atmosphere is $1 < Re < 200$ (List and Schemenauer 1971). Cho et al. (1981) studied ice crystal orientations in turbulent flow and found that turbulence did not affect the preferred aerodynamic orientations of ice crystals. The resulting consensus of the above studies is that ice crystals tend to fall with a horizontal orientation in steady and turbulent flow. The crystals produced in laboratory settings have been observed in natural clouds via airborne particle probes and direct in situ measurements on mountain tops (Hobbs et al. 1974, 1975).

To determine if electric fields have a significant impact on ice crystals in thunderstorms, it must be established that thunderstorm electric fields are correlated with fluctuations from ice crystals preferred horizontal orientation. Mendez (1969) used a passive optical scanning device to measure fluctuations in reflected sunlight and its polarizations off the upper levels of thunderstorms. Fluctuations in reflected light polarization were found to match fluctuations in electric fields due to lightning discharges measured on the ground, indicating lab experiments by Vonnegut (1965)

were valid in nature. To verify that these measurements were due to electric field fluctuations, Weinheimer and Few (1987) calculated electric field torques on ice crystals in comparison to the aerodynamics torque of air flowing past ice crystals. Their results showed that the degree of ice crystal alignment to electric fields was dependent on the major axis dimension of the crystal. For an electric field of 100 kV m^{-1}, ice crystals up to 0.2-1 mm in the major dimension (depending on type) align with the electric field despite aerodynamic torque and turbulent torque. Larger crystals experienced more aerodynamic torque than smaller crystals and did not orientate completely with the electric field. Aircraft measurements (Jones 1960, Houze et al. 1979, Heymsfield 1977, Platt 1997) of ice crystal sizes show that ice crystal concentrations increase exponentially for decreasing crystal size, following a Marshall-Palmer distribution (Marshall and Palmer 1948) in cumulonimbus clouds and frontal rainbands. This indicates that the majority of crystals present are small enough to be affected by 100 kV m^{-1} electric fields, commonly found in the upper regions of thunderstorms (Simpson and Scrase 1937, Marshall and Lin 1992, Rust and Marshall 1996, Stolzenberg et al., 1998).

1.2 Radar Detection of Ice Crystal Orientation

The above theories and observations show that ice crystals rotate in response to thunderstorm electric field. To measure ice crystal orientation over large regions in thunderstorms, the use of radar is required since in-situ devices are not available to measure particle orientation in a cloud without disturbing the particles and are limited in data coverage and timing.

One of the earliest studies of ice crystal orientation with radar was the work of Hendry and McCormick (1976), who studied the alignment of ice particles in thunderstorms with the use of dual-channel, circularly polarized 1.8 cm wavelength radar. The radar was pointed into one part of the storm to view the storm evolution with time along a fixed angle. Using a received frequency correlation product, they found that the orientation of particles intersected by the radar beam in the upper parts of the thunderstorm deviated from their preferred horizontal orientation. Additionally, the orientation of particles returned to horizontal following lightning discharges measured by their lightning detector, a low-frequency radio receiver. Hendry and Antar (1982) confirmed that the radar measurements they were receiving at the top of thunderstorms were snow and ice and not rain droplets by comparing the cancelation ratios and preferred orientation of measurements aloft to that of snowstorms. Additionally, they noted that the electric field-induced particle orientation values measured by the radar were caused by "unseen" particles in the propagation path, not the particles reflecting the radar's power.

Krehbiel et al. (1996) used circularly polarized dual-channel radar to detect particle orientations in the cloud by taking 24-second RHI (Range Height Indicator) cross sections of a Florida thunderstorm. Similar to Hendry et al. (1987) and Metcalf (1995, 1997), Krehbiel et al. (1996) found that vertical ice-alignment signatures in the upper portions of the thunderstorm which existed prior to a lightning discharge (Fig. 1) disappeared in the scan following the discharge (Fig. 2). Krehbiel et al. (1996) noted that the vertical orientation prior to the discharge agrees with conceptual models of

horizontally layered charge structures in thunderstorms (e.g. Stolzenburg 1998a), which would cause the electric field to generally point in the vertical.

An alternative to circularly polarized dual channel radar in studying ice-alignment is simultaneous H and V channel linear transmission radar (StaR, Doviak et al. 2000; Ryzhkov and Zrnic 2007). Measurements by STaR radars are fast since both polarization channels are transmitted and processed simultaneously. Zrnic and Ryzhkov (1999) found negative values of specific differential phase (K_{DP}) near the top of the cloud in the convective region of an Oklahoma thunderstorm, indicating strong vertical electric fields within the storm. Negative K_{DP} values occur when dipoles within the hydrometeor are able to align vertically more than horizontally. This happens when ice becomes polarized and then canted vertically by the vertical component of an electric field.

Another method for measuring particle orientation in thunderstorms is with the Linear Depolarization Ratio (LDR) provided by multiparameter radar that transmits alternating horizontally and vertically polarized signals (Caylor and Chandrasekar 1996, Carey and Rutledge 1998). LDR is measured by taking the ratio of the crosspolar and copolar reflectivities, Z_{HV} and Z_{HH}, where the first subscript represents the transmitted channel and the second represents the received channel. A constant copolar component of reflectivity indicates that changes in crosspolar values are due to orientation changes, not particle size distribution changes. Thus, changes in LDR when scanning small particles are dependent on the crosspolar component and can be used to detect orientation changes in small particles. Caylor and Chandrasekar (1996) studied how LDR and K_{DP} changed prior to a lightning flash. Prior to a flash, K_{DP}

decreases while LDR either increases or decreases depending on the initial orientation of the crystal. Since LDR is maximized when the particle is oriented at 45° from the radar beam, LDR increases as particles become more vertically oriented from an initial horizontal orientation, and decreases for a particle becoming more vertically oriented starting from a 45° cant. Carey and Rutledge (1998) also observed negative values of K_{DP} just above the top of reflectivity maxima in the convective region of thunderstorms using an alternating transmission radar.

1.3 Thunderstorm Charging Mechanisms

The above radar studies demonstrate that radar has successfully detected ice-crystal orientation changes in thunderstorms due to building electric fields and lightning discharges. These observations of strong electric fields can be explained by several theories of charging mechanisms in thunderstorms.

There are many different mechanisms theorized to influence the development of electric fields in thunderstorms; however, non-inductive charge transfer is the most dominant type of mechanism. Noninductive charging is a mechanism in which charge transfer is independent of existing electric field strength. The mechanism includes several different processes. One such process is charge separation at the ice-liquid interface of a supercooled water droplet, which undergoes the Hallet-Mossop mechanism of inward freezing of the water droplet. This results in the ice shell splintering off as deeper layers of ice inside the droplet expand due to freezing (Hallet and Mossop 1974). Although Workman and Reynolds (1950) showed through lab experiments that ice can gain different charges depending on the purity of the water,

the usual result of rime removal from graupel is positively charged graupel (Keith and Saunders 1990).

Another charging mechanism is due to sublimation or deposition of graupel. Saunders (1993) and Williams et al. (1991) verified that graupel gains negative charge while it sublimates and positive charge as it grows by deposition. The melting of ice (not exclusively graupel) is also found to produce charge regions in the stratiform region of squall lines (Matthews and Mason 1963, Drake 1968, Marshall and Rust 1993, Stolzenburg et al. 1994, Shepherd et al. 1996). While studies have found that as ice melts, it gains positive charge (Dinger and Gunn 1946, Magono and Kikuchi 1965, Dinger 1965), simulations by Schuur and Rutledge (2000b) found that charging due to melting was insignificant in comparison to ice-ice collisions and charge advection. Charge advection is the movement of ions and charged particles by particle motions flow away from their source region.

The most dominate noninductive charging mechanism that could develop the observed electric fields in thunderstorm convective regions is the graupel-ice mechanism, which occurs when an ice crystal deposits charge on riming graupel through a collision (Reynolds et al. 1957). The resulting sign and magnitude of charge deposited during this process is dependent on numerous factors. The amount of charge that gets transferred to the graupel depends on air temperature, liquid water content, (Takahashi 1978), the size of the ice crystal (Jayaratne et al 1983), and the velocity of the crystal upon collision (Brooks et al. 1997).

Graupel is most often found in the convective regions of squall lines because updrafts have high liquid water content and contain high concentration of supercooled

water droplets to support the riming of graupel. This is confirmed in observations by several experiments such as Dye et al. (1986), which used particle imagers on aircraft to detect precipitation development and particle interactions in the transition zone between updrafts and downdrafts between -10 and -20°C of a Montana storm. This was preceded by high lightning flash rates. This and other studies (e.g. Dye et al. 1988 in New Mexico, Gaskell et al. 1978 in Florida, Weinheimer et al. 1991 in New Mexico) have confirmed that the graupel-ice mechanism occurs most often in the convective line above the melting level, and is the dominant mechanism for generating thunderstorm electric fields; though, it is likely multiple mechanisms are contributing (Saunders 1993).

An important result of the non-inductive mechanism is the screening layer, which is a layer of charge that develops on the edges of cumulus clouds due to change in conductivity between water droplets and unsaturated air (Grenet 1947). Aircraft measurements were first made by Vonnegut (1962) that confirms charge regions that exist on the edge of clouds. This mechanism for charging is non-inductive and due to ion-particle interactions since it produced by the positive ions flowing in the fair weather electric field through the cloud (MacGorman and Rust 1998). This results in the bases becoming positively charged (where positive ions first intersect the cloud) and the edges of the tops of cumulus towers becoming negatively charged.

Another prominent mechanism in thunderstorms is the inductive charging mechanism, which occurs when charge-neutral hydrometeors of different sizes collide and rebound, charge of opposite sign interacts and gets transferred, leaving both particles with net charge of opposite polarity as proposed by (Elster and Geitel 1913)

for droplet-only interactions. Many studies have shown that ice-ice and liquid-ice inductive charging through rebounding collisions are also possible (Muller-Hillebrand 1954, Aufdermaur and Johnson 1972, Gaskell 1981). While it is agreed that this is a significant mechanism (Saunders 1993), it does not produce electric fields as strong as observations (Jennings 1975) nor can it produce highly charged particles in the early stages of the thunderstorm electrification process (Gaskell et al. 1978, Christian et al. 1980, and Marshall and Winn 1982) because the short contact time during a collision is not enough to transfer quantity of observed charge (Illingworth and Caranti 1985). Additionally, it requires an electric field to already be present in the cloud for it to occur.

1.4 Squall Line Charge Structures

The above charging mechanisms result in accumulations of charge in several regions of squall lines. These charge regions cause the strong electric fields that result in lightning. In order to identify the electric fields in thunderstorms, it is necessary to understand the charge regions that cause them. The model outlined by Biggerstaff and Houze (1991a) will be used for identifying regions of a squall line (Fig. 3).

The convective region of squall lines was thought to reflect a simple tripole model of a positive charge in the upper and lower levels and negative charge in the mid-levels (Simpson and Scrase 1937), as measured in many thunderstorms with electric field mill (EFM) soundings through thunderstorm updrafts in later studies (e.g. Marshall and Winn 1982, Krehbiel 1986, Koshak and Krider 1989, Marshall and Rust 1991).

However, Stolzenburg et al. (1998c) made a comprehensive sounding analysis of vertical electric fields through squall lines and found that the simple tripole model did not present the complete charge structure. Subsequent results showed that the tripole model needed to include a negatively charged screening layer at the top of thunderstorms above the convective thunderstorm updrafts (Fig. 11).

Stolzenburg et al. (1998a) found that the vertical thickness of the upper positive and negative charge regions increased in depth outside the convective updraft (Fig. 4). This is theorized to be the result of three effects. Firstly, a variety of types of charged hydrometeors are ejected from the updraft and have differing fall speeds and trajectories (Fig. 3). Secondly, similarly charged particles repel three-dimensionally, though this was found to be negligible (Bateman et al. 1995). Thirdly, the particles are in the region of turbulent mixing and downdrafts, which would cause them to be less consolidated.

Like Saunders (1993), Stolzenburg et al. (1998c) concluded that multiple charging mechanisms must be present in squall lines to produce the observed charge regions. While the noninductive graupel-ice collision mechanism can produce a tripole charge structure, the ion capture mechanism on the screening layer of the cloud (or some other mechanism) must be present to produce the upper level negative charge region.

Stolzenburg et al. (1998c) found that the stratiform region of squall lines has six vertically-layered and horizontally-extensive charge regions, which sloped downward in altitude just rearward of the convective region and flatten out (Fig. 5). There is an upper-most negative layer, lower-most positive layer in the stratiform

precipitation just above the ground, and the layers oscillate in between (Stolzenburg et al. 1998a).

Stolzenburg et al. (1994) found that the uppermost negative charge region was a screening layer (like the one found in the convective region). Stolzenburg et al. (1994) and Stolzenburg et al. (1998a) considered the uppermost positive charge layer to be the result of charge advection by particles from the updraft moving along trajectories conceptualized by Biggerstaff et al. (1991a). Stolzenburg et al. (1998a) and Shepard et al. (1996) considered the densest negative charge layer to be the result of either charge advection or noninductive ice-ice collision charging. A model by Rutledge et al. (1990) noted that the latter mechanism results in negative charging in the stratiform region. The positive charge region associated with the melting layer can be the result of the noninductive melting charging mechanism (Stolzenburg et al. 1994, Shepard et al. 1996). The negative charge layer just below the melting layer at the base of the cloud is a screening layer (Stolzenburg et al. 1994, Marshall et al. 1989). Observations of lower relative humidities just below this level (~85%) indicate that the air is unsaturated, though precipitation is falling through it. This observation matches observations of the mid-level jet advecting lower theta-e air to this level (Zipser 1969, Houze 1977, Zipser 1977). The positive layer below the cloud is possibly due to positive ions commonly found below clouds due to corona ions produced by Earth's surface (Standler and Winn 1979).

1.5 Lightning Patterns in Squall Lines

This discussion summarizes the known patterns in lightning initiation and propagation, which will be observed in this study.

Lightning is thought to initiate in areas with the strongest electric field (Kasemir 1960, Mazur and Ruhnke 1993, 1998). Lightning initiates when the electric field inside a thunderstorms becomes strong enough to trigger a fast positive breakdown followed by a narrow bipolar event, which is a high-powered discharge of electrons consisting of a volume of positive streamers (Rison et al. 2016) lasting 10-20 μs and extending several hundred meters (Smith et al. 1999, Eack 2004, Watson and Marshall 2007).

Initiation points also have a vertical bimodal distribution. Rust et al. (1985b) found flash initiation points to be around 7 km and 10 km above mean sea level on average, which corresponded to -14°C and -38°C. Similarly, Proctor (1991) observed initiation heights in 13 different storms at 5.3 km at -3°C and at 9.2 km at -38°C. Depending on the storm, these heights could correspond to the areas above and below the upper negative charge region from Stolzenburg et al. 1998c (Fig. 13), which would be locations of strong electric field.

After lightning initiates, positive and negative channel leaders propagate in opposite directions from the initiation location toward the charge regions generating the electric field (Kasemir 1960, Mazur and Ruhnke 1998, Maggio et al. 2005, Marshall et al. 2005, Lund et al. 2009). Upon reaching the charge regions, the lightning often turns horizontal and expands into the charge regions (MacGorman et al. 1981, MacGorman et al. 2001, Coleman et al. 2003, MacGorman et al. 2015).

Cloud-to-ground lighting flashes (CGs) typically initiate in the high electric field that exists between the mid-level negative charge and a lower altitude positive charge region (MacGorman et al. 1981, Rison et al. 2016).

The combined use of LMA and radar products has revealed several patterns about where lightning initiates and propagates in thunderstorms. Flashes were found to initiate in the convective region of thunderstorms, and do not often initiate in the stratiform region of MCSs (Lund et al. 2009). It has been found that for lightning that initiates in the upper regions of thunderstorms, initiation occurs in areas of low to moderate reflectivity (20-48 dBZ – Proctor 1991, Lund et al. 2009). In their squall line system, Lund et al. (2009) found that lower level lightning initiation occurred on top of positive Z_{DR} columns. Bruning et al. (2007) found that some lightning flashes initiate in and below regions of negative Z_{DR} where graupel may be found. Additionally, upper level initiation occurred above reflectivity maximums, a transition region from graupel below to cloud ice above (Lund et al. 2009). This transition zone would be an ideal place for graupel-ice collisions envisioned as the primary noninductive charging mechanism. This mechanism contributed mostly in the mature phase when updrafts are strong enough to loft graupel; however, as the MCS weakens and precipitation drops below the melting layer, it is likely that the inductive melting process becomes the dominant mechanism. Based on lightning propagation patterns, Lund et al. (2009) noticed the ICs propagated into upper positive and negative charge regions in individual cells, which agreed with corresponding EMF sounding measurements of electric fields and the charge structure conceptual model by Stolzenburg et al. 1998a (Fig. 14).

An interesting characteristic of lightning propagation in thunderstorms is its interaction with the melting layer. In an unorganized multicell convective cluster observed over Florida, MacGorman et al. (2015) showed a reflectivity maximum just below the altitude of the expected $0°C$ isotherm. During rocket-triggered flashes into the dissipating stage of this thunderstorm cluster, lightning propagated horizontally as it reached the negatively charged melting layer; however, during mature storms, triggered flashes propagated over the tops of the Z_{DR} indicated melting layer (MacGorman et al. 2015, Hill et al. 2012b, Hill et al. 2013). Triggered flashes turn horizontal at the melting level due to strong electric fields just above (Coleman et al., 2003, 2008) and concentrated amounts of charge present (Hill et al. 2013).

1.6 K_{DP} Signature Evolution and LMA Data Comparison

While LMA data has been compared to dual-pol radar signatures, the evolution of those signatures throughout the life cycle of thunderstorms and the comparison of lightning initiation and leader propagation to those signatures have not been well-documented. Additionally the use of K_{DP} underutilized as a determiner of lightning channel propagation. Negative K_{DP} can be used to indicate regions of heightened vertical electric fields because negative K_{DP} represents ice crystal orientation becoming more vertical along the radial and because ice crystals aligned by electric fields are vertically oriented. The positive K_{DP} areas surrounding the negative K_{DP} regions aloft can be used to identify regions of charge density of greater magnitude than that in the negative K_{DP} region. This inferred charge density distribution assumes that the negative K_{DP} region represents an extrema in the electric field and the 1-D

approximation to Gauss' Law (Marshall and Rust 1991) is applicable. If there are weak electric fields, the orientation of ice crystals horizontal, which would show up as positive K_{DP} values.

Herein, the relationships between flash channel structures and K_{DP} signatures and their evolution through the life cycle of squall lines is examined using the LMA data from the International Center for Lightning Research and Testing (ICLRT) and dual-pol RHIs (Range Height Indicator scans) from the dual-pol ground-based Shared Mobile Atmospheric Research and Teaching (SMART) radar. Observations from a squall line in Florida and a squall line in OK will be used to confirm the persistent negative K_{DP} region similar to Carey and Rutledge (1998) and Zrnic and Ryzhkov (1999) above and on the stratiform side of the convective region, show that this negative K_{DP} region sloped into the stratiform region as the stratiform region developed, and identify the existence of a second less consistent K_{DP} region on the forward side of the convective region. Data of the Florida squall line will be used to show that many intracloud lightning flashes follow the zero-K_{DP} contour on time-averaged plots.

This work is organized as follows: Chapter 2 will discuss the data and methods used to analyze the data. Chapter 3 will give an overview of the environmental conditions and timeline of each squall line. Chapter 4 will analyze the K_{DP} signatures, storm structure, and lightning during the developing, mature, and dissipating stages of each squall line. Chapter 5 discusses the results of the study, draws conclusions, and outlines future work.

Chapter 2: Methods

2.1 SMART Radar Overview and Scanning Strategies

SMART radars were described in Biggerstaff et al. (2005). This study made use of dual-polarimetric data from SMART radar 2 (SR2). SR2 has a half-power beam width of 1.5°, antenna diameter of 2.54 meters, peak power of 300 kW (150 kW per channel), and C-band frequency of 5570 MHz. SR2 operated in simultaneous transmission and reception (STaR) mode for quicker scanning (Doviak et al. 2000). Products produced by SR2 and used for this study include reflectivity (Z_H), differential reflectivity (Z_{DR}), differential phase (ϕ_{DP}), and specific differential phase (K_{DP}). The correlation coefficient (ρ_{hv}) was used for data quality tests.

During the Florida squall line, SR2 conducted narrow sector volume scans utilizing five consecutive Range Height Indicator scans (RHIs) with elevation 0.5° to 60° from the horizon at azimuths of 8.5°, 9.5°, 10.5°, 11.5°, and 12.5° from north, alternating between scanning from highest elevation to lowest and vice-versa. The azimuths were selected to sample more of the storm around the International Center for Lightning Research and Testing (ICLRT), which was located at an azimuth 10.5° from the radar at a range of 11.6 km. Each RHI scan lasted 15 seconds, with less than a second between RHIs and 5 seconds between volumes. Gate spacing was 150 m.

During the Oklahoma squall line, SR2 sampled consecutive RHIs with elevation 0.5° to 60° at a corrected azimuth of 176° from north (a four degree correction was applied to the heading after the event). Thirty minutes after beginning the data collection, the highest elevation of the RHI was lowered to 45° as the convective line propagated farther from the radar. The south scanning direction was

chosen since it pointed toward the convective line and was free of most obstructions. Each RHI scan lasted 20 seconds while sampling up to 60° elevation and 15 seconds when sampling up to 45° in elevation, with less than a second between RHIs. As for the Florida squall line, gate spacing was also 150 m.

In both cases, the RHI scans sampled through the stratiform region toward the convective region of the squall lines.

2.2 Florida LMA Overview

Lightning mapping array data was provided by the ICLRT, located 6.5 km east of Stark, FL and 11.6 km at an azimuth of 10.5° from SR2. Each LMA station records very high frequency (VHF) power peaks during consecutive 80 μs windows. LMA station locations at ICLRT are described by Hill et al. (2012, 2013) and Pilkey et al. (2013). A reduced chi-squared value of one (goodness of fit criteria) and a minimum six stations were applied to the LMA data to reduce location error in the points representing each flash, and to balance noise rejection with retaining detail. The results were similar to Pilkey et al. (2014) who used 7 stations and a chi-squared value less than or equal to five for the same storm.

2.3 Florida Case Analysis Technique

A charge analysis was performed on 46 flashes while SR2 was sampling RHIs for 80 minutes of the squall line's life cycle. This timeframe was selected because it captured the squall line's life cycle, and it was the timeframe in which the squall line

was most electrically active within 20 km of ICLRT. The charge analysis was completed using the methods outlined in Bruning et al. (2007), Rust et al. (2005), and Coleman et al. (2003) with the intention of identifying the dominant regions of charge in the squall line through noting where and how lightning propagated. Identification of charge based on LMA sources stems from our knowledge of leaders. Initial breakdown of the flash is bidirectional where the negative leader is more detectable (Shao and Krehbiel 1996). Negative leaders propagating through positive regions of charge were more impulsive and gave off more VHF sources for the LMA to detect (Thomas et al. 2001). Positive leaders propagating through negative regions of charge gave off weaker VHF sources, appeared to propagate more slowly, and contained recoil streamers that traversed the existing lightning channels toward the positive charge region. Flashes whose charge regions could not be identified were left as neutral charge.

Flashes were selected for a specific set of four criteria to ensure they could be compared to SR2 RHIs:

1. Flashes had to be almost entirely contained within a volume of space that was five km on either side of the RHI scan. This was to ensure that radar signatures were representative of the part of the storm that the flash was propagating through. While squall lines tend to be two-dimensional, the extent of that symmetry was not adequately sampled in this storm and the extent of the validity of applying that symmetry to dual-polarimetric signatures has not been established. Five km was selected somewhat empirically based on where

patterns started to emerge, and also because it was a small distance relative to the size of the squall line and spacing between convective cells.

2. Flashes had to have a discernable structure and, therefore, could not be in the form of a cluster or compact. It is difficult to perform a charge analysis of a flash without structure and such flashes provided little information regarding their propagation relative to radar signatures. This criterion typically limited flashes to within 20 km of ICLRT because LMA data became increasingly noisy with distance from the array.
3. Flashes had to contain greater than 80 LMA pts with a minimum chi-squared value of one while being viewed in XLMA, an LMA data-viewing program developed by New Mexico Tech. Flashes with fewer points had little structure to analyze and often looked noisy.
4. Flashes had to be mostly parallel to the radar beam. The only way to determine if flashes followed radar signatures is if the flashes were approximately propagating through the same cross-section of the storm represented on the RHIs. Otherwise, the RHIs would not be representative of the storm conditions the flashes were propagating through.

The LMA points for flashes that met the above qualifications were projected onto radar images with the axes “distance from radar” and “height above ground”. Distances from radar were calculated using the latitude and longitude coordinates for each LMA point and the Great Circle Equation with SR2’s coordinates. These points were first projected on the closest radar image prior to the flash. However, because

RHIs took at least 15 seconds to sample, flashes occurred during the scan and RHIs would not be representative of the storm structure immediately prior to the flash. Unfortunately, using the 2nd closest scan prior to the flash represented the storm structure 15-30 seconds prior to the flash. Given that flash rates were 5-15 flashes per minute throughout the storm and its life cycle, the 2nd closest scan was also not representative of the structure immediately prior to the flash.

Thus, it was resolved to take the time average of five scans: the closest scan, and the 2 scans prior to and following the closest scan. This would represent the dominant radar signatures prior to, during, and after the flash. Hendry and McCormick (1976) noted that lightning flashes caused particles to reorient from vertically to horizontally in less than 1 second. Following a flash, it would also take a few seconds for particles to reorient vertically as the electric field built back up. This duration may change for storms with higher flash rates, but it suggests that majority of the time in between flashes, particles are not in their horizontal steady state. Thus, a time average of K_{DP} would capture the dominant values during which the electric fields were rebuilding or rebuilt prior to and following a flash. K_{DP} was computed from ϕ_{DP} using a three km least squares fit window developed by Addison Alford as an alternative to using the noisier K_{DP} produced by the IRIS software internal to SR2. The new method preserved key features. Z_{DR} and radar reflectivity were both converted to linear scales before averaging and then converted back to a logarithmic scale for plotting.

Various other statistics were produced from the radar images. The radar values within 150 m of an LMA point were averaged to get the associated K_{DP} values around

the LMA point locations. The dominant negative K_{DP} and maximum reflectivity regions were identified using Gaussian smoothing and interpolation to track the size and attributes of each area as the storm developed. Note that these filters were only used to identify the contour outlining the radar signatures of interest. Smoothed values in the regions were not used in gathering the value statistics of the regions. The negative K_{DP} regions were identified by values between -0.1 and -2.5 $deg\ km^{-1}$ and the reflectivity core was identified by values greater than 50 dBZ. These values were determined experimentally as the best values for the computer to use to identify the relevant regions.

Multi-flash composites were also produced to demonstrate the locations of many flashes relative to radar signatures lasting longer than the duration of five RHIs. Six consecutive flashes were selected and plotted onto the time average of all RHIs between two scans before the first flash and two scans after the last flash. Following that composite, the first flash was removed and the next flash in the sequence was added on top of the new time average of the RHIs. This process repeated until the last flash in the sequence was included. These plots were not consistent in the amount of RHIs that were averaged, but it revealed similarities in the radar signatures across multiple flashes.

Horizontal reflectivity data from the WSR-88D radar at the Jacksonville International Airport (KJAX) located on the northern edge of Jacksonville and 68 km NNE of ICLRT was used to supplement SR2 and give perspective as to the horizontal structure and location of the squall line.

2.4 Oklahoma Case Analysis Technique

The Oklahoma LMA (OKLMA) data was unusable for this case due to a random 1-sec time error in the GPS clock of some of the stations, but SR2 data was still able to be analyzed. Every five scans were time-averaged in the same manner as the Florida case. Area data was also recorded with the same filters and bounds. Horizontal reflectivity data from the WSR-88D radar in Oklahoma City (KTLX) located on the southeast edge of the city and 33 km ENE of ICLRT was used to supplement SR2 and give perspective as to the horizontal structure and location of the squall line. For this case, the SR2 ϕ_{DP} field needed to be unfolded because SR2 bounds were set from 0^o to 180^o. ϕ_{DP} exceeded 180^o on the downshear side of the reflectivity core, hence the folded values.

Chapter 3: Dataset Overview

3.1 Florida Squall Line

Based on the 1200 UTC sounding in Jacksonville, FL that was 80 km north-northeast of SR2 the 17 July 2012 squall line initiated in a tropical environment, with weak winds at most levels of the atmosphere over Florida, a moist vertical profile, and 1200 J kg^{-1} CAPE (Figure 6). The 1200 UTC sounding also showed the atmosphere initially had modest Convective Inhibition of about 80 J kg^{-1} of CIN, which likely eroded during the day through mixing. The later 00 UTC sounding is not shown because it was contaminated by the passage of another thunderstorm through Jacksonville. The 1200 UTC 500 mb upper air analysis (Figure 7) shows that cyclonic flow and lower heights existed over Florida, which may have provided some weak midlevel forcing to support initiation of the Florida squall line.

This Florida squall line formed in the broken line fashion (Bluestein and Jain 1985) and was relatively short-lived. Cells that formed the Florida squall line initiated at 1900 UTC five km southeast of SR2 (see Figure 8 for the 88D PPIs displaying the Florida squall line). By 1952 UTC, multiple thunderstorms had developed reflectivity values greater than 60 dBZ and an outflow boundary was visible on radar. At this time, SR2 began performing RHI scans approximately northward toward ICLRT through one of the cells shortly after it had passed SR2's location. The radar beam was approximately perpendicular to the convective line, which propagated northward at 20 kph. Individual cells moved westward at less than 5 kph. During this time, there may have been hail in the mid-levels of the storm, indicated by the hail spike (e.g. Zrnic 1987; Wilson and Reum 1986, 1988; and Lemon 1998) on the far side of the

storm from the radar (e.g. Figure 12(a)). Prior to this time, the only negative K_{DP} region appeared to be aloft slightly south of the reflectivity maximum. After this time, a second negative K_{DP} region developed aloft slightly north of the reflectivity maximum.

At 2011 UTC the cells congealed into a line and began to propagate with new cells developing on the north side of the complex just south of the boundary. This marked the end of its formative stage and the beginning of its intensifying stage (Leary and Houze 1979). Around this time, both the reflectivity maximum and negative K_{DP} regions weakened noticeably in the individual scans and time means (Figure 12(b)). Oscillations in the size and values of the negative K_{DP} regions and reflectivity maxima occurred throughout the mature phase of this storm. By 2044 UTC, the squall line had entered its mature stage, had developed a stratiform region extending south, and had an E-W diameter of about 70 km. At this point, the negative K_{DP} region aloft extended from above the convective region through the transition zone and into the stratiform region. The negative K_{DP} region on the north side of the storm had disappeared.

By 2112 UTC, the squall line had started to dissipate as the outflow boundary had surged well north of the convective line and northward propagation slowed. The large negative K_{DP} region on the stratiform side had disappeared and a negative K_{DP} region developed above a weak reflectivity maximum. The general relationship between the K_{DP} region and reflectivity maximums is addressed in Chapter 4.

The lack of vertical low-level shear perpendicular to the northward propagation of the squall line explains the short lifespan of this Florida squall line. A squall line

can be long-lived if the perpendicular environmental low-level shear can balance the shear generated by the cold pool and minimize updraft tilting (e.g. Rotunno et al. 1988, Weismann and Rotunno 2004). The Florida squall line's cold pool surged out ahead of the convective line because there was not enough low-level environmental shear to oppose the cold pool, as seen in the environmental sounding (Figure 6).

3.2 Oklahoma Squall Line

The Oklahoma squall line initiated in a convective environment just after 00 UTC on 18 September 2016. According to the 00 UTC Amarillo sounding from that day (Figure 9), there were veering winds in the low levels, a 100-kt jet at 250 mb, steep midlevel laps rates, 1914 J kg^{-1} CAPE, almost no CIN, and moist low levels. It can be expected that the CIN increased and the temperature decreased between the sounding launch and the squall line propagating through Amarillo, TX at 0400 UTC. Due to the lack of convection in the area apart from the squall line and slowly evolving upper level pattern, the sounding can be a good approximation of the environment the squall line propagated through. The 00 UTC 500mb analysis (Figure 10) shows a shortwave trough extended from northern Nebraska into the Texas panhandle. The region of positive vorticity was a source of lift that initiated the squall line. There was also a weak dryline extending through southeast Colorado that may have contributed to forming the initial cells.

Between 0000-0400 UTC the Oklahoma squall line formed in broken-line fashion (Bluestein and Jain 1985) similar to the Florida squall line and intensified. Here, however, the Oklahoma storm was longer-lived and traveled a longer distance

during its mature stage, which was reached at 0525 UTC when a second reflectivity maximum became visible in the stratiform region in the WSR-88D data. By 0750 UTC, the squall line was symmetric (Houze et al. 1990), extended 300 km in SW-NE direction and propagated at 40 kph to the southeast. Individual cells appeared to move north-northeastward at 10 kph. At this time, SR2 began scanning RHIs toward the south shortly after the convective line passed SR2's location (Figure 11). A large negative K_{DP} region was present aloft above the primary reflectivity maximum extending and sloping downward into the transition zone, but with a flatter slope than in the Florida squall line (Figure 13). This region persisted while SR2 scanned it, though its strength and size would fluctuate, and it often appeared to be made of multiple smaller pockets of negative K_{DP} rather than one large region. Oscillations in the negative K_{DP} region aloft and reflectivity maxima occurred in the Oklahoma squall line as in the Florida squall line. The Oklahoma squall line did not change in strength during the hour SR2 was scanning it.

3.3 Data Quality Concerns

Few datasets are flawless and this dataset is no different. This subsection describes negative quality aspects in the data worth noting and why they do not affect the results of this study.

a. **Scanning directions**. In the Florida case, the radar beam pointed perpendicular to the convective line, while the Oklahoma scanning strategy scanned at a 45° angle to the convective line. The analyses for these cases were conducted in the same way to observe the time evolution of the radar

signatures. Even though the storm orientation was very different, the cell motion was similar in both cases. In the Florida case, individual cells were almost stationary, moving west slowly. In the Oklahoma case, individual cells were moving north-northeast. In both cases, the time evolution of individual cells was accurately sampled since the cross-beam movement of the cells was not significant compared to the lifespan of each cell. It should be noted, however, that due to the non-perpendicular radar beam orientation, relative to the convective line orientation, resulted in the Oklahoma case sampling more cells within the convective region than was sampled in the Florida case.

b. **Far-side K_{DP} artifacts**. Throughout much of the data in both cases, there was a K_{DP} artifact comprised of extremely negative K_{DP} values on the far-side of the convective region adjacent to the reflectivity maximum and high positive K_{DP} values in the convective region (e.g. Figure 12). It is highly nonphysical to have vertically orientated equilibrium shapes for particles below the freezing level since raindrops are horizontally oriented due to drag from air resistance while falling. One of the only hydrometeors known to be vertically oriented in steady state is conical graupel (Zikmunda and Vali 1972). However, this precipitation sized hydrometeor would likely produce a region of negative Z_{DR} if it was present. It was found that Z_{DR} was not often negative in the regions with the negative K_{DP} artifact. Thus, the negative K_{DP} artifact was not associated with the hydrometeors present at that location. Instead, the negative K_{DP} artifact was the result of resonance in the heavy rain region producing

anomalously large ϕ_{DP} values in the convective cores, which caused the radial gradient of ϕ_{DP} to become negative on the far side of the convective region. Indeed, K_{DP} was also anomalously negative in the spaces between convective cores when individual cells were more isolated. Additionally, regions of weak reflectivity along the edges of the convective cells had noisy ϕ_{DP} values. The noise for the Florida case had ϕ_{DP} values in the range from 40° to 160°, which is much lower than the ϕ_{DP} values in the reflectivity maximum (greater than 130°). The noise induced drop in ϕ_{DP} contributed to the erroneously negative K_{DP} values on the far side of the convective region. This erroneous feature was generally confined to a narrow strip. Filtering out range gates based on low ρ_{HV} values (less than 0.9) enabled removal of most of this artifact.

c. **Melting level K_{DP} signature**. At and just above the melting level in the stratiform region in mature stage of both cases was a dipole band of K_{DP}. The positive band of K_{DP} values were found just below the reflectivity bright band and the negative band of K_{DP} values were found just above the bright band (Figure 12(c)). Some studies have explained this as resonance due to the beam passing through liquid coated large aggregates of ice in the melting layer (e.g. Ryzhkov and Zrnic 1998, Ryzhkov 2007). However, EMF soundings launched through the stratiform region have measured strong electric fields near the melting level (e.g. Stolezenburg et al. 1998a). Studies have observed cloud ice crystals in the region right above the melting layer (e.g. Willis and Heymsfield 1989), which may be tilting vertically in the electric fields above the melting

layer. Additionally, there were a couple flashes which propagated adjacent to the negative K_{DP} band in the Florida case (though, the flash points exceeded the 5 km distance from the RHI criteria applied in this study by 2-5 km and were filtered out), suggesting the K_{DP} feature may have been due to ice crystals aligning in electric fields instead of just an artifact of resonance. To determine if the negative K_{DP} regions above the melting level and further aloft were affected by resonance in the melting layer, ϕ_{DP}values were removed where ρ_{HV} was less than 0.90 and K_{DP} was recomputed. Filtering of values of ρ_{HV} below 0.95 (Figure 15) or 0.97 (Figure 16) resulted in too much data loss at the cloud edges and did not affect the upper level negative K_{DP} regions. It is important to note that K_{DP} is computed using a least squares fit to the radial distribution of ϕ_{DP} over a ± 1.5 km window from the point of interest. While many points were removed from ϕ_{DP} at the level of the bright band through the ρ_{HV} filter, the fundamental aspects of the K_{DP} dipole band near the melting region still remained, though weaker (Figure 15Figure 16). More importantly, the negative K_{DP} region aloft remained largely intact. Hence, the negative K_{DP} aloft does not appear to be significantly impacted by resonance effects at lower altitudes.

d. **ρ_{HV} at a distance**. Blanket filtering of ϕ_{DP} by ρ_{HV} worked well in the Florida case since all features were less than 30 km from the radar. However, the threshold had to be lowered to 0.8 for the Oklahoma case because too much data was being removed farther from the radar (> 50 km range; see Figure 17).

The inability for high quality correlation coefficient measurements at far ranges from the mobile radars is likely due to the relatively small reflector used on the mobile platform, which affects both the gain and the cross-pol isolation of the system. The motivation for the ρ_{HV} filtering was to evaluate the effects of resonance from the melting level on the K_{DP} values aloft. Filtering ρ_{HV} below 0.95 did not change K_{DP} within 30 km in either case (except for at cloud edges). This means that the loss of data at far distances due to ρ_{HV} filtering was not the result of resonance, but a hardware limitation. This hardware limitation justifies filtering on ρ_{HV} at lower values in the Oklahoma case to retain distant data for analysis. It should also be noted that the correlation coefficient values in the melting band were less than 0.8 in the Oklahoma squall line. Hence, most of the points that would have experienced resonance were likely removed using this lower threshold.

e. **Z_{DR} Fluctuations**. The SR2 radar experienced fluctuating biases in Z_{DR} for significant periods of time in the Florida dataset. The magnitude of the biases were as high as $\pm$ 2 dB. Furthermore, bias jumps sometimes occurred during an individual RHI scan. For other periods, the bias seemed to grow gradually before making a rapid transition. The cause of these fluctuations is undetermined. The radar had several receiver chain elements fail in the following year and the transmitter itself failed. It is possible that one of more of these components were in the process of failing during the data collection conducted in Florida. Fortunately, there was a 20 minute section of time in

which Z_{DR} displayed values consistent with expected patterns without fluctuations. All analysis of Z_{DR} for the Florida case came from this 20 minute period. The fluctuations in Z_{DR} do not appear to be correlated with any changes in the other variables. The radar reflectivity and Doppler velocity is computed from just the horizontal channel. The other dual-channel variables (correlation coefficient and differential phase) did not exhibit any detectable variation with regard to changes in Z_{DR} bias.

Chapter 4: Analysis

4.1 Florida Squall Line Lightning

There were forty-six flashes that met the four analysis criteria described in Chapter 2. Of the 46 flashes, 38 appeared to at least loosely follow contours in K_{DP} and were associated with regions of negative K_{DP}. Discussion on the errors which may have caused the remaining flashes to diverge from the rest can be found in Chapter 5.

Figure 18 is a conceptual model of the relationship between electric fields, charge density, and K_{DP}. It is based on the 1-D approximation to Gauss' law (e.g. Mashall and Rust 1991) (Eq. 2) and aides in understanding why most flashes followed the zero-K_{DP} contours.

(Eq. 2) $$\overrightarrow{E_z} = \frac{\partial \vec{E}}{\partial z} = \frac{\rho}{\epsilon}$$

The 1-D Gauss law relates the vertical gradient in electric field $\left(\frac{\partial \vec{E}}{\partial z}\right)$ to the charge density (ρ) and the permittivity of air (ϵ). The magnitude in electric field is maximized where the vertical gradient of the electric field changes sign between two charge layers of opposite polarity. This is demonstrated in many studies with EFM (electric field meter) soundings (e.g. Bruning et al. 2007, Lund et al. 2009). In accordance to equation (2), the altitude where the vertical gradient of the electric field is zero is also where the charge density is zero. If the negative K_{DP} regions are associated with an extremum in the electric field, then regions of negative K_{DP} are also regions of low charge density. Due to increasing charge symmetry towards the center of the individual charge layers, the magnitude of the electric field decreases towards

the center of the charge layers. The resultant vertical gradient in electric field implies a region of higher charge density (positive or negative) relative to the altitude of the extrema in the electric field associated with the negative K_{DP} region. Hence, the zero and positive K_{DP} areas surrounding the negative K_{DP} region would have comparatively higher magnitude of charge density than the negative K_{DP} region itself.

Thus, according to this conceptual model, lightning should initiate in the negative K_{DP} values where the electric field is the strongest (Kasemir 1960, Mazur and Ruhnke 1993, 1998) and propagate near the zero and positive K_{DP} values in regions of higher charge density (Kasemir 1960, Mazur and Ruhnke 1998, Maggio et al. 2005, Marshall et al. 2005, Lund et al. 2009).

4.1.1. Vertically Dominant flashes

The following are detailed descriptions of the most structurally interesting vertically dominant flashes. Mean K_{DP} products were used for this analysis to determine how lightning matched the most dominant K_{DP} signatures. The means were computed by taking an average of the five RHIs within narrow sector volume scans. The five RHIs included the RHI that began closest to and prior to a flash, the two RHIs prior to this nearest scan, and the two RHIs following the nearest scan. Logarithmic values of reflectivity and Z_{DR} were converted to a linear scale before computing the mean, which was then converted back to logarithmic value for display. These means will be referred to as 5-RHI means henceforth to distinguish from other averaged products. Additionally, the scans prior to and following each flash were examined to determine if the flash had an effect on radar inferred electric fields and

particle orientations in the cloud. Time series of areal extent and mean values of the two negative K_{DP} regions and the reflectivity maximum are shown in panels (h) and (i) in Figure 19-Figure 37. Area 1 is the transition zone K_{DP} region, Area 2 is the convective K_{DP} region, and Area 3 is the reflectivity maximum.

Figure 19 (b) shows a vertically oriented flash found within the convective K_{DP} region at 195301 UTC overlayed on the nearest 5-RHI mean K_{DP}. This flash occurred in the squall line's formative stage. Flash initiation (indicated by the pink star) occurred inside the southern side of the convective K_{DP} region. This would suggest it initiated in a region of particles that were vertically tilted by the electric field. Initiation was not within the most negative K_{DP}.

Branching out upward from the initiation point were two channels that propagated through a region of positive charge (based on analysis of the channel behavior described in Chapter 2.3). One of these channels followed the top of the convective K_{DP} region, presumably propagating through a region of weaker electric fields and possibly higher charge than would be found in the most negative K_{DP} area. The other branch entered a region of positive K_{DP}, which would suggest horizontally oriented particles that were not being tilted strongly by the electric field. Branching downward from the initiation point was one main channel propagating through a region of inferred negative charge. This channel followed the bottom of the negative K_{DP} region along the zero K_{DP} contour before descending into a positive K_{DP} region. Like the upward channel, this suggests the channel propagated through a region of lower electric fields and likely higher charge than where the flash initiated.

Figure 20(b) and Figure 21(b) show individual RHIs that most closely bracket (scans began fourteen seconds prior and three seconds after) the time of the flash. Initially, the convective K_{DP} region was rather strong with a mean value across the region of -0.63 deg km^{-1} with an areal extent of 5.79 km^2. After the flash, it weakened to -0.40 deg km^{-1} with an areal extent of 0.48 km^2. This decrease in both the size and magnitude of the K_{DP} region is indicative of the particles becoming more horizontally oriented in the weakened electric fields following the flash. In this data set, sampling so close in time to the actual flash was relatively uncommon. Thus, there were few opportunities to observe this rapid change in K_{DP}. Additionally, the subsequent scan showed an even stronger convective K_{DP} region, indicating a rapid recovery of the electric field. This was a relatively isolated flash in terms of the time before and after it occurred. No flash extended into the region around the convective K_{DP} region for twelve seconds before the 195301 flash, and twenty-four seconds after. There was a weak flash that occurred above the transition zone K_{DP} region four seconds after, after but it remained isolated from the convective K_{DP} region. Even if the 195305 flash affected the convective K_{DP} region, the fifteen second RHI began one second prior to the flash, and the fields still appeared weaker in the convective K_{DP} region, as expected following a flash. While it is appropriate to identify this positive increase in K_{DP} as direct result of the isolated flash, it should be noted that electric fields within strong convection are known to recover in a few seconds following a flash. Moreover, the flash rate of the storm (approximately 10-15 flashes per minute) was fast compared to the time it took to sample an RHIs (15 seconds). Given the longer sampling period

of the radar, it is difficult to assign each change observed by radar to a specific flash. The effect of temporal sampling is discussed further in section 4.1.3.

Figure 22(b) shows a vertically dominant flash around the transition zone K_{DP} region overlayed on the nearest 5-RHI mean K_{DP}. The flash initiated in negative K_{DP} values near the top of the cloud during the formative stage of the squall line at 195651 UTC. One branch extended upward from the initiation point into a region of inferred positive charge and clustered near the cloud edge in mostly weak positive K_{DP} values. Another branch extended downward from the initiation point into a region of inferred negative charge, following the zero-K_{DP} contour with a slight positive bias, implying propagation through weaker electric fields and higher charge.

Figure 23(b) and Figure 24(b) show the scans immediately prior to (by fifteen seconds) and following the flash (by ten seconds). Unlike the last flash, the transition zone K_{DP} region did not appear to change much. This may be explained by the fact that the post-flash scan started ten seconds after the flash, which gave fields enough time to recover before being sampled by the radar. It is not due to another flash since there was not one in the storm for over thirty seconds before and after the 195651 flash. Other aspects of the K_{DP} field did change, such as the small negative K_{DP} pocket near the cloud tops and the positive K_{DP} values above the reflectivity maximum, possibly a longer lasting change caused by the flash or a limit in horizontal symmetry of K_{DP} in this stage of the storm. Regardless, the more dominant transition zone K_{DP} region did not significantly change. This suggests that charge may be regenerated quickly in this area, or that the flash did not consume enough charge to significantly alter the broader electric field.

Figure 25(b) shows a vertically dominant flash overlayed on the nearest 5-RHI mean K_{DP}. It initiated in the intensifying stage of the squall line at 202431 UTC on the north side of the transition zone K_{DP} region in weak positive K_{DP} values. Several branches extended upward from the initiation point into a region of inferred positive charge and positive K_{DP} values. Other branches extended downward from the initiation point through a region of inferred negative charge and positive K_{DP} values, matching a similar shape as the zero-K_{DP} contour. The tendency for these lightning channels to propagate through positive K_{DP} surrounding the negative K_{DP} area is consistent with the other flashes and with the tendency for flashes to propagate into regions of high charge density, as proposed conceptually in Fig. 19.

Figure 26(b) and Figure 27(b) display the scans immediately prior and following the 202431 flash. The transition zone K_{DP} region was much more extensive prior to the flash, to the point that the initiation point was in weakly negative K_{DP} values. Following the flash, the K_{DP} values in this region are more positive and the transition zone K_{DP} region receded south slightly. This is similar to the first flash in that SR2's post-flash scan may have been close enough in time to the flash to capture the weaker fields following the flash. No flashes occurred for thirteen seconds following the 202431 flash, but a flash did occur six seconds prior and was horizontally dominant. Fortunately, based on where the radar beam was located when this prior flash occurred, Figure 26(b) still adequately represents the K_{DP} field prior to both flashes.

These three vertically dominant flashes exhibited two traits that were not typical of horizontally dominant flashes: (i) all of the 11 vertically dominant flashes in

the dataset initiated and propagated around a region of negative K_{DP} that itself was not horizontally extensive and (ii) the lightning channels did not have a preference in the horizontal direction they propagated when they did branch horizontally. It should be noted that K_{DP} regions grew larger horizontally as the squall line evolved into the mature stage, and simultaneously flashes became more horizontally dominant.

4.1.2. Horizontally Dominant flashes

Detailed descriptions of the most structurally interesting horizontally dominant flashes in presented here. Flashes were analyzed in the same way as vertically dominant flashes.

Figure 28(b) illustrates a horizontally dominant flash overlayed on the nearest 5-RHI mean of K_{DP}. This flash initiated at 195026 UTC during the formation stage of the squall line on the south side of the convective K_{DP} region in negative K_{DP} values. Similar to vertically dominant flashes, channels extended upward through the inferred positive charge region and downward through the inferred negative charge region. However, after initially travelling vertically, the channels sloped downward toward the south where old updrafts were dissipating. The channels propagated with the zero-K_{DP} contours with a slight bias toward positive values above and below the negative K_{DP} values of the convective K_{DP} and transition zone K_{DP} regions, which were loosely connected. Propagation through slightly positive K_{DP} values is consistent with the vertically dominant flashes and indicates the flashes propagated through weaker fields than found in the negative K_{DP} region and likely higher charge density than would be found within the core of the negative K_{DP} region.

Figure 29(b) and Figure 30(b) are the closest RHIs prior to and following the flash. Similar to the first and third vertically dominant flash examples from the previous subsection, negative K_{DP} values were greater prior to the flash and weakened drastically following the flash. The second scan began sampling right as the flash occurred and arrived at the flash location after approximately 8 seconds. The flash also seemed to shift the convective K_{DP} region farther north, suggesting that a significant part of the charge may have been dissipated on the southern end of the convective K_{DP} area. There were no flashes eighteen seconds prior and ten seconds after the 195026 flash, so the entire region the lightning propagated through would have been sampled by the radar sweep before the next flash affected the K_{DP} field. Even so, the next flash was more compact and was located four kilometers west of the 195026 flash and may not have affected the charge regions within the radar sweep.

Figure 31(b) shows another horizontally dominant flash overlayed on the closest 5-RHI mean of K_{DP}. The flash initiated at 203925 UTC in the negative K_{DP} values on the northern side of the transition zone K_{DP} region. From the initiation point, branches extended upward into the inferred positive charge region and downward into the inferred negative charge region. These branches propagated along the zero-K_{DP} contour through positive K_{DP} values, surrounding the transition zone K_{DP} region. Portions of the branches extended northward slightly, but the majority of the horizontal extent was southward through the transition zone toward the stratiform region. This is similar to the previous horizontally dominant flash in that the flash propagated toward the region where old cells were dissipating. This may be the result of advection carrying charge from the convection region to the stratiform region,

though the residual convective motions may also have produced charge in-situ. The charge advection hypothesis is supported by the fact that charge regions descend in altitude toward the rear of the stratiform region, as would charged particles from dissipating convective cells. However, multiple flashes similar to this one propagated through the transition zone and stratiform region. Charge advection by itself may not be sufficient to explain the regeneration of the charge region as quickly as was inferred from the radar diagnosed electric fields associated with the negative K_{DP} area. Hence, other processes may be involved in restoring charge in these regions.

Figure 32(b) and Figure 33(b) are RHIs prior to and following the 203925 flash. Similar to the previous flashes, the transition zone K_{DP} region was largest prior to the flash and weakened significantly following the flash. In this case, the K_{DP} region seemed to break up into many smaller pockets of negative K_{DP} values. It is possible the flash left pockets of charge in the cloud that created localized regions of strong fields. Regardless, the majority of the charge was depleted. There could have been other processes occurring as well, since the post scan started seven seconds after the flash initiated and this flash initiated when the squall line had a relatively high flash rate of eleven flashes per minute. No flashes traversed the same area of the squall line as the 203925 flash did within twenty-one seconds prior to and thirty seconds after this flash. There was a flash four seconds prior and another flash fourteen seconds after, but they propagated at least five km from the 203925 flash and were at least ten km from the radar cross-section. The extent of horizontal symmetry of squall line K_{DP} signatures has not been investigated nor has the distance at which lightning affects the resultant electric field within a cloud, so it is difficult to state

whether or not these flashes affected the electric fields from a distance. However, the K_{DP} fields sampled suggest these flashes did not have the same impact on the local electric fields as the 203925 flash did. The areal extent of the transition zone K_{DP} region grew in the twenty-five seconds prior to the flash before decreasing rapidly as elucidated in the scan following the flash (see time series subplot (h) in Figure 32 and Figure 33). Nevertheless, it should be noted again that the time scale of electric field evolution is much shorter than the radar scan times, making it difficult to relate the observed changes in K_{DP} to specific lightning events as the flash rate increased.

Figure 34(b) showed another horizontally dominant flash overlayed onto the closest 5-RHI mean K_{DP}. The flash initiated at 204225 UTC in negative K_{DP} values at the center top of the transition zone K_{DP} region. Like the previous flashes, branches extended into the inferred positive charge region above and inferred negative charge region below the transition zone K_{DP} region. While the branches sloped downward toward the stratiform region following the zero-K_{DP} contour with a positive bias like the previous flash, the branches also extended well into the convective region. This "slanted-I" shape appeared in other horizontally dominant flashes. Charge advection and particle fall speed could explain the slope of the negative K_{DP} region and inferred charge regions, but not the rapid regeneration of charge throughout the squall line. It appears that both the transition zone and stratiform regions have in situ charge occurring. Given the continuity of the slope of the radar and lightning features, the charging mechanisms in these parts of the squall line are likely similar to the primary charging mechanisms within the convection

Figure 35(b) and Figure 36(b) are the scans of K_{DP}, which started immediately prior to the 204225 flash. Both are shown because the flash occurred in the middle of sampling Figure 36(b). The radar beam was descending from approximately 5^{o} elevation above the flash initiation point when the flash occurred. Despite this, the transition zone K_{DP} region did not change much between Figure 35(b) and Figure 36(b). In fact, the areal extent of the transition zone K_{DP} region increased between the two scans. It is possible that the charge regions strengthened between Figure 35(b) and Figure 36(b), and this flash did not consume enough charge to significantly alter the electric fields.

Figure 37(b) shows the K_{DP} field following Figure 36(b). It is interesting that the areal extent of the negative K_{DP} region weakened significantly between those scans. A strong flash did occur nearby was at 204237 UTC, twelve seconds after the 204225 flash, which would have occurred early in sampling Figure 37 when the radar beam was at a low elevation angle and ascending. This second flash was over three km from the 204225 flash and over seven km from the radar beam. This implies that not all flashes affect the negative K_{DP} regions the same way, and that some flashes are strong enough to affect the electric fields of a storm even from seven kilometers away.

Horizontally dominant flashes exhibited two traits not commonly found in vertically dominant flashes: (i) 23 of the 29 horizontally dominant flashes initiated and propagated where the negative K_{DP} region(s) was horizontally extensive, possibly indicating horizontally extensive charge regions as K_{DP} became more horizontally extensive in the later stages of the squall line. The other six flashes did not propagate around a negative K_{DP} region. This is unusual because there should have been electric

fields and negative K_{DP} around the regions of charge the lightning propagated through. These six flashes are part of a set of eight outlier flashes and are addressed in chapter 5. (ii) the lightning channels sloped downward toward the stratiform region more than they extended into the convective region, possibly due to the front to rear flow of the squall line advecting charge rearward along with sedimentation as the dissipating cells became more shallow towards the rear of the transition zone.

4.1.3. Flashes within a Sweep

One way to definitively show that electric fields affect K_{DP} is to capture a change in K_{DP} due to a lightning flash in the middle of SR2 sampling the negative K_{DP} region. RHIs took 14-15 seconds to collect, and occasionally, the flash rates increased to 15 flashes per minute. Only 46 flashes met the four flash analysis criteria outlined in Chapter 2, but there were still other flashes in the near proximity of the radar sweeps and could have affected the local electric fields and resultant K_{DP}. This was part of the motivation for analyzing K_{DP} and flashes using the 5-RHI means, since the means would capture the dominant, more slowly varying regions of K_{DP}. It could then be shown that the flashes were strongly associated with those dominant features without needing to determine the effects of every flash in the storm.

It was found that ray-by-ray changes in K_{DP} due to a flash were only significant if the flash nearly exactly intercepted the radar beam spatially and temporally. If there was not an exact intersection , the only way to determine if a flash affected the negative K_{DP} regions was to analyze the scan prior to the flash and after (as performed in section 4.1.2). There were nine flashes that occurred in the middle of

collecting RHIs where the radar beam was near the flash location spatially and temporally. Only one of the nine flashes intersected the radar beam.

Figure 39(a) shows this flash overlayed on the K_{DP} field, where the beam is ascending. At around 10 km north from the radar and 4-5 km above the ground, there was a visible couplet of relatively extreme K_{DP} values. The flash channels pass through the radar beam at this location and cause a visible effect on the K_{DP} field. Following the intersection, as the beam continued to ascend weak positive K_{DP} values were recorded instead of the extreme negative K_{DP} values that would otherwise have been expected. This suggests that that the electric fields weakened and particles returned to horizontal orientation in less than a tenth of second (time between rays). The strong positive K_{DP} values were not present in the previous scan (Fig. 39a), indicating that they were induced by the flash.

For flashes that occurred near the location of the radar beam as it was sampling the negative K_{DP} region, K_{DP} values are expected to become more positive since a flash would deplete charge, weaken the electric field, and cause particles to return to horizontal orientation. Measurements by Mendez (1969) and Hendry and McCormick (1976) showed that particles returned to horizontal steady state in fractions of a second following a flash, but it took sometimes as long as 10 seconds for the fields to return to a similar strength as before the flash. Note that the 10 seconds would vary with charging rate, but it is much longer than the time it takes for particles to return to horizontal.

The effects of lightning on the K_{DP} field can be more complex. Lightning may not deplete all the charge in a region, and instead may cause non-uniform charge

distributions, or gaps, in existing layers of charge (Mansell et al. 2010). This would leave irregular electric fields before mixing and charging mechanisms homogenizes the charge distribution. The scan time durations are relatively long compared to the time scales of electric field changes due to lightning flashes.

4.1.4. Multi-flash Composites

Figure 42 shows a multi-flash composite for 203305-203925 UTC, during the squall line's mature stage. Five initiation points occurred in the upper portions or north of the transition zone K_{DP} region. The sixth was just above the melting level in the reflectivity maximum and initiated a cloud-to-ground strike. At this point, both branches showed visible downward sloping toward the stratiform region. Both branches propagated in positive K_{DP} values following the zero-K_{DP} contour, "hugging" the transition zone K_{DP} region. It should also be noted that the initiation points, channels, and the negative K_{DP} region are farther north than earlier in the squall line's life cycle.

Figure 43 shows a multi-flash composite for 204917-205721 UTC, as the squall line approached its dissipation stage. Five initiation points occurred in the transition zone K_{DP} region, and the sixth was just above the melting level in the reflectivity maximum associated a cloud-to-ground flash. The negative K_{DP} region seems much more disorganized than in the mature stage. The lightning channels still slope downward toward the stratiform region loosely following the zero K_{DP} contours.

The most notable detail in Figure 40-Figure 43 is the fact that the K_{DP} regions were surrounded by two horizontally stratified layers of charge throughout all stages

of the squall line life cycle. These horizontal layers would cause the vertically oriented electric fields that tilt ice crystals and show up as negative K_{DP} regions in SR2 RHIs. The fact that the lightning flashes and negative K_{DP} regions move northward and are always together suggests that the negative K_{DP} regions depict the general locations of the electric fields that cause the lightning.

It should be noted that the effects of the northward propagation of the squall line and the composite means using scans during a timespan as long as 3-9 minutes caused some of the negative K_{DP} signal to be lost due to averaging between negative and positive values on the edges of the negative K_{DP} regions. This made the zero-K_{DP} contours much thicker than in previous figures. Because of the northward and sinking movement of the K_{DP} regions with time, it can be inferred that zero-K_{DP} values on the north and north-lower sides of the negative K_{DP} regions are becoming negative with time by the effects of propagation, and zero-K_{DP} values on the south and south-upper sides of the negative K_{DP} regions are becoming positive.

4.1.5. General Distributions of Radar Values

There are numerical patterns worth noting in the radar values associated with lightning channels. The nearest bins within 150 m of each LMA point were interrogated to generate time series and histograms. Panel (g) of Figures Figure 19-Figure 37 are of histogram distributions of the K_{DP} values closest to the LMA sources. The distribution for 5-RHI mean scans was found to be much more narrowly centered on the mean than the single scans. However, the means of the K_{DP} values that flashes propagated through were near zero for both 5-RHI mean scans and single scans, with a

slight positive bias on the order of 0.2 deg km^{-1}. This suggests that flashes propagate through weak positive K_{DP} values, as seen visually earlier in the analysis.

Figure 44 shows a histogram of the values of K_{DP} for the 5-RHI mean scan and closest single scan prior to the flash at the location of the initiation point. The 5-RHI mean had a mean initiation K_{DP} value of 0.053 deg km^{-1} and the closest single scan had a mean initiation K_{DP} value of 0.042 deg km^{-1}. Both of these values are very close to zero, suggesting that flashes initiate where there would be some electric fields to rotate particles to 45^{o}, but not necessarily the strongest electric fields as would be expected in the more negative K_{DP} regions. It is possible that other flashes are interfering with the K_{DP} fields prior to the flash being analyzed. The 5-RHI means depict the most slowly varying K_{DP} signatures over an 80-second period, but rapidly changing areas are smoothed out or simply not captured by the radar.

Another factor of note are the Z_{DR} values in the negative K_{DP} regions. Figure 45 shows a time series of Z_{DR} during the period when it was reliable. It was found that the mean Z_{DR} was approximately 0 dB for both K_{DP} regions, suggesting that the particles in these regions were in fact ice crystals and not conical graupel. This supports the concept that negative signatures in K_{DP} are due to vertical alignment of ice crystals induced by electric fields.

4.2. K_{DP} Structure and Evolution of Oklahoma Squall Line

Figures Figure 46-Figure 49 show the K_{DP} fields of the Oklahoma squall line as it progressed southward from the radar. These figures were picked to illustrate the various characteristics of the negative K_{DP} regions as the squall line progressed.

One detail of note is that the convective K_{DP} region that was well established in the Florida squall line was often absent in the Oklahoma squall line. Even in Figure 48, there appears to be a developing negative K_{DP} region ahead of the main reflectivity maximum, but this is actually the north (upshear) side of a new reflectivity maximum developing aloft. This may be due to the environment and propagation speed of the Oklahoma squall line compared to the Florida squall line. The Florida environmental wind was weak, the squall line propagated slowly, and the individual cells were close to stationary, moving parallel to the convective line. This may have caused some charged particles to be advected both behind and a little ahead the squall line's convective line. The Oklahoma environmental wind was strongly westerly and veered with height in the low levels. Additionally, the Oklahoma squall line propagated twice as fast as the Florida squall line with the individual cells moving rearward away from the convective line. It is possible that charged particles were advected toward the stratiform region and the upper level flow did not advect a significant amount of charged particles ahead of the convective line. Without sufficient amounts of charged particles ahead of the convective line, electric fields would be weak and negative K_{DP} would not appear in this region.

Another interesting detail is that the transition K_{DP} region was often broken into smaller pockets and was not as contiguously elongated as in the Florida squall line. This is possibly due to the faster propagation speed of the Oklahoma squall line extenuating the spacing between individual updraft cells. But it also appears that the distribution of charging within the Oklahoma squall line was different from the Florida squall line. For much of the time it was sampled by SR2, the squall line had relatively

weak reflectivity above 6 km altitude. Hence, there may have been less graupel aloft in the part of the Oklahoma squall line sampled by SR2 than was in the part of the Florida squall line sampled by SR2. Both early (Fig. 47) and then late (Fig. 50), the 40 dBZ contour extended to greater altitudes and the negative KDP region was more extensive than for the times shown in Figs. 48-49.

Additionally, as the cells within the Florida squall line were nearly stationary with respect to the ground, it is possible that the transition zone K_{DP} region from the Florida squall line was the conglomeration of smaller negative K_{DP} regions that would normally be associated with individual cells like in Figures Figure 47 and Figure 48. Individual updrafts would generate ice crystals, supercooled droplets, and graupel that are the necessary ingredients for charge separation. It is possible that the resulting high-density charged particles remained mostly with their original cell while the lower-density particles were advected rearward consistent with the large, smooth sloping charge region in the conceptual models of Biggerstaff and Houze (1991a) and Stolezenburg (1998a) and consistent with the observed transition zone K_{DP} region in the Florida squall line.

One way to test if there was a simple relationship between negative K_{DP} areas aloft and precipitation-sized hydrometeors within individual cells is to examine correlations between the size and magnitude of the negative K_{DP} regions and the reflectivity maximas associated with the cells.

4.3. Area Analyses of K_{DP} and Reflectivity in both Squall Lines

An attempt was made to find correlations between the negative K_{DP} regions and the reflectivity maxima of the squall lines. These regions were identified by isolating the zero-K_{DP} and 35 dBZ contours above the melting level using multiple Gaussian smoothing techniques. The cross-sectional areal extent, means, height, center distance, and most extreme values for each region were computed and presented as time-series plots in Figures Figure 50-Figure 55 for the Florida squall line and Figure 56-Figure 60 for the Oklahoma squall line. Correlations were made between the transition zone K_{DP} region and the reflectivity maxima (Table 1). Correlations with the convective K_{DP} region were not included because none were statistically significant. This may be due to the fact that the convective K_{DP} region was not always present and fluctuated strongly. However, some of the correlations between the transition zone K_{DP} region and the reflectivity maxima were statistically significant.

The areal extents of the reflectivity maxima and transition zone K_{DP} region had a moderate correlation for both cases: 40.7% in Florida and 77.3% in Oklahoma. This implies that the transition zone K_{DP} region grew as the reflectivity region grew to a certain extent. Such a pattern is somewhat illustrated in Figure 50 and Figure 56. While the lower-frequency inflections do seem to follow each other loosely, the correlation is not obvious. The development of a new cell may cause a growth in the negative K_{DP} region because it would have created additional charge separation and more ice crystals to be tilted in the electric field. However, reflectivity is most strongly affected by larger particles. Higher reflectivity would not necessarily indicate that more ice particles are being injected into the upper levels, but possibly larger

ones. If lower density charged particles did develop in the new cells, the increase in upper level divergence induced by a new cell would advect smaller particles into the transition zone along trajectories as described by Biggerstaff and Houze (1991a). This would lead to more extensive charge regions and a growth in the transition zone K_{DP} region. Unfortunately, it is not possible to accurately determine the size distribution of cloud ice particles from radar reflectivity and verify that this is the reason for the areal extent correlations.

The mean values in both regions had weak correlations in both cases. The only statistically significant correlation was achieved by lagging the K_{DP} time series by 7.65 minutes, and the correlation was still only -43.5%. The inverse correlation could be explained by the fact that an increase in reflectivity could suggest an increase in particles. This could cause more charge separation through collisions, which would lead to increased electric fields and the negative K_{DP} region. Thus, an increase in reflectivity value could lead to a decrease in K_{DP} value. However, the correlation is weak and it was hardly present in the Oklahoma case. This inverse correlation is somewhat apparent in Figure 52, where the K_{DP} y-axis has been flipped to more easily see the peaks and valleys that align. Even visually, there appears to only be a weak relationship.

Mean height had moderately-high correlations of 57.9% and 83.8% for the Florida and Oklahoma cases, respectively, without any time lag. This would suggest that descending reflectivity maxima lower the charge region through the life cycle of the cell. The oscillation in heights due to new cells developing aloft can be seen visually in Figure 53 and Figure 58.

Mean distance had high correlations above 90% in both cases without time lag. This is because both the reflectivity maxima and transition zone K_{DP} region propagated with the storm.

Most extreme values of each region had almost no correlation. It is likely that many complex processes could cause large local fluctuations in reflectivity without affecting the storm electric fields.

Overall, there was at least moderate correlation between the transition zone K_{DP} region and the reflectivity cores in areal extent, mean height, and mean distance. Thus, it is reasonable to entertain the possibility that the transition zone K_{DP} region was associated with or affected by individual convective cells. However, the evolution of electric fields may change at a faster rate compared to updraft cell life cycles. While there may be a link in the long-term fluctuations of both features, the long term signal experienced high frequency fluctuations as a result of other processes. These may include microscale charging mechanisms, mixing from cell interactions, or affects from non-sampled features adjacent to the RHIs. Such difference in timescales between the K_{DP} region and reflectivity may also have prevented higher correlations.

Additionally, reflectivity may be too simple of a measurement to depict the amount of graupel, ice crystals, or supercooled water droplets available for interactions to cause charging. A possible way to achieve higher correlations would be to find how many of each type of hydrometeor exist in the upper portions of the updraft region. Unfortunately, size distributions are difficult to compute for frozen particles due to the low dielectric factor which limits the utility of differential radar reflectivity for estimating particle size distributions. Moreover, cloud particles do not have sufficient

size to significantly affect radar reflectivity. It may be possible to look at graupel volume using a dual-pol hydrometeor classification algorithm, and correlating that with the negative K_{DP} regions. A hydrometeor classification analysis would be tedious to perform using this dataset since Z_{DR} had a non-steady bias, but it could possibly be better related to the charging better since graupel-ice collisions is a significant mechanism for charging in the convective region (e.g. Saunders 1993).

Most correlations were not strong for this study, but improvements could be made to the methods in future studies to possibly obtain stronger relationships and to better evaluate how individual convective cells are related to the physical characteristics of the negative K_{DP} regions.

Chapter 5: Discussion

5.1 K_{DP} and Lightning Flashes

Thirty-eight of the forty-six flashes propagated along contours in K_{DP}, usually initiating in an area of near zero K_{DP} in or adjacent to a major negative K_{DP} region and propagating into positive K_{DP} values that surrounded the negative K_{DP} area.

Initiation is expected to occur in the area with the largest electric fields (e.g. Kasemir 1960; Leob 1966; Mazur and Ruhnke 1993, 1998). The strongest electric fields can orient larger particles (Weinheimer and Few 1987). Since thunderstorm charge regions are believed to be predominantly horizontally stratified (e.g. as in the squall line charge conceptual model in Stolezenburg et al. 1998a), electric fields are assumed to have the strongest component in the vertical direction. Strong vertical orientation of particles in the upper area of clouds prior to a flash has been observed by Krehbiel et al. (1996) and others.

In this study, lightning did not always initiate in the region of strongest vertical orientation, which presumably would be associated with the strongest electric field. The average K_{DP} value in the 5-RHI means associated with the initiation point was 0.053 deg km^{-1} (Figure 44), and while near zero K_{DP} values indicate some (~45°) vertical tilting of ice crystals, it was not the strongest vertical alignment signature that was observed. The conceptual model in Figure 18 suggests the zero K_{DP} contour around the negative K_{DP} region is not where the maxima in electric field would be located. Instead, the initiation points appear to be farther into the positive charge regions. It is possible that the electric field and charge regions changed too drastically prior to the flashes to be depicted in the 5-RHI means. Moreover, the 3-km scale of

the least-square fit window in computing K_{DP} may have smoothed the gradients between negative and positive K_{DP} regions, making it difficult to infer too much about the magnitude of the electric field at the initiation location. However, it is interesting that initiation points occurred inside or adjacent to the dominant negative K_{DP} regions depicted in the 5-RHI means. This suggests that the broader scale character of the negative K_{DP} region and implied electric fields did not change too drastically prior to a flash.

Flash channels were found to propagate through positive K_{DP} values usually surrounding the negative K_{DP} region. The mean K_{DP} value that flashes propagated through was 0.242 deg km^{-1} (Figure 69), and all but three flashes averaged propagating through positive K_{DP} values. This is consistent with the conceptual model in Figure 18 since zero and positive K_{DP} contours around the negative K_{DP} region correspond to regions of changing and weaker electric fields than the maximum. Though the 1-D approximation to Gauss' Law (Eq. 2), this corresponds to a region of high charge density. Lightning propagates through high charge density regions (Kasemir 1960, Mazur and Ruhnke 1998, Maggio et al. 2005, Marshall et al. 2005, Lund et al. 2009). However, flash channels did diverge from zero-K_{DP} contours and branch well into the positive K_{DP} regions. According to (Eq. 2) if there is non-zero charge density, then the electric field must be changing with height. However, electric fields can still change with height in a region of uniform charge density without becoming strong enough to rotate ice crystals. This is conceptualized in the vertical profiles of electric field and charge density in Figure 18. There is significant positive charge density aloft even in the region where electric fields do not change much with height.

It should be noted that flash leaders seek out the highest charge densities in a local area relative to the flash leader. A flash leader depletes the charge of a region it enters and alters local electric fields since lightning can be modeled as a charged conductor. This allows a flash leader to seek regions of charge that are locally high, even if they are not the greatest charge density in the squall line. Experiments by Williams et al. 1985 revealed that lightning jumps from charge region to charge region once consuming charge locally. Recent lightning modeling simulations have produced relatively realistic flash behaviors by allowing flash leaders to alter local electric fields and charge regions as they propagate (Mazur and Ruhnke 1998, MacGorman et al. 2001, Mansell et al. 2002, Mansell et al. 2010). Indeed, lightning can propagate through regions of positive K_{DP} values aloft, which it is hypothesized may contain only locally rich pockets of charge.

The eight flashes that did not propagate around a negative K_{DP} region were generally different from those that did. Five of the eight flashes initiated and/or propagated along the edge of the clouds and K_{DP} field (Figure 61-64, 66-67). The flashes may have propagated through charge in the screening layer of clouds. The screening layers were not diagnosed by the radar K_{DP} field for several reasons. First, filtering of K_{DP} on ρ_{HV} removed most edge values. Second, computing K_{DP} from ϕ_{DP} using a 3-km wide least squares fit led to erroneous values when ingesting noisier ϕ_{DP} values on the edges and outside the cloud. This made it difficult to separate electric field effects from data uncertainty. Third, screening layers are thin, based on inferred measurements from electric field meters (e.g. Vonnegut et al. 1962, Marshall et. al. 1989, Marshall and Rust 1991) and may be weak compared to the magnitudes needed

to tilt ice crystals. Fourth, fewer crystals on the edge of the cloud would lead to less rotation of ϕ_{DP} and there would not be precipitation-sized particles present to back-scatter the forward-scatter phase shift if it did occur. Many of the charged particles in the screening layer are aerosols, which would not be observable by cm-wavelength weather radars even if the electric fields were strong.

One of the remaining three flashes was a bidirectional cloud-to-ground flash (see Figure 67), structured with the upward branch extending into a negative charge region, and the downward branch extending to the ground through positive charge. Both branches extended through mostly positive K_{DP} values; however, the signature at this altitude does not indicate that electric fields were weak. Since the melting level was at around 6 km in the convective region, the downward propagating branch was extending through rain, which would cause positive K_{DP} values since falling rain drops are oblate spheroids. The upward branch did follow the zero-K_{DP} contour like other flashes with a positive bias, but this is again close to the melting level. It is possible the particles were either liquid water, coated in liquid water, or precipitation-sized aggregates. Thus, it is not possible to attribute the positive K_{DP} values to horizontal alignment from weak electric fields in this region.

The final two flashes (see Figures Figure 64 and Figure 68), did propagate in a manner to avoid negative K_{DP} regions but mostly travelled through regions of positive K_{DP}. The first flash (Fig. 65) initiated near a small, negative, convective K_{DP} region with several of the LMA sources propagating around the negative K_{DP} region, as in the other analyzed flashes. But here, there was also a cluster of sources along the front-edge screening layer and several LMA sources that appeared to extend rearward

towards the transition zone negative K_{DP} region. This combination of flash activity gave an unusual appearance to the propagation of the flash relative to the overall K_{DP} field. In the later flash (Fig. 69), the flash activity was also diverse. The flash initiated at a relatively low altitude (about 6.8 km) near the bottom edge of the forward part of the transition zone negative K_{DP} region. Much of the negative leader navigated around regions of negative K_{DP} that sloped rearward through the transition zone. However, one branch of the negative leader propagated forward and tapped into the forward-edge screening layer. Meanwhile, the positive leader propagated into inferred negative charge in regions of relatively high radar reflectivity that would mask any electric field effect on K_{DP}. The complex nature of these two flashes made generalization about the relationship between K_{DP} and flash structure difficult to ascertain.

As mentioned earlier, one of the biggest problems with analyzing flashes projected onto K_{DP} RHIs is the time difference between the evolution of electric fields and the scan time. This is problematic not only because of electric fields changing rapidly prior to and following a flash, but also because of contamination from other flashes. Several flashes in this study's dataset which met the analysis criteria outlined in Chapter 2 had other flashes in the same region of the squall line within a few seconds prior to or following the analyzed flash. Thus, the radar-observed changes in K_{DP} may not have been due entirely to the specific flash being analyzed. It is likely the radar did not depict rapid changes in the electric field due to the difference in scan time and electric field evolution time. Measurements by Mendez (1969) and Hendry and McCormick (1976) found that ice crystals reorient to horizontal in less than a

second, and return to vertical in a few more seconds or less. Fifteen-second RHIs cannot capture such rapid changes.

To compensate for the mismatch in sampling frequency compared to the frequency of the phenomena, the flash structures were compared to 5-RHI mean fields. This time and spatial average helped delineate the stronger and slower varying part of the negative K_{DP} region. Overall, the lightning propagated as expected within the 5-RHI means, but not perfectly.

Another factor that negatively affects the analysis is the extent to which it is reasonable to apply horizontal symmetry of K_{DP} signatures along the convective line. The east-west distance between a K_{DP} measurement over ICLRT between the 8.5 and 12.5 azimuth scans was 0.77 km, and between scans, there were occasionally visible differences in the radar signatures simply from scanning in slightly different directions (especially early on in the squall line's life cycle). The assumption was that 5 km from the radar beam was the extent of the horizontal symmetry. It is very possible that the K_{DP} ice-alignment signatures vary spatially between individual cells in the squall line. The spatial variability in K_{DP} should be investigated using several radars to sample RHIs through a squall line from different locations along the line and comparing the signatures.

One assumption made in this study is that electric fields are primarily vertically oriented, hence, the vertical alignment of ice crystals and the focus on negative K_{DP} signatures. However, on the microscale, several modeling studies have indicated that electric fields point in many directions in thunderstorms due to complex charging, turbulence, and lightning dissipating the charge non-uniformly (e.g. Mansell et al.

2005, Mansell et al. 2010). Detection of horizontal electric fields is not possible with the use of K_{DP} because horizontal alignment of crystals in horizontal electric fields is the same alignment as non-electrified ice crystal aerodynamically forced orientation.

The macroscopic examination at how flashes compare to the K_{DP} fields in a squall line reveals that the lightning flashes are generally associated with the dominant regions of vertically aligned crystals and generally propagate around the negative K_{DP} region with a positive bias throughout the life cycle of the squall line. To draw definite conclusions on how individual flashes affect ice crystal alignment and K_{DP} signatures, phased array radars with much faster scanning capabilities would be needed.

The motivation for filtering out lower values of ρ_{HV} on ϕ_{DP} when computing K_{DP} was to remove the effects of resonance. For C-band radars like SR2, backscatter resonance occurs when the radar beam passes through particles 4 mm in diameter or larger (e.g. Trömel et al. 2013). This causes a rapid increase in differential phase in the back-scattered signal. When the beam passes through a region of large particles and emerges on the other side, the resonance effects stop and there is an apparent decrease in ϕ_{DP}. This causes a negative K_{DP} signature on the far side of the region of large particles. This is seen above the melting layer and on the far side of convective cells. ρ_{HV} is relatively low (< 0.9) in the melting layer, and filtering out those values from ϕ_{DP} also removes some of the anomalously high values caused by resonance. Interestingly, the negative K_{DP} region above the melting layer was a little weaker, but still present after the filtering up to 0.97 (as seen in Figure 16). This could mean that these values may be partially the product of electric fields near the melting layer,

which have been measured by electromagnetic field meter soundings (e.g. Stolezenburg et al. 1998a). Willis and Heymsfeld (1989) found that cloud ice crystals were present just above the melting level in a similar squall line observed over Oklahoma, which could be tilted in the electric fields.

Resonance does pose a problem in analyzing K_{DP} in squall lines with distinct spacing between cells (such as the Oklahoma squall line) because it becomes difficult to determine which negative K_{DP} signatures are a product of resonance and which are due to electric fields. The transition zone K_{DP} region in both the Florida and Oklahoma squall lines tended to be located on the near side of the cells and would not have been affected by resonance from convective cores. On occasion, the convective K_{DP} region was in the locations that may be affected by resonance. However, in the Florida squall line, this was also a region of flash initiation and propagation. Thus, it is not likely that negative K_{DP} region is simply an artifact of resonance. In the Oklahoma squall line, however, many negative K_{DP} regions between cells looked as though they could be associated with resonance, while others were above and on the near side of the cells. Without LMA data, it is not possible to discern if these were also electrically active regions. More case studies would need to be collected to draw conclusions as to the electrical activity between cells.

5.2 K_{DP} Evolution and Driving Mechanisms

This evolution of the K_{DP} regions with the squall line evolution is displayed in the K_{DP} evolution conceptual model in

Figure 70. The structures are based mostly on the 5-RHI mean fields and multi-flash composites in the Florida squall line; though, the incorporation of individual convective cell structures was influenced by the 5-RHI mean fields of the Oklahoma squall line.

In the formative stage of the Florida squall line, there are two convective K_{DP} regions, one upshear (that eventually becomes the transition zone K_{DP} region) and the other downshear, which has been referred to in this study as the convective, negative K_{DP} region. Initially, these two regions are nearly symmetric around the convective core, assuming the upper level flow is dominated by the updraft divergence.

In the intensifying stage, the squall line begins to propagate downshear and new cells developed from low-level convergence along the gust front. The transition zone K_{DP} region starts to elongate as new cells form and additional charge advection occurs from the mature cell updraft. The convective K_{DP} region shrinks as a more dominant front to rear flow (from vertical transport of storm-relative low-level momentum) reduced the charge advection ahead of the convection. Additionally, increased subsidence beneath the forward anvil sublimates some of the charged ice crystals, decreasing the charge region in this area. As the melting band developed, so did the negative K_{DP} layer above the melting level, which may possibly be due to resonance effects, but could also be due to in situ charging mechanisms.

In the mature stage, the transition zone K_{DP} region elongates even more and slopes well into the transition zone K_{DP} region and a little into stratiform region. This is in response to charge particles and in-situ charging in new cells merging with those of old cells and strong, deeper, front-to-rear flow through the squall line allowing for

more upshear charge advection as the mature-stage updrafts are tilted rearward by excessive horizontal vorticity gained through buoyancy gradients along the cold pool (Rotunno et al. 1988). The convective K_{DP} region is an inconsistent feature in this stage, as it merges with the transition zone K_{DP} region shortly after developing above a new convective cell, possibly due to in-situ charging.

In the dissipating stage, the transition zone and convective K_{DP} regions merge, weaken and descend. The gust front surges ahead of the convective line, reducing the depth of forced lifting and generating few and weaker new cells. Hence, charge advection weakens and existing charged particles fall out of the squall line.

Overall, multi-flash composites revealed that the transition zone K_{DP} region elongated horizontally as the squall line matured. Simultaneously, flashes also elongated horizontally and continued to surround the transition zone K_{DP} region. In both squall line cases, the convective K_{DP} region weakened in the squall lines' mature stage, and in the Florida case vertically dominant flashes became less frequent in the mature stage. This horizontal elongation of negative K_{DP} signatures and associated flashes may have been related to the horizontal spreading of charge throughout the squall line.

The graupel-ice non-inductive charging mechanism in thunderstorm updrafts is thought to provide much of the charge separation that produce observed electric fields in the convective region (e.g. Saunders 1993, MacGorman and Rust 1998, Lund et al. 2009). Updrafts in ordinary thunderstorms and low shear environments distribute charge quasi-symmetrically because the flow out of the updraft has no bias in its direction (MacGorman and Rust 1998). This was depicted in the symmetry of the

negative K_{DP} regions in the Florida squall line during its formative stage. However, as the squall line intensified and began to propagate more quickly, the flow would have been directed more toward the rear of the storm, as depicted by the 2-D conceptual model for trailing stratiform squall line systems from Houze et al. (1989). Thus, most charge that separated in the updraft would have been advected to the rear of the storm instead of ahead of the storm's motion. However, charge advection may not have been the only charging mechanism responsible for electric fields that caused the transition zone K_{DP} region. Depositional-growth charging (e.g. Dong and Hallett 1992) may have played a role in developing upper level charge regions, specifically in the stratiform region mesoscale updraft where deposition is thought to take place (e.g. Biggerstaff and Houze 1993). By contrast, however, the transition zone is an area of subsidence, causing depositional growth to be more limited compared to growth in the stratiform region (Biggerstaff and Houze 1993).

Another charging mechanism that could have caused the electric fields that produced the transition zone K_{DP} signature would be the melting charging mechanism (e.g. Stolzenburg et al. 1994, Shepard et al. 1996). This would result in a region of negative charge above the melting layer region bright band as seen in studies like Stolzenburg et al. (1998a). Similarly, in this study, it was found through charge analysis that flash branches propagated through a negative charge region just above the melting layer. One caveat worth mentioning though is that this negative charge region sloped upward toward the convective region. It is not certain if melting was occurring along this slope. The convective region would have moist adiabatic ascent that would have increased the altitude of the melting level. The transition zone would

be associated with dissipating convection that would have some residual positive buoyancy but also negative buoyance associated with sublimation and evaporational cooling in the downdrafts (Byers and Braham 1949). It is not clear how perturbed the melting altitude would be through this region and what consequence that would have on the slope of the negative transition zone K_{DP} region.

Despite complications associated with different charging mechanisms, the primary feature worth noting is the general evolution of the vertical alignment, which started off as two isolated pockets and grew substantially toward the stratiform region with maturity. This was followed by a weakening in K_{DP} as the squall line dissipated.

The Oklahoma squall line negative K_{DP} structure differed from the Florida squall line. There was a significantly less sloping of the transition zone K_{DP} in the Oklahoma squall line, which may be due to the propagation speed and spacing between cells and the vertical distribution of precipitation-sized hydrometeors. It is possible that the faster propagation prevented the charge regions from coalescing and they remained as pockets tied to individual cells. However, this implies that in situ charging was dominant over charge advection processes as advection would tend to more evenly distribute the charged particles. Given the relatively high correlation between the heights of the transition zone K_{DP} region and reflectivity maxima, it would seem that the in situ charging associated with convective cell lifecycle was an important part of the overall K_{DP}structure. Additionally, there was moderate to high correlation between the areal extents of the transition zone K_{DP} region and reflectivity maxima. This again suggests that the development of new cells led to a growth in the negative K_{DP} region.

However, it should be noted that these correlations do not depict the correlation of individual cells with individual pockets of K_{DP}. Only the most dominant reflectivity maxima above the melting level was correlated with the most dominant K_{DP} region in the transition zone. There was also a lot of missing data in the reflectivity core due to technical issues with selecting the regions and the fact that the 35 dBZ contour did not always extend much above the freezing level. It should also be noted that the melting level used for this analysis was the level of the bright band, not the melting level in the convective region. This was chosen because of technical limitations in selecting the reflectivity maxima with a low reflectivity threshold. Additionally, there would be even more missing data since the storm's 35 dBZ contour max height fluctuated from 4 to 12 km throughout cell life cycles. The melting level in the convective region would have been around 6 km. This was found by following the moist adiabat on a sounding with a surface temperature of 30 ^{o}C and dewpoint temperature of 21 ^{o}C at 2007 UTC. The main problem with assuming the melting level is 4 km is that the reflectivity contours do not capture just ice crystals. This is also limited by the fact that ice crystals often show up in reflectivity values less than 35 dBZ (e.g. Pokharel and Vali 2011). Thus, it would be inaccurate to correlate the amount of ice generated by an updraft cell as depicted by reflectivity greater than 35 dBZ to the electric fields as depicted by the transition zone K_{DP} region. However, the areal extent data does show that an influx of precipitation sized particles is moderately correlated to vertical alignment signatures. This could imply that the reflectivity maxima are depicting collisions of precipitation particles in the updraft. A better method to use for determining which storm attributes lead to electric fields would be

to use hydrometeor classification algorithms (c.f., Park et al. 2009) to relate ice or graupel content to the negative K_{DP} regions.

Overall, the transition zone K_{DP} region in the Oklahoma squall line did not evolve the same way as in the Florida case. It should be noted that the convective K_{DP} region was much weaker in the Oklahoma squall line, possibly due to stronger front-to-rear flow preventing collection of charge above and ahead of the convective region. Indeed, it is possible that the negative K_{DP} regions are related to the degree at which the flow within the storm produces sufficient charge advection.

5.3 Future Work

This study identifies a relationship between lightning and K_{DP}, but there are further questions that need to be investigated. Future work should investigate the 3-D structure of K_{DP}. Conceptual models like Stolzenburg et al. (1998a) depict charge regions as horizontally stratified parallel to the convective line by assuming 3-D symmetry. The extent of this symmetry could be tested by using dual-pol radar to sample parallel to a convective line as it passes, or multiple radars sampling perpendicular to a convective line from different locations. This could show that charge regions are well mixed behind a convective line. In contrast, it may reveal pockets of K_{DP} associated with individual cells in the line that get mixed out as they move into the stratiform region.

Another topic that needs investigation is the effects lightning has on K_{DP}. It is still not known whether the entire K_{DP} field fluctuates in response to a flash, or if lightning only causes changes in certain areas. This can be tested using a phased-array

or imaging radar and taking rapid volumetric samples though the upper portions of cloud systems. This could reveal how spatially extensive charge regions are depleted by a single flash. Furthermore, this study did not address the impacts of cloud-to-ground flashes. It remains unclear to what extent the negative K_{DP} aloft is affected by the dissipation of charge in the lower portions of the cloud.

In addition to the effects of individual flashes on the K_{DP} field, it would be important to study the evolution of the negative K_{DP} region and determine the processes responsible for the implied electric fields. The area analysis done in this study was limited by the fact that reflectivity is not a good depicter of the presence of charging mechanisms. A better technique would be to use hydrometeor classification to diagnose the concentrations of graupel and ice. This would be a better indication of where charge separation is occurring within the squall line, since the graupel-ice collision mechanism is thought to be responsible for most of the charging that occurs in deep convection (e.g. MacGorman and Rust 1998). The locations of these hydrometeors in relation to K_{DP} could hint at the electrical processes responsible for electric fields in various locations of the squall line. Additionally, it could reveal whether or not electric fields are dependent on individual convective updrafts. Previous studies such as Lhermitte and Krehbiel (1979) have linked flash rates to increased updraft velocities and increased reflectivity from the development of new cells. Further investigation could reveal exactly how convective updrafts affect electric fields.

A motivation for gathering more data on the structural relationship between K_{DP} and lightning is to someday apply this relationship to operations. If there is in

fact a relationship between the negative K_{DP} region and lightning, then it may be possible to diagnose lightning cessation in thunderstorms. Understanding when storms cease electrical activity could allow for a way to determine when it is safe to resume outdoor activities.

Chapter 6: Summary and Conclusions

The negative K_{DP} signatures from RHIs through a Florida squall line were compared to flash channel locations. It was found that 38 of 46 flashes which met this study's analysis criteria initiated around the dominant negative K_{DP} regions in the upper levels in the transition zone and ahead of the convective line. Flashes then propagated through weakly positive K_{DP} values along the zero-K_{DP} contours surrounding the negative K_{DP} regions. These positive K_{DP} values may have been regions of weak electric fields and high charge density. Flash channels tended to be vertically dominant in orientation early in the squall line's life cycle, but became more horizontally dominant and more prevalent around the transition zone K_{DP} region as the squall line matured. This was matched by how the transition zone K_{DP} region elongated as the squall line entered its mature phase. Such elongation may have been due to the advection of charged particles into the stratiform region, or different charging mechanisms (such as melting charging or deposition-growth charging) becoming significant in response to the development of the stratiform region.

The negative K_{DP} signatures from RHIs through an Oklahoma squall line were compared to the K_{DP} signatures from the Florida squall line. It was found that the Oklahoma squall line lacked a consistent convective K_{DP} region. It was also found that the transition K_{DP} region often appeared more as pockets than a single region, and did not slope downward toward the stratiform region. These features could be attributed to the faster propagation speed causing dominant front to rear flow increasing updraft cell spacing, and in situ charging with individual convective cells. These may have lessened the advection of charged particles ahead of the convective

line compared to the Florida squall line, and explains the absence of a convective K_{DP} region.

An area analysis was performed and found moderate correlations between the areal extents and mean heights of the reflectivity maxima and transition zone K_{DP} regions in both squall lines. This indicates that individual convective cells may contribute to the horizontal extent of electric fields. In the Oklahoma squall line, it appeared as though some individual cells induced an enhancement in the negative K_{DP} region, or a separate negative K_{DP} pocket. Thus, the results of this study suggest that squall line electric fields may be tied to the life cycles of individual convective pulses before being smoothed by advection through the transition zone.

Indeed, it appears plausible to monitor thunderstorm electrification through the use of K_{DP}, but faster sampling is needed to accurately predict individual strikes.

Tables

Table 1. Correlations between variables of the reflectivity maxima and the transition zone K_{DP} region. Associated P-values and lag times are to the right of the correlations. Two correlations were computed for each variable in each case: one without lagging the K_{DP} region time series, and the other with the amount of lag that maximizes the correlation.

CORRELATIONS: Between REF Maxima and 5-RHI Means of Transition Zone K_{DP} Region						
	Florida			Oklahoma		
	Coor	P-val	Lag Time (min)	Coor	P-val	Lag Time (min)
Areal Extent	40.7%	5×10^{-12}	0	77.3%	2×10^{-27}	0
	40.7%	5×10^{-12}	0	77.3%	2×10^{-27}	0
Mean Values	12.5%	0.041	0	-19.5%	0.029	0
	-43.5%	2×10^{-12}	7.65	-22.1%	0.013	0.28
Mean Height	57.9%	4×10^{-25}	0	83.8%	3×10^{-34}	0
	59.4%	2×10^{-26}	0.85	85.9%	5×10^{-37}	0.57
Mean Distance	96.4%	8×10^{-153}	0	92.6%	6×10^{-54}	0
	96.4%	8×10^{-153}	0	93.5%	2×10^{-56}	0.57
Extreme Values	3.5%	0.566	0	37.1%	2×10^{-5}	0
	5.1%	0.413	0.28	43.7%	5×10^{-7}	0

Figures

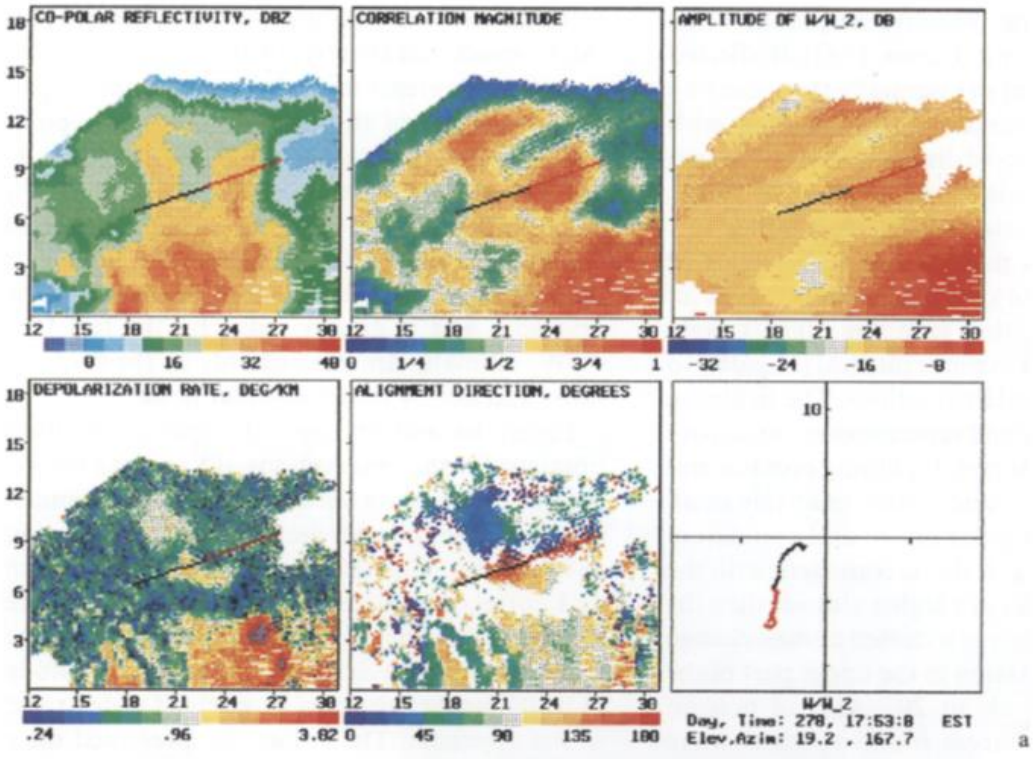

Figure 1: Dual-polarimetric scans prior to a lightning discharge in the storm. From left to right and top to bottom: co-polar reflectivity, correlation magnitude, amplitude, depolarization rate, alignment direction, and orientation plot. Feature of interest is in the alignment direction, where there is a visible coupling of changing orientation in the upper areas of the storm. ***Adapted from Krehbiel et al. (1996)***

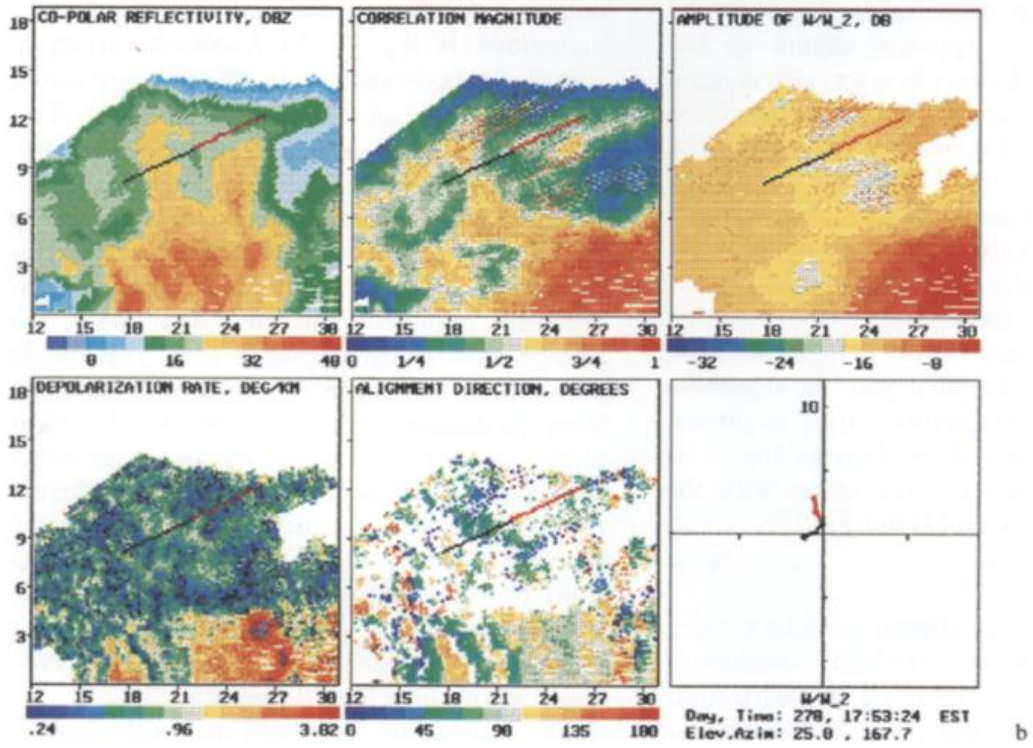

Figure 2: Same as Figure 1 except after the flash discharge. Feature of note is that the alignment direction pattern from Fig. 13 has disappeared. ***Adapted from Krehbiel et al. (1996)***

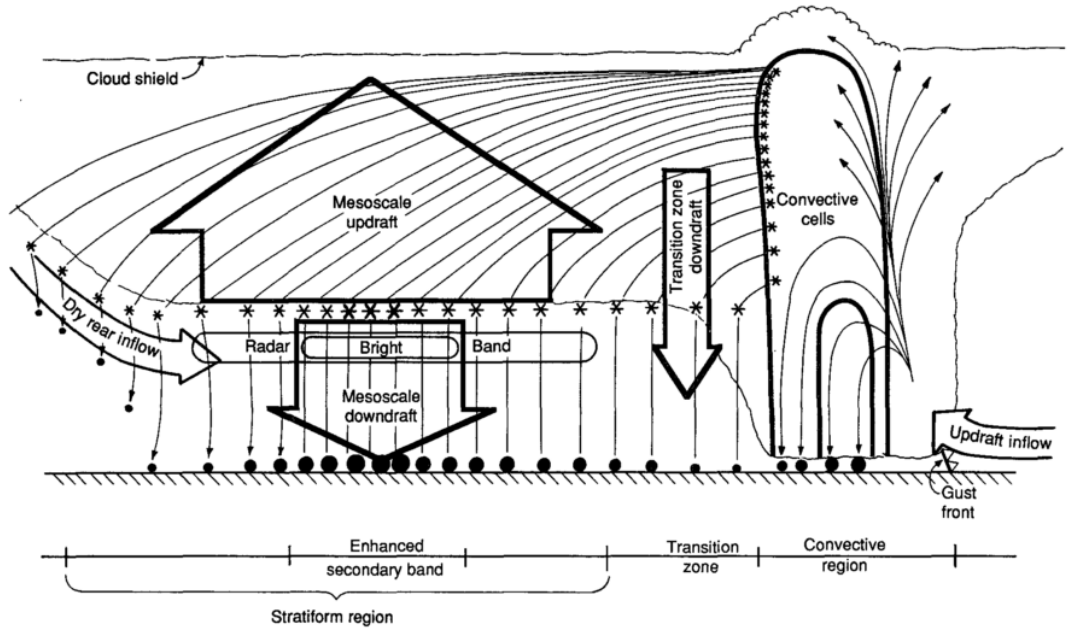

Figure 3: Cross-section of an idealized leading-line/trailing-stratiform (TS) squall line with associated hydrometeor trajectories and mesoscale flows. ***Adapted from Biggerstaff and Houze (1991a)***

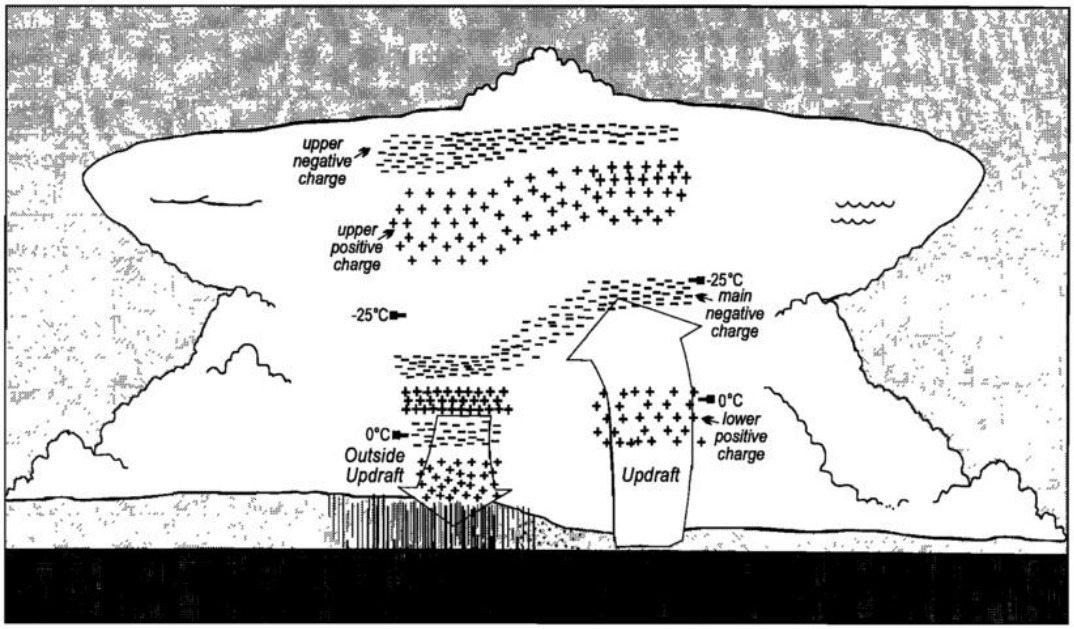

Figure 4: Cross-section of charge structure in ordinary cell thunderstorm with a single updfraft and downdraft, and no stratiform region. Plus signs indicate positive charge. Minus signs indicate negative charge. 0°*C* and -25°*C* levels indicated. ***Adapted from Stolzenburg et al. 1998c.***

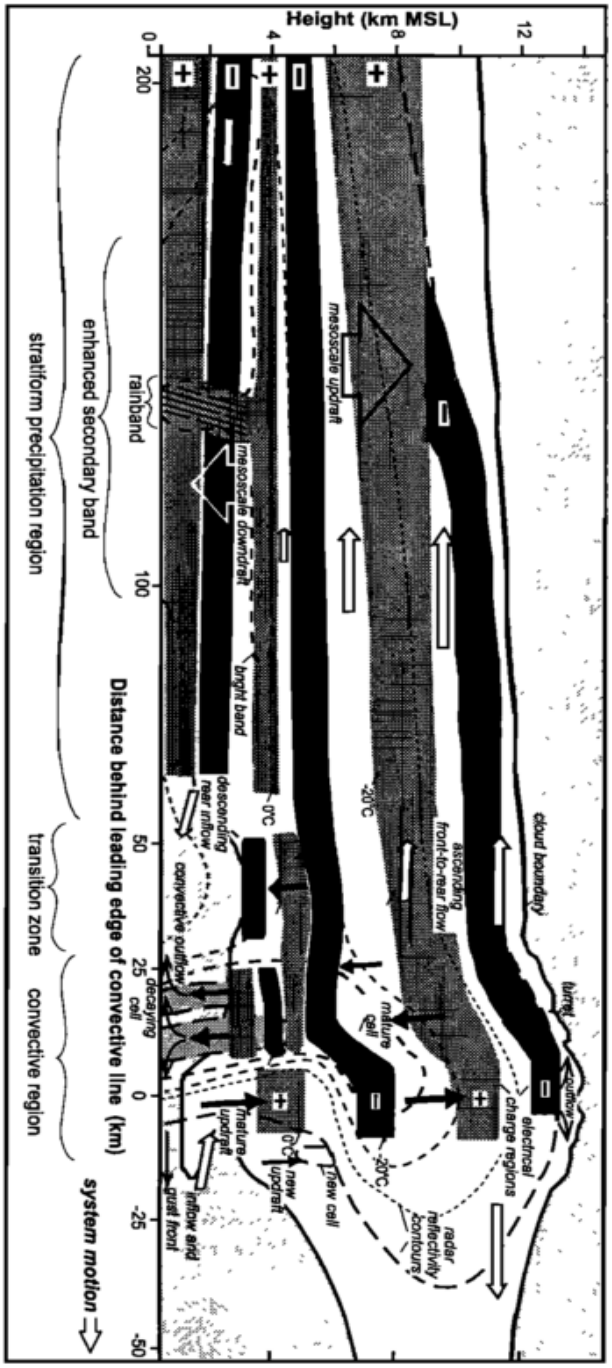

Figure 5: Line-normal cross-section of idealized TS squall line and associate charge regions with convective region on right and stratiform region on left. Plus signs indicate positive charge region, minus signs indicate negative charge region. Small arrows indicate convective flows and large arrows indicate mesoscale flows. ***Adapted from Stolzenburg et al. (1998a)***

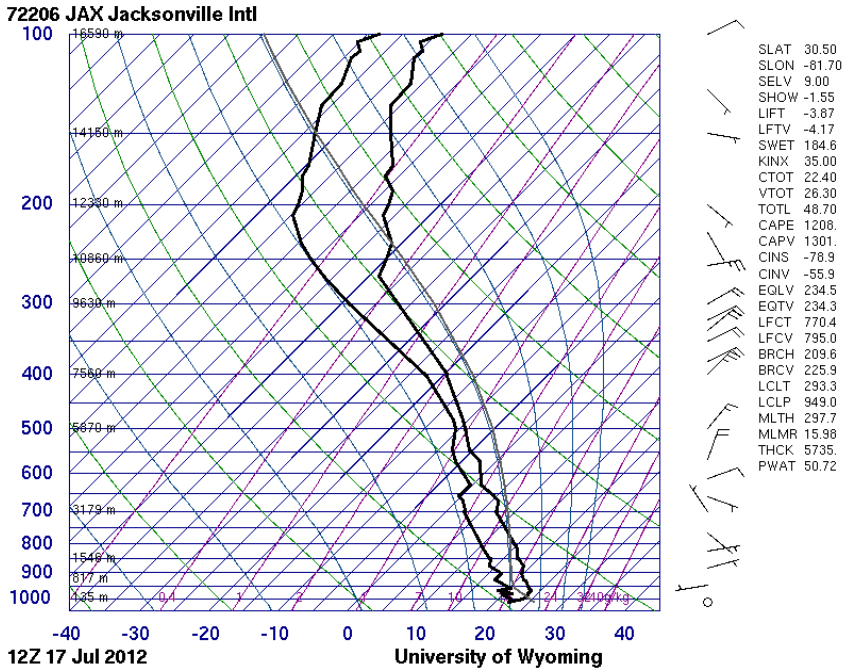

Figure 6: Sounding launched from Jacksonville, FL at 12z on July 17, 2012. Right black line is vertical temperature profile, left is vertical dewpoint temperature profile. Plot was acquired from the University of Wyoming website.

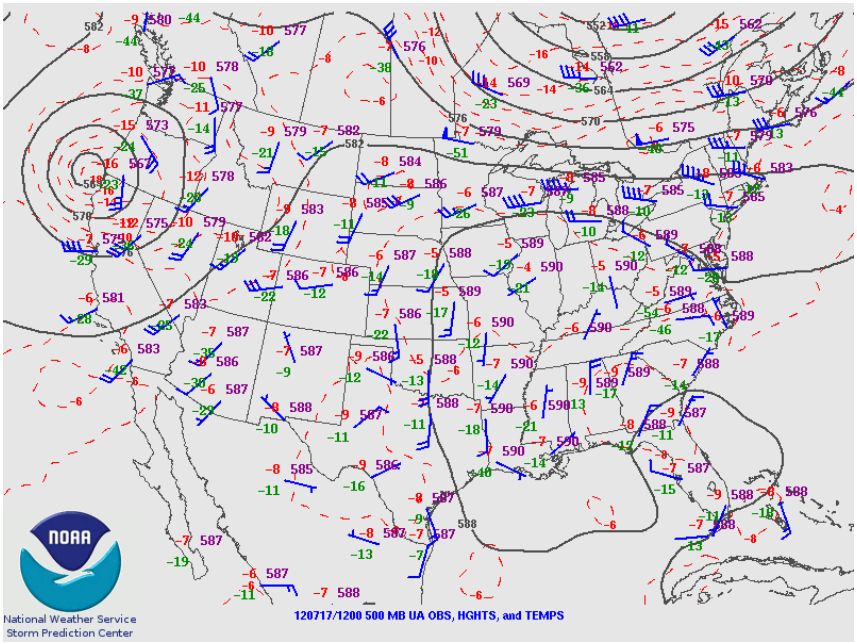

Figure 7: 500mb height analysis of the contiguous USA on 12z on July 17, 2012. Isoheights denoted by black contours and temperature denoted by red dashed contours. Plot was acquired from the SPC website.

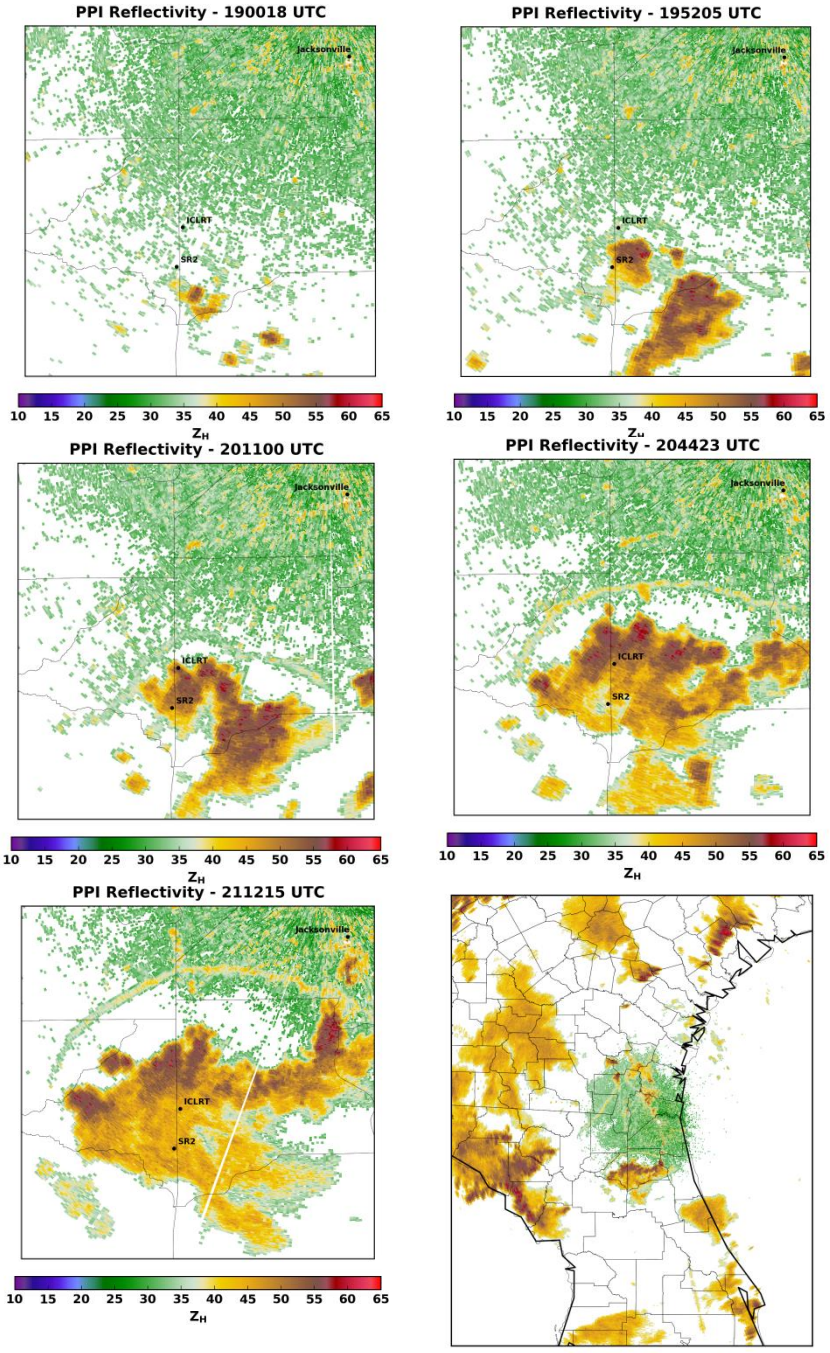

Figure 8: (Listed left to right, top down) 88D PPIs of reflectivity from the KJAX radar at 190018 UTC, 195205 UTC, 201100 UTC, 204423 UTC, 211215 UTC, and 211215 UTC. The first fifth panels are zoomed in to the squall line where the distance between ICLRT and SR2 was 11 km. The sixth panel was zoomed out to show northern Florida and southern Georgia and illustrate the size of the squall line.

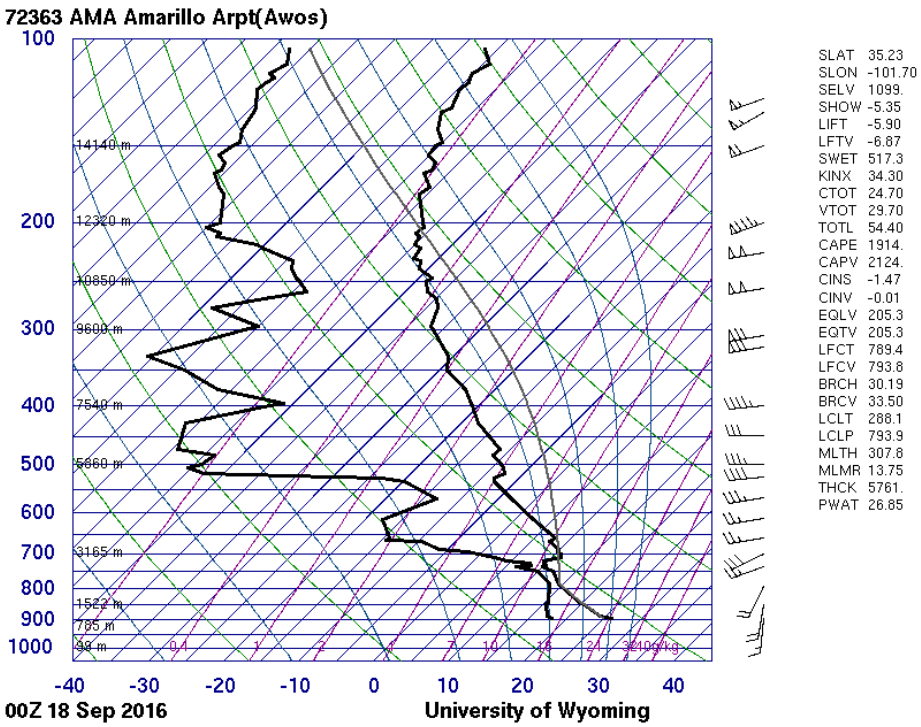

Figure 9: Same as Figure 6, but launched from Amarillo, TX at 00z on September 18, 2016.

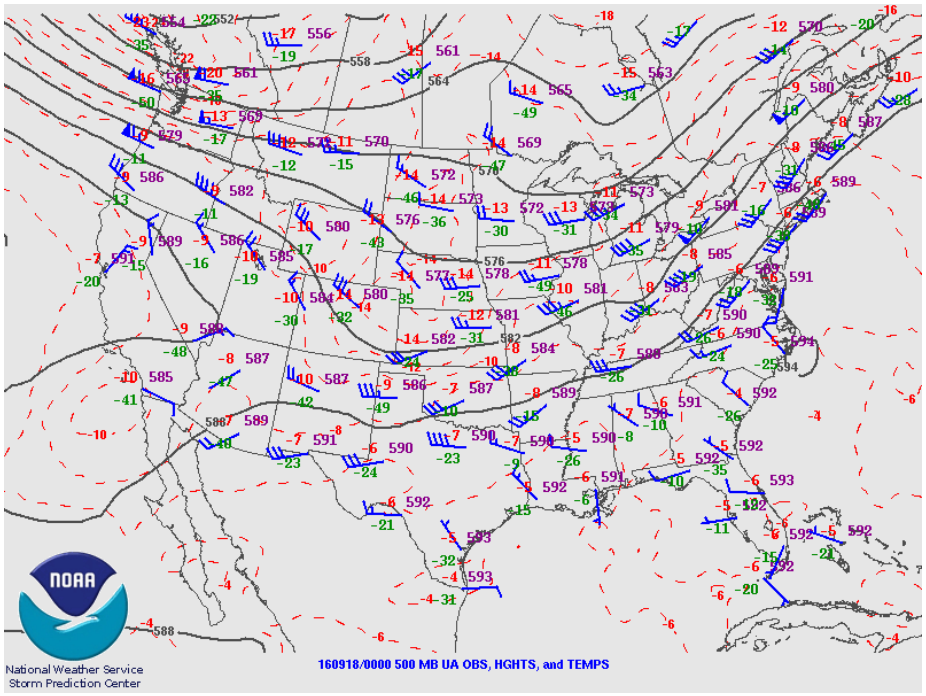

Figure 10: Same as Figure 7, but at 00z on September 18, 2016.

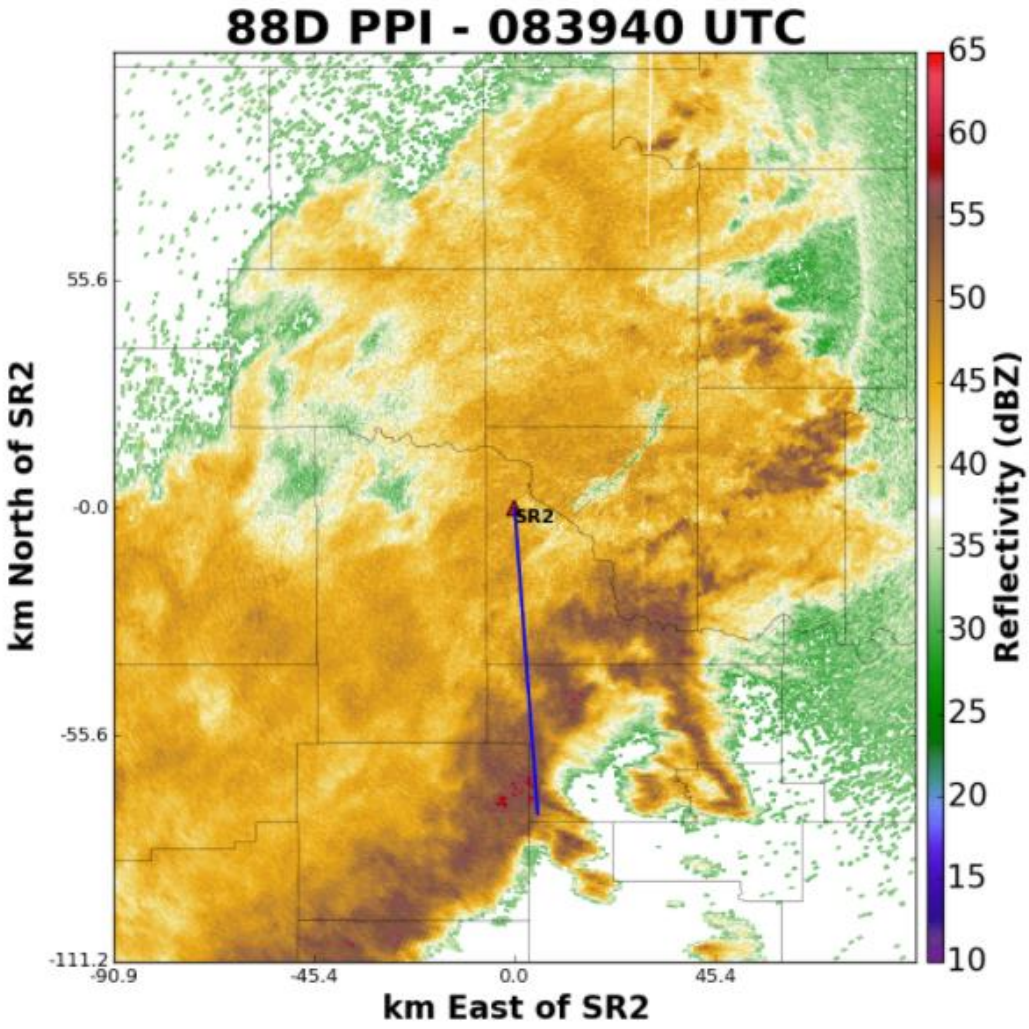

Figure 11: Same as Figure 8, but data is from KTLX radar in Oklahoma depicting the Oklahoma squall line at 0845 UTC. Blue line is approximate scan direction of SR2.

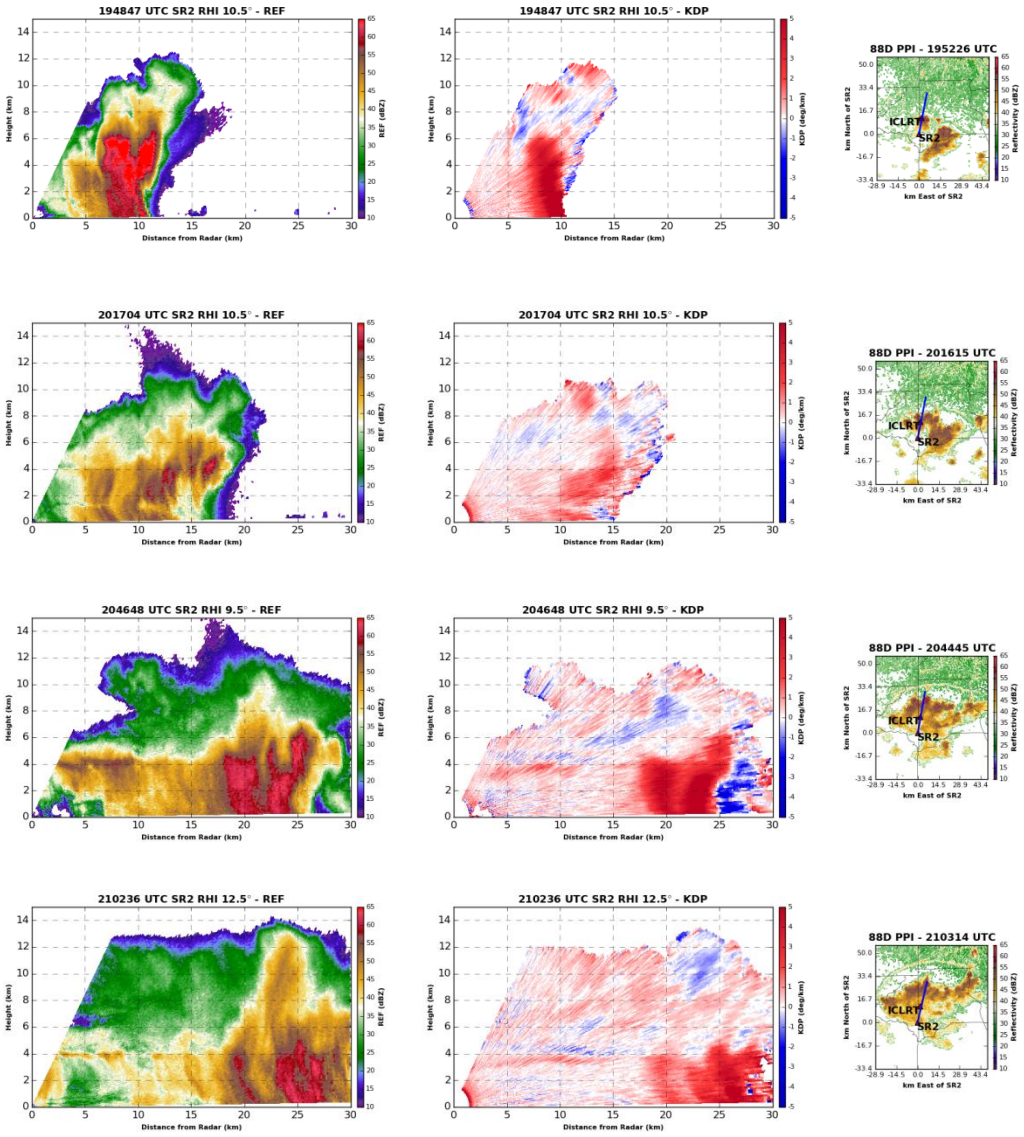

Figure 12: RHIs of reflectivity (left) and K_{DP} (middle), and PPI of 88D reflectivity data (right) at times closest to 194847 UTC, 201704 UTC, 204648 UTC, and 210236 UTC (listed from top down) on July 17, 2012. Blue line in right panel represents radar beam. Each panel depicts the squall line in its (listed from top down) formation stage, intensifying stage, mature stage, and dissipating stage.

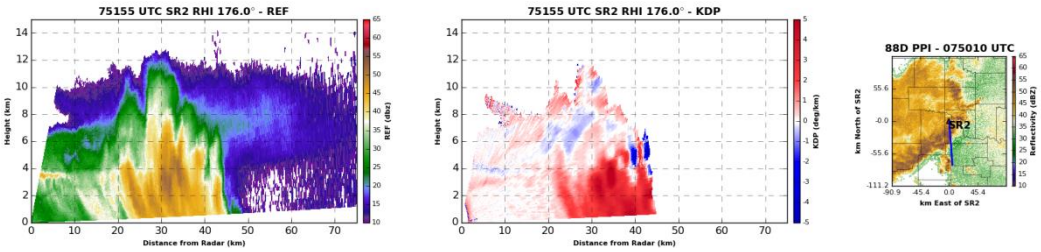

Figure 13: RHIs of reflectivity (left) and K_{DP} (middle), and PPI of 88D reflectivity data (right) at times closest to 075155 UTC on September 18, 2016 near Blanchard, OK. Blue line in right panel represents radar beam. Squall line was in the mature phase at the time of scanning with convective line propagating southeast.

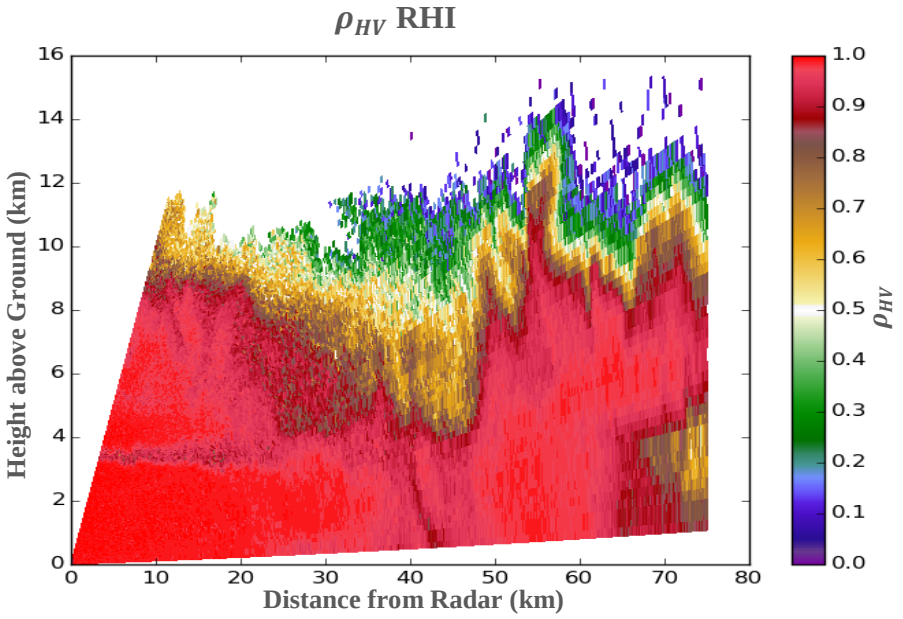

Figure 14: RHI of ρ_{HV} sampled at 084329 UTC. Melting level can be denoted by the elongated dark reds and browns closer to the radar at about 3.5 km AGL.

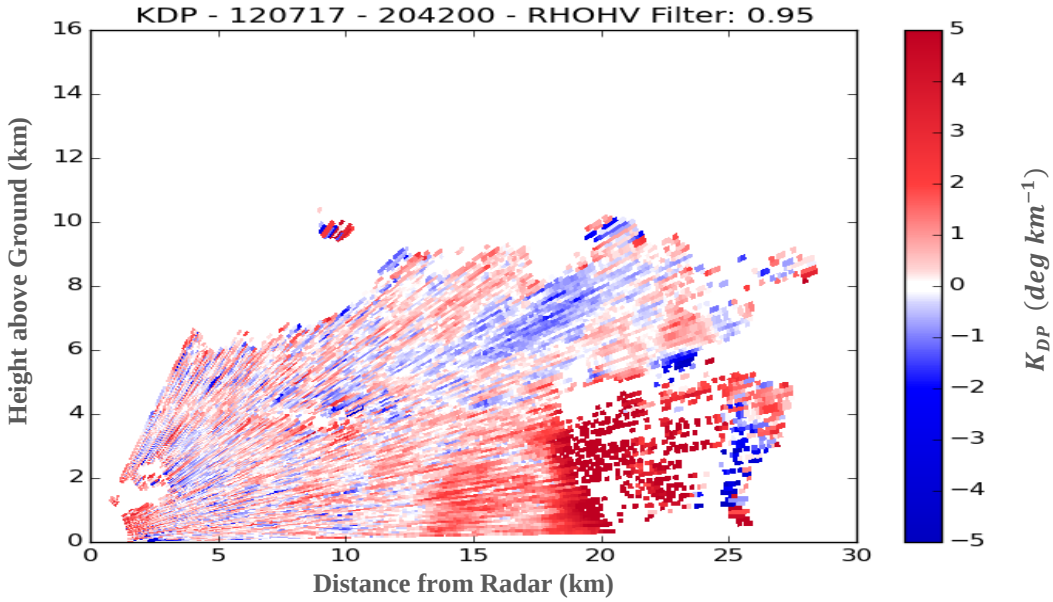

Figure 15: K_{DP} field after computed from a filtered ϕ_{DP} on values of ρ_{hv} less than 0.95. Negative K_{DP} region aloft and melting layer K_{DP} region remain present.

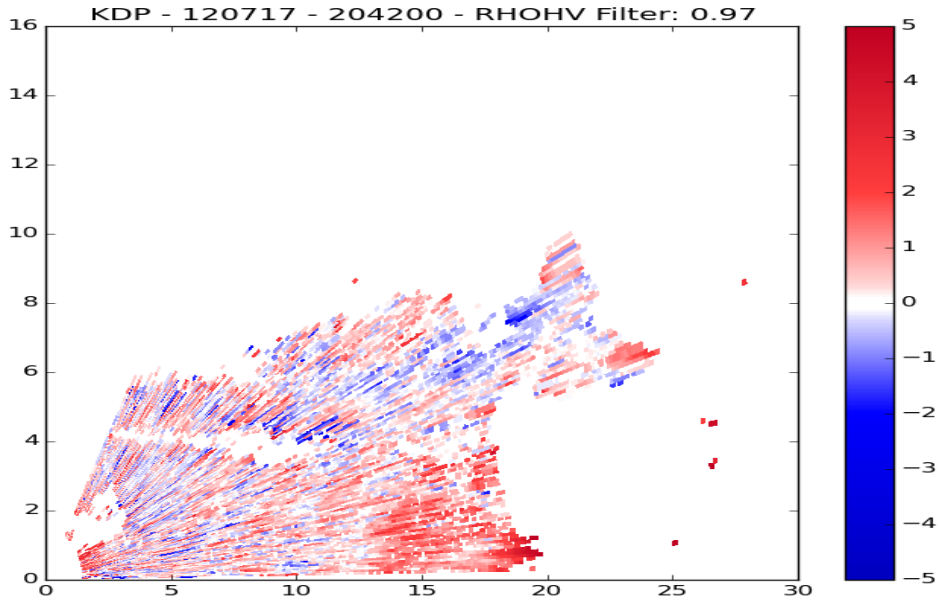

Figure 16: Same as Figure 15, but filtered on ρ_{hv} less than 0.97. Negative K_{DP} region aloft and melting layer K_{DP} region remain present.

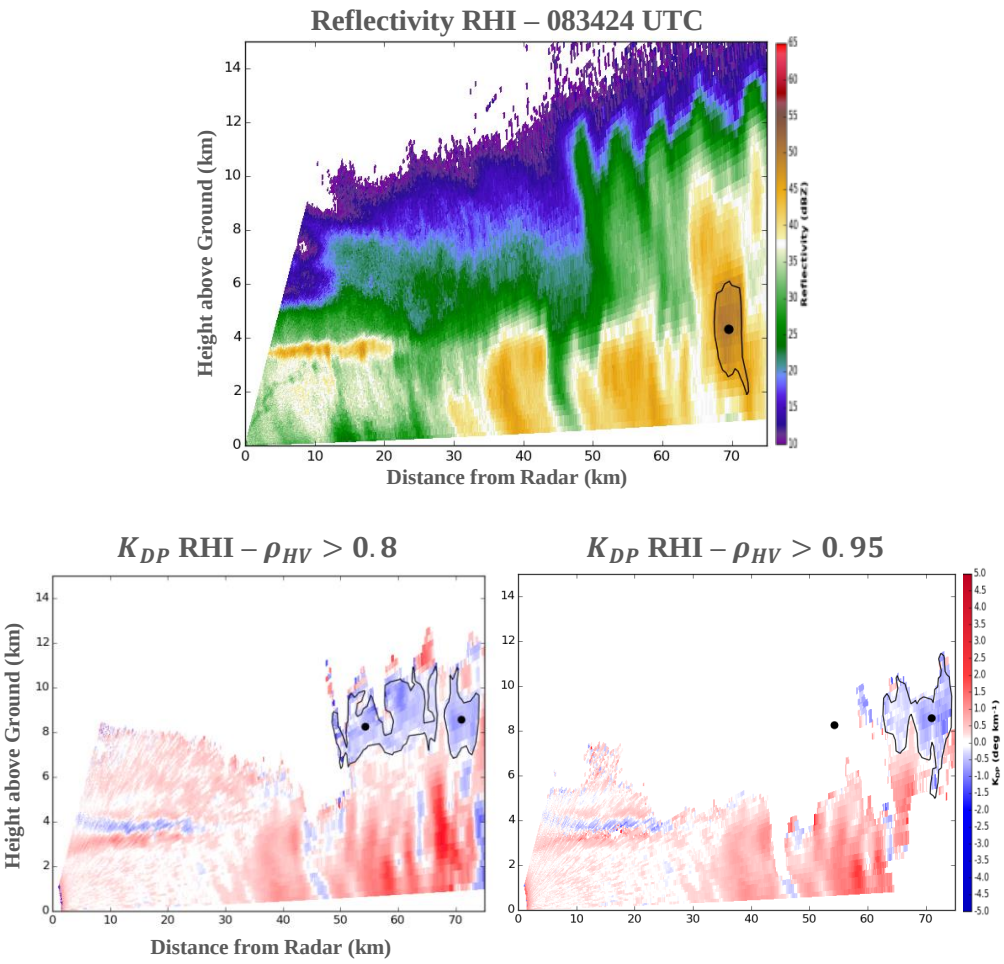

Figure 17: RHIs taken at 083424 UTC on September 18, 2016 pointing south through the Oklahoma squall line. Top is reflectivity, bottom left is K_{DP} with a filter on ρ_{HV} values less than 0.8, and bottom right is K_{DP} with a filter on ρ_{HV} less than 0.95. The black contour is of the 50 dBZ contour and the zero-K_{DP} contour surrounding the negative K_{DP} region.

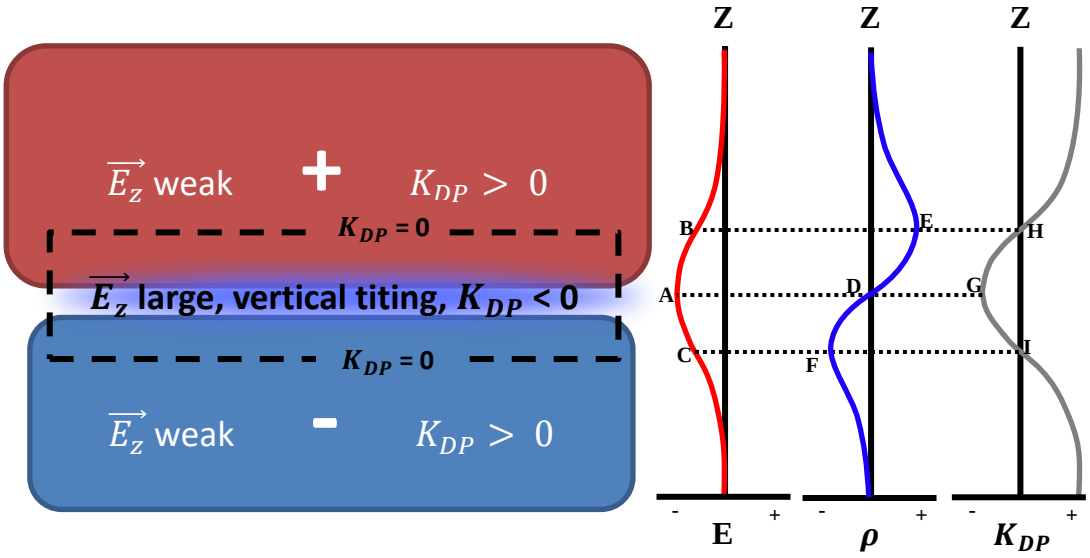

Figure 18: Conceptual model relating electric fields, charge regions, and K_{DP} values. The red box is a region of positive charge density ($\rho > 0$) and the blue box is a region of negative charge density ($\rho < 0$). The black dashed line is the zero-K_{DP} contour, enclosing a region of negative K_{DP} represented by the blue haze. Outside the box are K_{DP} values greater than zero. On the right are vertical profiles of three different variables resulting from the charge regions on the left. Electric field in red has an extrema at point A and changes most rapidly with height at points B and C. Charge density in blue is zero at point D, has a maxima at point E, and a minima at point F. K_{DP} in grey has a minima at point G and is zero at points H and I. Note that the points of max slope in electric field (B and C) are at the same altitude as the inflections in charge density (E and F) and the zero-K_{DP} points (H and I). Also note that the extrema in electric field (A) is at the same altitude as the point of zero charge density (D) and minima in K_{DP} (G).

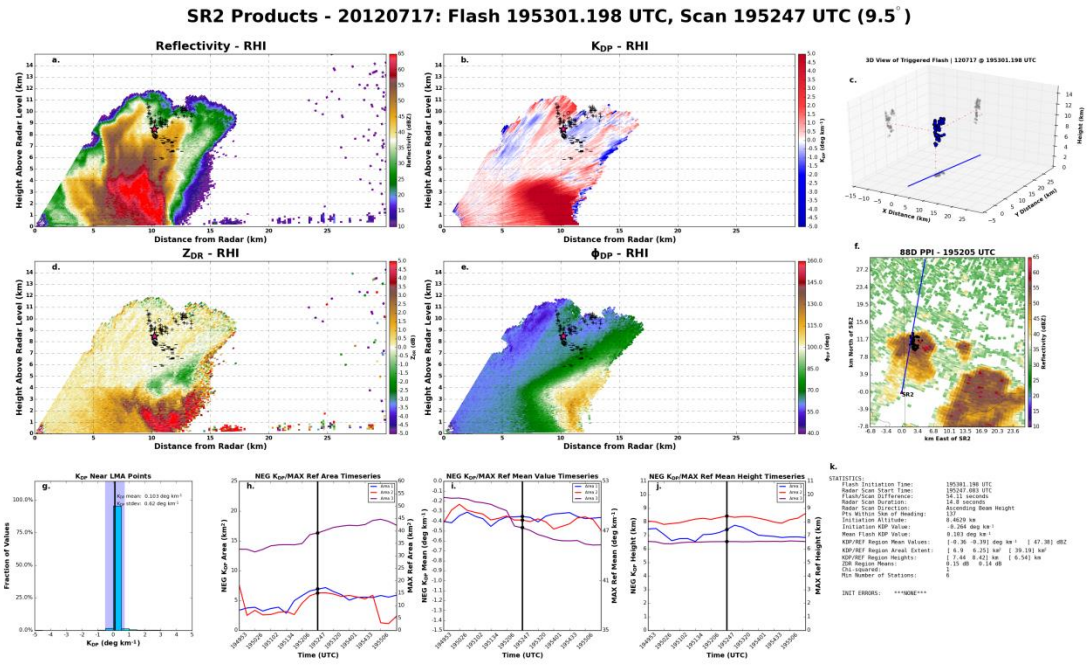

Figure 19: vertically dominant flash on the convective K_{DP} region at 195301 UTC overlayed on 5-RHI mean scan. Pink star shows initiation location, + indicates positive charge region, and - indicates negative charge region. Subfigures include (listed left to right and top to bottom) (a) reflectivity RHI, (b) K_{DP} RHI, (c) 3D view of flash with radar beam line in blue, (d) Z_{DR} RHI, (e) ϕ_{DP} RHI, (f) 88D PPI with radar beam line in blue, (g) historgram of K_{DP} values at flash points, (h) timeseries of K_{DP} and reflectivity regions areal extents, (i) timeseries of K_{DP} and reflectivity regions mean values, (j) timeseries of K_{DP} and reflectivity regions mean heights, and (k) metadata.

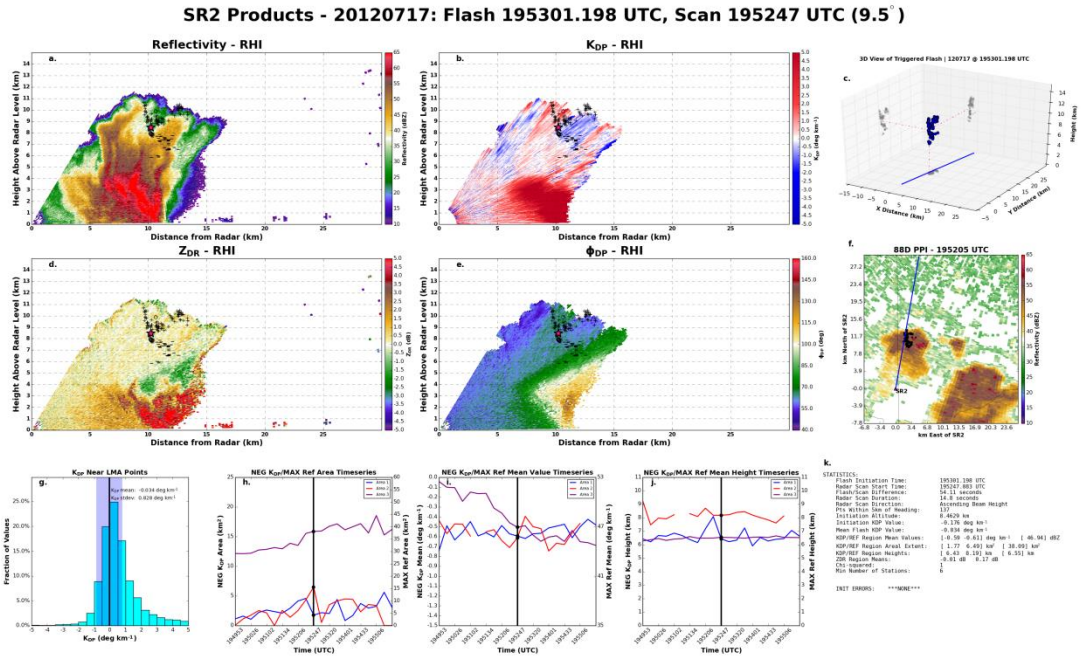

Figure 20: Same as Figure 19 except single RHI at 195247 UTC.

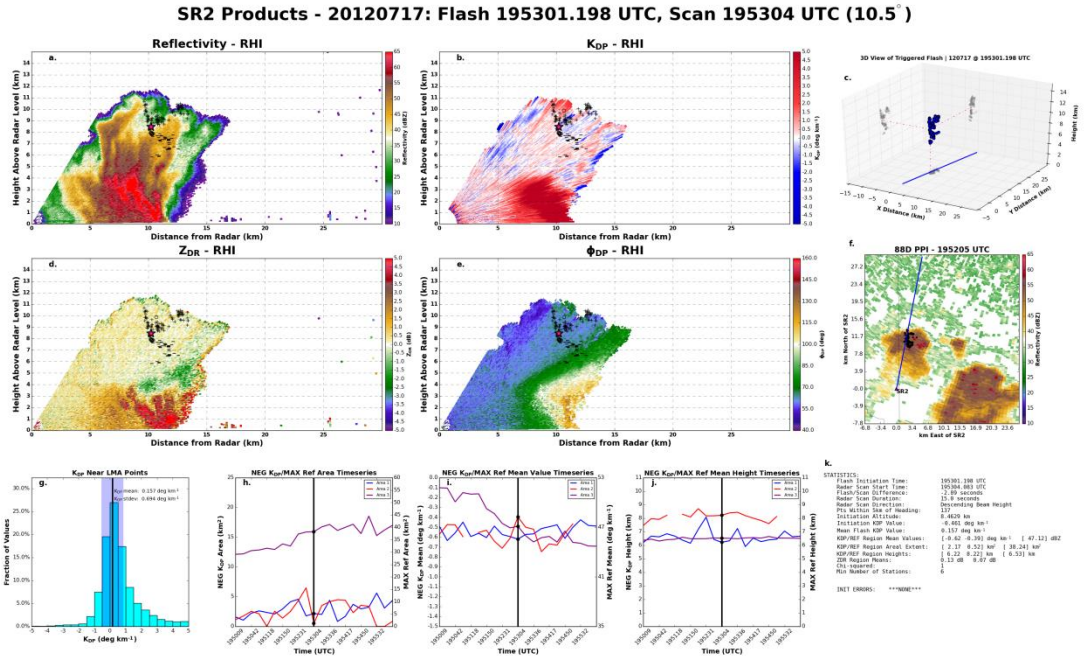

Figure 21: Same as Figure 20 at 195304 UTC.

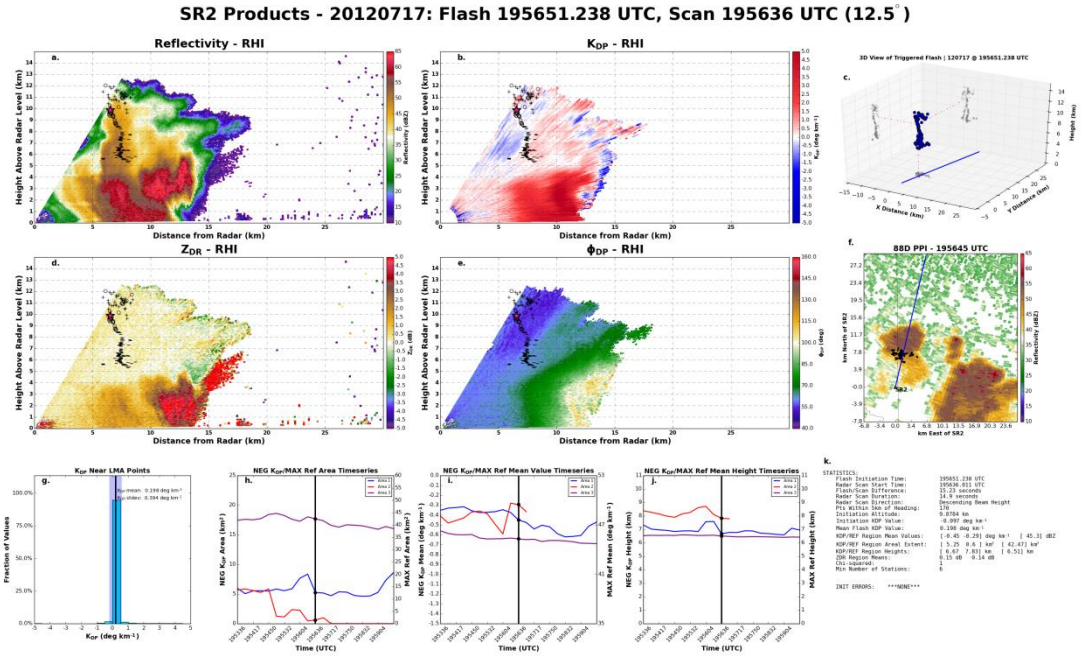

Figure 22: Same as Figure 19, but for the flash at 195651 UTC.

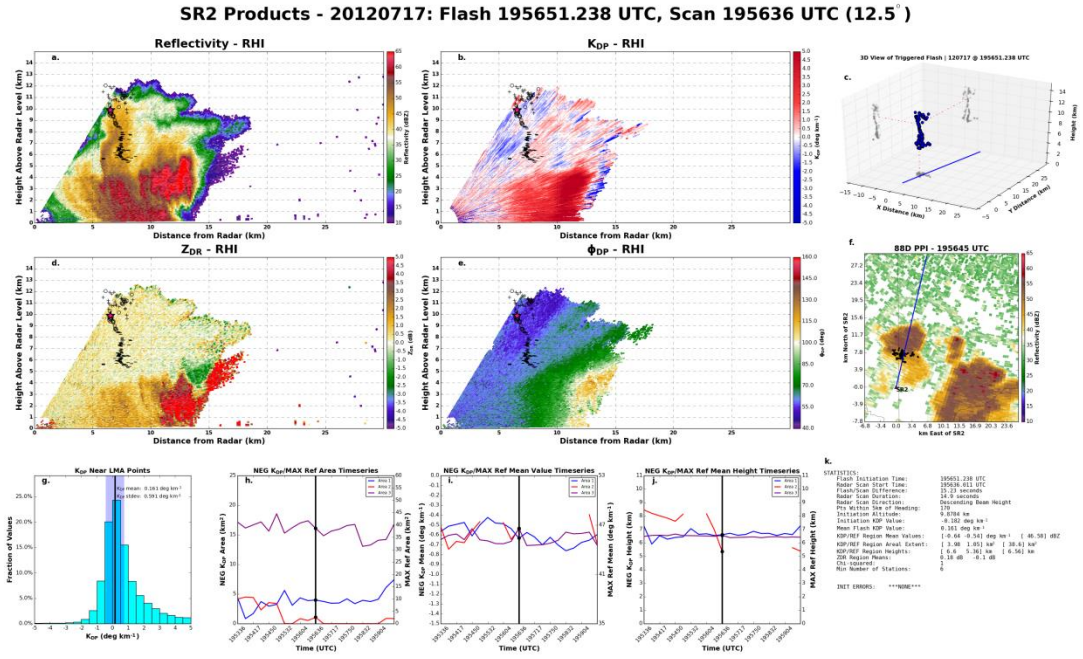

Figure 23: Same as Figure 20, but for flash 195651 UTC.

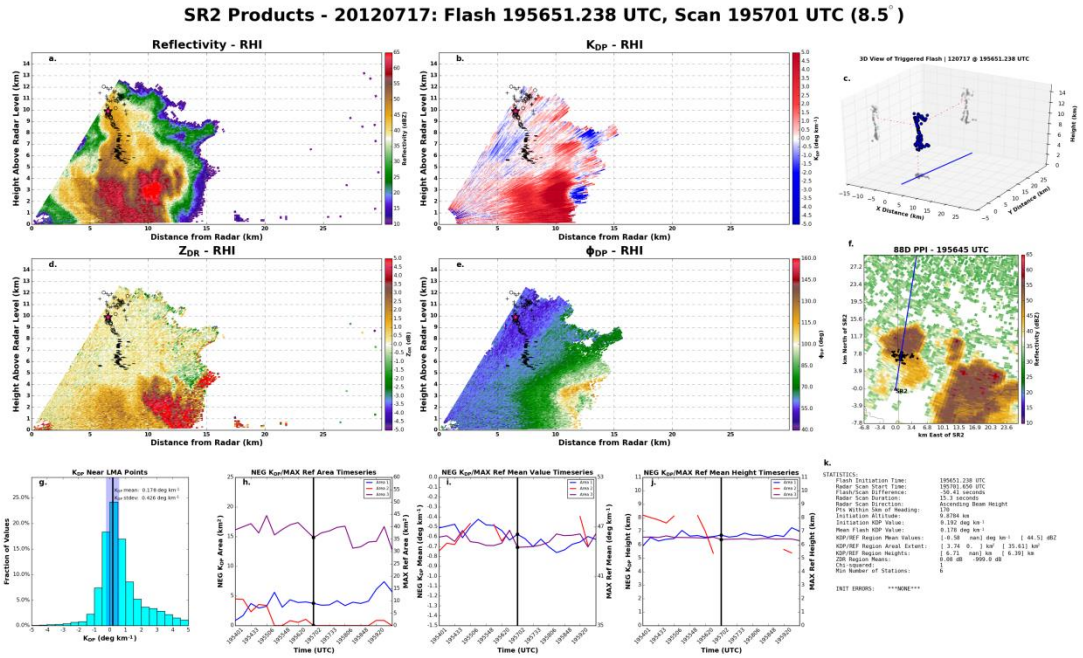

Figure 24: Same as Figure 21, but for the flash at 195651 UTC.

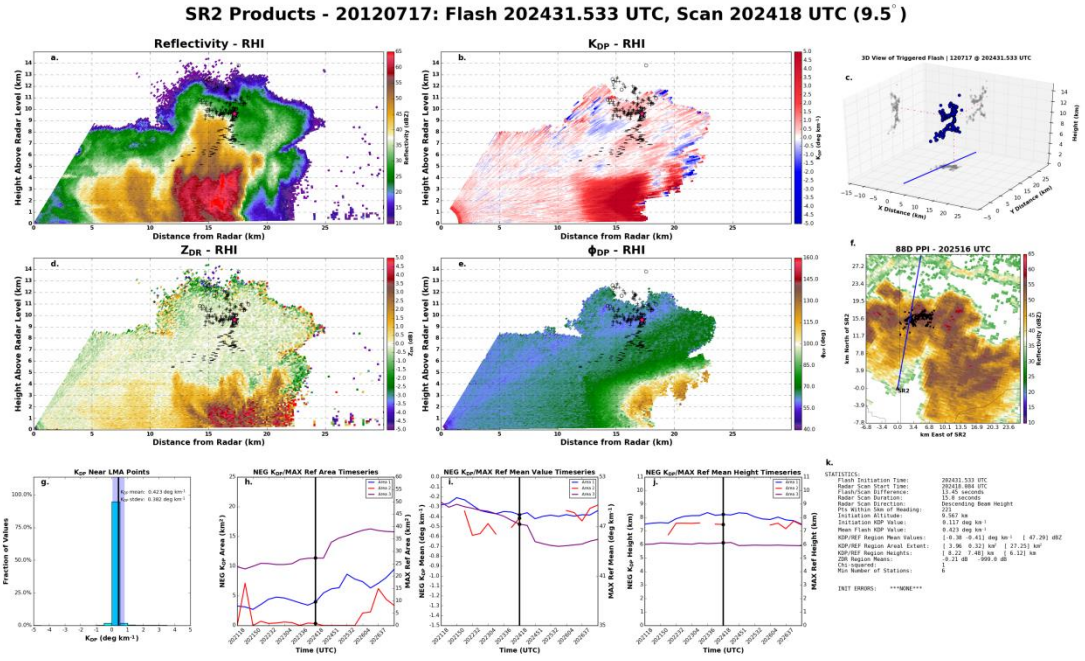

Figure 25: Same as Figure 19, but for the flash at 202431 UTC.

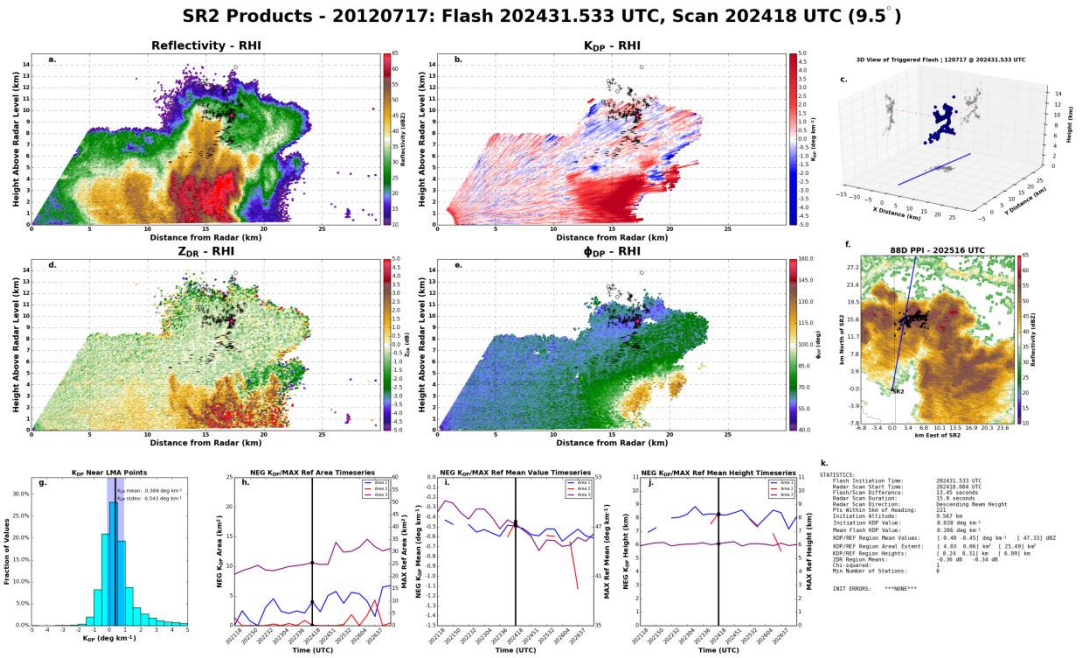

Figure 26: Same as Figure 20, but for the flash at 202431 UTC.

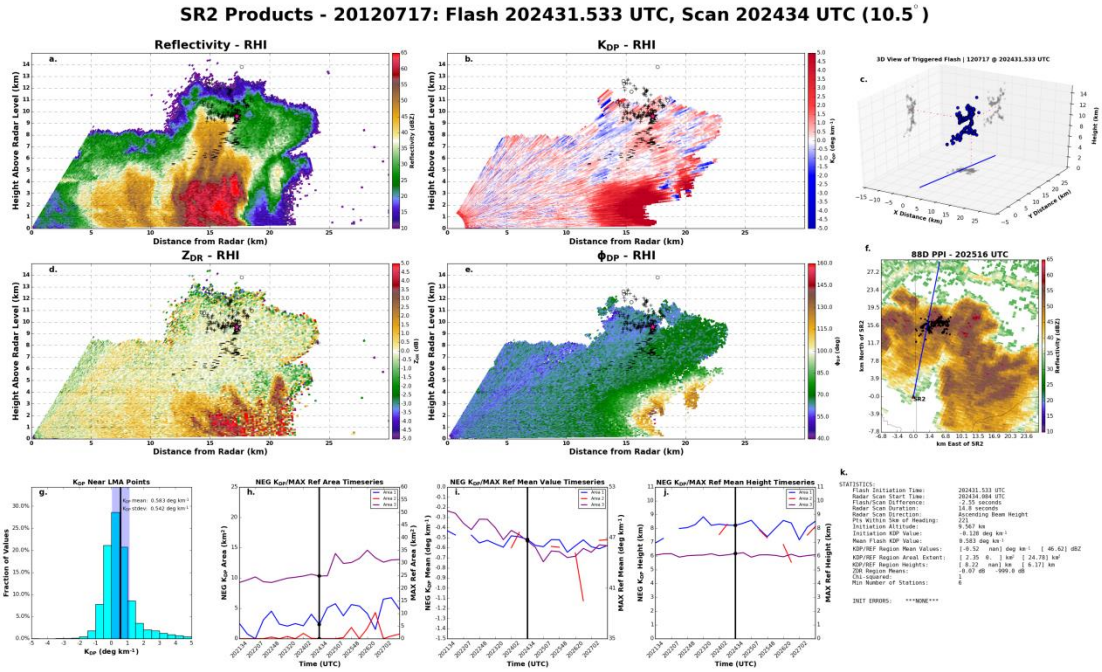

Figure 27: Same as Figure 21, but for the flash at 202431 UTC.

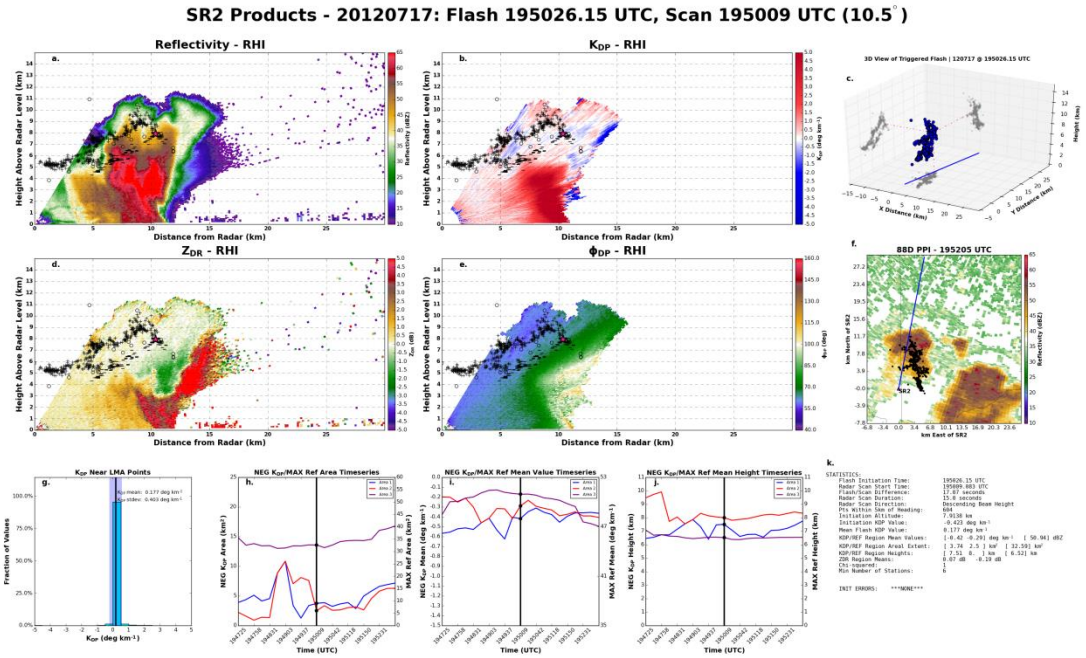

Figure 28: Same as Figure 19, but for a horizontally dominant flash at 195026 UTC.

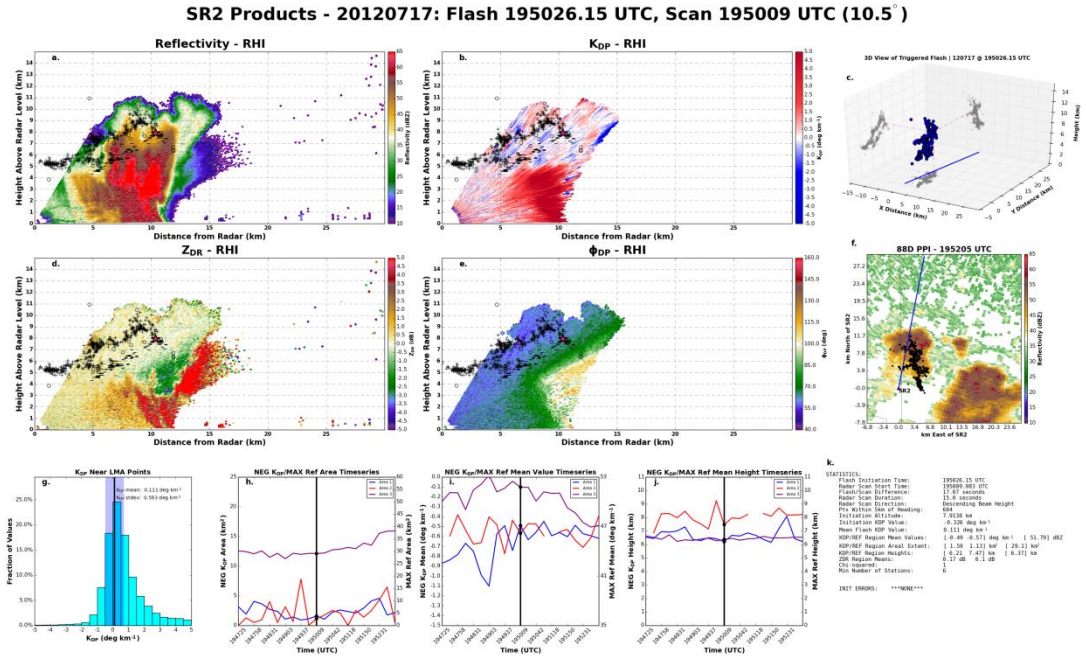

Figure 29: Same as Figure 20, but for the flash at 195026 UTC.

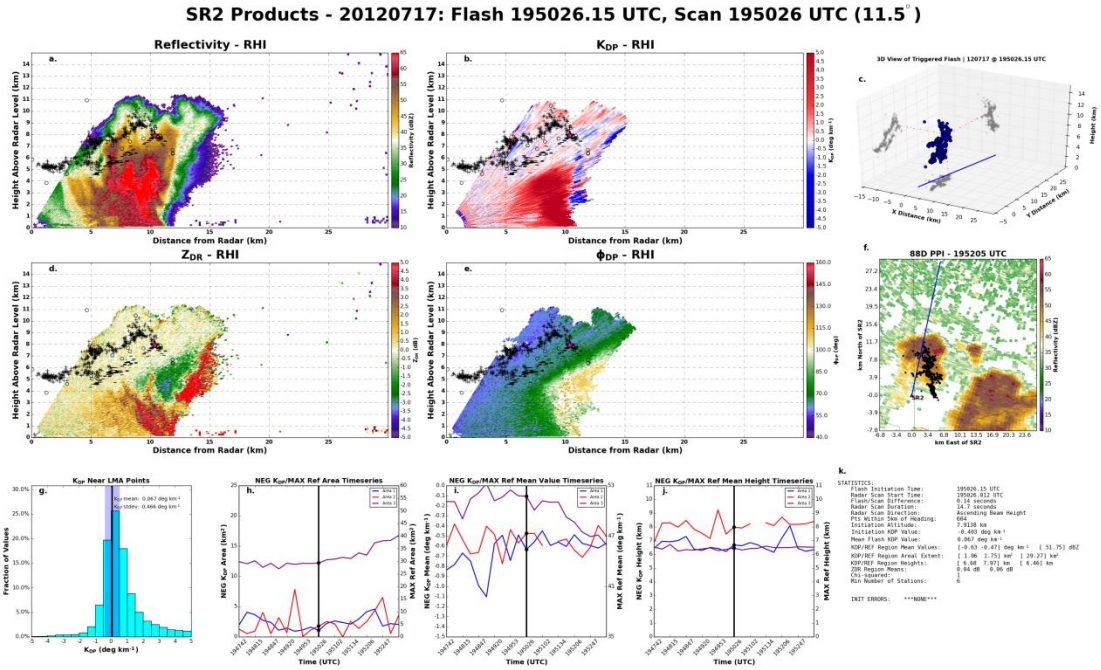

Figure 30: Same as Figure 21, but for the flash at 195026 UTC.

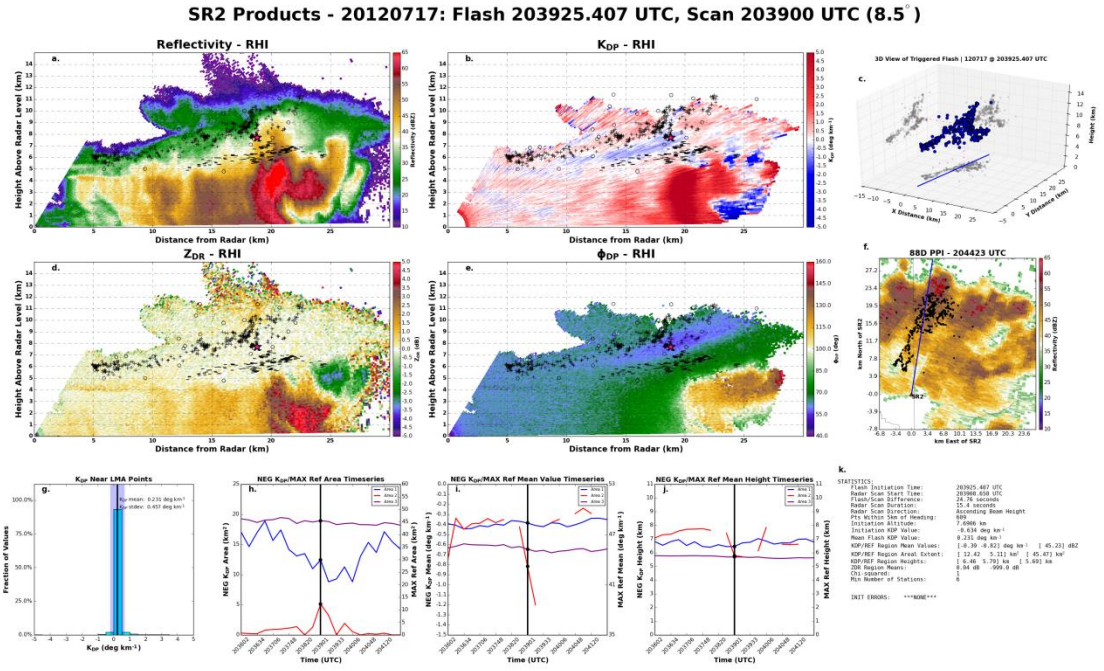

Figure 31: Same as Figure 28, but for the flash at 203925 UTC.

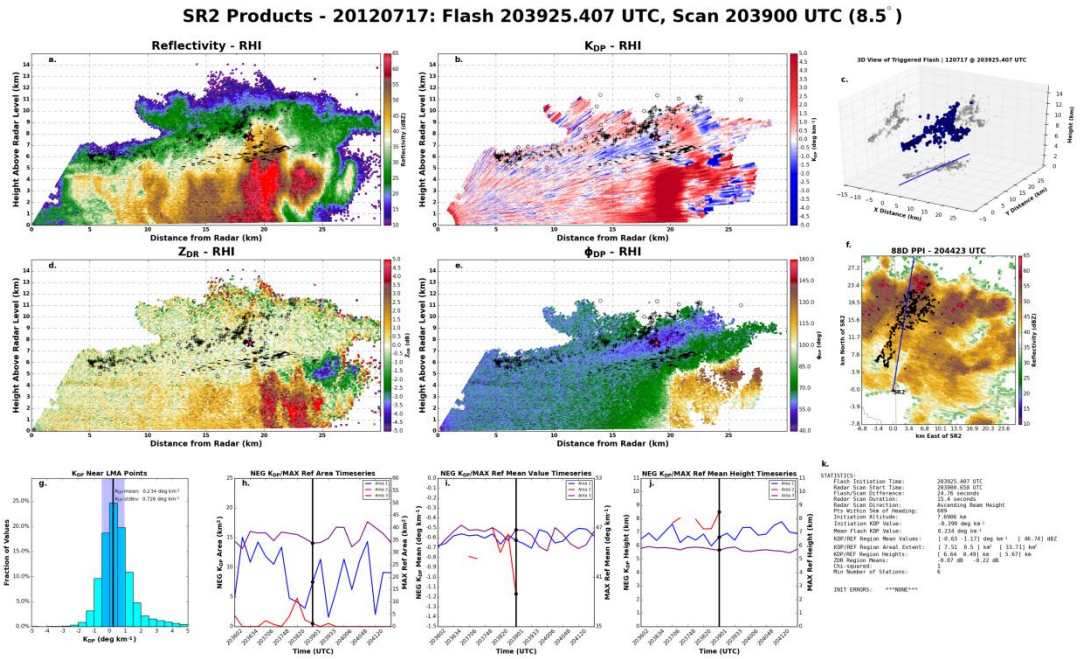

Figure 32: Same as Figure 20, but for the flash at 203925 UTC.

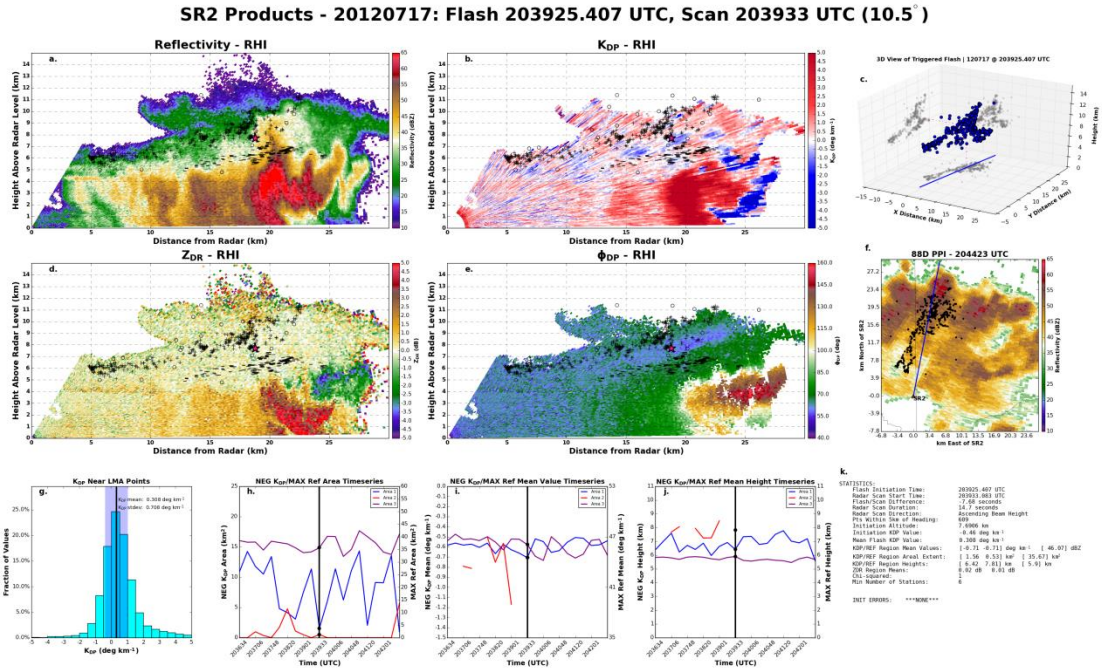

Figure 33: Same as Figure 21, but for the flash at 203925 UTC.

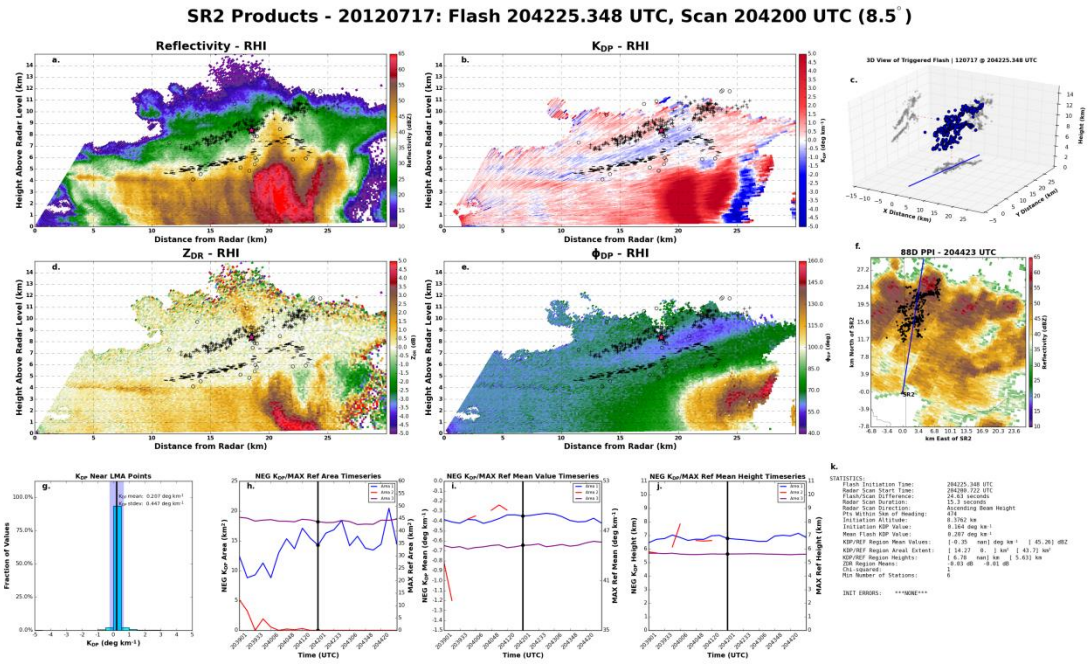

Figure 34: Same as Figure 28, but for the flash at 204225 UTC.

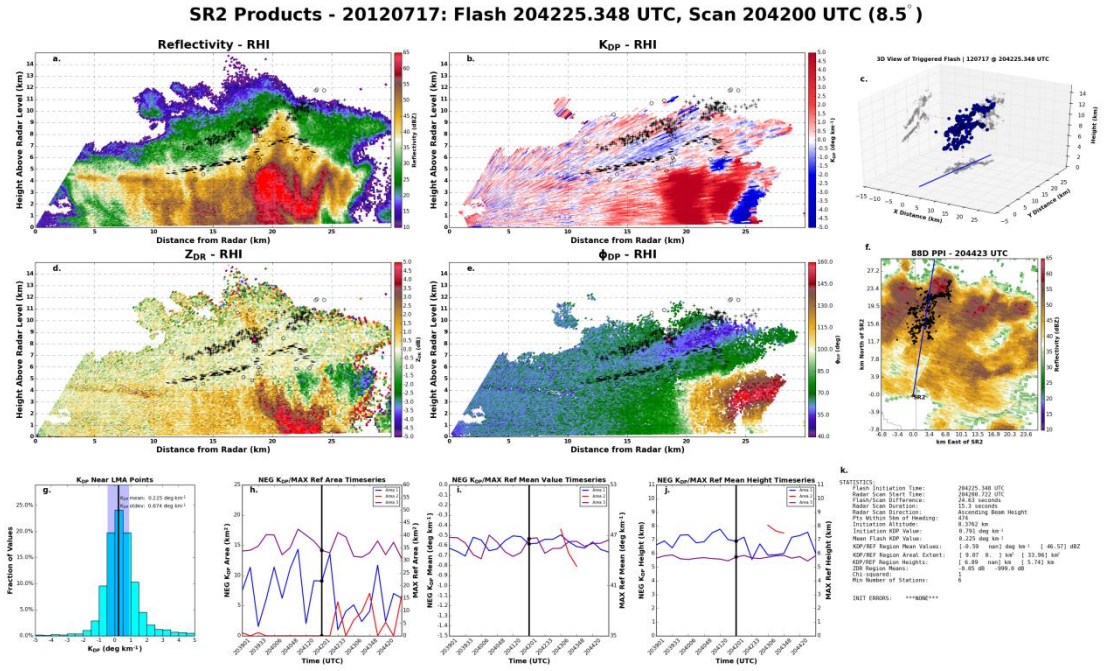

Figure 35: Same as Figure 28, but for the flash at 204225 UTC and 2 scans prior to flash.

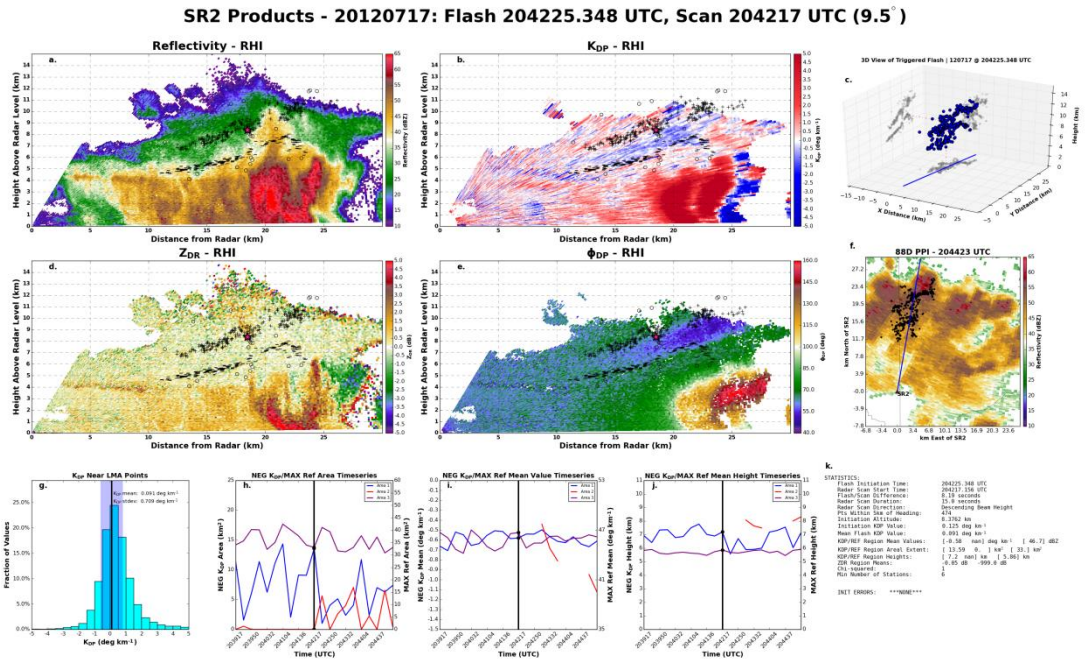

Figure 36: Same as Figure 20, but for the flash at 204225 UTC.

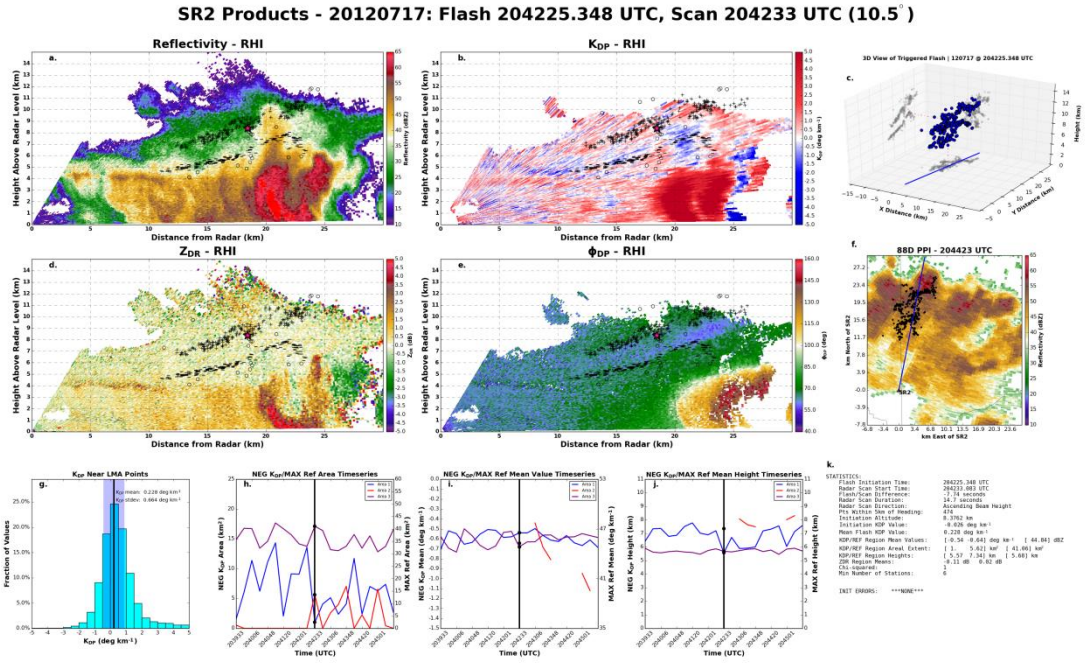

Figure 37: Same as Figure 21, but for the flash at 204225 UTC.

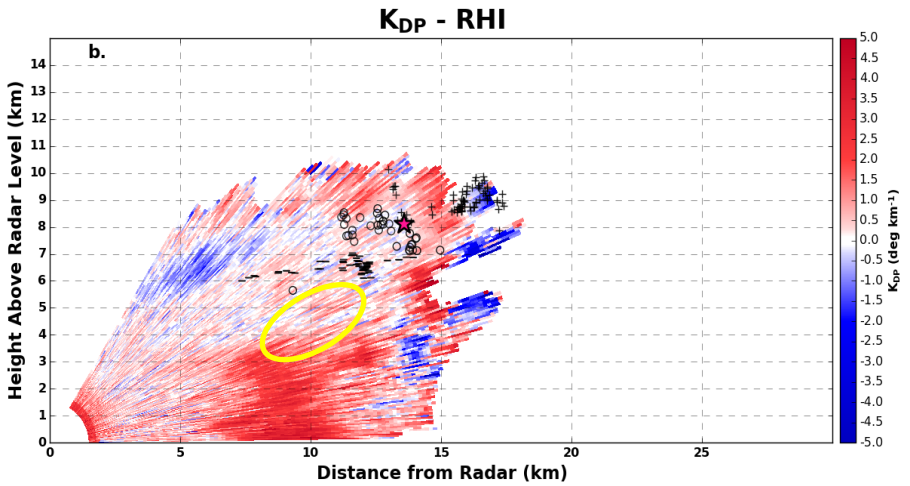

Figure 38: RHI at 200950 UTC of K_{DP} immediately prior to the scan in Figure 39. Flash overlayed was from 200949 UTC. The yellow circle represents the region of interest in Figure 39.

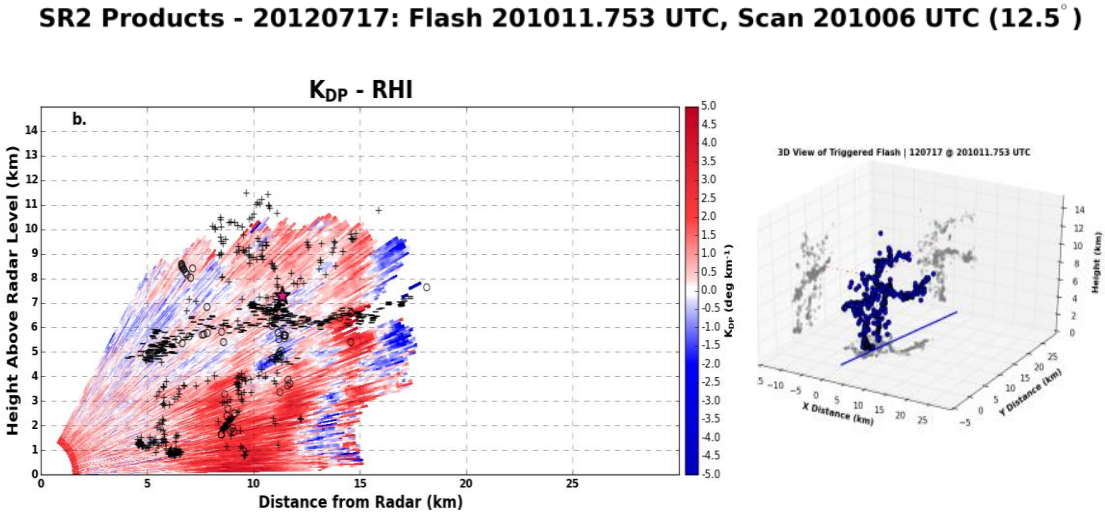

Figure 39: Same as Figure 38(b,c), but for flash at 201011 UTC. The dashed green line is the location of the radar beam when the flash occurred. The green arrow denotes that the radar beam was ascending. The yellow circle highlights the region where the flash passed through the radar beam plane. The yellow circle also highlights how the radar was scanning extreme K_{DP} values, which abruptly stopped when the flash occurred.

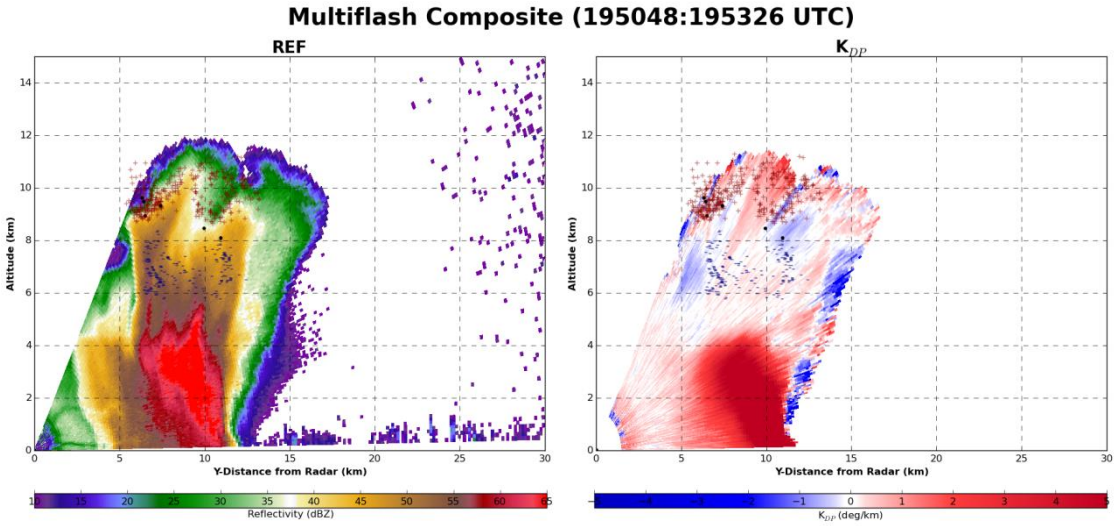

Figure 40: Multiflash composite of all flashes between 195048 and 195326 UTC superimposed on the mean of the RHIs between those times for (a) reflectivity (left) and (b) K_{DP} (right). Dark red + indicates location positive charge that the flashes propagated through, dark blue – indicates location of negative charge that the flashes propagated through, and black dots indicate initiation points. In panel (b), negative K_{DP} regions are in shades of blue.

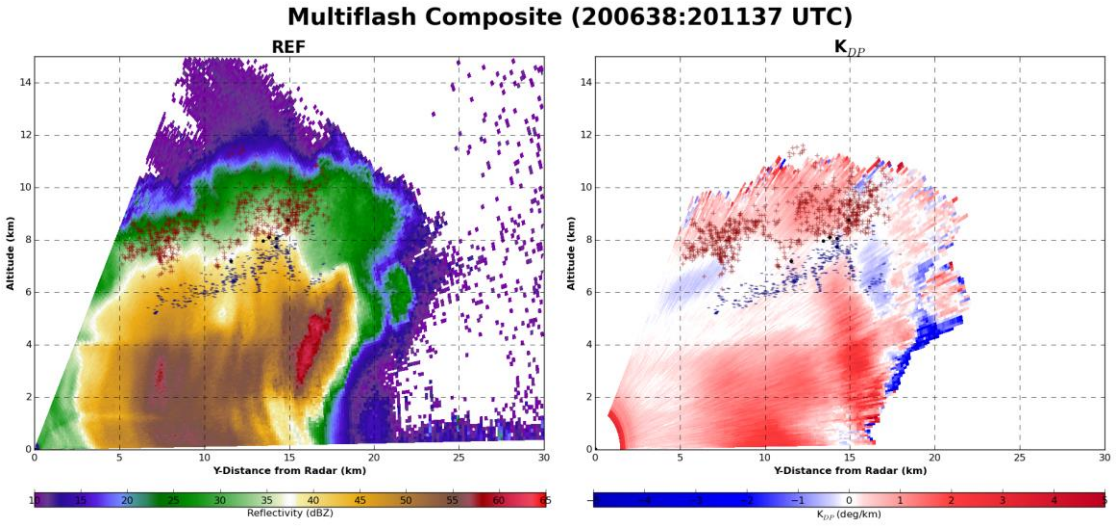

Figure 41: Same as Figure 40, but for flashes 200638-201137 UTC.

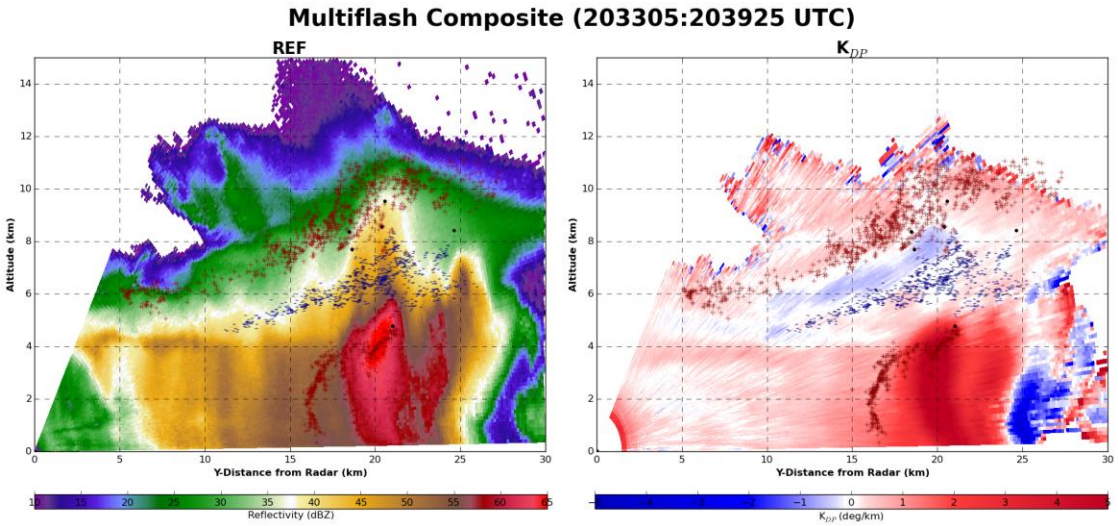

Figure 42: Same as Figure 40, but for flashes 203305-203925 UTC.

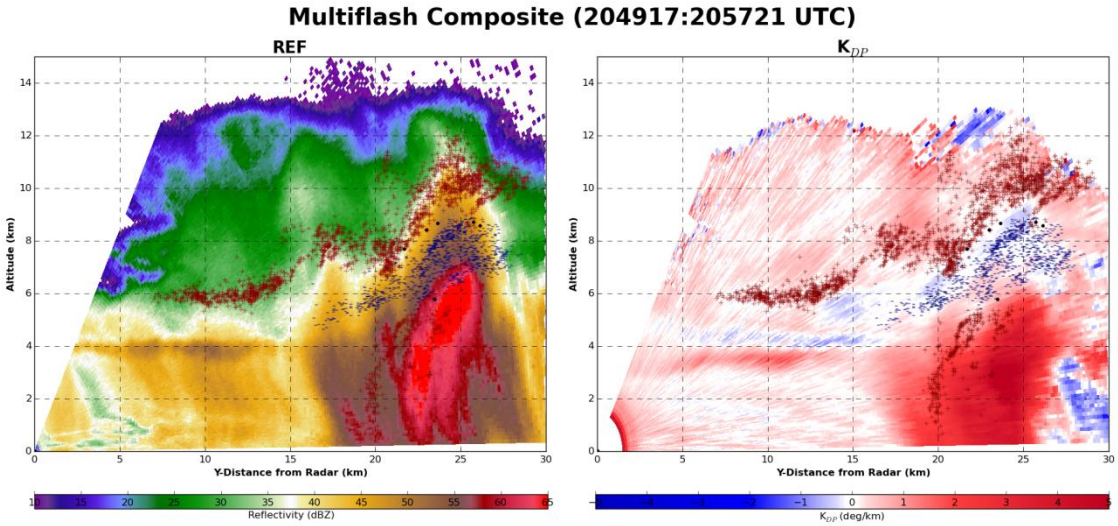

Figure 43: Same as Figure 40, but for flashes 204917-205721 UTC.

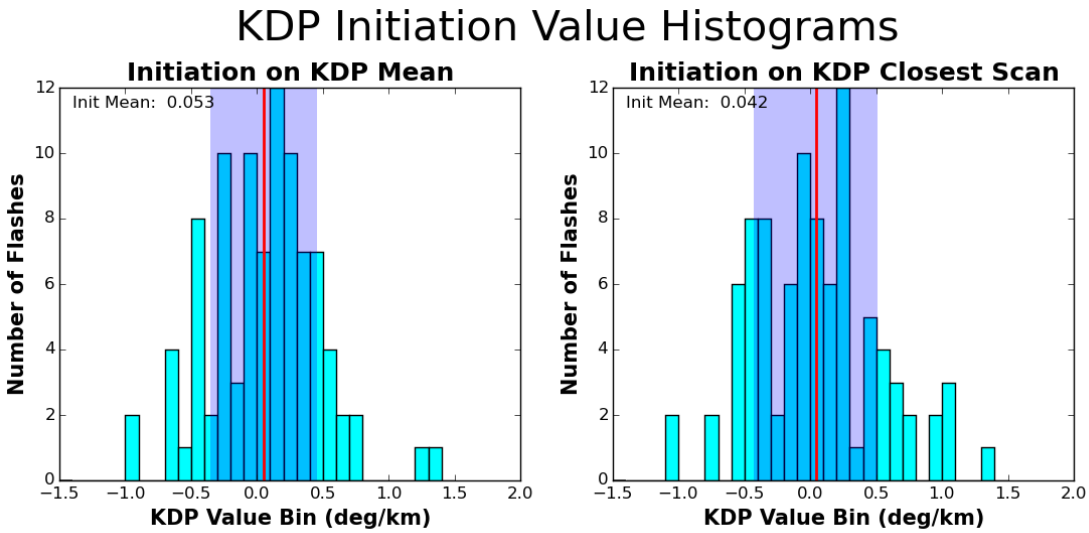

Figure 44: Histograms of the values of K_{DP} in the 5-RHI mean scan (left) and closest single scan prior to the flash (right) at the flash initiation location. Red line denotes the mean of all the initiation values, blue shading represents the middle 2 standard deviations of initiation values.

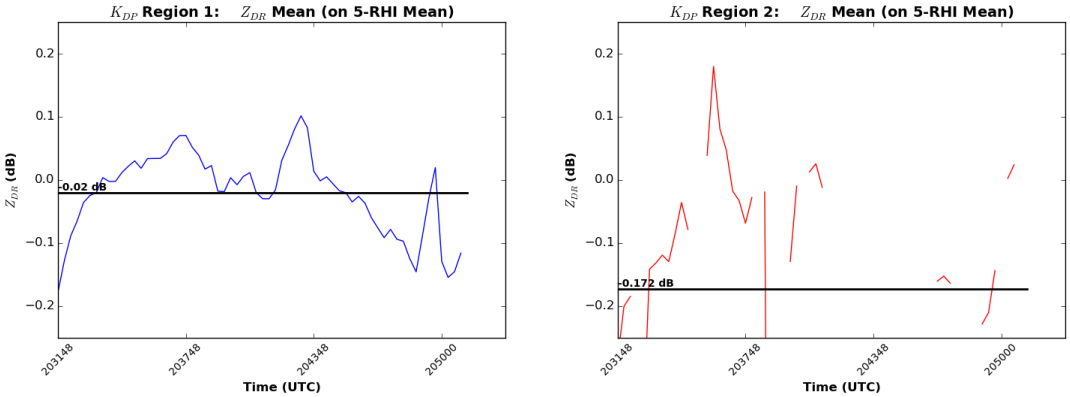

Figure 45: Timeseries of mean Z_{DR} values in the negative K_{DP} regions 2032 - 2051 UTC. The mean is indicated by the black horizontal line.

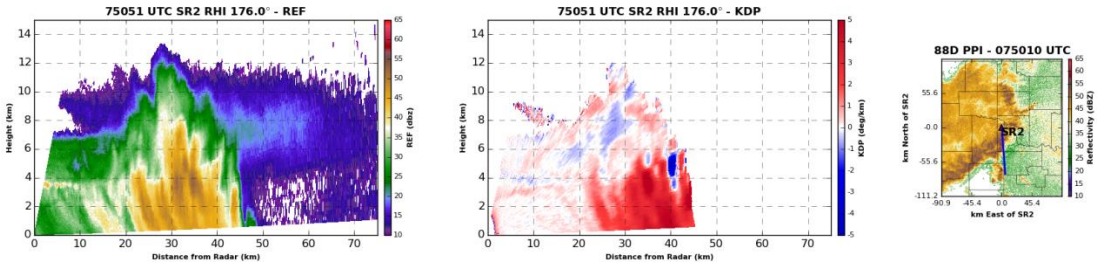

Figure 46: 5-RHI mean around 075051 UTC of (a) reflectivity (left) and (b) K_{DP}. The far right panel (c) is data from the nearest 88D scan of reflectivity. The blue line is SR2's radar beam.

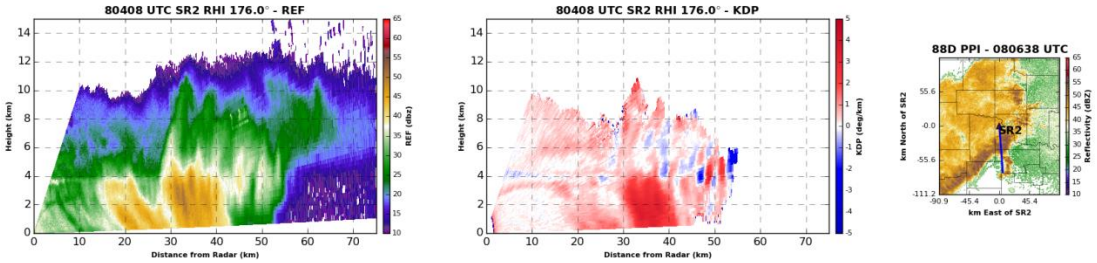

Figure 47: Same as Figure 46 at 081036 UTC.

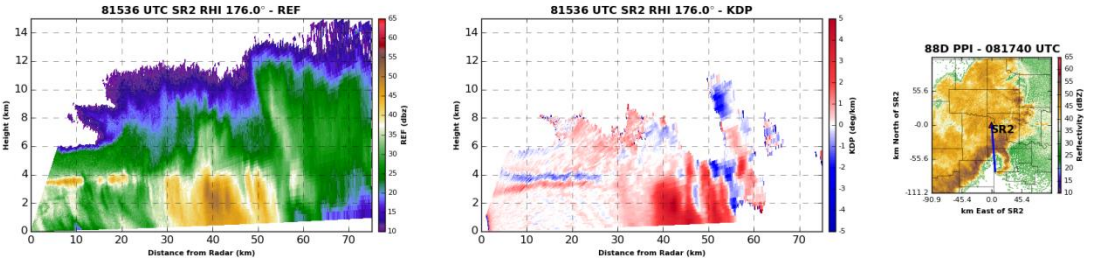

Figure 48: Same as Figure 46 at 082335 UTC.

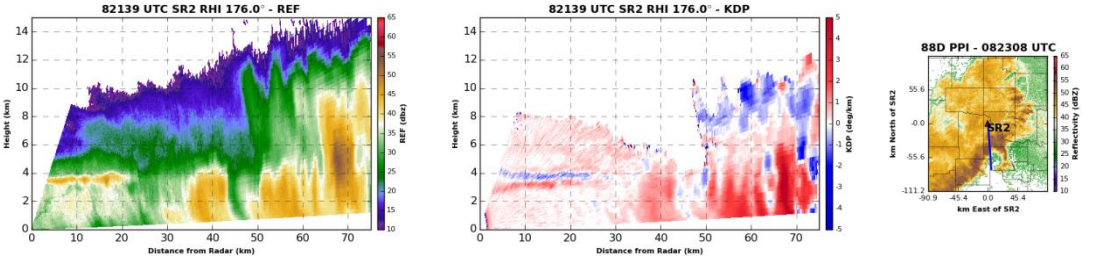

Figure 49: Same as Figure 46 at 083710 UTC.

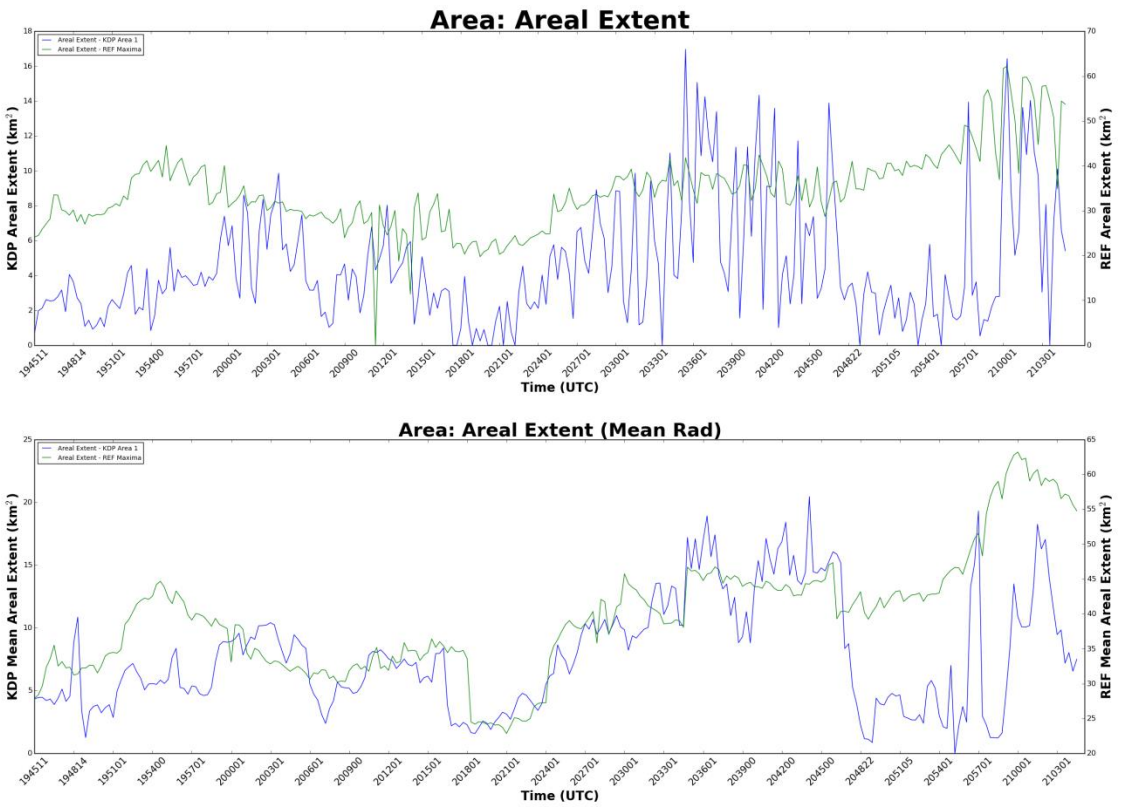

Figure 50: Areal extent time series of the transition zone K_{DP} region and the reflectivity maxima in the Florida squall line on July 17, 2012. Top panel are computed using individual RHIs, bottom is computed using 5-RHI means.

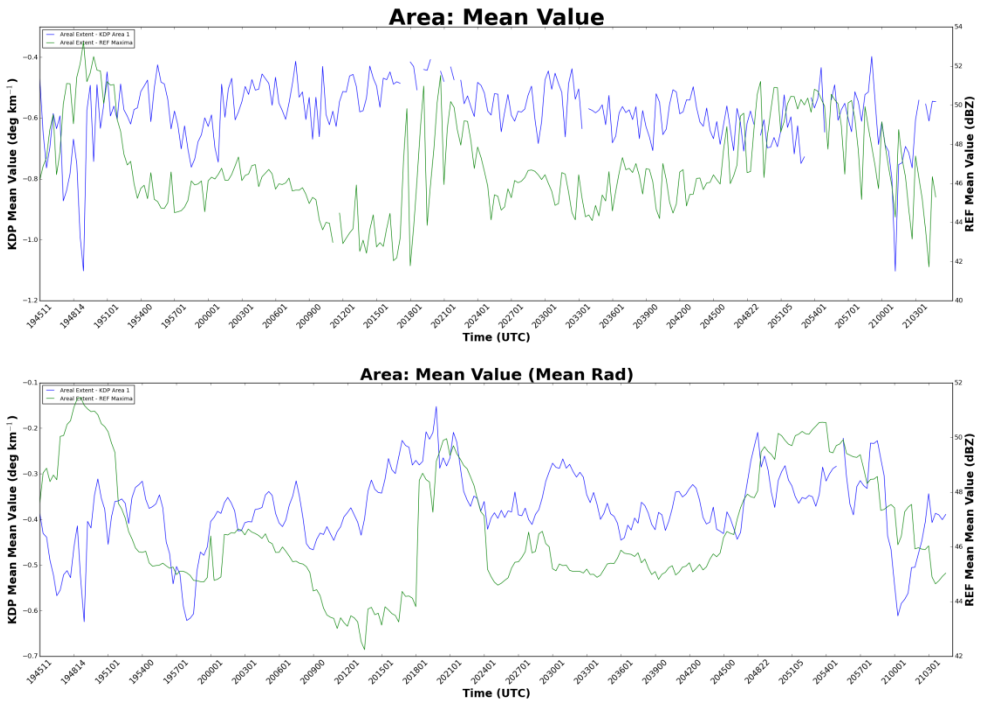

Figure 51: Same as Figure 50, except plotting the mean value of each region.

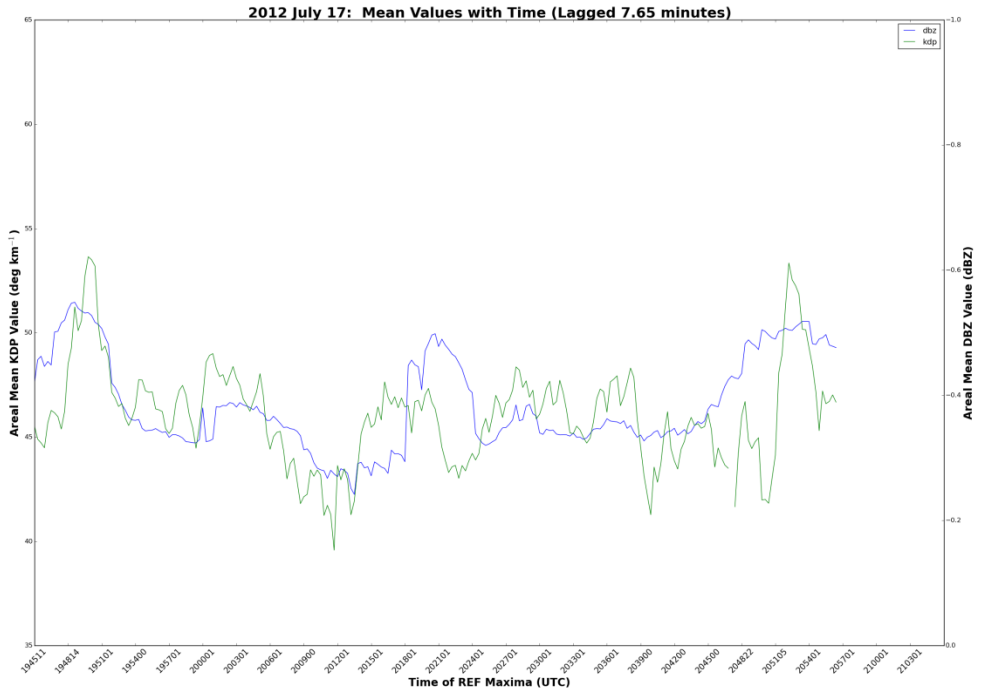

Figure 52: Same as Figure 51(b), except with a 7.65 minute delay in K_{DP} transposed on each other. The times on the bottom are of the time of the reflectivity maxima. Note that the y-axis is flipped for K_{DP} since a stronger K_{DP} region contains more negative values.

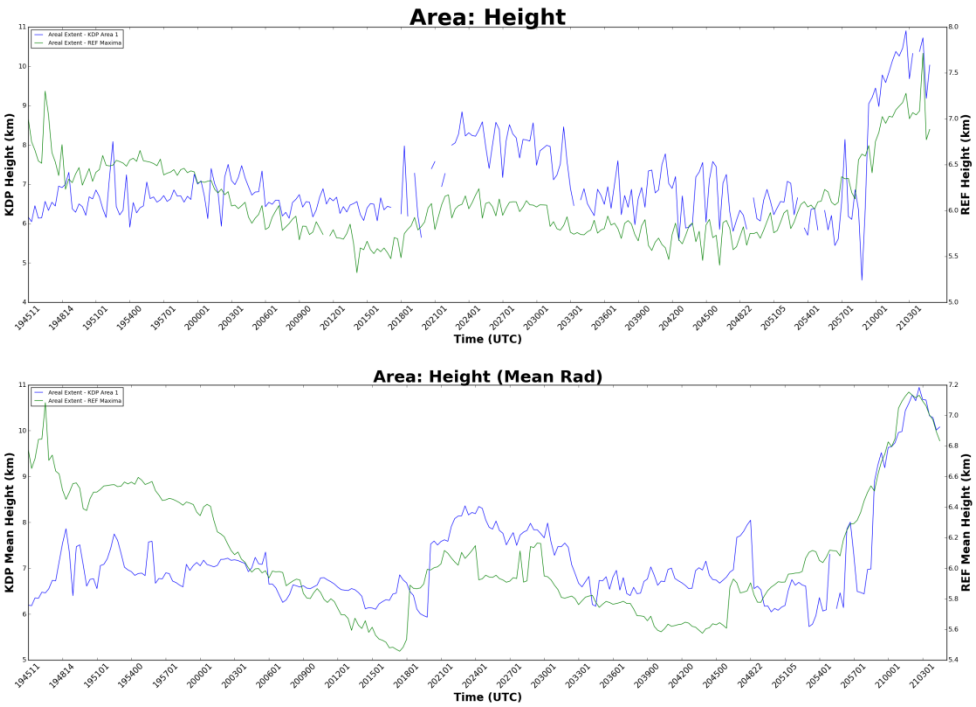

Figure 53: Same as Figure 50, except plotting the mean height of each region

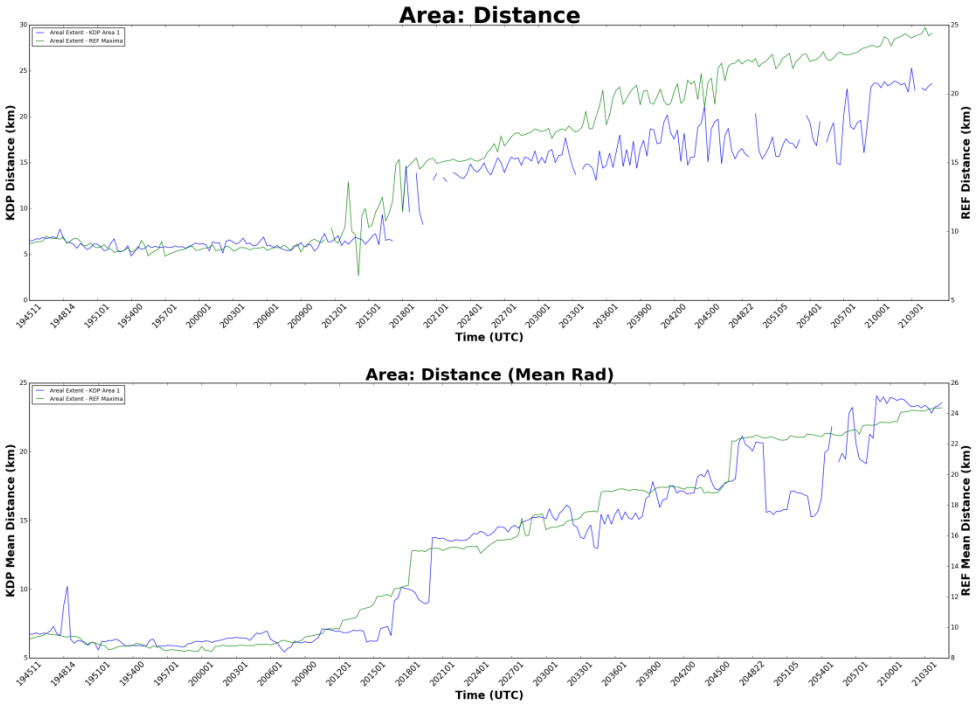

Figure 54: Same as Figure 50, except plotting the mean distance of each region

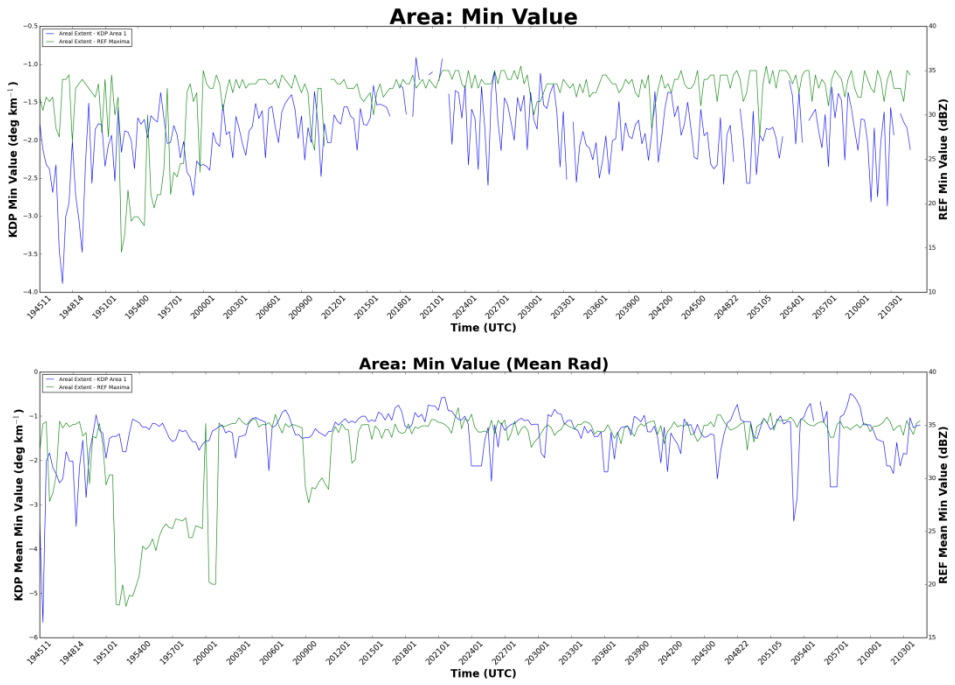

Figure 55: Same as Figure 50, except plotting the most extreme values of each region.

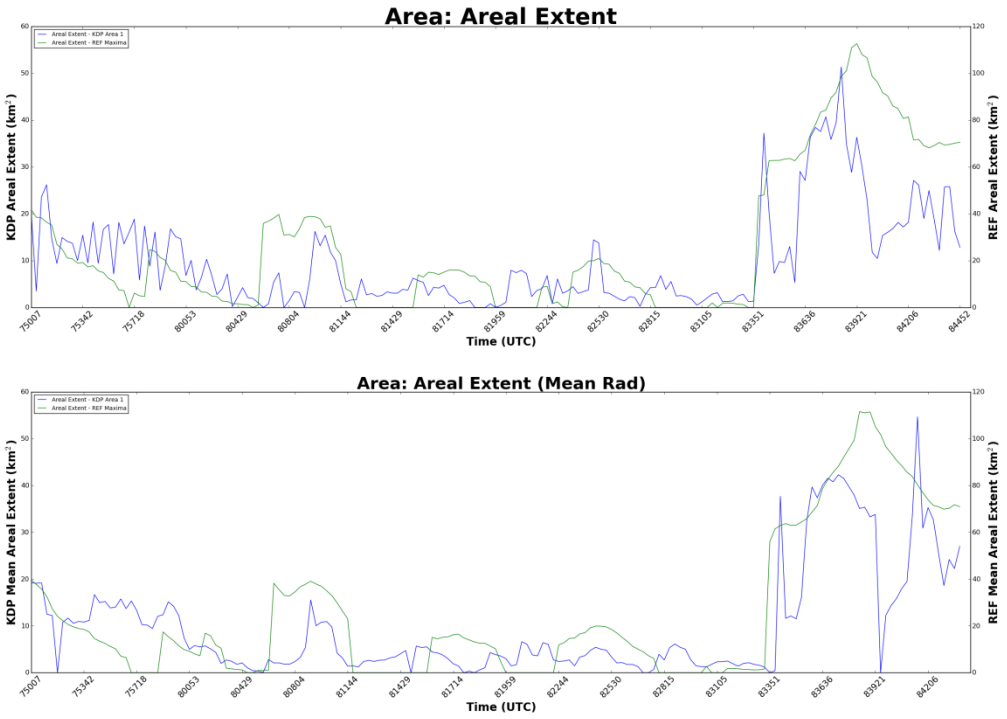

Figure 56: Areal extent time series of the transition zone K_{DP} region and the reflectivity maxima in the Florida squall line on September 18, 2016. Top panel are computed using individual RHIs, bottom is computed using 5-RHI means.

Figure 57: Same as Figure 56 except plotting the mean value of each region

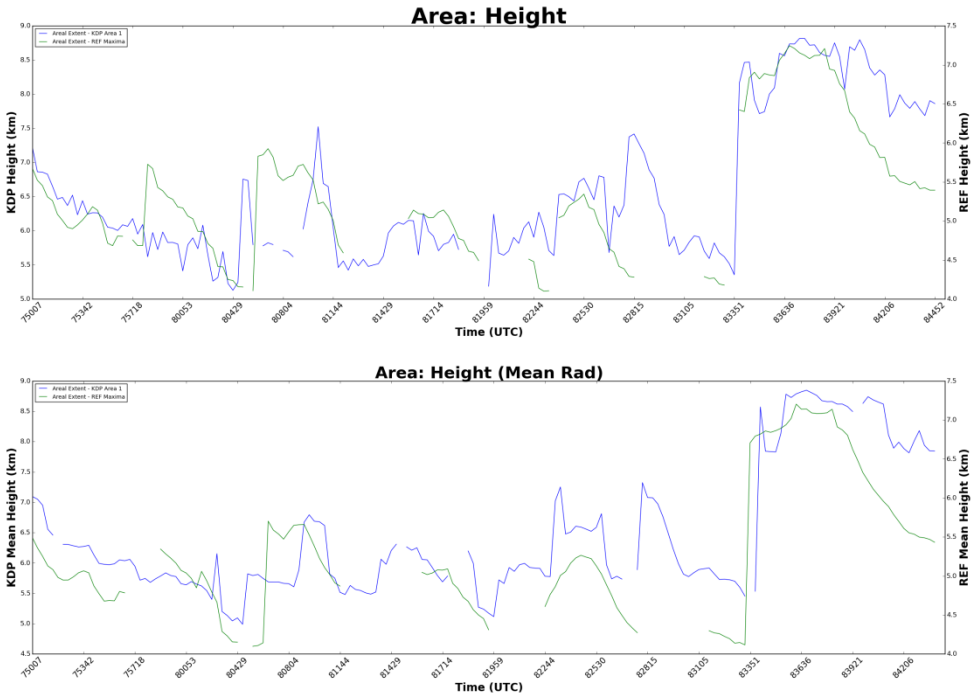

Figure 58: Same as Figure 56, except plotting the mean height of each region

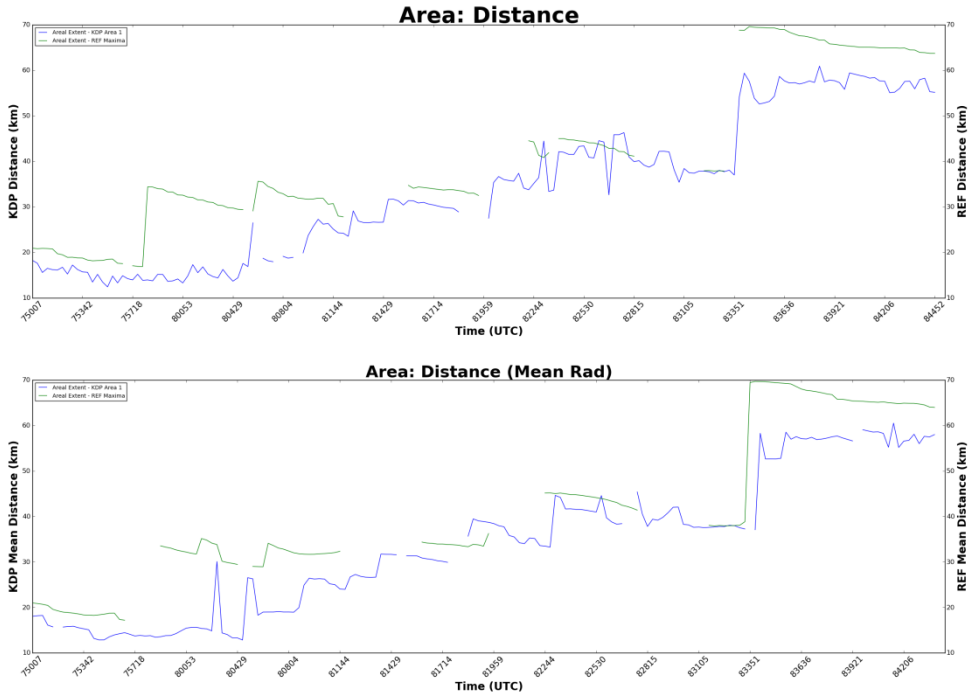

Figure 59: Same as Figure 56 except plotting the mean distance of each region

Figure 60: Same as Figure 56, except plotting the most extreme value of each region

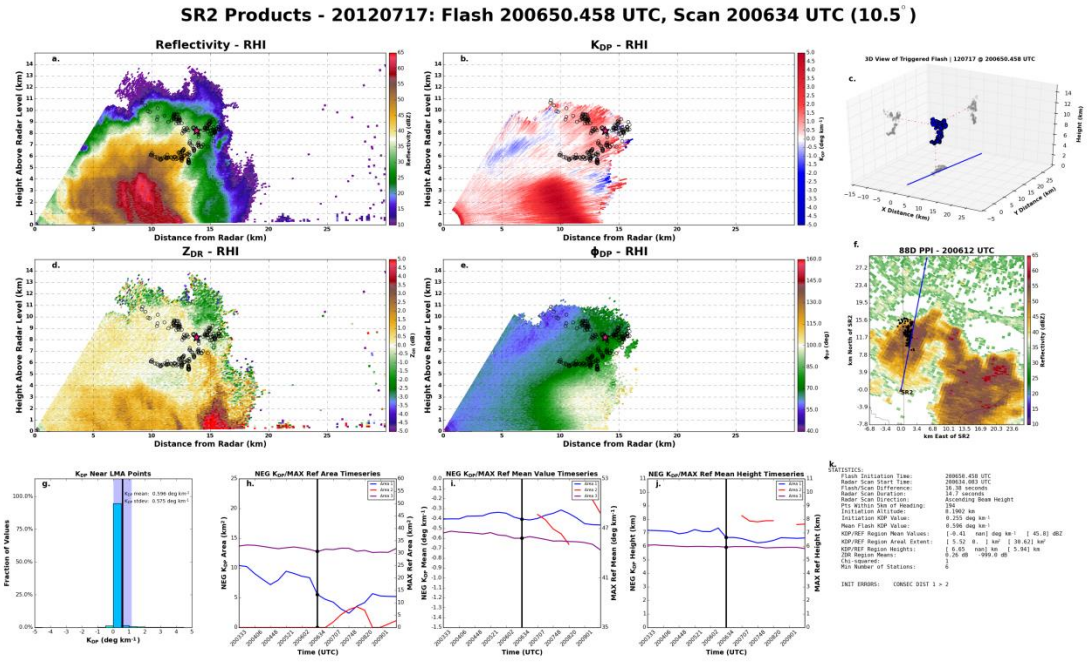

Figure 61: Outlier flash on the convective K_{DP} region at 200650 UTC overlayed on 5-RHI mean scan. Pink star shows initiation location, + indicates positive charge region, and - indicates negative charge region. Subfigures include (listed left to right and top to bottom) (a) reflectivity RHI, (b) K_{DP} RHI, (c) 3D view of flash with radar beam line in blue, (d) Z_{DR} RHI, (e) ϕ_{DP} RHI, (f) 88D PPI with radar beam line in blue, (g) historgram of K_{DP} values at flash points, (h) timeseries of K_{DP} and reflectivity regions areal extents, (i) timeseries of K_{DP} and reflectivity regions mean values, (j) timeseries of K_{DP} and reflectivity regions mean heights, and (k) metadata.

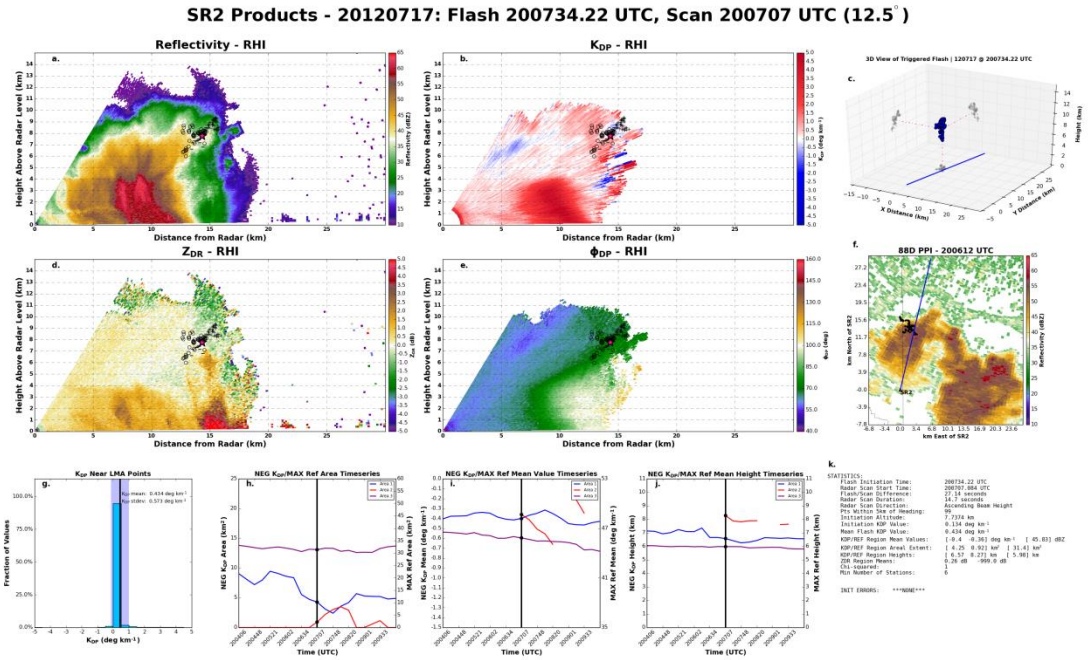

Figure 62: Same as Figure 61, but for the 200734 UTC flash.

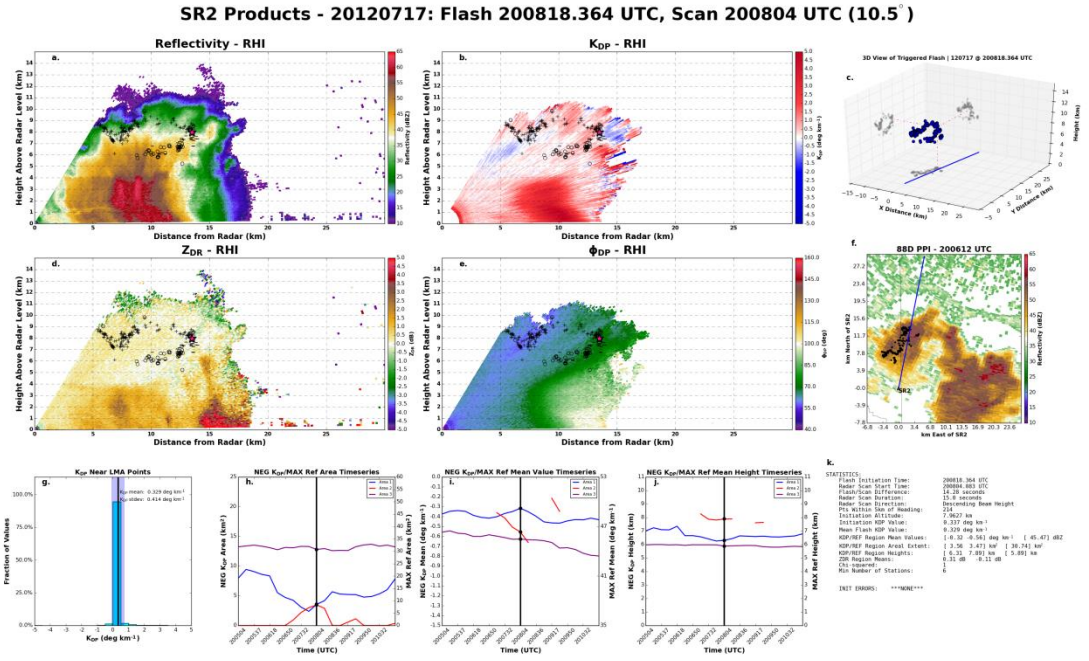

Figure 63: Same as Figure 61, but for the 200818 UTC flash.

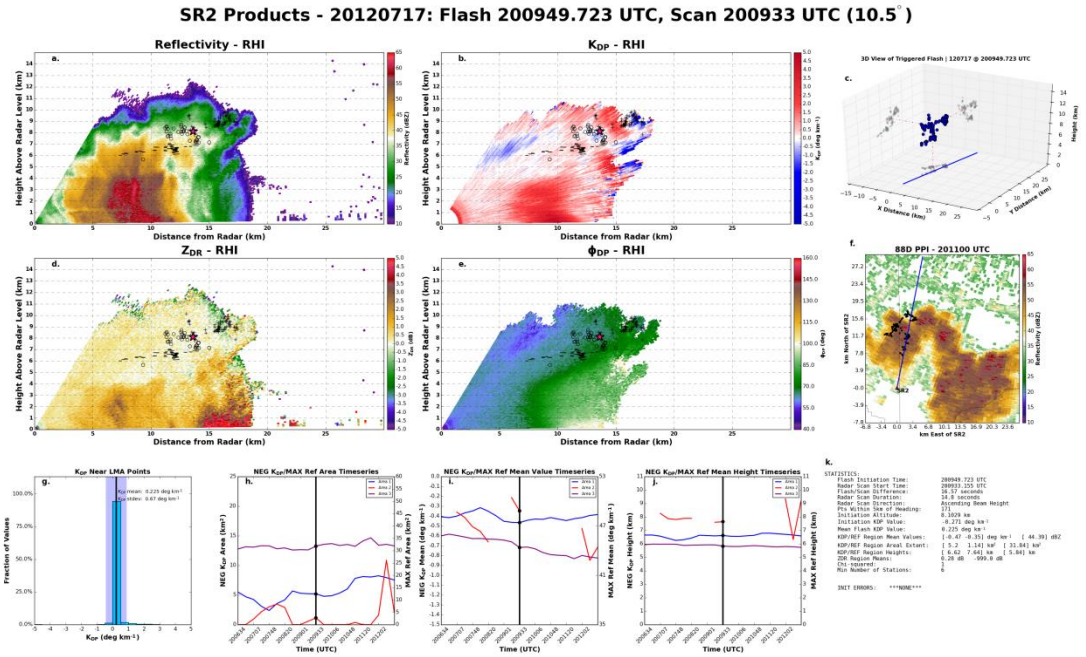

Figure 64: Same as Figure 61, but for the 200949 UTC flash.

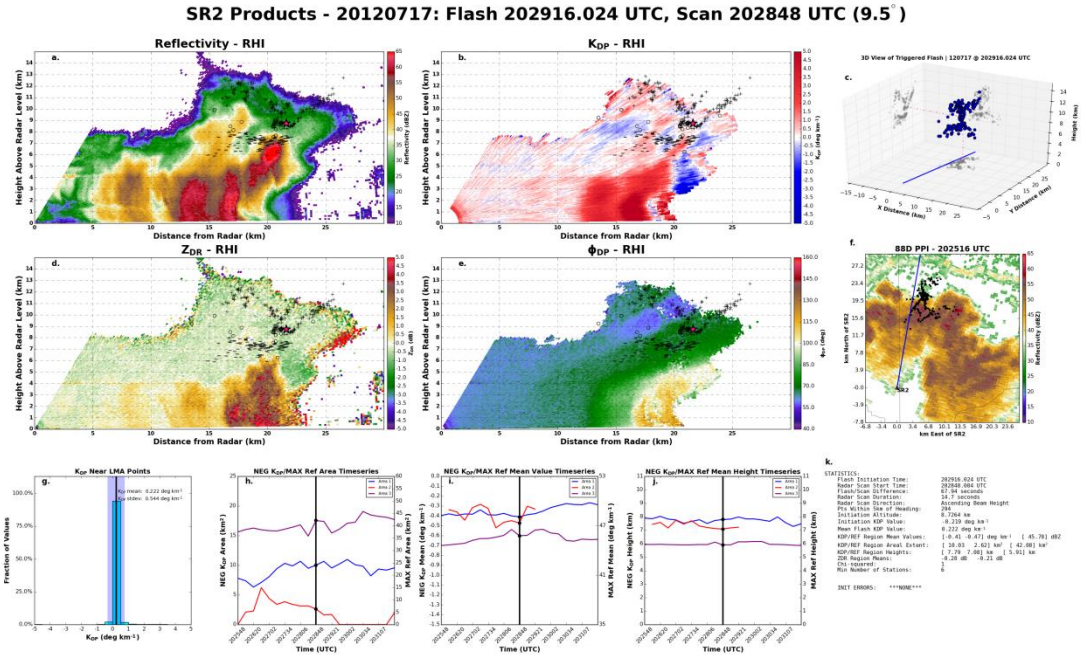

Figure 65: Same as Figure 61, but for the 202916 UTC flash.

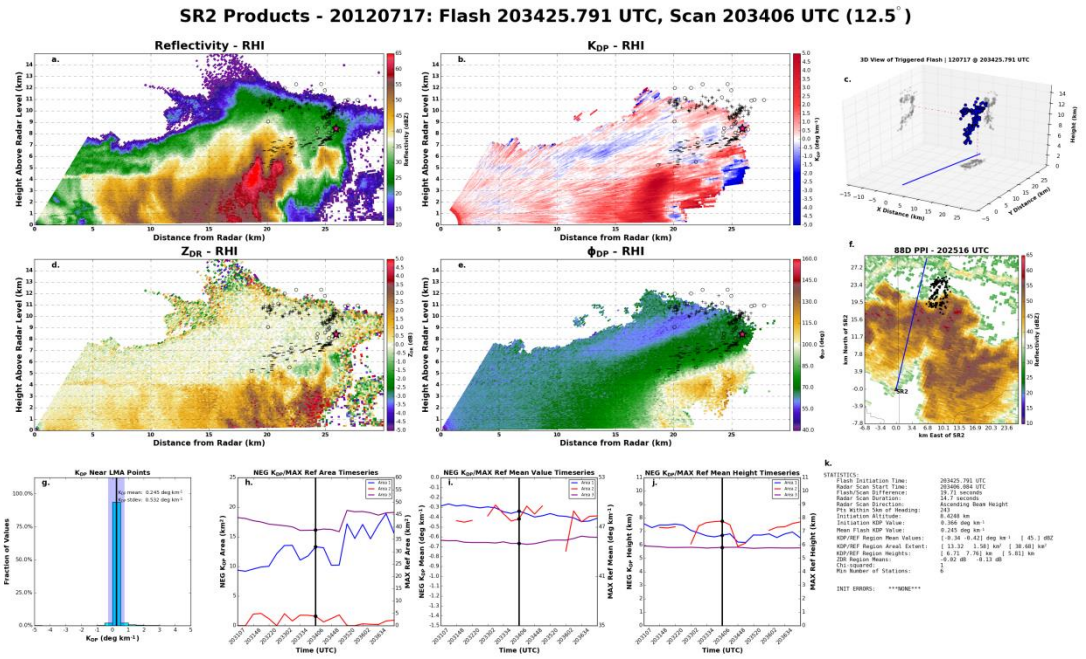

Figure 66: Same as Figure 61, but for the 203425 UTC flash.

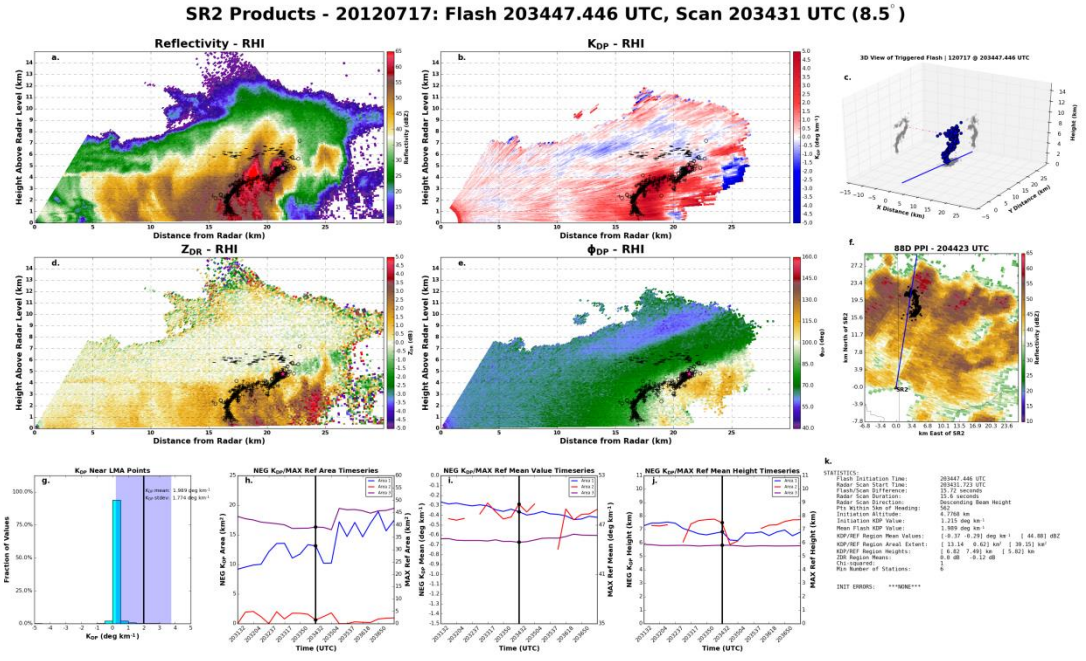

Figure 67: Same as Figure 61, but for the 203447 UTC flash.

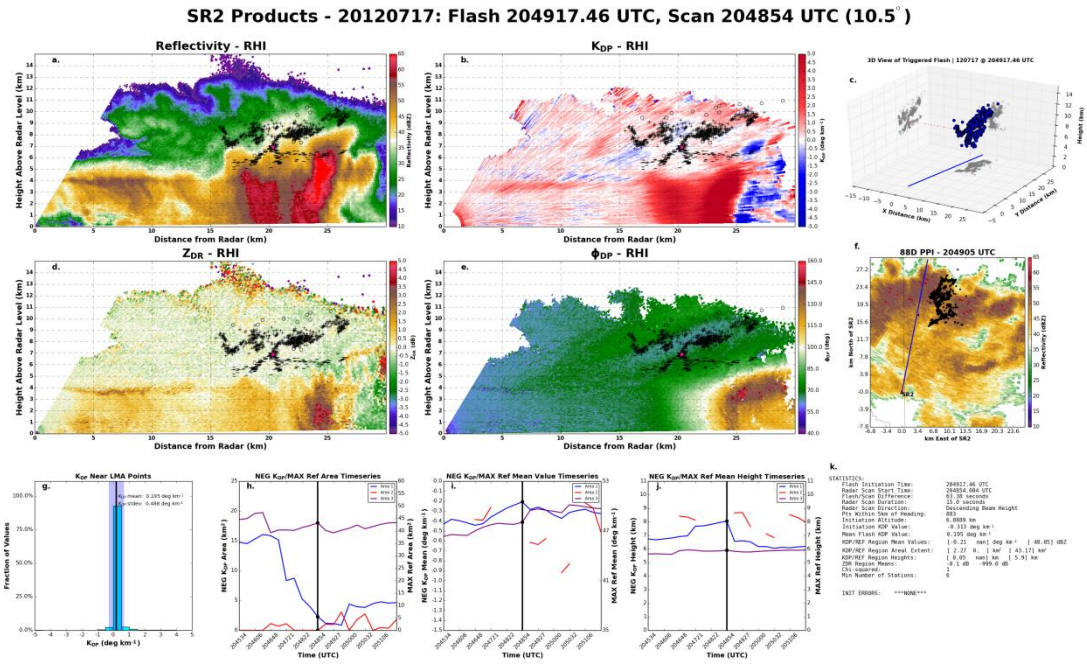

Figure 68: Same as Figure 61, but for the 204917 UTC flash.

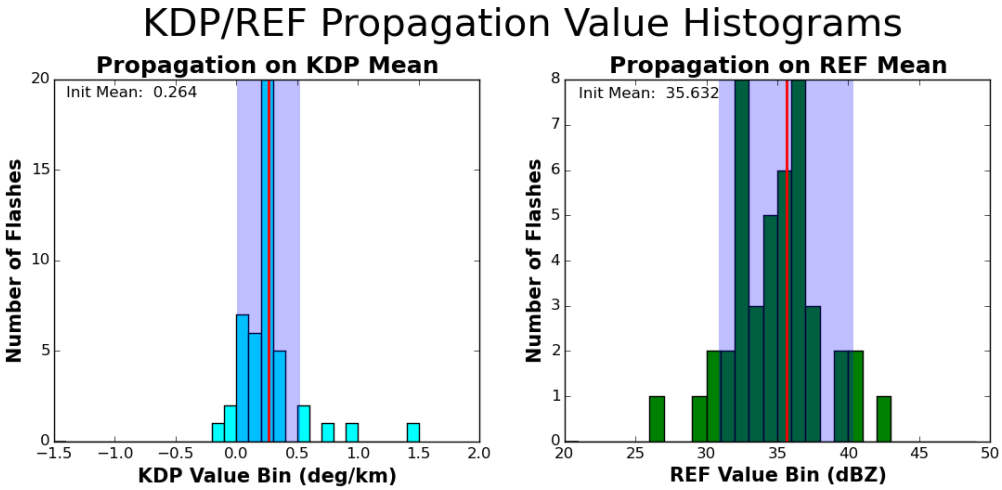

Figure 69: Distribution of the mean values each flash propagated through, including 5-RHI mean K_{DP} (left) and reflectivity values (right) that flashes propagated through after initiation. Mean is denoted by the red vertical line and the middle three standard deviations is the light blue region.

Evolution of Negative K_{DP} Regions

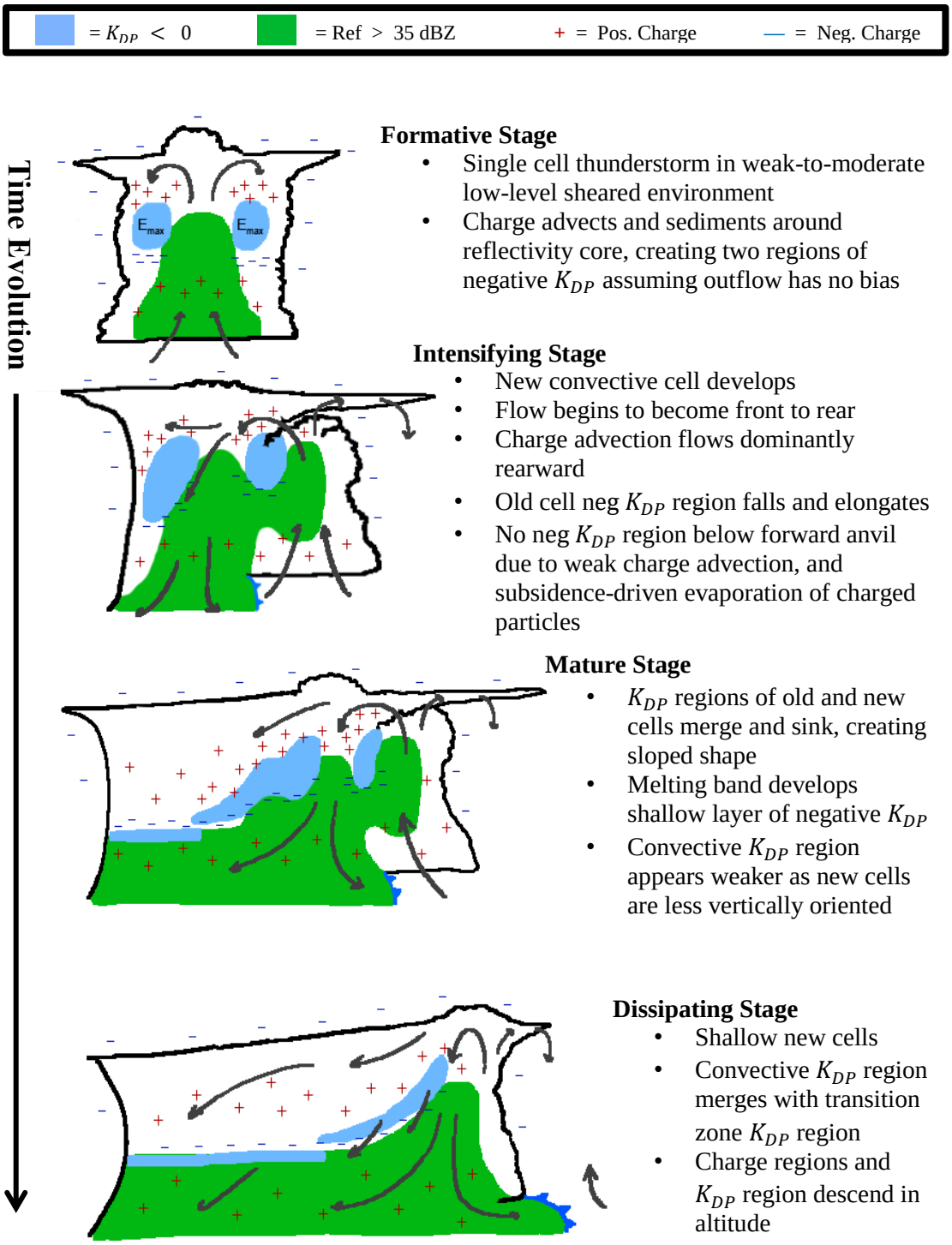

Figure 70: Time evolution of a squall line with associated K_{DP} regions, charge regions, reflectivity, and flows. Notable attributes of each stage are listed on the right.

References

Aufdermaur, A. N., and D. A. Johnson, 1972: Charge separation due to riming in an electric field. *Q. J. R. Meteorol. Soc.*, **98**, 369–382, doi:10.1002/qj.49709841609.

Bateman, M. G., W. D. Rust, B. F. Smull, and T. C. Marshall, 1995: Precipitation charge and size measurements in the stratiform region of two mesoscale convective systems. *J. Geophys. Res.*, **100**, 16341, doi:10.1029/95JD01280.

Biggerstaff, M. I., and R. a Houze, 1991: Kinematic and Precipitation Structure of the 10-11 June 1985 Squall Line. *Mon. Weather Rev.*, **119**, 3034–3065.

Biggerstaff, M. I., and R. A. Houze, 1993: Kinematics and Microphysics of the Transition Zone of the 10–11 June 1985 Squall Line. *J. Atmos. Sci.*, **50**, 3091–3110, doi:10.1175/1520-0469(1993)050<3091:KAMOTT>2.0.CO;2.

Bluestein, H. B., and M. H. Jain, 1985: Formation of Mesoscale Lines of Precipitation: Severe Squall Lines in Oklahoma during the Spring. *J. Atmos. Sci.*, **42**, 1711–1732.

Brooks, I. M., C. P. R. Saunders, R. P. Mitzeva, and S. L. Peck, 1997: The effect on thunderstorm charging of the rate of rime accretion by graupel. *Atmos. Res.*, **43**, 277–295, doi:10.1016/S0169-8095(96)00043-9.

Bruning, E. C., W. D. Rust, T. J. Schuur, D. R. MacGorman, P. R. Krehbiel, and W. Rison, 2007: Electrical and Polarimetric Radar Observations of a Multicell Storm in TELEX. 2525–2544, doi:10.1175/MWR3421.1.

Byers, H. R., and R. R. Braham Jr., 1949: *The Thunderstorm*. U.S. Govt. Printing Office,.

Carey, L. D., W. Petersen, and W. Deierling, 2009: Radar Differential Phase Signatures of Ice Orientation for the Prediction of Lightning Initiation and Cessation. *34th Conf. Radar Meteorol.*, 5–9.

Carey, L. D., and S. A. Rutledge, 1998: Electrical and multiparameter radar observations of a severe hailstorm. *J. Geophys. Res.*, **103**, 13979–14000.

Caylor, I. J., and V. Chandrasekar, 1996: Time-varying ice crystal orientation in thunderstorms observed with multiparameter radar. *IEEE Trans. Geosci. Remote Sens.*, **34**, 847–858, doi:10.1109/36.508402.

Cho, H. R., J. V. Iribarne, and W. G. Richards, 1981: On the Orientation of Ice Crystals in a Cumulonimbus Cloud. *J. Atmos. Sci.*, **38**, 1111–1114.

Christian, H., C. R. Holmes, J. W. Bullock, W. Gaskell, A. J. Illingworth, and J. Latham, 1980: Airborne and ground-based studies of thunderstorms in the vicinity of Langmuir Laboratory. *Q. J. R. Meteorol. Soc.*, **106**, 159–174, doi:10.1002/qj.49710644711.

Coleman, L. M., 2003: Effects of charge and electrostatic potential on lightning propagation. *J. Geophys. Res.*, **108**, 1–27, doi:10.1029/2002JD002718.

Coleman, L. M., M. Stolzenburg, T. C. Marshall, and M. Stanley, 2008: Horizontal lightning propagation, preliminary breakdown, and electric potential in New Mexico thunderstorms. *J. Geophys. Res. Atmos.*, **113**, 1–12, doi:10.1029/2007JD009459.

Dinger, J. E., 1965: Electrification Associated with the Melting of Snow and Ice. *J. Atmos. Sci.*, **22**, 162–166.

Dinger, J. E., and R. Gunn, 1946: Electrical Effects Associated with a Change of State of Water. *Terr. Magn. Atmos. Electr.*, **51**, 477–494.

Dong, Y., and J. Hallett, 1992: Charge Separation by Ice and Water Drops During Growth and Evaporation. **97**, 20361–20371.

Doviak, R. J., V. Bringi, A. Ryzhkov, A. Zahrai, and D. Zrnić, 2000: Considerations for polarimetric upgrades to operational WSR-88D radars. *J. Atmos. Ocean. Technol.*, **17**, 257–278, doi:10.1175/1520-0426(2000)017<0257:CFPUTO>2.0.CO;2.

Drake, J. C., 1968: Electrification accompanying the melting of ice particles. *Q. J. R. Meteorol. Soc.*, **94**, 176–191, doi:10.1002/qj.49709440007.

Dye, J. E., J. J. Jones, A. J. Weinheimer, and W. P. Winn, 1988: Observations within two regions of charge during initial thunderstorm electrification. *Q. J. R. Meteorol. Soc.*, **114**, 1271–1290, doi:10.1002/qj.49711448306.

Eack, K. B., 2004: Electrical characteristics of narrow bipolar events. *Geophys. Res. Lett.*, **31**, L20102, doi:10.1029/2004GL021117.

Edens, H. E., and Coauthors, 2012: VHF lightning mapping observations of a triggered lightning flash. **39**, 1–5, doi:10.1029/2012GL053666.

Elster, I. ., and H. Geitel, 1913: Zur Influenztheorie der Niederschlagselektrizitat. *Phys. Z.*, 1287–1292.

Fritsch, J. M., R. J. Kane, and C. R. Chelius, 1986: The contribution of mesoscale convective weather systems to the warm-season precipitation in the united states. *J. Clim. Appl. Meteorol.*, **25**, 1333–1345.

Gaskell, W., 1981: A laboratory study of the inductive theory of thunderstorm electrification. *Q. J. R. Meteorol. Soc.*, **107**, 955–966.

Gaskell, W., A. J. Illingworth, J. Latham, and C. B. Moore, 1978: Airborne studies of electric fields and the charge and size of precipitation elements in thunderstorms. *Q. J. R. Meteorol. Soc.*, **104**, 447–460, doi:10.1002/qj.49710444016.

Grenet, G., 1947: Essai d'explication de la charge électrique des nuages d'orages. *Ann. Geophys.*, **8**, 306–307.

Hale, R. B., F. H. Ludlam, and R. E. Lacy, 1950: *Unsual Lightning*.

Hallett, J., and S. C. Mossop, 1974: Production of secondary ice particles during the riming process. *Nature*, **249**, 26–28.

Hendry, A., and Y. M. M. Antar, 1982: Radar observations of polarization characteristics and lightning-induced realignment of atmospheric ice crystals. *Radio Sci.*, **17**, 1243–1250, doi:10.1029/RS017i005p01243.

Hendry, A., Y. M. M. Antar, and G. C. McCormick, 1987: On the relationship between the degree of preferred orientation in precipitation and dual-polarization radar echo characteristics. *Radio Sci.*, **22**, 37–50, doi:10.1029/RS022i001p00037.

Hendry, a., and G. C. McCormick, 1976: Radar observations of the alignment of precipitation particles by electrostatic fields in thunderstorms. *J. Geophys. Res.*, **81**, 5353–5357, doi:10.1029/JC081i030p05353.

Heymsfield, A. J., 1977: Precipitation Development in Stratiform Ice Clouds: A Microphysical and Dynamical Study. *J. Atmos. Sci.*, **34**, 367–381, doi:10.1175/1520-0469(1977)034<0367:PDISIC>2.0.CO;2.

Hill, J. D., and Coauthors, 2013: Correlated lightning mapping array and radar observations of the initial stages of three sequentially triggered Florida lightning discharges. *J. Geophys. Res. Atmos.*, **118**, 8460–8481, doi:10.1002/jgrd.50660.

Hill, J. D., J. Pilkey, M. a Uman, D. M. Jordan, M. I. Biggerstaff, and P. Hyland, 2012: Correlated Lightning Mapping Array (LMA) and Radar Observations of the Initial Stages of Florida Triggered Lightning Discharges. *Light. Prot. (ICLP), 2012 Int. Conf.*,.

Hobbs, P. V., 1975: The nature of winter clouds and precipitation in the Cascade Mountains and their modification by artificial seeding. Part I: Natural conditions. *J. Appl. Meteor.*, **14**, 783–804.

Hobbs, P. V, S. Chang, and J. D. Locatelli, 1974: The dimensions and aggregation of ice crystals in natural clouds. *J. Geophys. Res.*, **79**, 2199–2206, doi:10.1029/JC079i015p02199.

Houze, R. a., 1977: Structure and Dynamics of a Tropical Squall–Line System. *Mon. Weather Rev.*, **105**, 1540–1567.

Houze, R. a., B. F. Smull, and P. Dodge, 1990: Mesoscale Organization of Springtime Rainstorms in Oklahoma. *Mon. Weather Rev.*, **118**, 613–654.

Houze, R. a, P. V. Hobbs, P. H. Herzegh, and D. B. Parsons, 1979: Size Distributions of Precipitation in Frontal Clouds. *J. Atmos. Sci.*, **36**, 156–162.

Illingworth, A. J., and J. M. Caranti, 1985: Ice conductivity restraints on the inductive theory of thunderstorm electrification. *J. Geophys. Res.*, **90**, 6033, doi:10.1029/JD090iD04p06033.

Jayaratne, E. R., 1993: The Heat Balance of a Riming Graupel Pellet and the Charge Separation during Ice–Ice Collisions. *J. Atmos. Sci.*, **50**, 3185–3193, doi:10.1175/1520-0469(1993)050<3185:THBOAR>2.0.CO;2.

Jayaweera, K. O. L. F., and B. J. Mason, 1965: The behaviour of freely falling cylinders and cones in a viscous fluid. *J. Fluid Mech.*, **22**, 709, doi:10.1017/S002211206500109X.

Jennings, S. G., 1975: Charge separation due to water drop and cloud droplet interactions in an electric field. *Q. J. R. Meteorol. Soc.*, **101**, 227–233, doi:10.1002/qj.49710142806.

Johns, R. H., and W. D. Hirt, 1987: Derechos: Widespread convectively induced windstorms. *Weather Forecast.*, **2**, 32–49.

Jones, R. F., 1960: Size-distribution of ice crystals in cumulonimbus clouds. *Q. J. R. Meteorol. Soc.*, **86**, 187–194, doi:10.1002/qj.49708636808.

Kasemir Heinz W., 1960: A contribution to the electrostatic theory of a lightning discharge. *J. Geophys. Res.*, **65**, 1873–1878, doi:.

Kasemir, H. W., 1960: A contribution to the electrostatic theory of a lightning discharge. *J. Geophys. Res.*, **65**, 1873–1878, doi:10.1029/JZ065i007p01873.

Keith, W. D., and C. P. R. Saunders, 1989: Further laboratory studies of the charging of graupel during ice crystal interactions. *Atmos. Res.*, **25**, 445–464.

Koshak, W. J., and E. P. Krider, 1989: Analysis of lightning field changes during active Florida thunderstorms. *J. Geophys. Res.*, **94**, 1165, doi:10.1029/JD094iD01p01165.

Krehbiel, P. R., 1986: The Electrical Structure of Thunderstorms. *The Earth's Electrical Environment*, The National Academies Press, Washington D.C., 90–113.

Krehbiel, P. R., T. Chen, S. Mccrary, W. Rison, G. Gray, and M. Brook, 1996: Meteorology , and Atmospheric Physics The Use of Dual Channel Circular-Polarization Radar Observations for Remotely Sensing Storm Electrification. *Meteorol. Atmos. Phys.*, **59**, 65–82.

Krehbiel, P. R., R. J. Thomas, W. Rison, T. Hamlin, J. Harlin, and M. Davis, 2000: Lightning Mapping Observations in Central Oklahoma. *Eos (Washington. DC).*,.

Krehbiel, P., T. Chen, S. Mccrary, W. Rison, G. Gray, and M. Brook, 1996: The Use of Dual Channel Circular-Polarization Radar Observations for Remotely Sensing Storm Electrification. *Meteorol. Atmos. Phys.*, 65–82.

Leary, C. A., and R. A. Houze, 1979: The Structure and Evolution of Convection in a Tropical Cloud Cluster. *J. Atmos. Sci.*, **36**, 437-.

Lemon, L. R., 1998: The Radar "' Three-Body Scatter Spike '": An Operational Large-Hail Signature. *Weather Forecast.*, **13**, 327–340, doi:10.1175/1520-0434(1998)013<0327:TRTBSS>2.0.CO;2.

Lhermitte, R., and P. R. Krehbiel, 1979: Doppler Radar and Radio Observations of Thunderstorms. *IEEE Trans. Geosci. Electron.*, **GE-17**, 162–171, doi:10.1109/TGE.1979.294644.

List, R., and R. S. Schemenauer, 1971: Free-Fall Behavior of Planar Snow Crystals, Conical Graupel and Small Hail. *J. Atmos. Sci.*, **28**, 110–115, doi:10.1175/1520-0469(1971)028<0110:FFBOPS>2.0.CO;2.

Loeb, L. B., 1966: The mechanisms of stepped and dart leaders in cloud-to-ground lightning strokes. *J. Geophys. Res.*, **71**, 4711–4721, doi:10.1029/JZ071i020p04711.

Lopez, R. E., and R. L. Holle, 1998: Changes in the Number of Lightning Deaths in the United States during the Twentieth Century. *J. Clim.*, **11**, 2070–2077.

Lund, N. R., D. R. MacGorman, T. J. Schuur, M. I. Biggerstaff, and W. D. Rust, 2009: Relationships between Lightning Location and Polarimetric Radar Signatures in a Small Mesoscale Convective System. *Mon. Weather Rev.*, **137**, 4151–4170, doi:10.1175/2009MWR2860.1.

Macgorman, D. R., A. A. Few, and T. L. Teer, 1981: Layered Lightning Activity. *J. Geophys. Res.*, **86**, 9900–9910.

Macgorman, D. R., M. I. Biggerstaff, S. Waugh, and P. Hyland, 2014: Coordinated LMA , Balloon-borne Electric Field , and Polarimetric Radar Observations of a Triggered Lightning Flash at Camp Blanding. 15–20.

MacGorman, D. R., M. I. Biggerstaff, S. Waugh, and P. Hyland, 2015: Coordinated Lightning, Balloon-borne Electric Field, and Radar Observations of Triggered Lightning Flashes in North Florida. *Geophys. Res. Lett.*, **42**, 5635–5643.

MacGorman, D. R., J. M. Straka, and C. L. Ziegler, 2001: A Lightning Parameterization for Numerical Cloud Models. *J. Appl. Meteorol.*, **40**, 459–478, doi:10.1175/1520-0450(2001)040<0459:ALPFNC>2.0.CO;2.

MacGorman, D. R., J. M. Straka, and C. L. Ziegler, 2001: A Lightning Parameterization for Numerical Cloud Models. *J. Appl. Meteorol.*, **40**, 459–478, doi:10.1175/1520-0450(2001)040<0459:ALPFNC>2.0.CO;2.

Maggio, C., and Coauthors, 2005: Lightning-initiation locations as a remote sensing tool of large thunderstorm electric field vectors. *J. Atmos. Ocean. Technol.*, **22**, 1059–1068, doi:10.1175/JTECH1750.1.

Magono, C., and K. Kikuchi, 1965: On the Positive Electrification of Snow Crystals in the Process of Their Melting (II). *J. Meteorol. Soc. Japan*, **43**, 331–342.

Makowski, J. A., D. R. MacGorman, M. I. Biggerstaff, and W. H. Beasley, 2013: Total Lightning Characteristics Relative to Radar and Satellite Observations of Oklahoma Mesoscale Convective Systems. *Mon. Weather Rev.*, **141**, 1593–1611, doi:10.1175/MWR-D-11-00268.1.

Mansell, E. R., D. R. MacGorman, C. L. Ziegler, and J. M. Straka, 2002: Simulated three-dimensional branched lightning in a numerical thunderstorm model. *J. Geophys. Res. Atmos.*, **107**, doi:10.1029/2000JD000244.

Mansell, E. R., C. L. Ziegler, and E. C. Bruning, 2010: Simulated Electrification of a Small Thunderstorm with Two-Moment Bulk Microphysics. *J. Atmos. Sci.*, **67**, 171–194, doi:10.1175/2009JAS2965.1.

Mansell, E. R., D. R. Macgorman, C. L. Ziegler, and J. M. Straka, 2005: Charge structure and lightning sensitivity in a simulated multicell thunderstorm. *J. Geophys. Res.*, **110**, 1–24, doi:10.1029/2004JD005287.

Marshall, J. S., and W. M. K. Palmer, 1948: THE DISTRIBUTION OF RAINDROPS WITH SIZE. *J. Meteorol.*, **5**, 165–166, doi:10.1175/1520-0469(1948)005<0165:TDORWS>2.0.CO;2.

Marshall, T. C., and W. D. Rust, 1991: Electric Field Soundings Through Thunderstorms. *J. Geophys. Res.*, **96**, 22297–22306.

Marshall, T. C., and W. D. Rust, 1993: Two Types of Vertical Electrical Structions in Stratiform Precipitation Regions of MCSs. *Bull. Am. Meteorol. Soc.*, **74**, 2159–2170.

Marshall, T. C., M. Stolzenburg, C. Maggio, L. M. Coleman, P. R. Krehbiel, T. Hamlin, R. J. Thomas, and W. Rison, 2005: Observed electric fields associated with lightning initiation. *Geophys. Res. Lett.*, **32**, L03813, doi:10.1029/2004GL021802.

Marshall, T. C., and B. Lin, 1992: Electricity in dying thunderstorms. *J. Geophys. Res. Atmos.*, **97**, 9913–9918, doi:10.1029/92JD00463.

Marshall, T. C., and W. P. Winn, 1982: Measurements of charged precipitation in a New Mexico thunderstorm: lower positive charge centers. *J. Geophys. Res.*, **87**, 7141, doi:10.1029/JC087iC09p07141.

Marshall, T. C., W. D. Rust, W. P. Winn, and K. E. Gilbert, 1989: Electrical structure in two thunderstorm anvil clouds. *J. Geophys. Res.*, **94**, 2171–2181, doi:10.1029/JD094iD02p02171.

Matthews, J. B., and B. J. Mason, 1963: Electrification accompanying melting. 376–380.

Mazur, V., and L. H. Ruhnke, 1998: Model of electric charges in thunderstorms and associated lightning. *J. Geophys. Res.*, **103**, 23299–23308.

Mazur, V., and L. H. Ruhnke, 1993: Common physical processes in natural and artificially triggered lightning. *J. Geophys. Res.*, **98**, 12913–12930, doi:10.1111/j.1555-2934.2009.01042.x.

Mendez, D. J., 1969: Optical Polarization Induced by Electric Fields of Thunderstorms. *J. Geophys. Res.*, **74**, 7032–7037, doi:10.1007/BF01249599.

Metcalf, J. I., 1995: Radar observations of changing orientations of hydrometeors in thunderstorms.

Metcalf, J. I., 1997: Temporal and Spatial Variations of Hydrometeor Orientations in Thunderstorms. *J. Appl. Meteorol.*, **36**, 315–321, doi:10.1175/1520-0450(1997)036<0315:TASVOH>2.0.CO;2.

Muller-Hillebrand, D., 1954: Charge generation in thunderstorms by collision of ice crystals with graupel, falling through a vertical electric field. *Tellus*, **6**, 156–163.

Nesbitt, S. W., R. Cifelli, and S. A. Rutledge, 2006: Storm Morphology and Rainfall Characteristics of TRMM Precipitation Features. *Mon. Weather Rev.*, **134**, 2702–2721.

Pilkey, J. T., M. A. Uman, J. D. Hill, T. Ngin, W. R. Gamerota, D. M. Jordan, J. Caicedo, and B. Hare, 2014: Rocket-triggered lightning propagation paths relative to preceding natural lightning activity and inferred cloud charge. *J. Geophys. Res. Atmos.*, **119**, 13427–13456, doi:10.1002/2014JD022139.

Pilkey, J. T., and Coauthors, 2013: Rocket-and-wire triggered lightning in 2012 tropical storm Debby in the absence of natural lightning. *J. Geophys. Res. Atmos.*, **118**, 13158–13174, doi:10.1002/2013JD020501.

Platt, C. M. R., 1997: A Parameterization of the Visible Extinction Coefficient of Ice Clouds in Terms of the Ice/Water Content. *J. Atmos. Sci.*, **54**, 2083–2098, doi:10.1175/1520-0469(1997)054<2083:APOTVE>2.0.CO;2.

Pokharel, B., and G. Vali, 2011: Evaluation of collocated measurements of radar reflectivity and particle sizes in ice clouds. *J. Appl. Meteorol. Climatol.*, **50**, 2104–2119, doi:10.1175/JAMC-D-10-05010.1.

Proctor, D. E., 1991: Regions Where Lightning Flashes Began. *J. Geophys. Res.*, **96**, 5099–5112.

Reynolds, S. E., M. Brook, and M. F. Gourley, 1957: Thunderstorm Charge Separation. *J. Meteorol.*, **14**, 426–436, doi:10.1175/1520-0469(1957)014<0426:TCS>2.0.CO;2.

Rison, W., R. J. Thomas, P. R. Krehbiel, T. Hamlin, and J. Harlin, 1999: A GPS-based Three-Dimensional Lightning Mapping System: Initial Obsercations in Central New Mexico. **26**, 3573–3576.

Rison, W., P. R. Krehbiel, M. G. Stock, H. E. Edens, X. Shao, R. J. Thomas, M. A. Stanley, and Y. Zhang, 2016: Observations of narrow bipolar events reveal how lightning is initiated in thunderstorms. *Nat. Commun.*, **7**, 1–12, doi:10.1038/ncomms10721.

Rotunno, R., J. B. Klemp, and M. L. Weisman, 1988: A Theory for Strong Long-Lived Squall Lines. *J. Atmos. Sci.*, **45**, 463–485.

RUST, W. D., and Coauthors, 1985: Lightning and related phenomena in isolated thunderstorms and squallline systems. *J. Aircr.*, **22**, 449–454, doi:10.2514/3.45147.

Rust, W. D., and Coauthors, 2005: Inverted-polarity electrical structures in thunderstorms in the Severe Thunderstorm Electrification and Precipitation Study (STEPS). *Atmos. Res.*, **76**, 247–271, doi:10.1016/j.atmosres.2004.11.029.

Rust, W. D., and T. C. Marshall, 1996: On abandoning the thunderstorm tripole-charge paradigm. *J. Geophys. Res. Atmos.*, **101**, 23499–23504, doi:10.1029/96JD01802.

Rutledge, S. A., C. Lu, and D. R. MacGorman, 1990: Positive cloud-to-ground lightning in mesoscale convective systems. *J. Atmos. Sci.*, **47**, 2085–2100, doi:10.1175/1520-0469(1990)047<2085:pctgli>2.0.co;2.

Ryzhkov, A. V., and D. S. Zrnić, 2007: Depolarization in ice crystals and its effect on radar polarimetric measurements. *J. Atmos. Ocean. Technol.*, **24**, 1256–1267, doi:10.1175/JTECH2034.1.

Saunders, C. P. R., 1993: A review of Thunderstorm Electrification Processes. *J. Appl. Meteorol.*, **32**, 642–655.

Schaefer, V. J., 1946: The Production of Ice Crystals in a Cloud of Supercooled Water Droplets. *Science (80-.).*, **104**, 457–459.

Schumacher, R. S., and R. H. Johnson, 2005: Organization and Environmental Properties of Extreme-Rain-Producing Mesoscale. *Mon. Weather Rev.*, **133**, 961–976.

Schuur, T. J., and S. A. Rutledge, 2000: Electrification of Stratiform Regions in Mesoscale Convective Systems . Part II : Two-Dimensional Numerical Model Simulations of a Symmetric MCS. *J. Atmos. Sci.*, **57**, 1983–2006.

Shao, X. M., and P. R. Krehbiel, 1996: The spatial and temporal development of intracloud lightning upward at a speed established the beginning of one or is characterized streamers that. *J. Geophys. Res.*, **101**, 26641–26668.

Shepherd, T. R., W. D. Rust, and T. C. Marshall, 1996: Electric Fields and Charges near 0°C in Stratiform Clouds. *Mon. Weather Rev.*, **124**, 919–938, doi:10.1175/1520-0493(1996)124<0919:EFACNI>2.0.CO;2.

Simpson, G., and M. A. Scrase, 1937: The Distribution of Electricity in Thunderclouds. *Proc. R. Soc. London*, 309–352, doi:10.1098/rspa.1974.0120.

Smith, D. a., and Coauthors, 1999: A distinct class of isolated intracloud lightning discharges and their associated radio emissions. *J. Geophys. Res.*, **104**, 4189–4212, doi:10.1029/1998JD200045.

Standler, R. B., and W. P. Winn, 1979: Effects of coronae on electric fields beneath thunderstorms. *Q. J. R. Meteorol. Soc.*, **105**, 285–302, doi:10.1002/qj.49710544319.

Stolzenburg, M., T. C. Marshall, W. D. Rust, and B. F. Smull, 1994: Horizontal distribution of electrical and meteorological conditions across the stratiform region of a mesoscale convective system. *Mon. Weather Rev.*, **122**, 1777–1797, doi:10.1175/1520-0493(1994)122<1777:HDOEAM>2.0.CO;2.

Stolzenburg, M., W. D. Rust, and T. C. Marshall, 1998: Electrical structure in thunderstorm convective regions: 1. Mesoscale Convective Systems. *J. Geophys. Res.*, **103**, 14059–14079, doi:10.1029/97JD03547.

Stolzenburg, M., W. D. Rust, and T. C. Marshall, 1998: Electrical structure in thunderstorm convective regions: 3. Synthesis. *J. Geophys. Res.*, **103**, 14079, doi:10.1029/97JD03547.

Takahashi, T., 1978: Riming Electrification as a Charge Generation Mechanism in Thunderstorms. *J. Atmos. Sci.*, **35**, 1536–1548.

Thomas, R. J., P. R. Krehbiel, T. Hamlin, J. Harlin, and D. Shown, 2001: Observations of VHF source powers radiated by lightning. *Geophys. Res. Lett.*, **28**, 143–146, doi:10.1029/2000GL011464.

Thomas, R. J., P. R. Krehbiel, W. Rison, S. J. Hunyady, W. P. Winn, T. Hamlin, and J. Harlin, 2004: Accuracy of the Lightning Mapping Array. **109**, 1–34, doi:10.1029/2004JD004549.

Thompson, R. L., B. T. Smith, J. S. Grams, A. R. Dean, and C. Broyles, 2012: Convective Modes for Significant Severe Thunderstorms in the Contiguous United States . Part II : Supercell and QLCS Tornado Environments. *Weather Forecast.*, **27**, 1136–1154, doi:10.1175/WAF-D-11-00116.1.

Trömel, S., M. R. Kumjian, A. V. Ryzhkov, C. Simmer, and M. Diederich, 2013: Backscatter differential phase-estimation and variability. *J. Appl. Meteorol. Climatol.*, **52**, 2529–2548, doi:10.1175/JAMC-D-13-0124.1.

Vonnegut, B., 1965: Orientation of Ice Crystals in the Electric Field of a Thunderstorm. *R. Meteorol. Soc.*, **20**, 310–312.

Watson, S. S., and T. C. Marshall, 2007: Current propagation model for a narrow bipolar pulse. *Geophys. Res. Lett.*, **34**, 1–5, doi:10.1029/2006GL027426.

Weinheimer, A. J., J. E. Dye, D. W. Breed, M. P. Spowart, J. L. Parrish, T. L. Hoglin, and T. C. Marshall, 1991: Simultaneous measurements of the charge, size, and

shape of hydrometeors in an electrified cloud. *J. Geophys. Res.*, **96**, 20809–20829, doi:10.1029/91JD02262.

Weinheimer, A. J., and A. a. Few, 1987: The electric field alignment of ice particles in thunderstorms. *J. Geophys. Res.*, **92**, 14833, doi:10.1029/JD092iD12p14833.

Weisman, M. L., and R. Rotunno, 2004: "' A Theory for Strong Long-Lived Squall Lines '" Revisited. *J. Atmos. Sci.*, **61**, 361–382.

Williams, E. R., R. Zhang, and J. Rydock, 1991: Mixed-Phase Microphysics and Cloud Electrification. *J. Atmos. Sci.*, **48**, 2195–2203, doi:10.1175/1520-0469(1991)048<2195:MPMACE>2.0.CO;2.

Williams, E. R., C. M. Cooke, and K. a. Wright, 1985: Electrical discharge propagation in and around space charge clouds. *J. Geophys. Res.*, **90**, 6059–6070, doi:10.1029/JD090iD04p06059.

Willis, P. T., and A. J. Heymsfield, 1989: Structure of the Melting Layer in Mesoscale Convective System Stratiform Precipitation. *J. Atmos. Sci.*, **46**, 2008–2025, doi:10.1175/1520-0469(1989)046<2008:SOTMLI>2.0.CO;2.

Wilson, J. W., and D. Reum, 1986: The "hail spike": reflectivity and velocity signature. In Preprint Vol 1, 23rd Conference on Radar Meteorology. *Am. Meteorol. Soc.*, **1**, 62–65.

Wilson, J. W., and D. Reum, 1988: The Flare Echo: Reflectivity and velocity signature. *J. Atmos. Ocean. Technol.*, **5**, 197–205.

Winn, W. P., T. A. Cerni, B. Gardiner, D. Lamb, J. Hallett, and C. P. Saunders, 1986: Early Electrification and Precipitation Development in a Small , Isolated Montana Cumulonimbus. *J. Geophys. Res.*, **91**, 1231–1247.

Workman, E. J., and S. E. Reynolds, 1950: Electrical Phenomena Occurring during the Freezing of Dilute Aqueous Solutions and Their Possible Relationship to Thunderstorm Electricity. *Phys. Rev.*, **78**, 254–259, doi:10.1103/PhysRev.78.254.

Zikmunda, J., and G. Vali, 1972: Fall Patterns and Fall Velocities of Rimed Ice Crystals. *J. Atmos. Sci.*, **29**, 1334–1347, doi:10.1175/1520-0469(1972)029<1334:FPAFVO>2.0.CO;2.

Zipser, E. J., 1977: Mesoscale and Convective-Scale Downdrafts as Distinct Components of Squall-Line Structure. *Mon. Weather Rev.*, **105**, 1568–1589.

Zipser, E. J., 1969: The role of organized unsaturate convective downdrafts in the structure and rapid decay of an equatorial disturbance. *J. Appl. Meteorol.*, **8**, 799–814.

Zrnić, D., 1987: this paper is to develop the radar equation for triple Radar meteorologists have occasionally observed reflections and compare the echo power with fingerlike reflectivity pertrusions from the edge of measurements made by a 10-cm weather From thunderstorm. *Radio Sci.*, **22**, 76–86.

Zrnic, D. S., and A. V Ryzhkov, 1999: Polarimetry for Weather Surveillance Radars. *Bull. Am. Meteorol. Soc.*, **80**, 389–406.

APPENDIX: Supplemental Figures

This appendix is a record of all 46 flashes from the Florida case that met the four analysis criteria from Chapter 2.2. Displayed are the 5-RHI mean fields nearest to each flash described in Chapter 4.1.1, which represent the most dominant fields preceding, during, and following each flash. Discussion regarding flashes that do not follow the conceptual model can be found in Chapter 5.1.

The 5-RHI means are displayed chronologically. Subfigures include (listed left to right and top to bottom) (a) reflectivity field, (b) K_{DP} field, (c) 3D view of flash with radar beam line in blue, (d) Z_{DR} field, (e) ϕ_{DP} field, (f) 88D PPI reflectivity field with radar beam line in blue, (g) historgram of K_{DP} values at flash points, (h) timeseries of K_{DP} and reflectivity regions areal extents, (i) timeseries of K_{DP} and reflectivity regions mean values, (j) timeseries of K_{DP} and reflectivity regions mean heights, and (k) metadata.

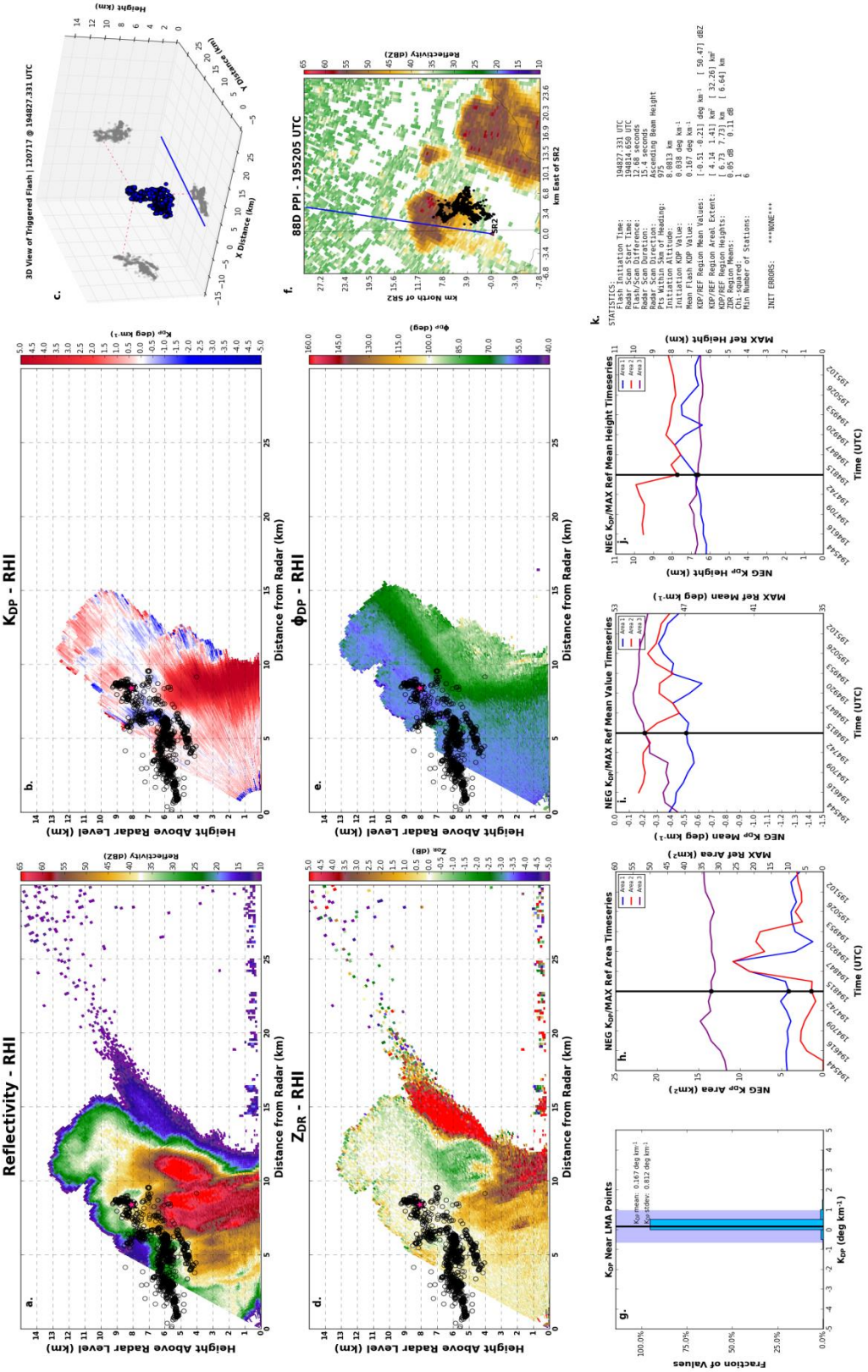

Figure A - 1: Flash 194827.331 UTC

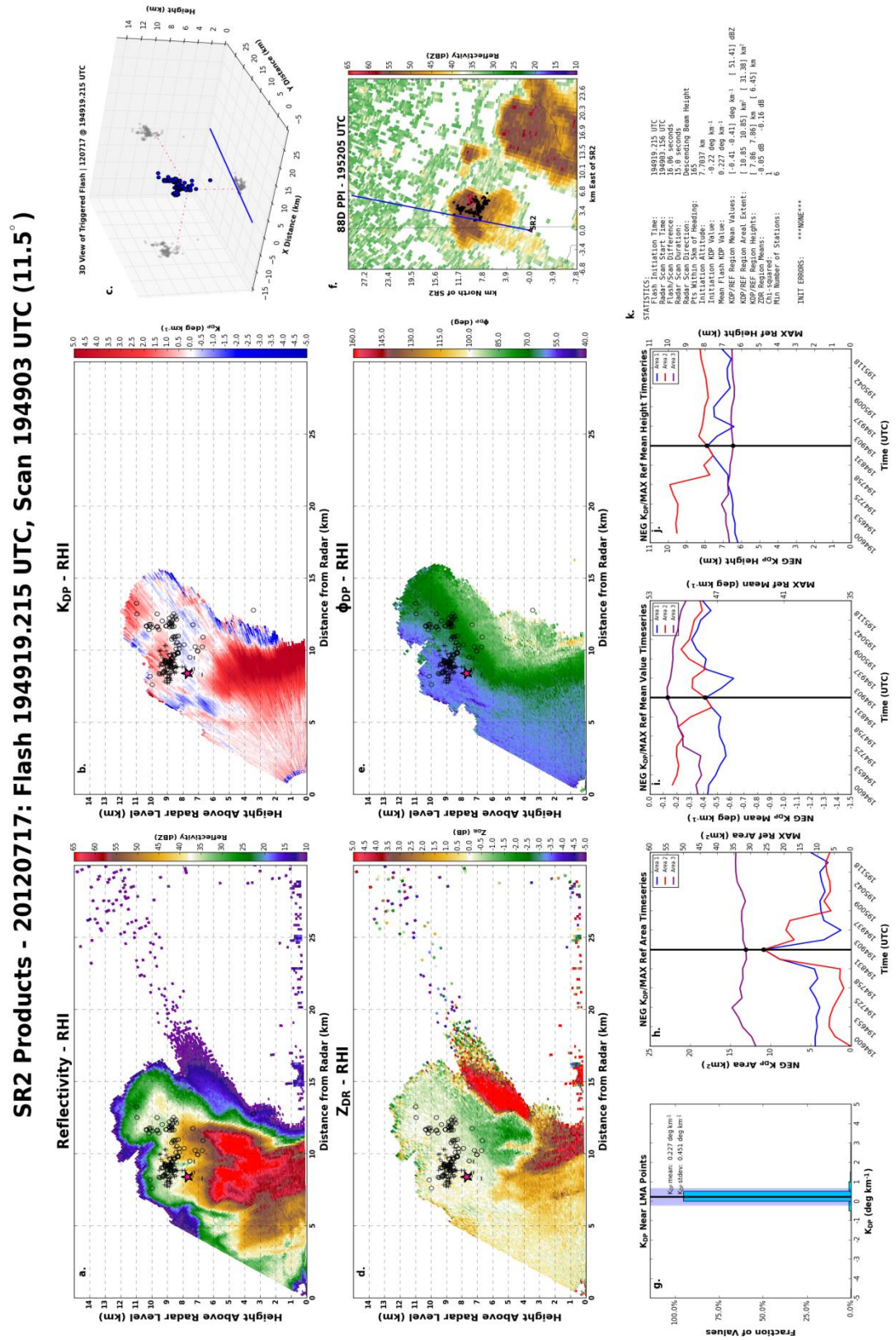

Figure A - 2: Flash 194919.215 UTC

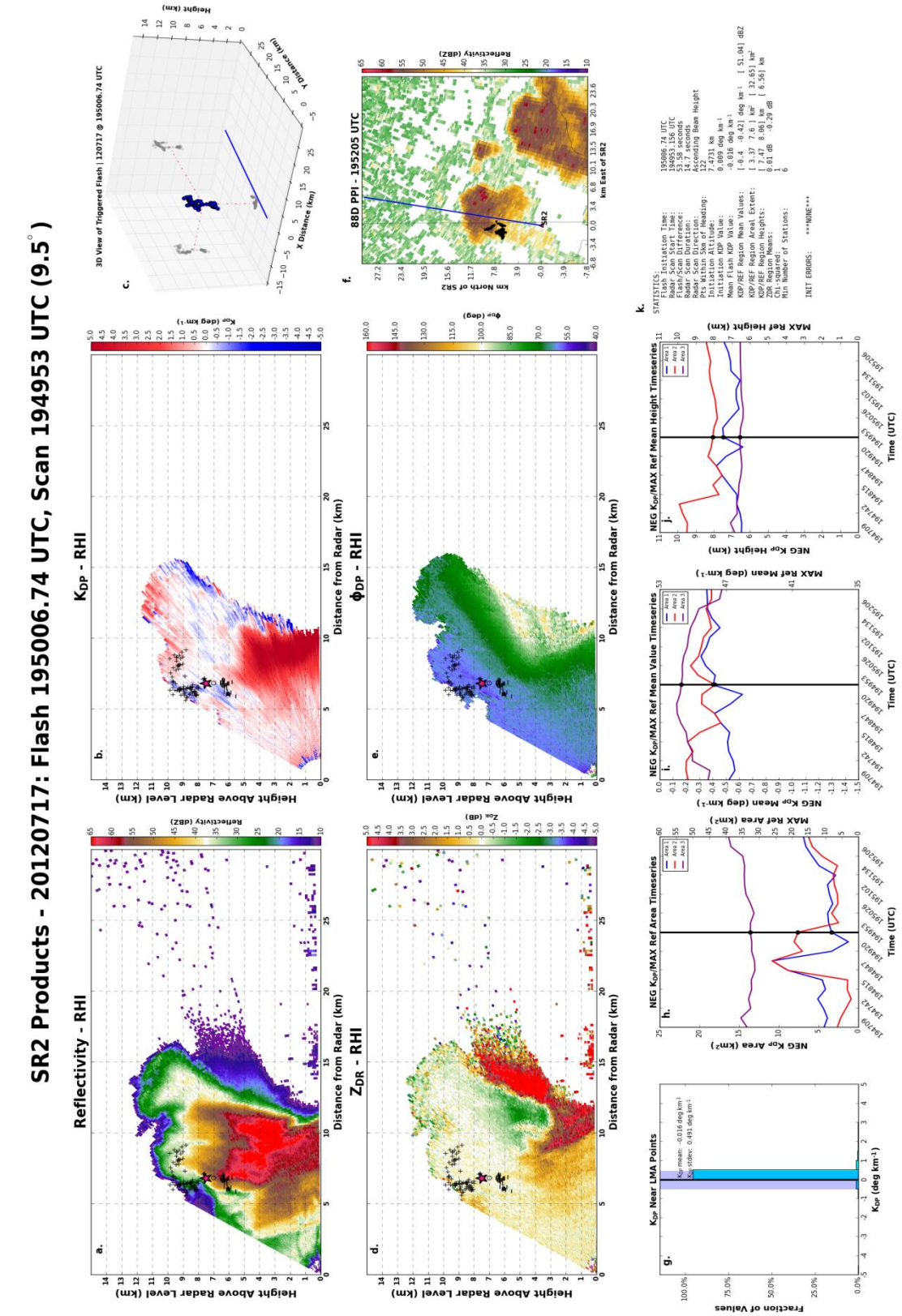

Figure A - 3: Flash 195006.74 UTC

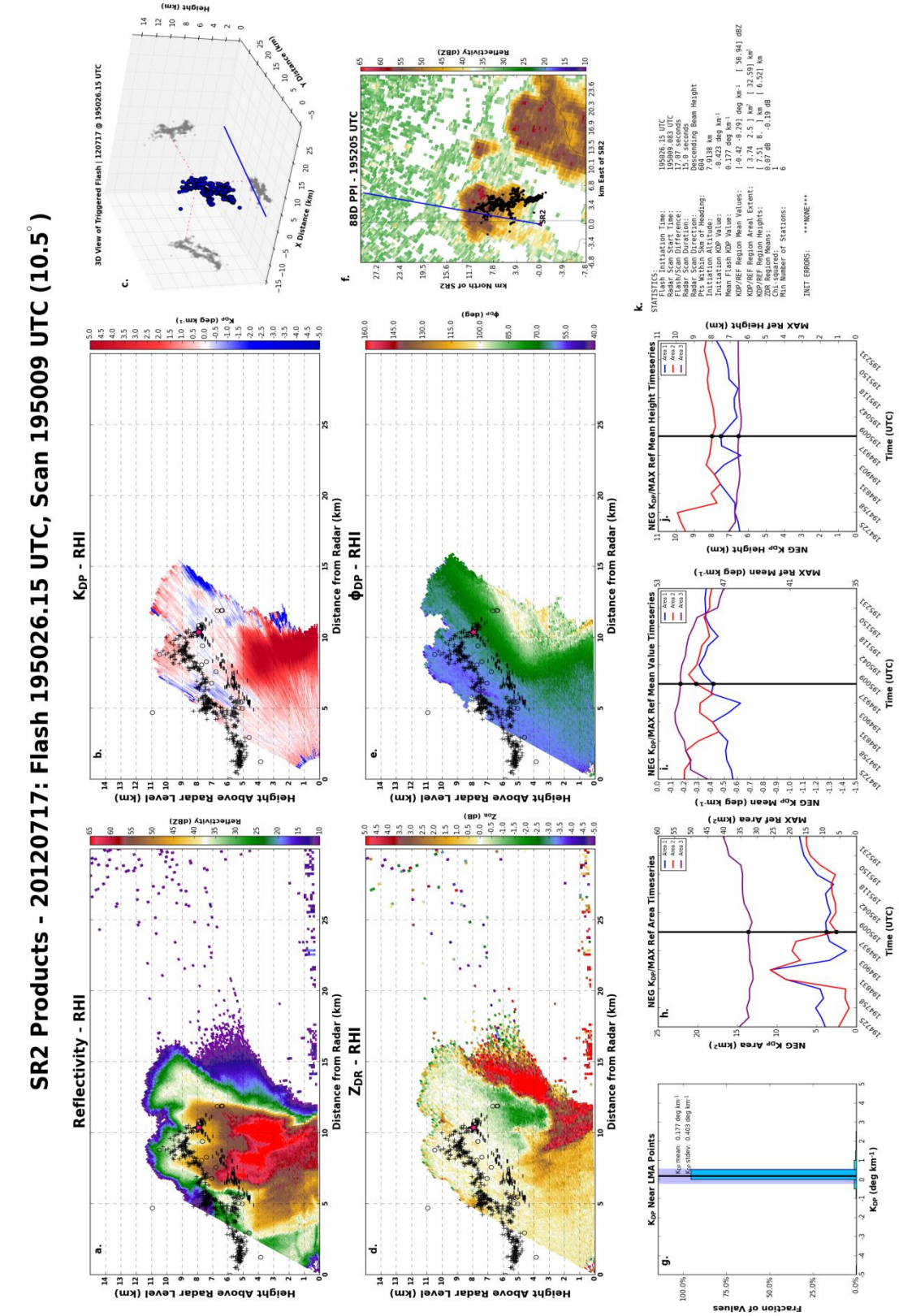

Figure A - 4: Flash 195026.15 UTC

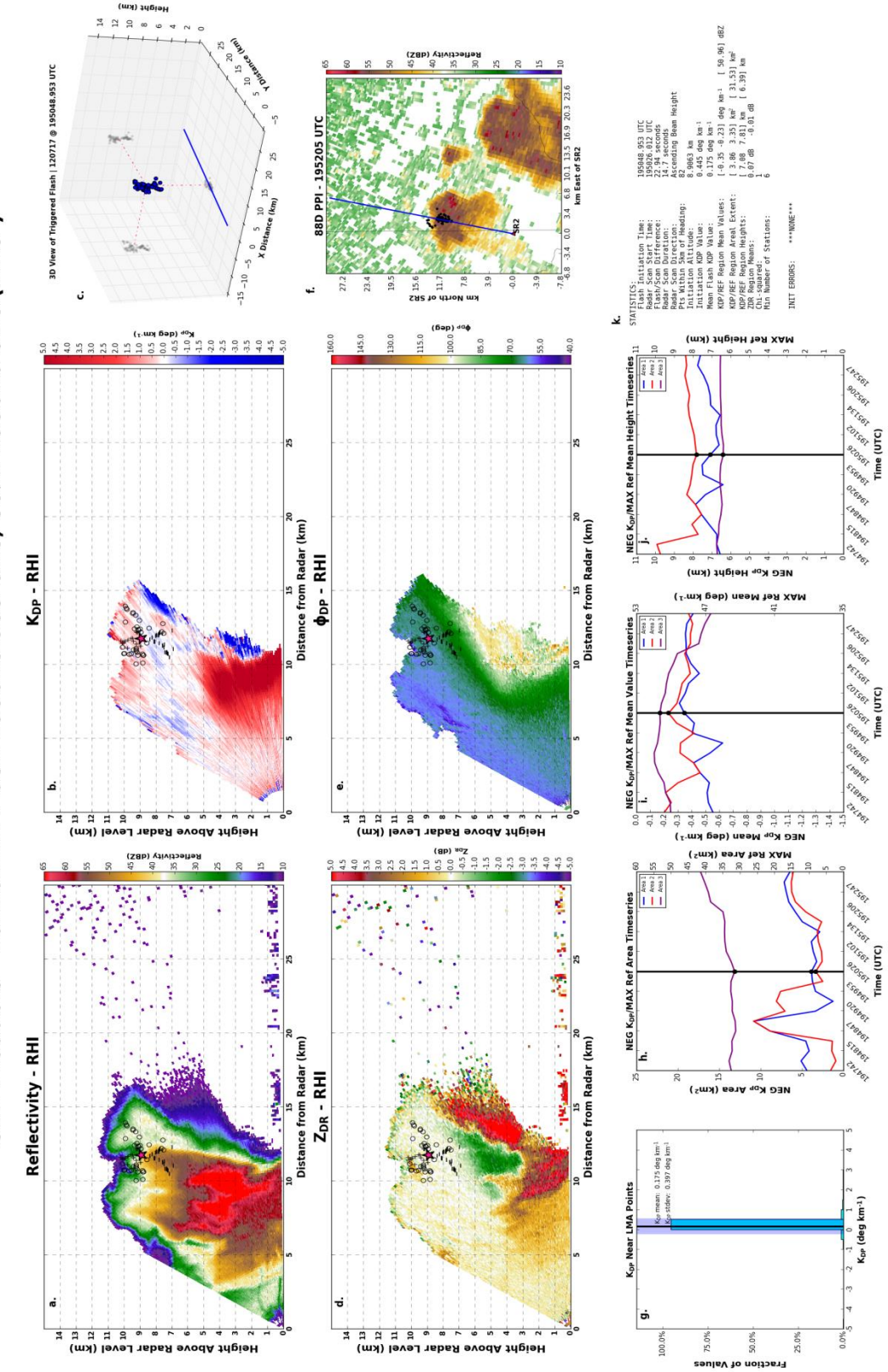

Figure A - 5: Flash 195048.953 UTC

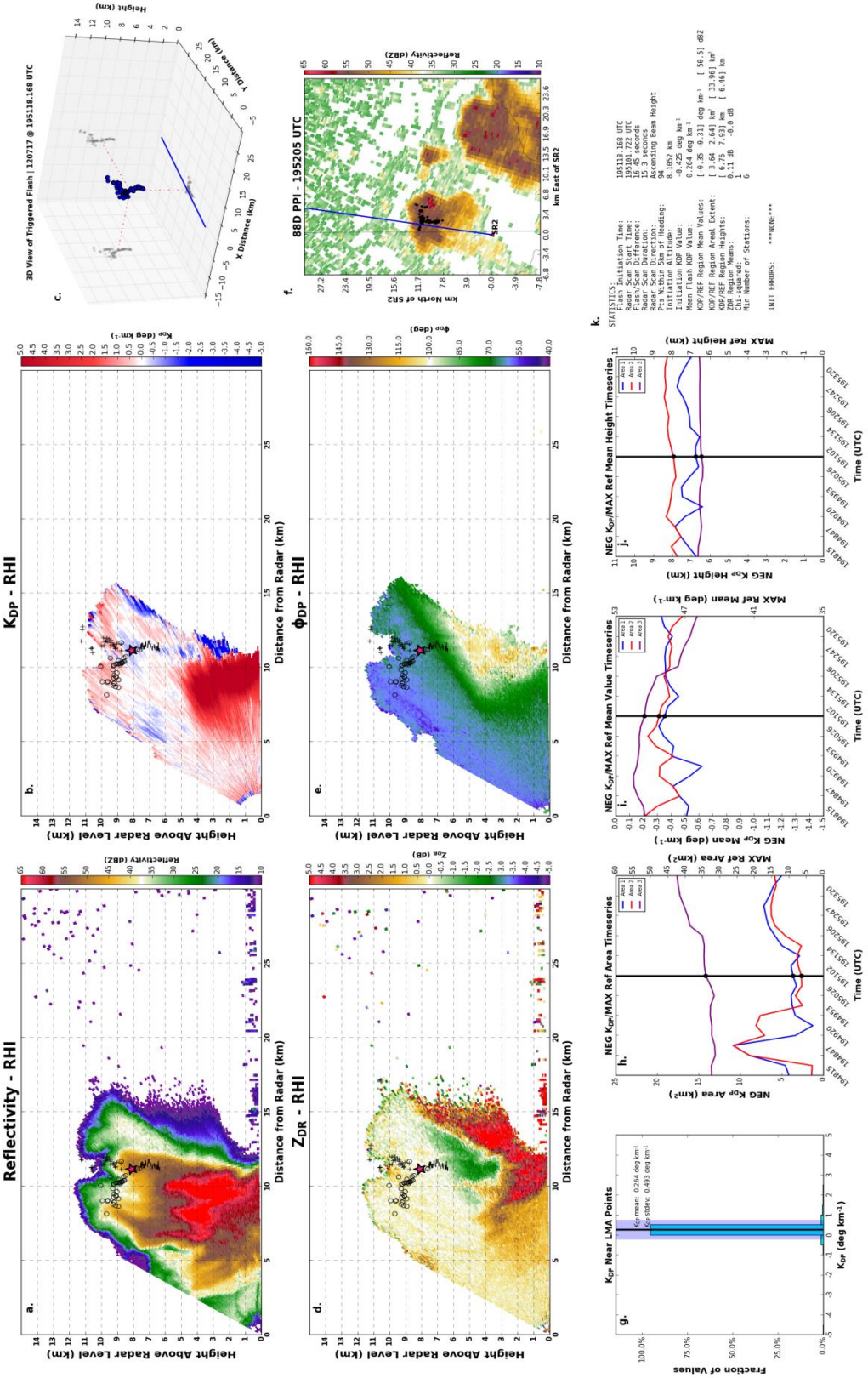

Figure A - 6: Flash 195118.168 UTC

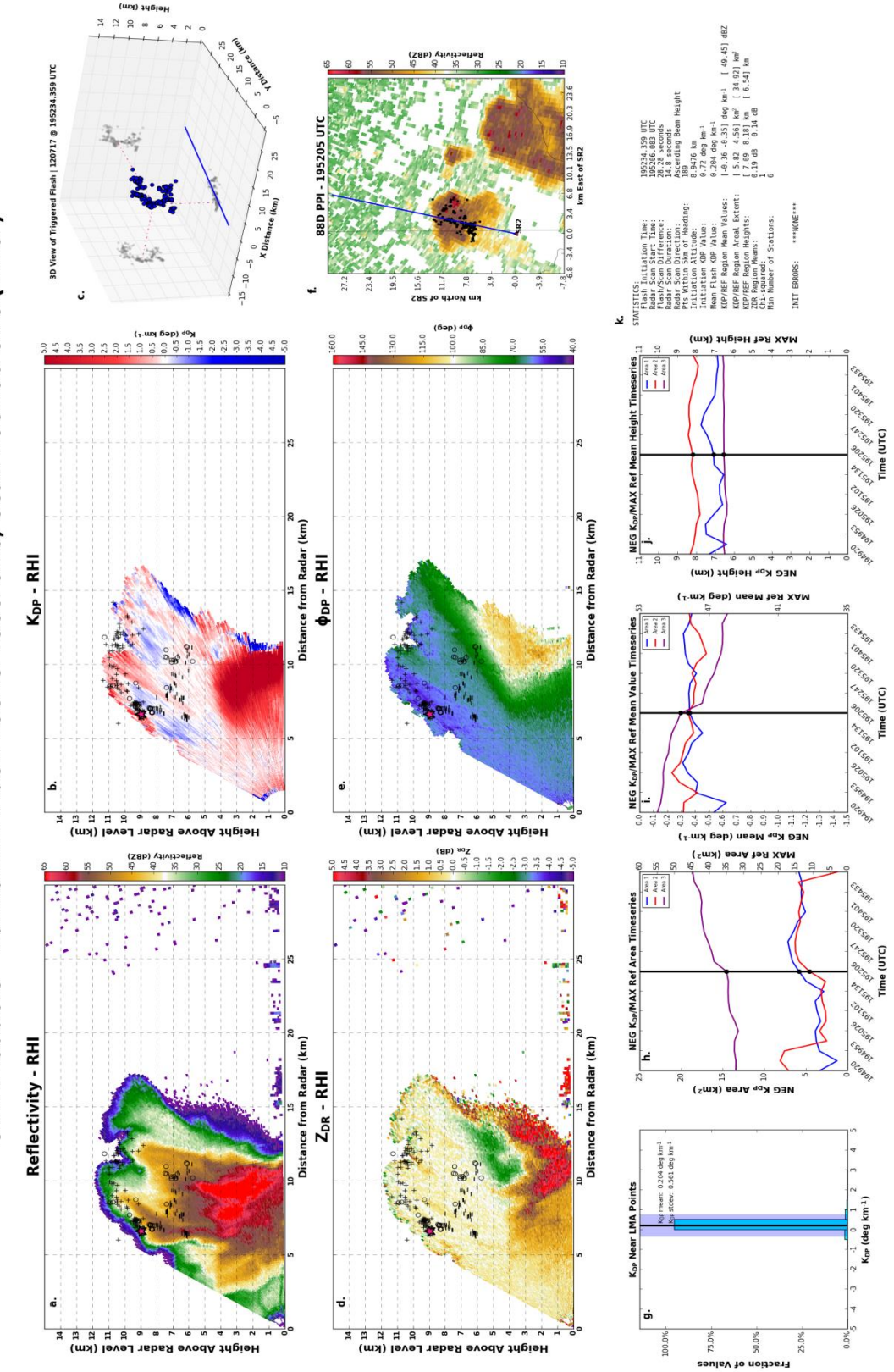

Figure A - 7: Flash 195234.359 UTC

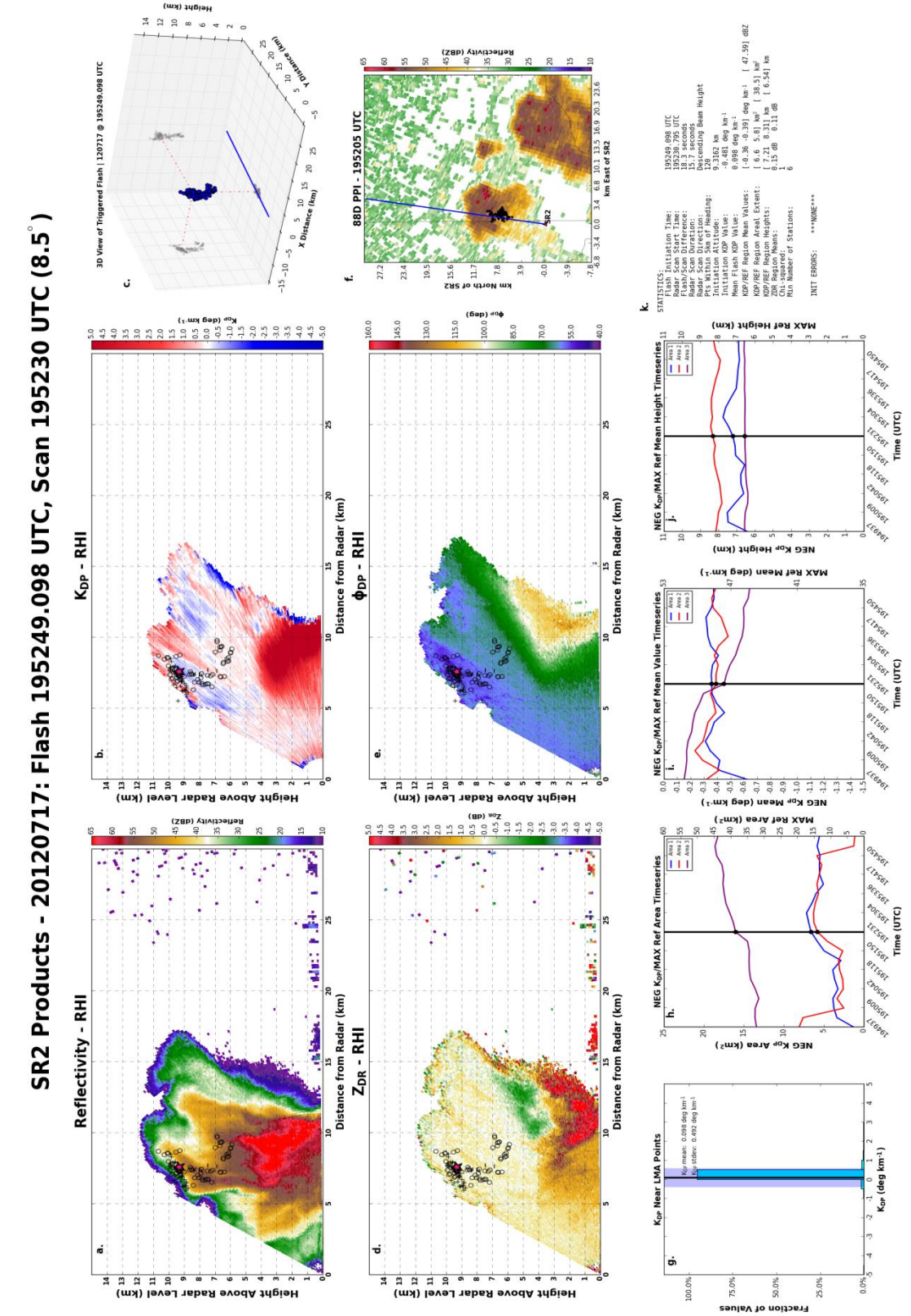

Figure A - 8: Flash 195249.098 UTC

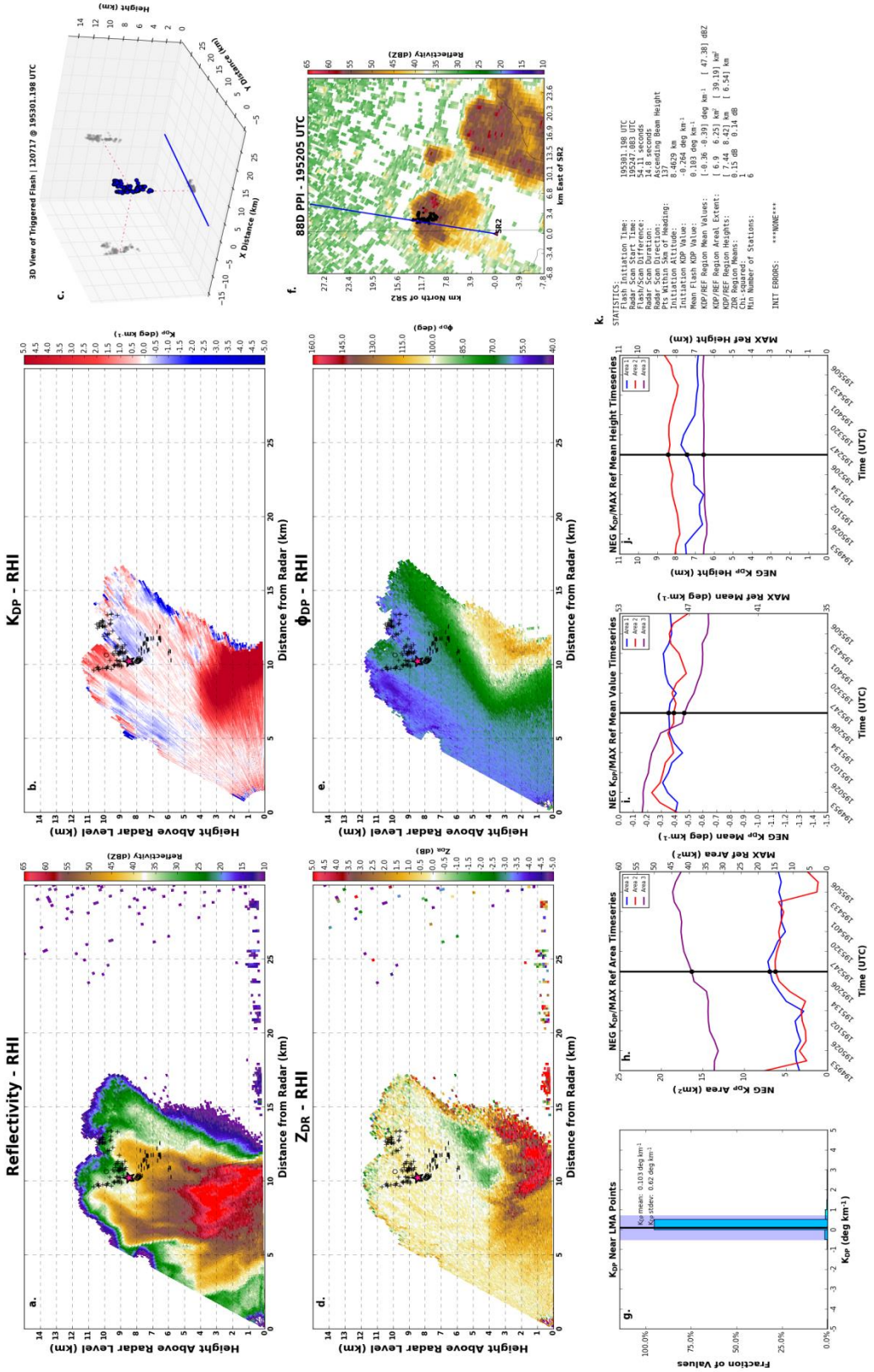

Figure A - 9: Flash 195301.198 UTC

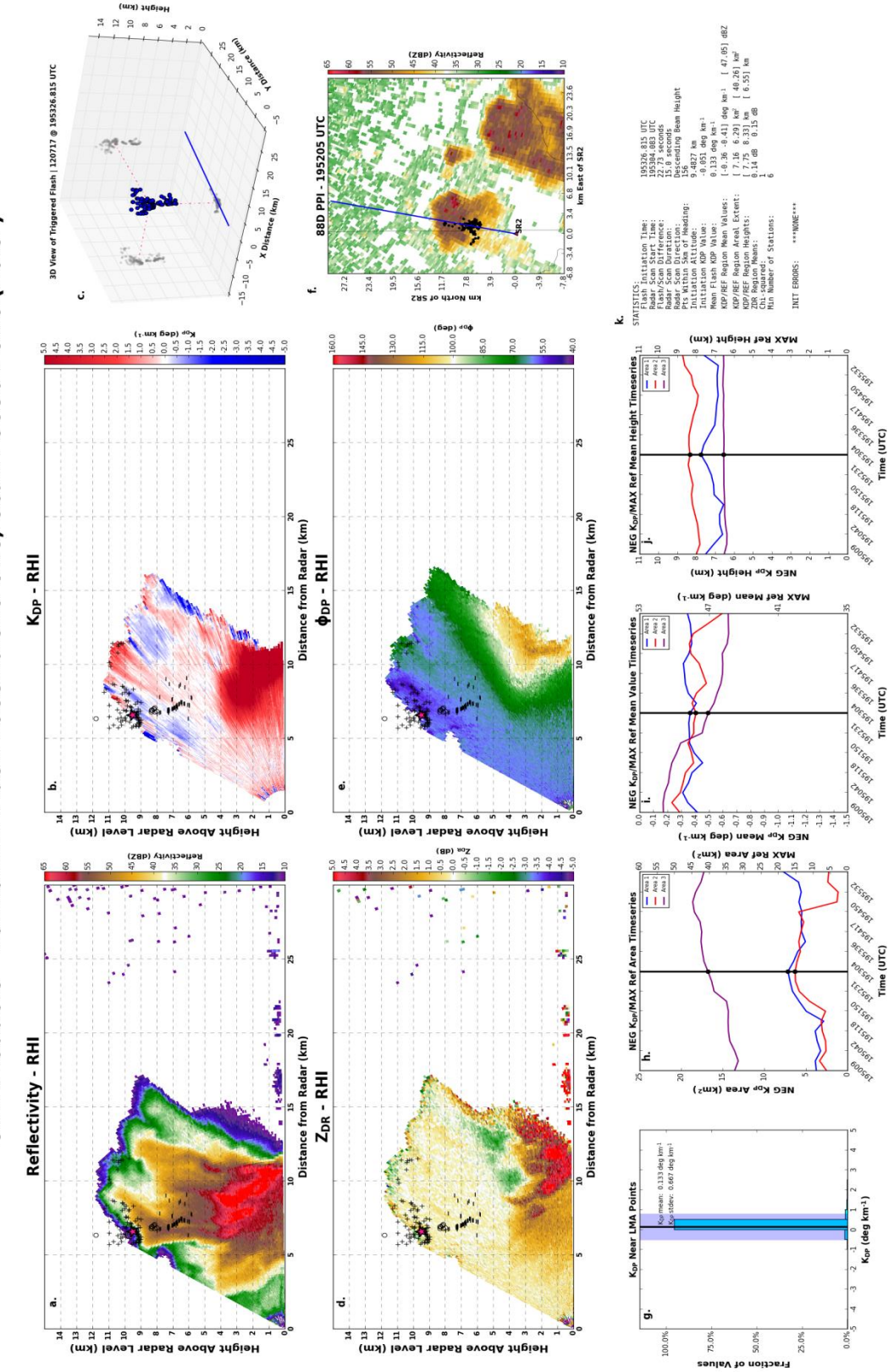

Figure A - 1011: Flash 195326.815 UTC

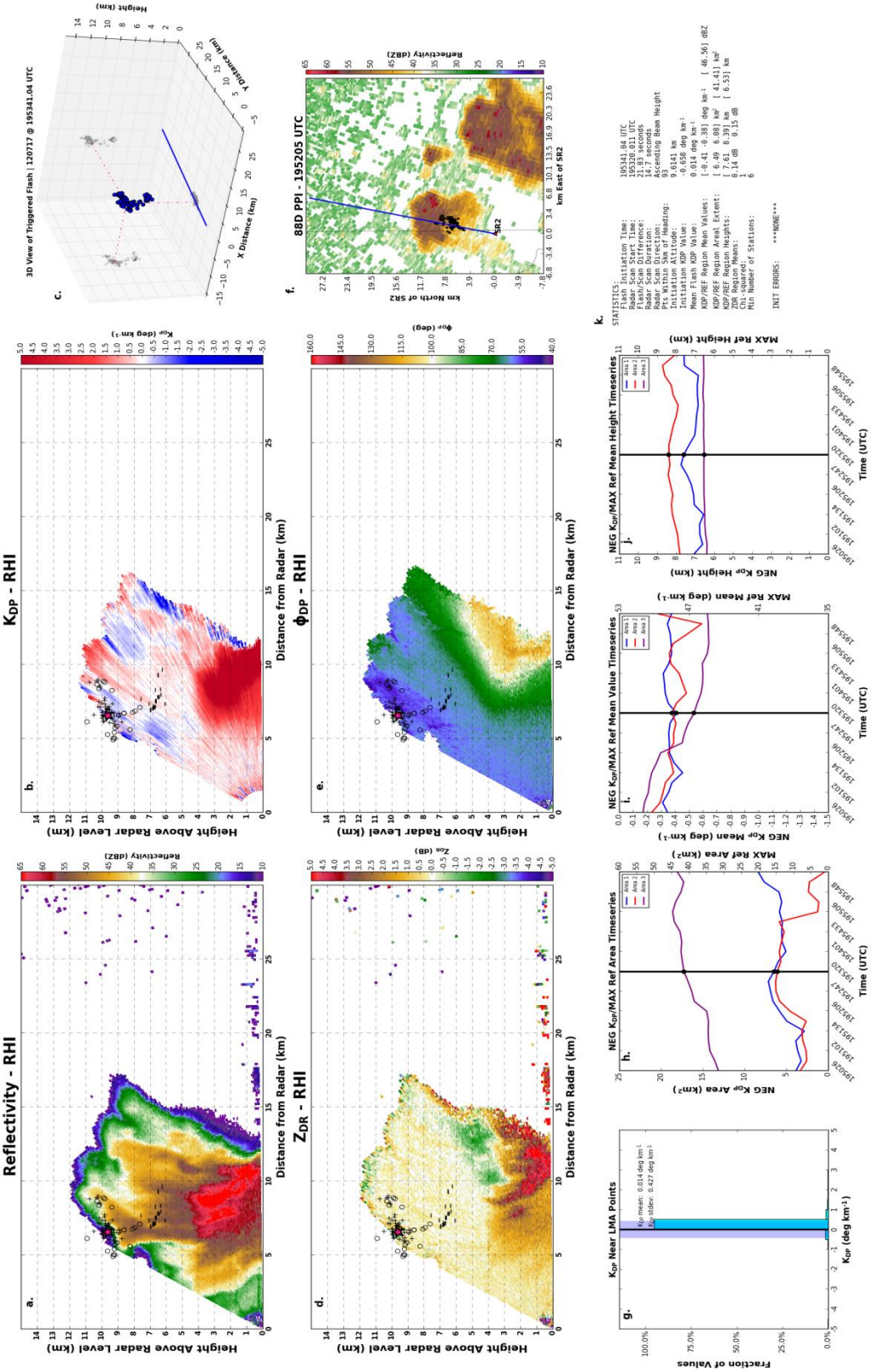

Figure A - 12: Flash 195341.04 UTC

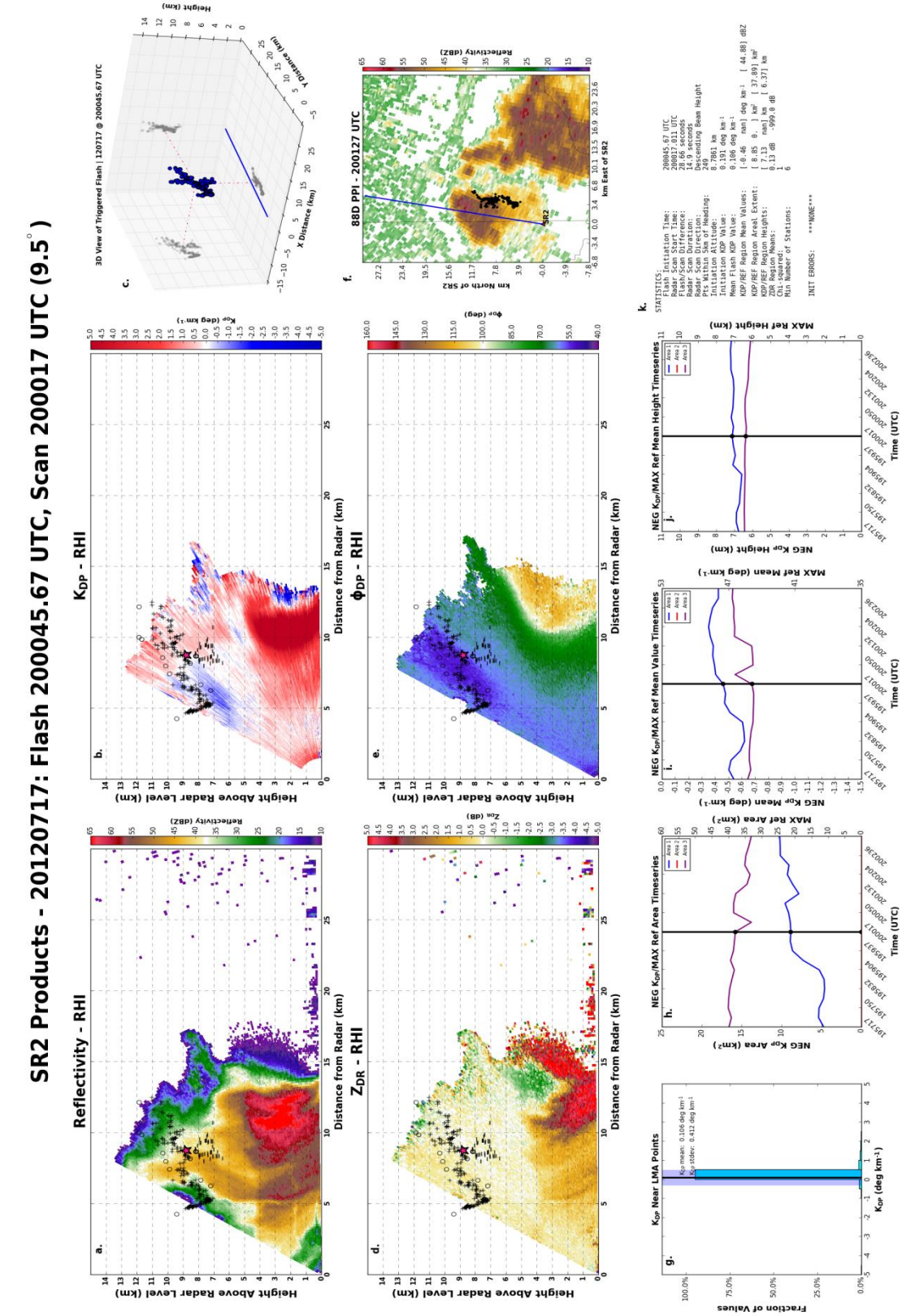

Figure A - 13: Flash 200045.67 UTC

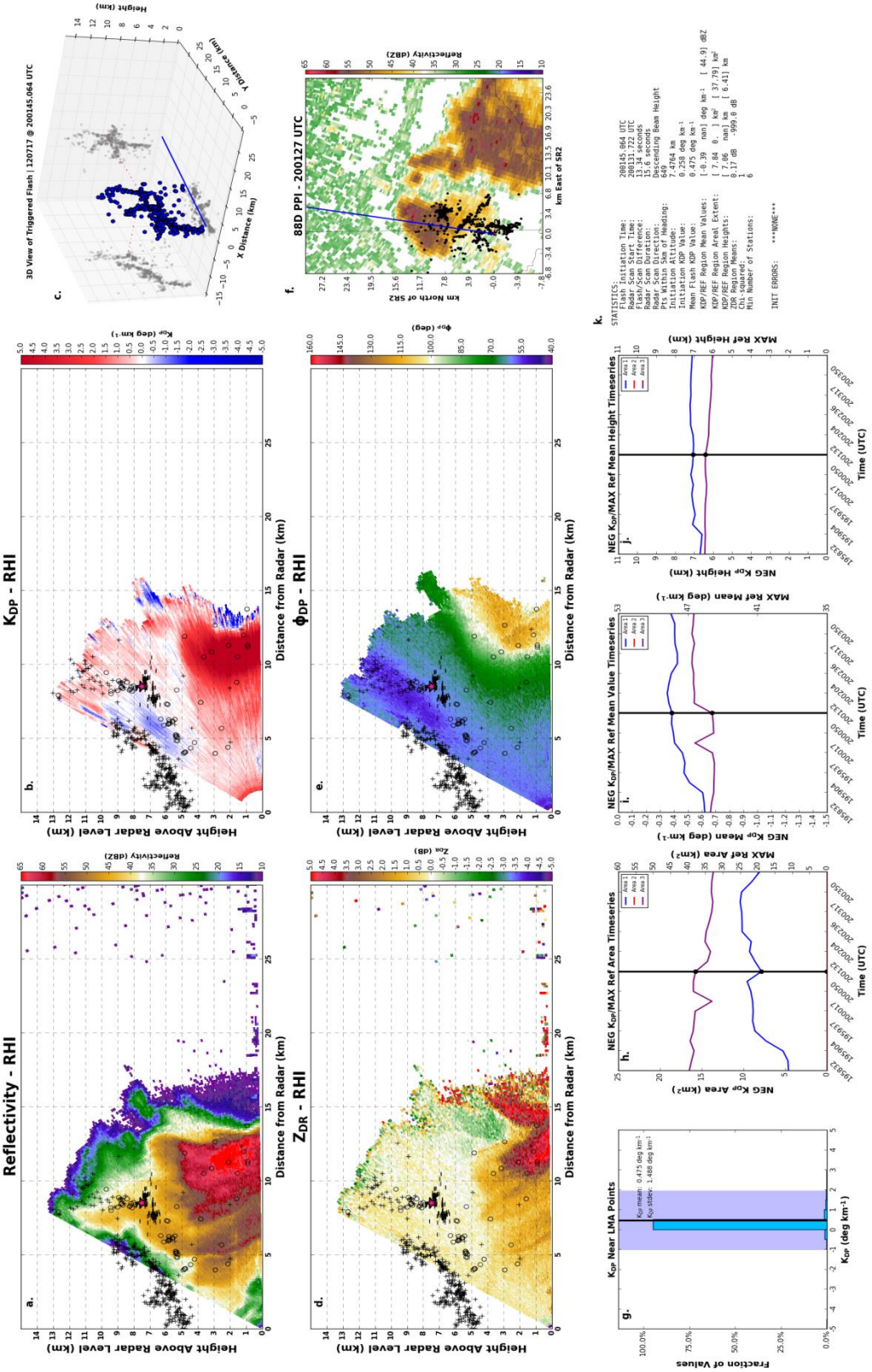

Figure A - 14: Flash 200145.064 UTC

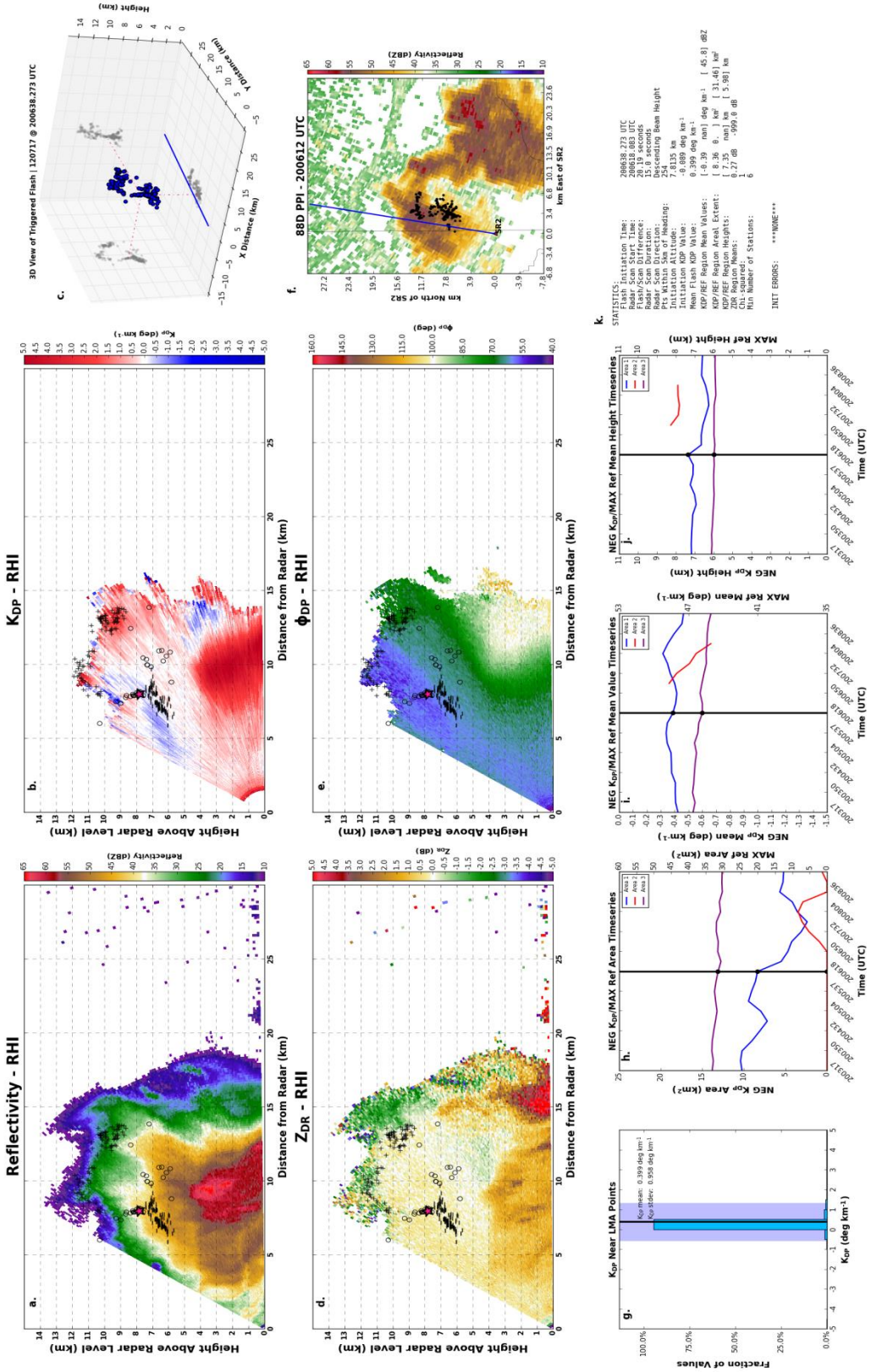

Figure A - 15: Flash 200638.273 UTC

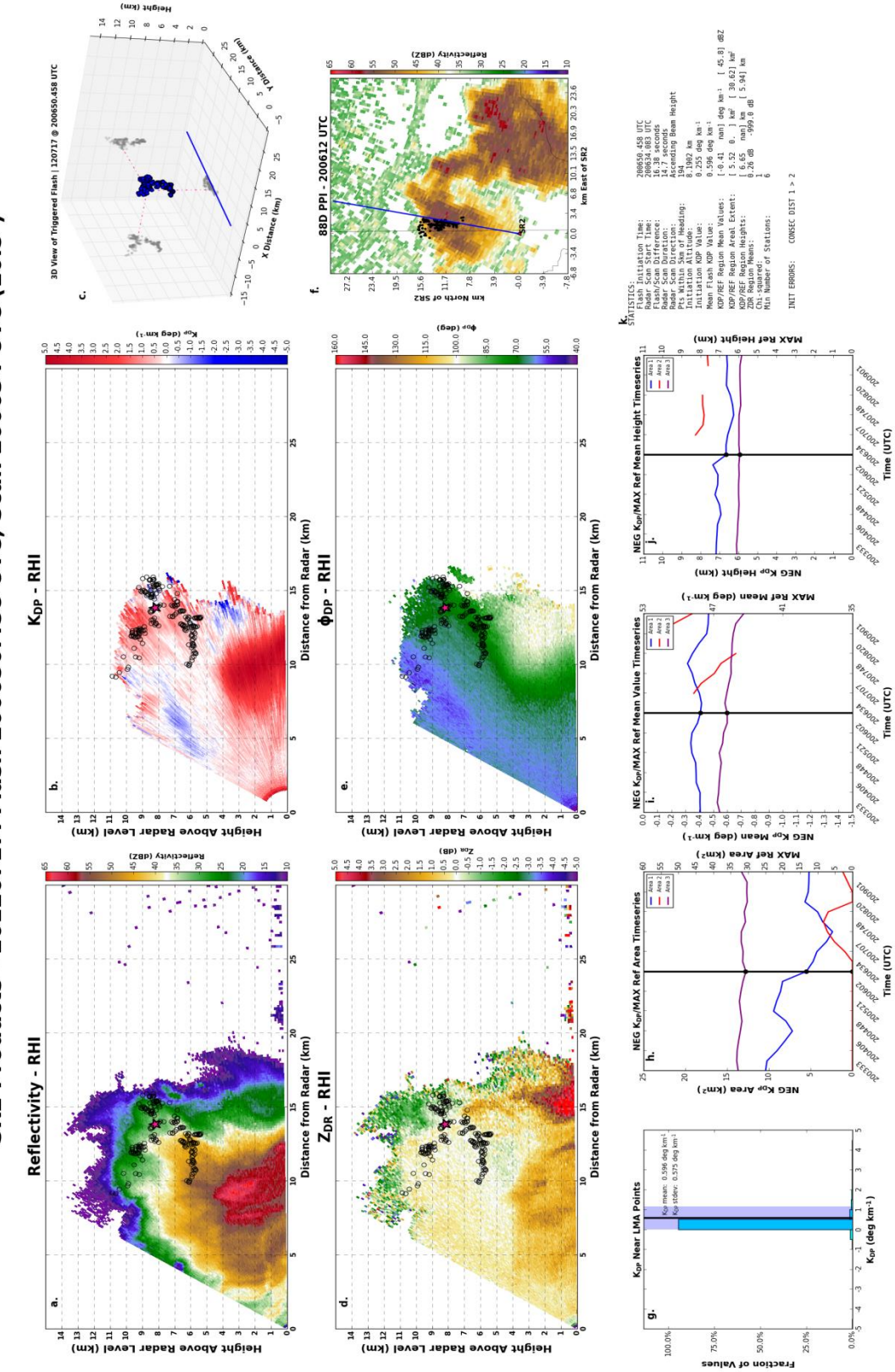

Figure A - 16: Flash 200650.458 UTC

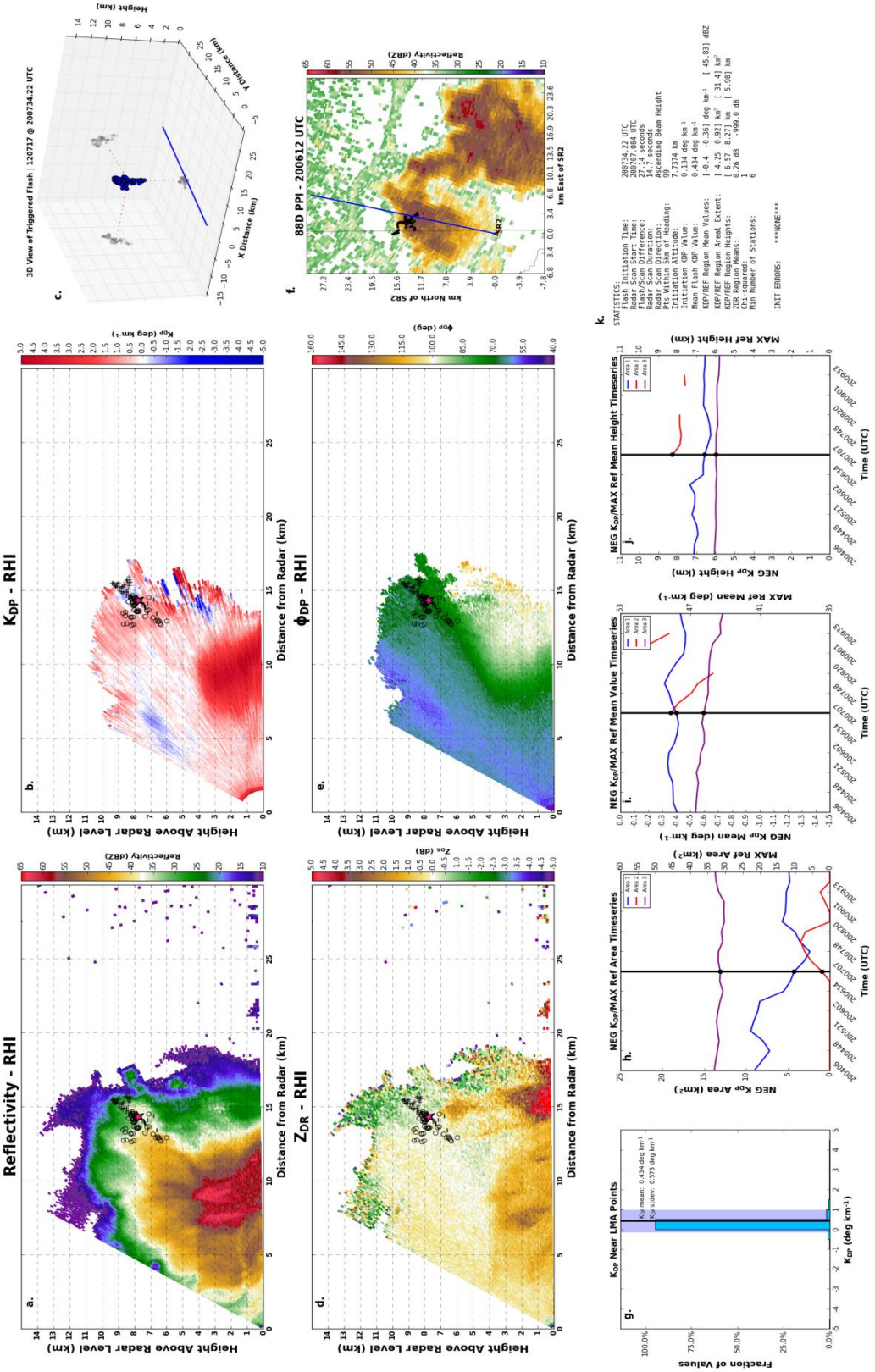

Figure A - 17: Flash 200734.22 UTC

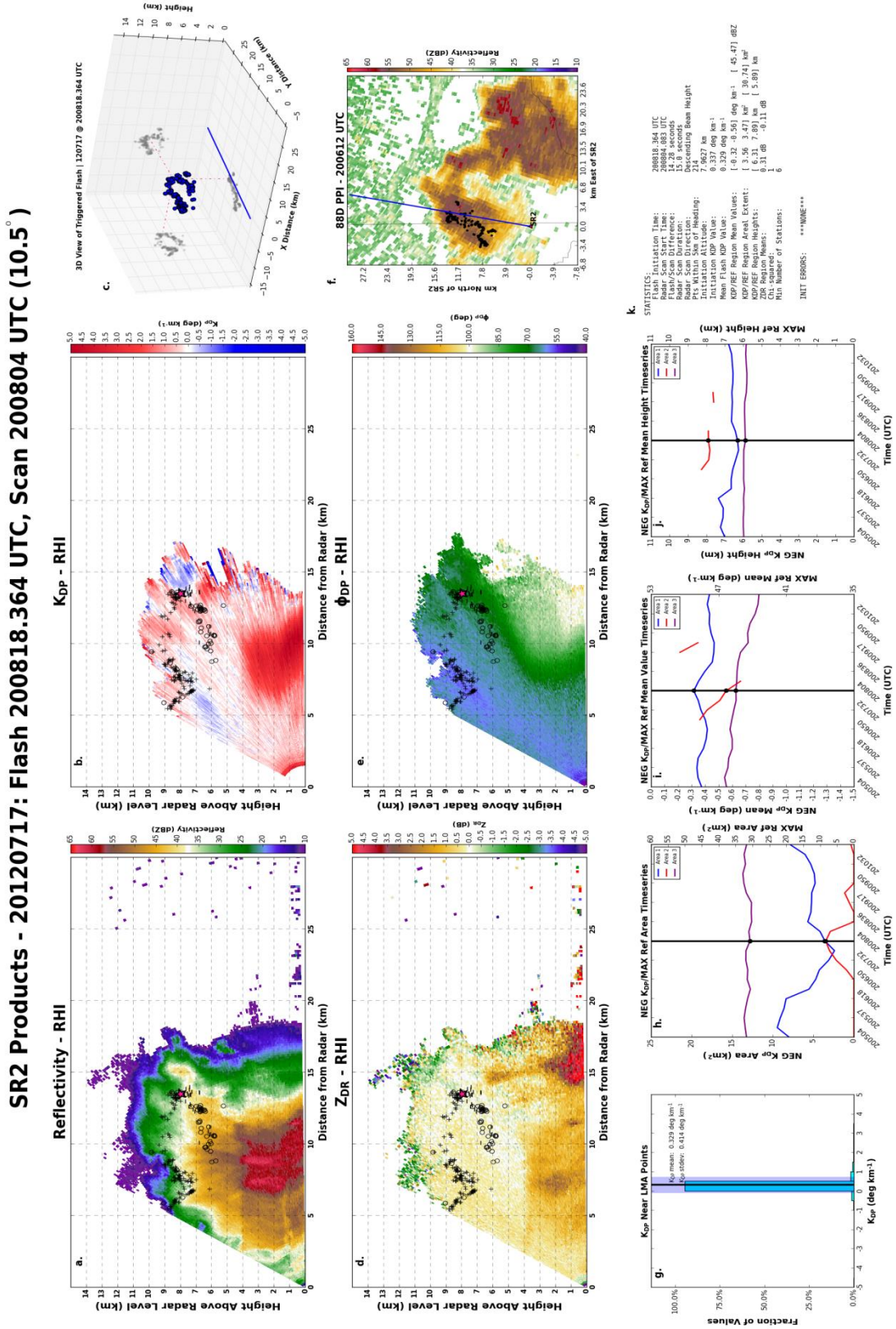

Figure A - 18: Flash 200818.364 UTC

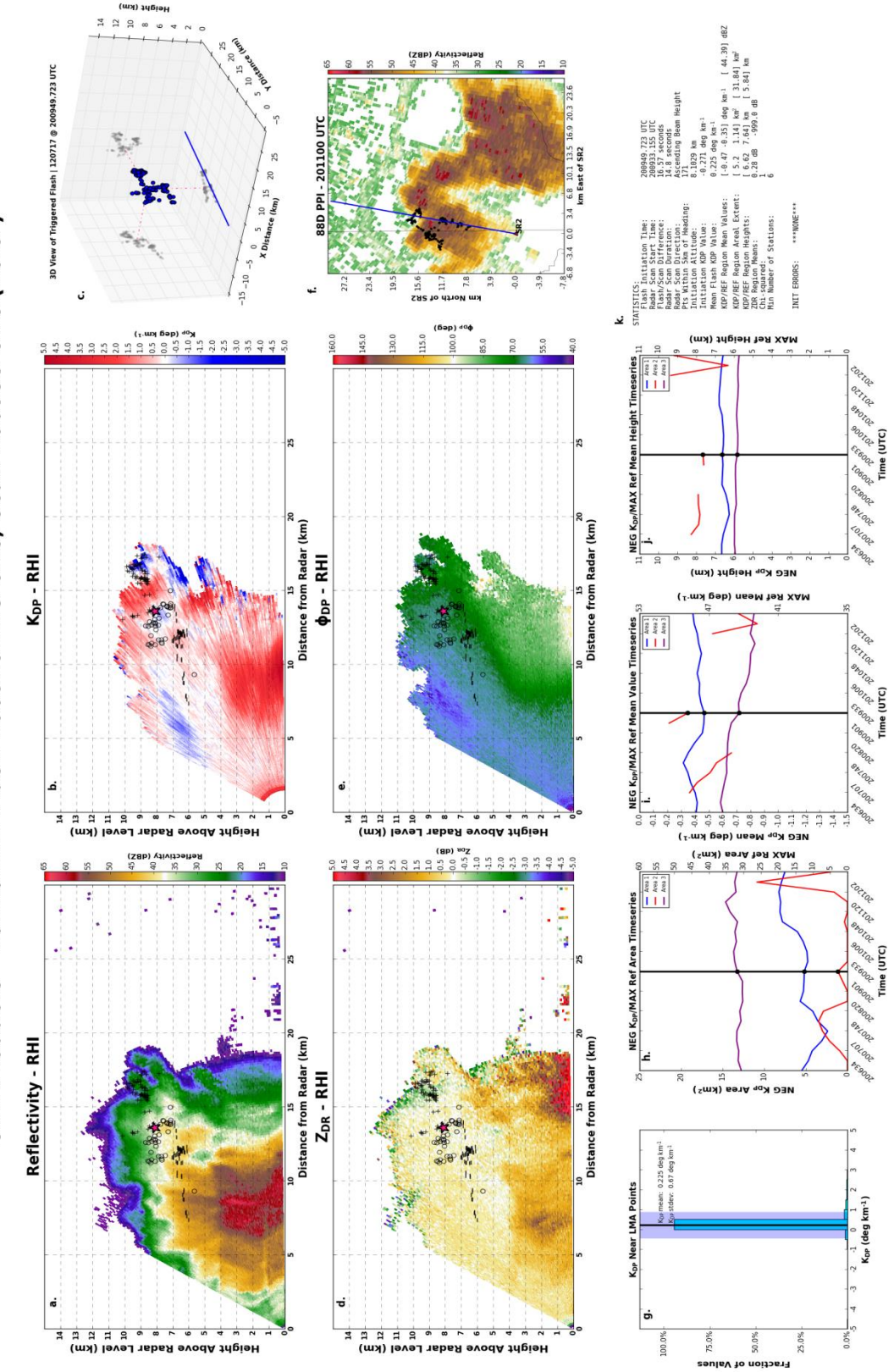

Figure A - 19: Flash 200949.723 UTC

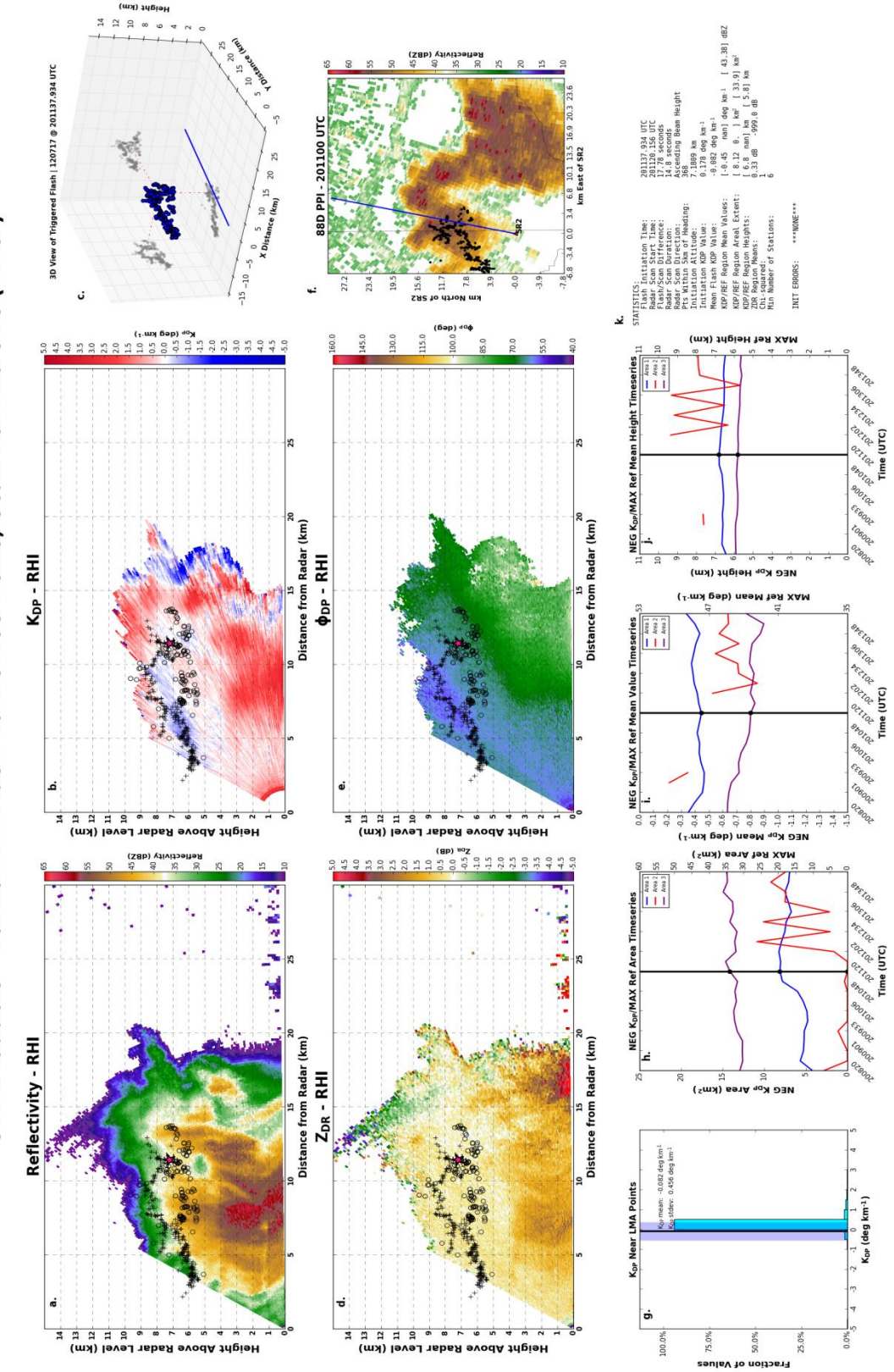

Figure A - 20: Flash 201137.934 UTC

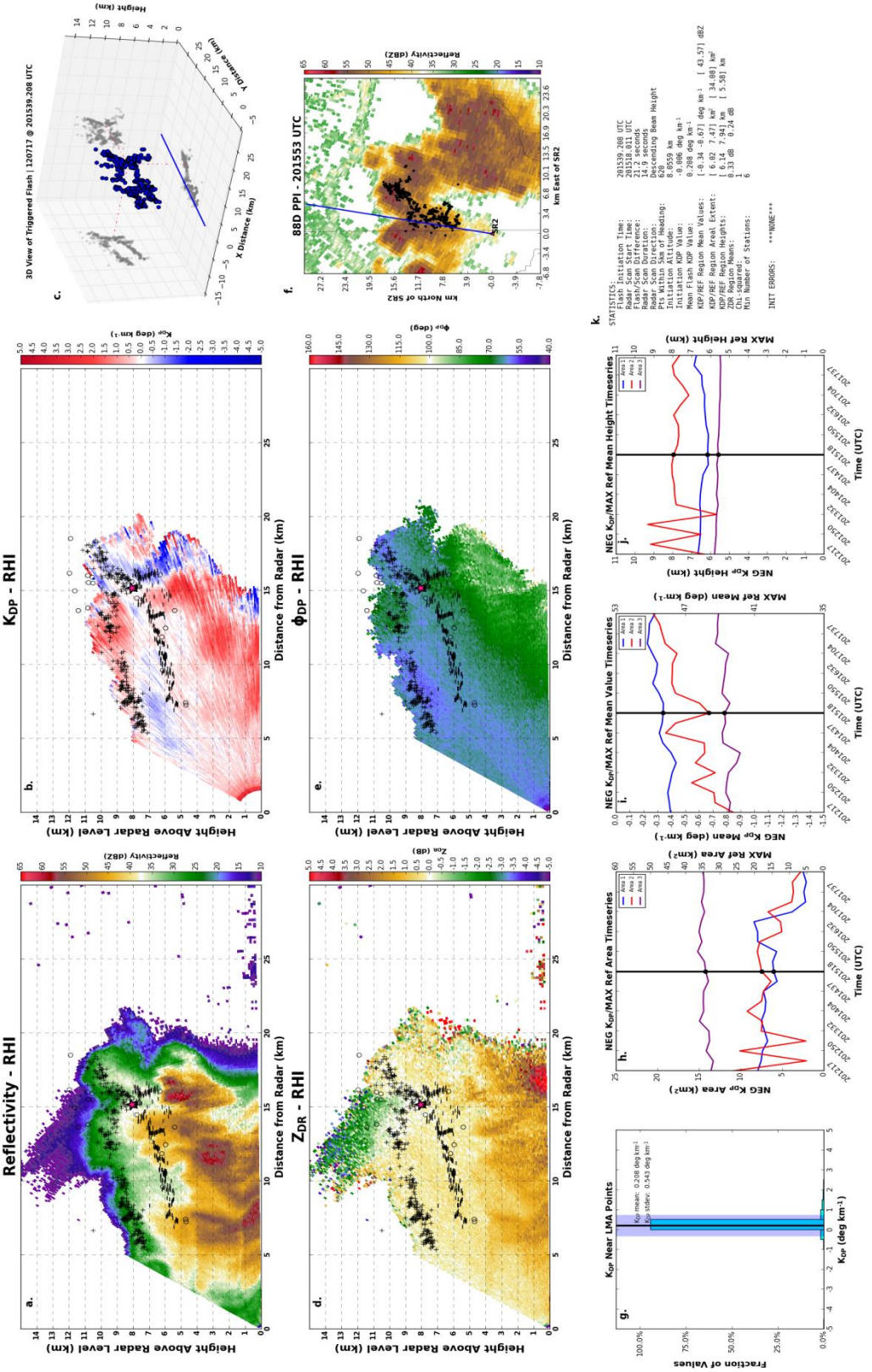

Figure A - 21: Flash 201539.208 UTC

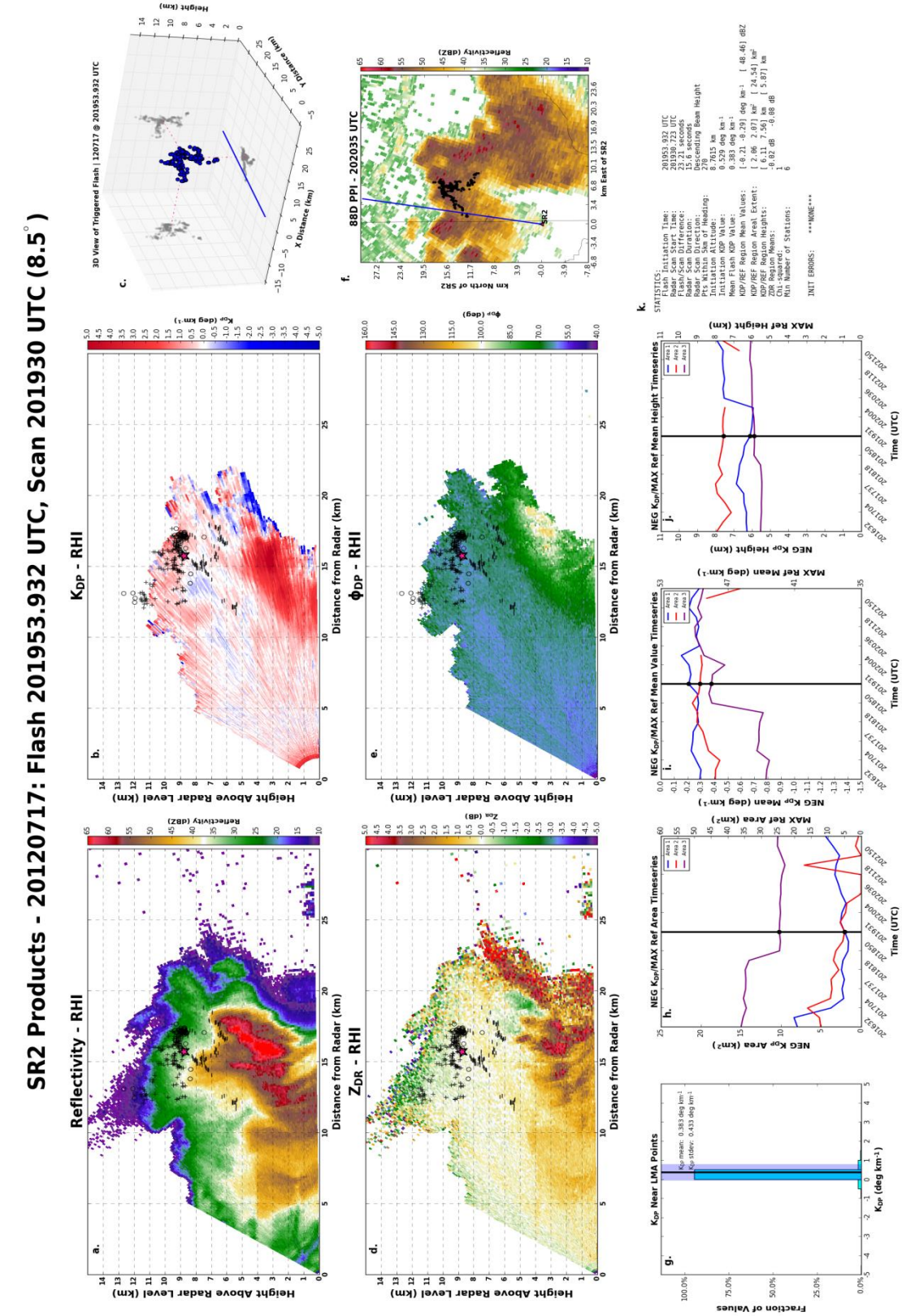

Figure A - 22: Flash 201953.932 UTC

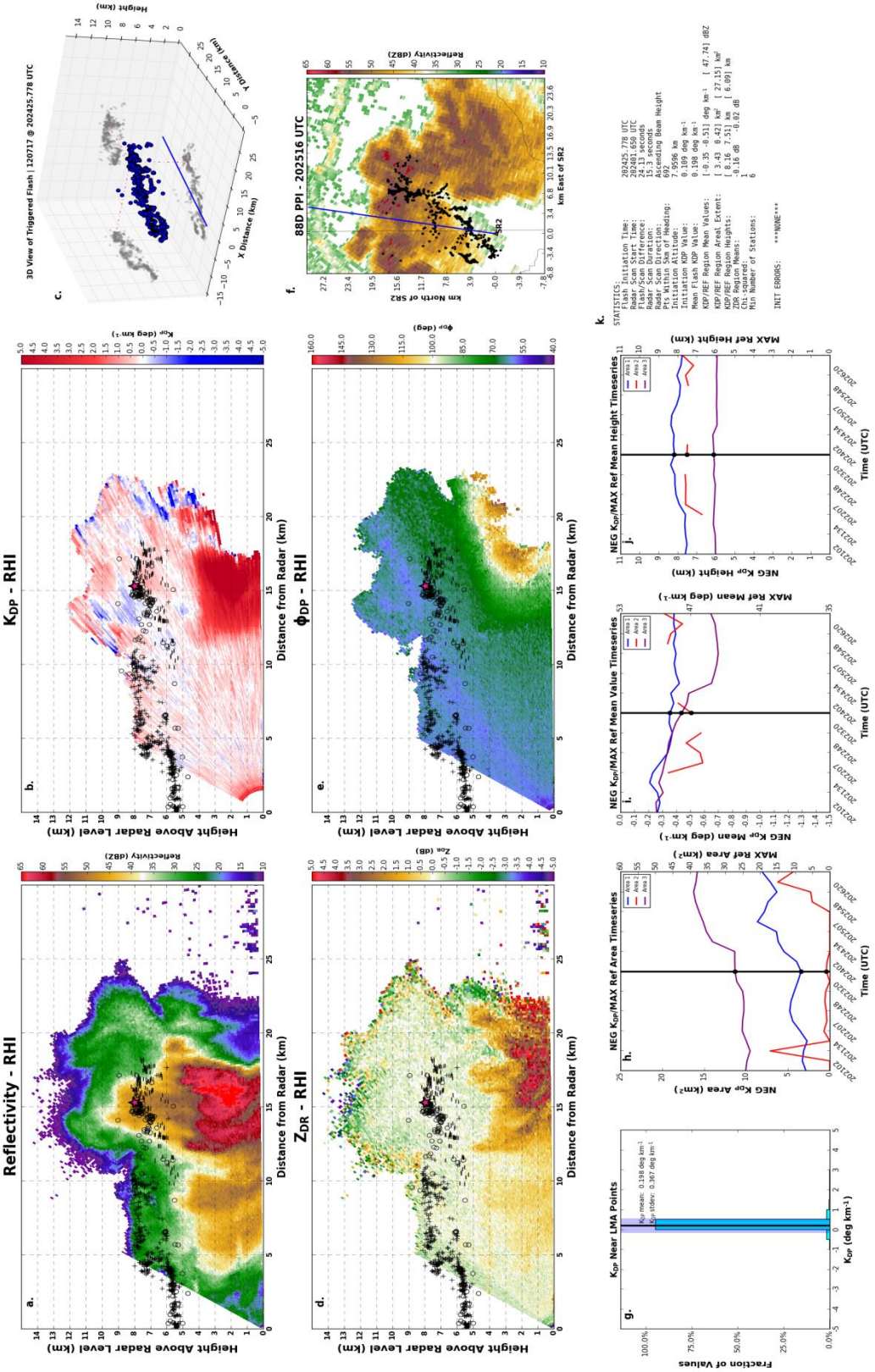

Figure A - 23: Flash 202425.778 UTC

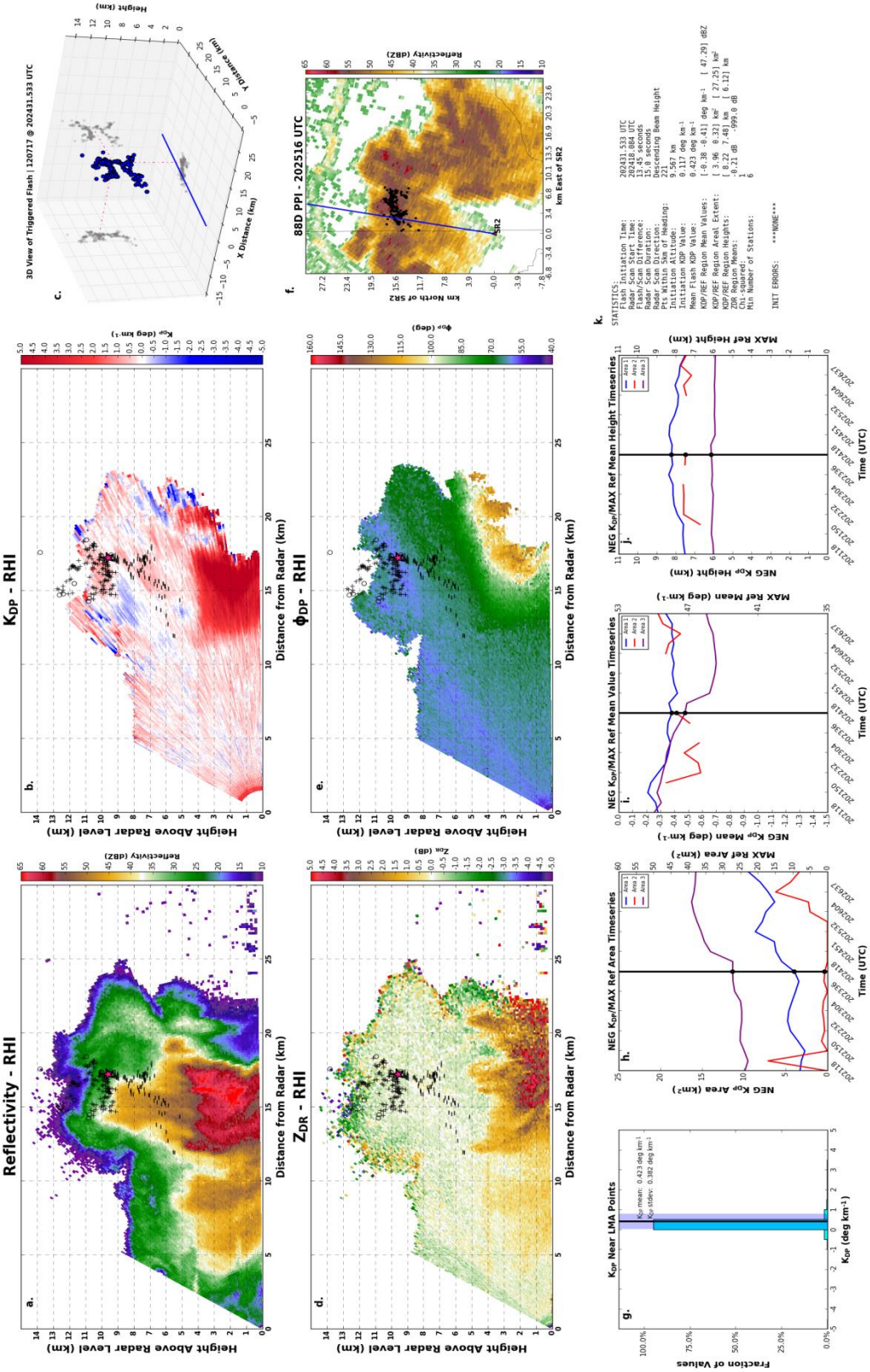

Figure A - 24: Flash 202431.533 UTC

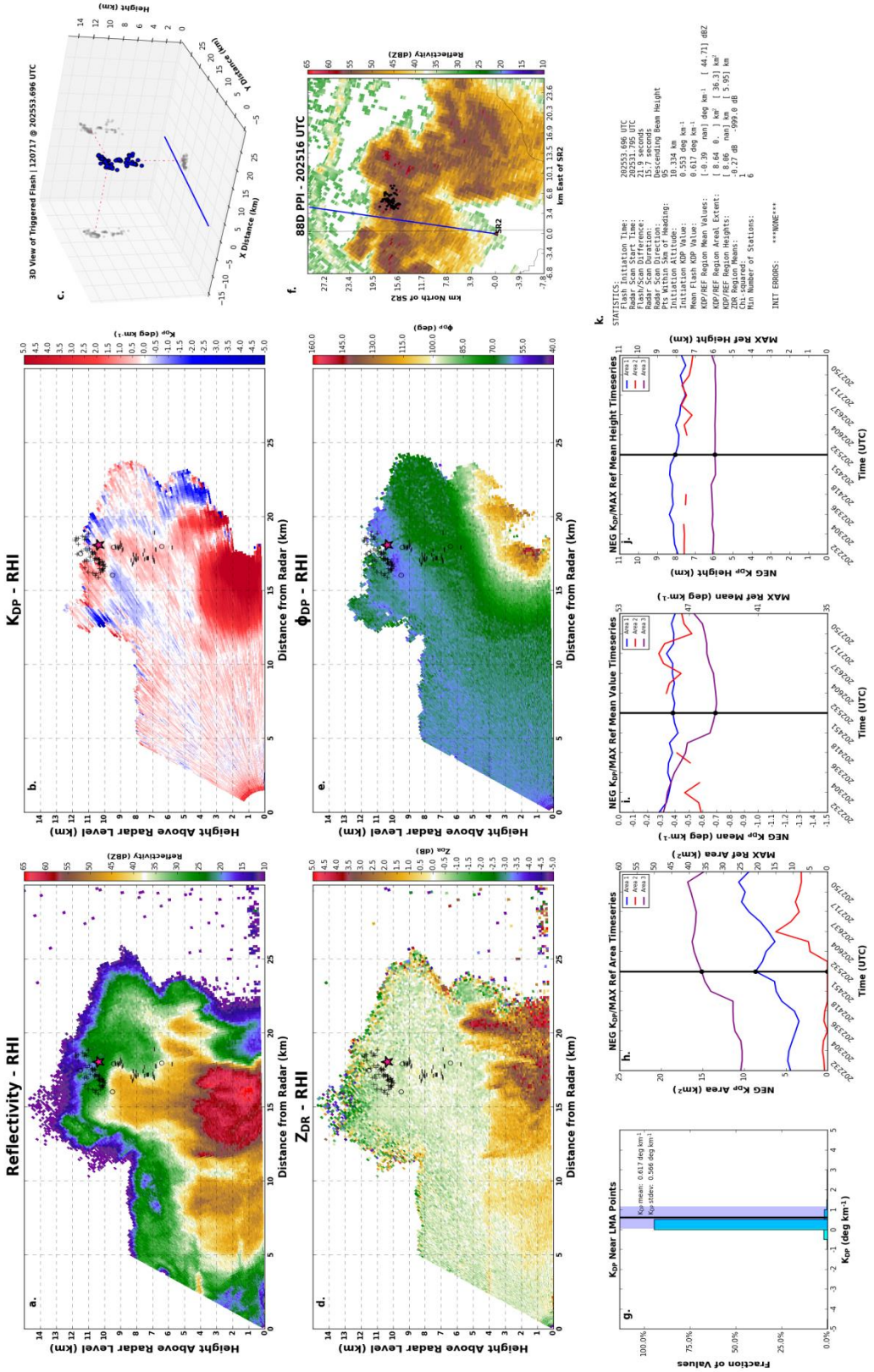

Figure A - 25: Flash 202553.696 UTC

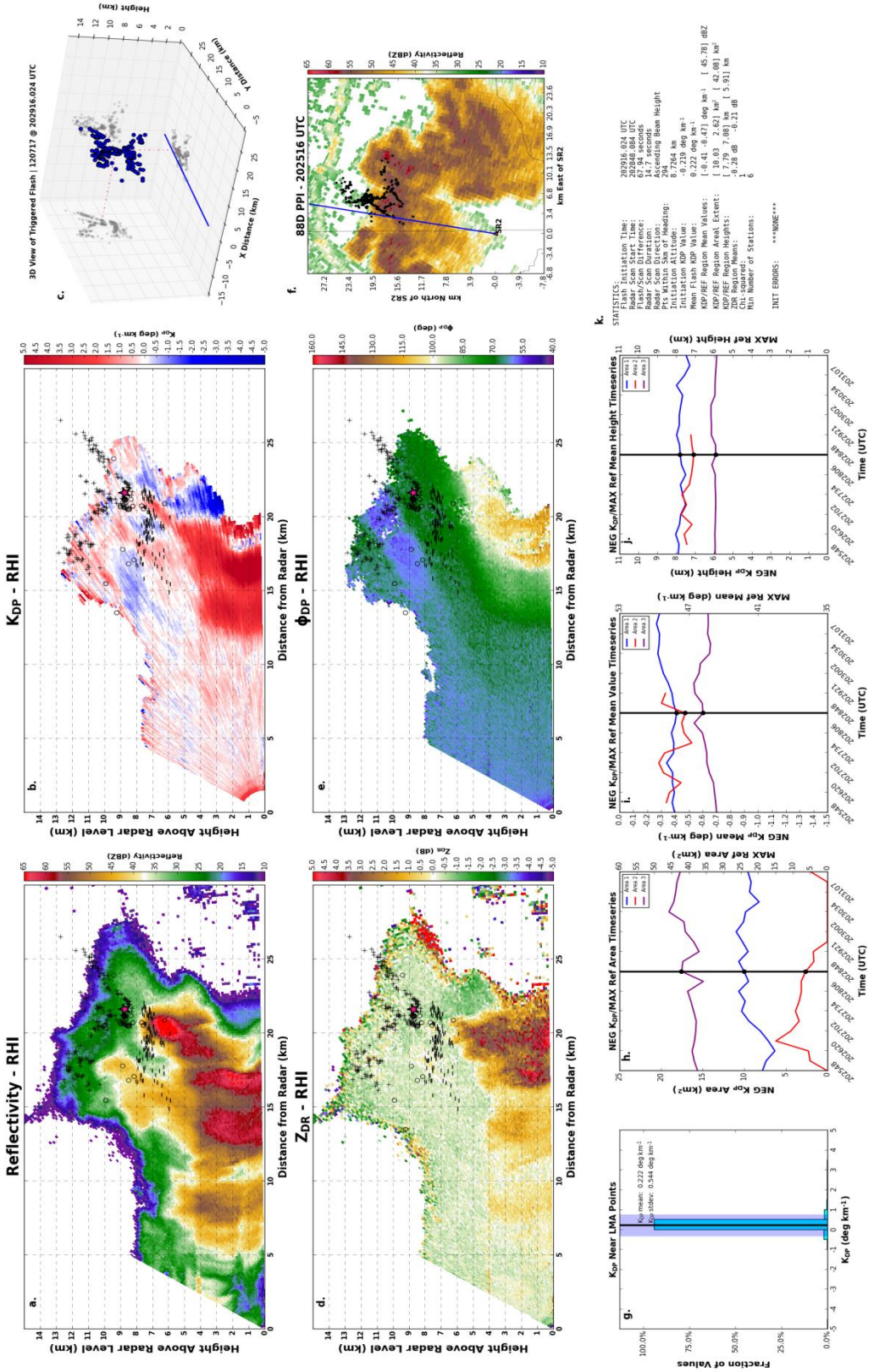

Figure A - 26: Flash 202916.024 UTC

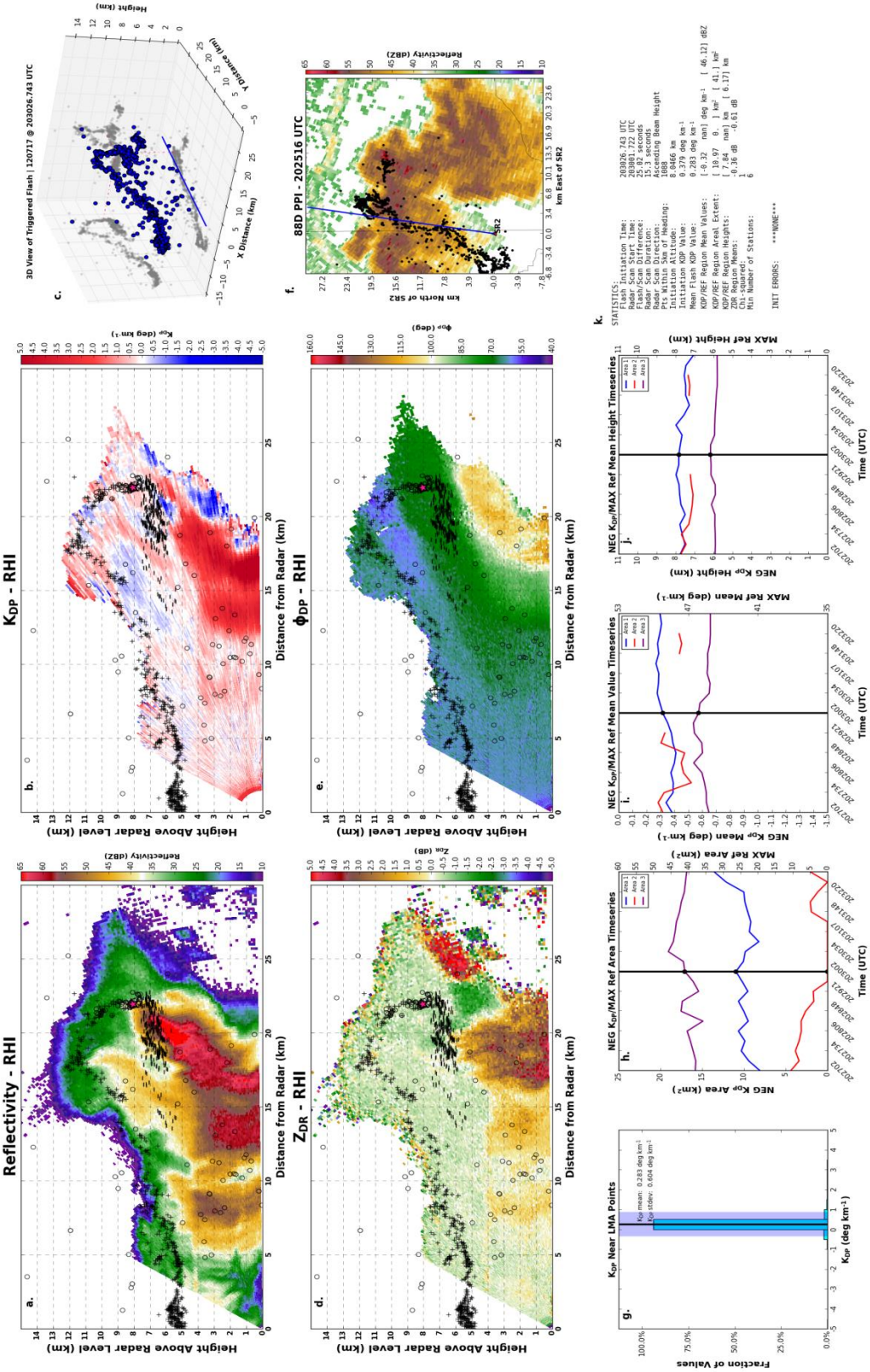

Figure A - 27: Flash 203026.743 UTC

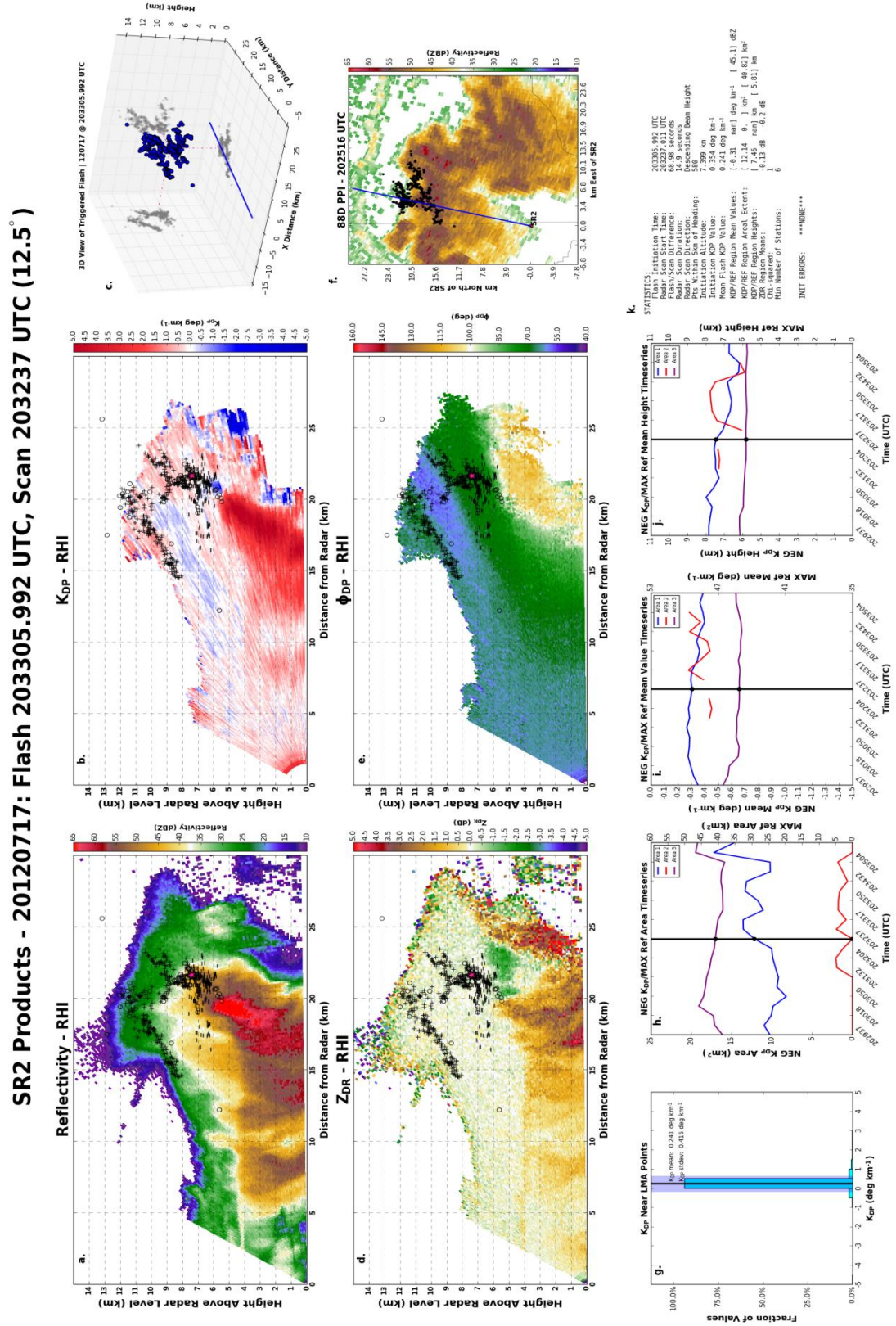

Figure A - 28: Flash 203305.992 UTC

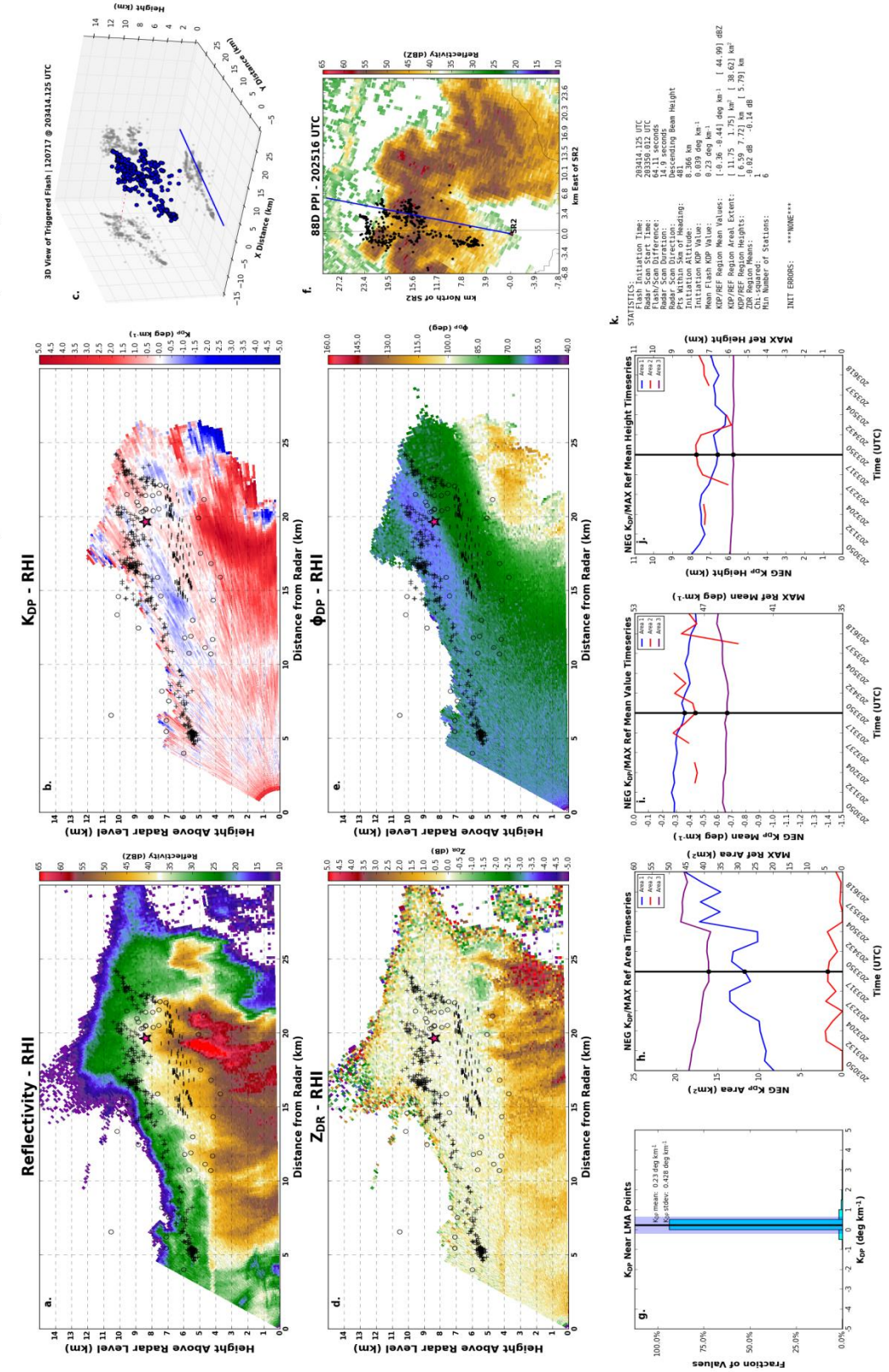

Figure A - 29: Flash 203414.125 UTC

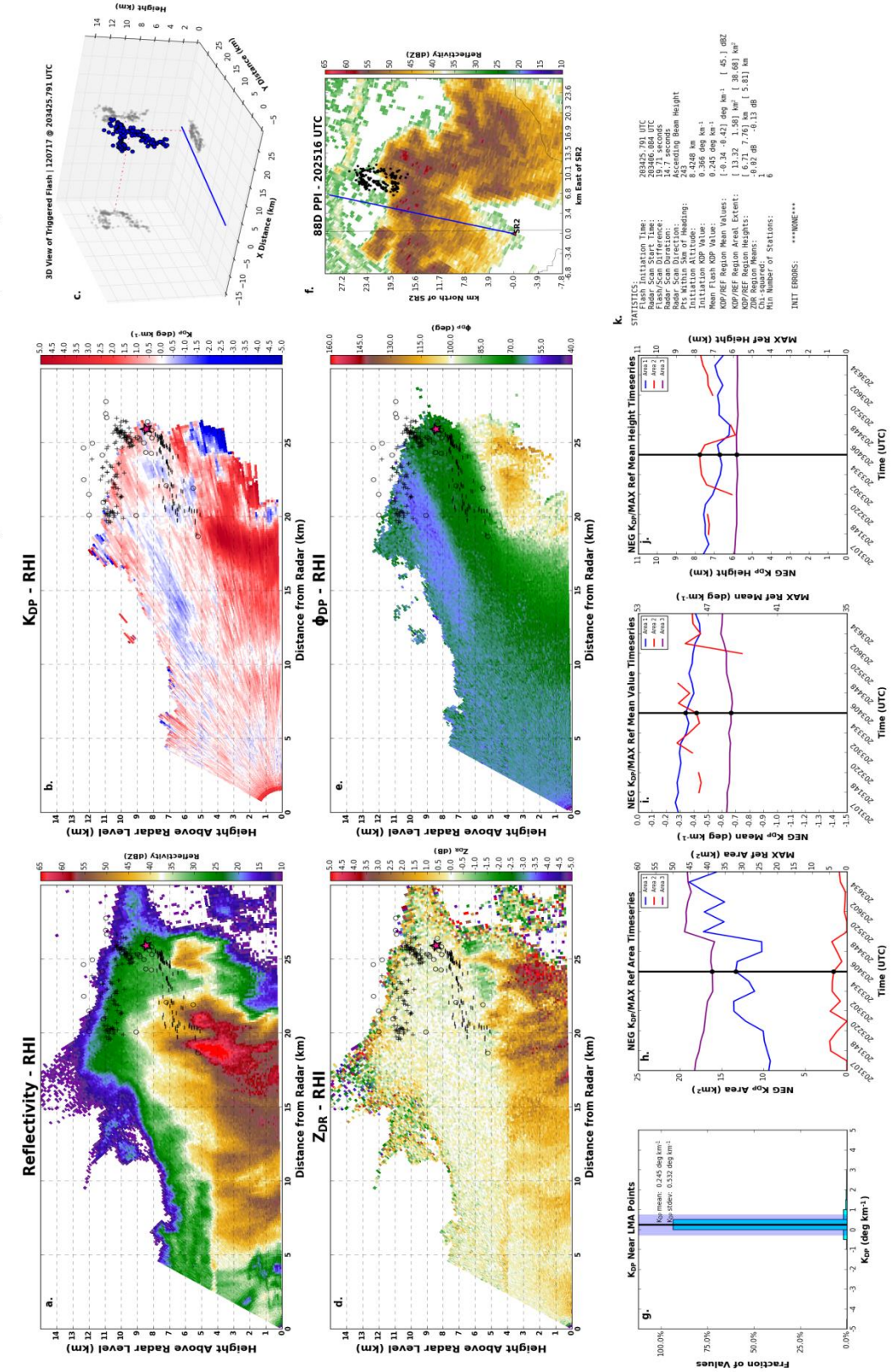

Figure A - 30: Flash 203425.791 UTC

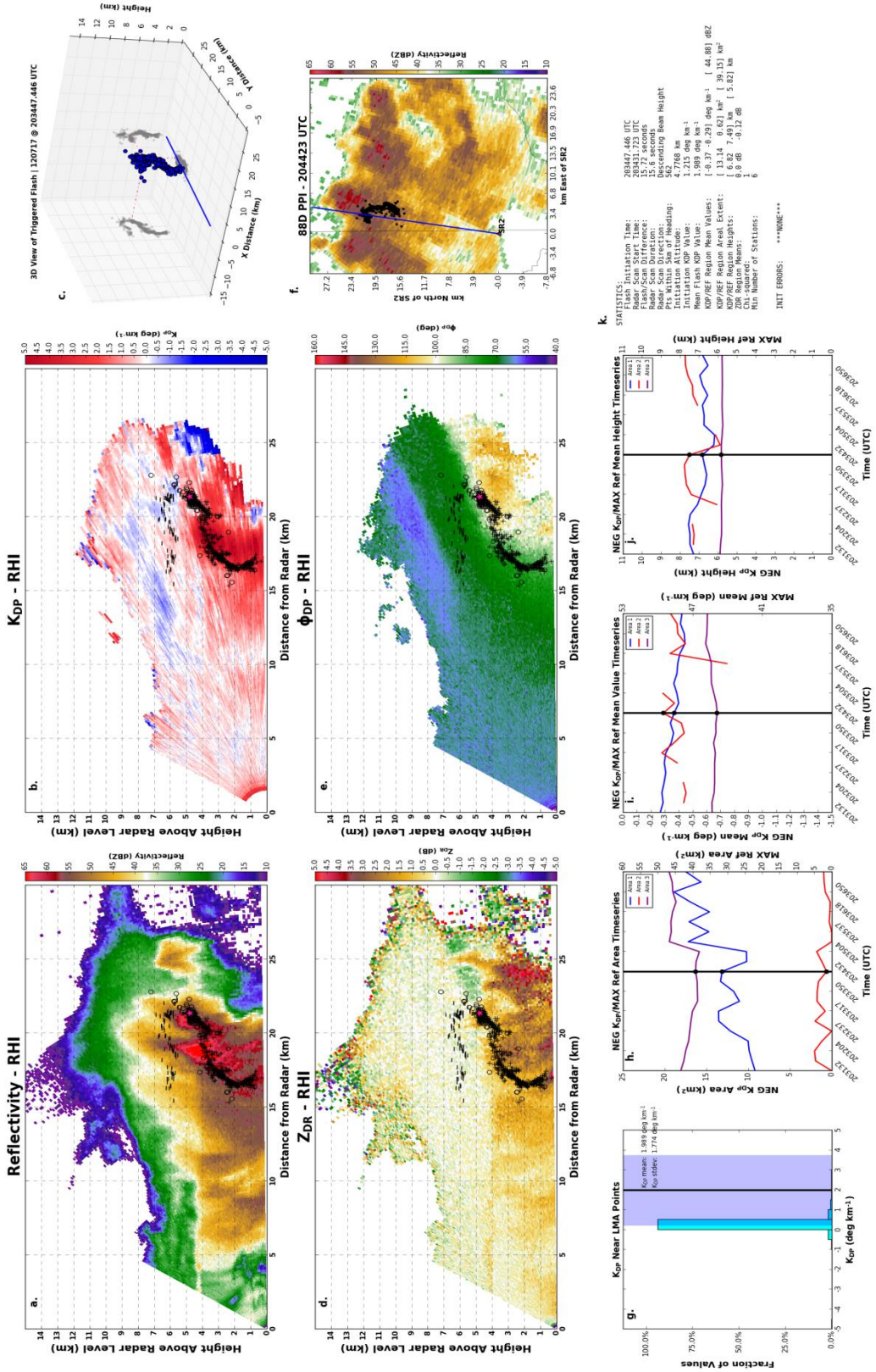

Figure A - 31: Flash 203447.446 UTC

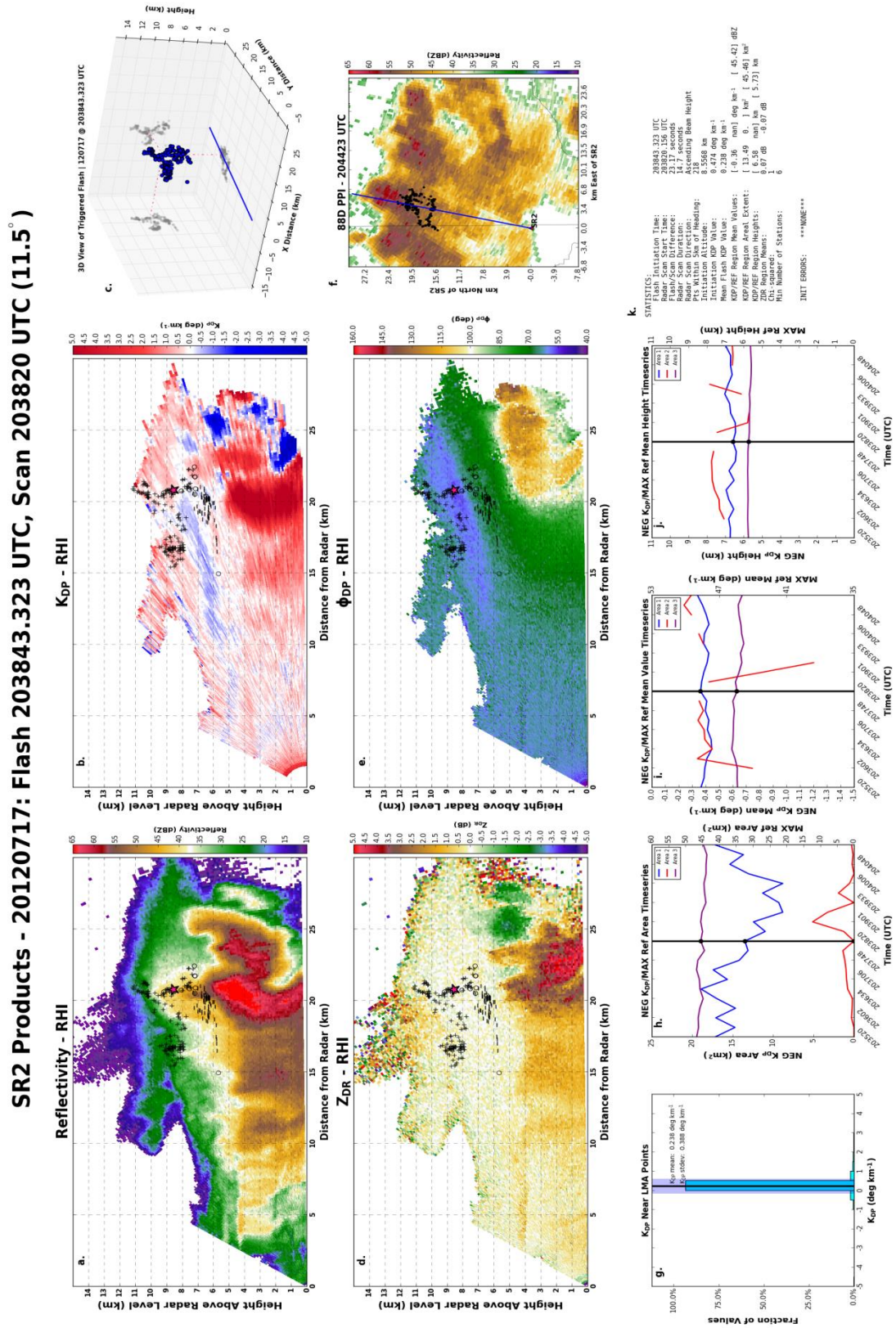

Figure A - 32: Flash 203843.323 UTC

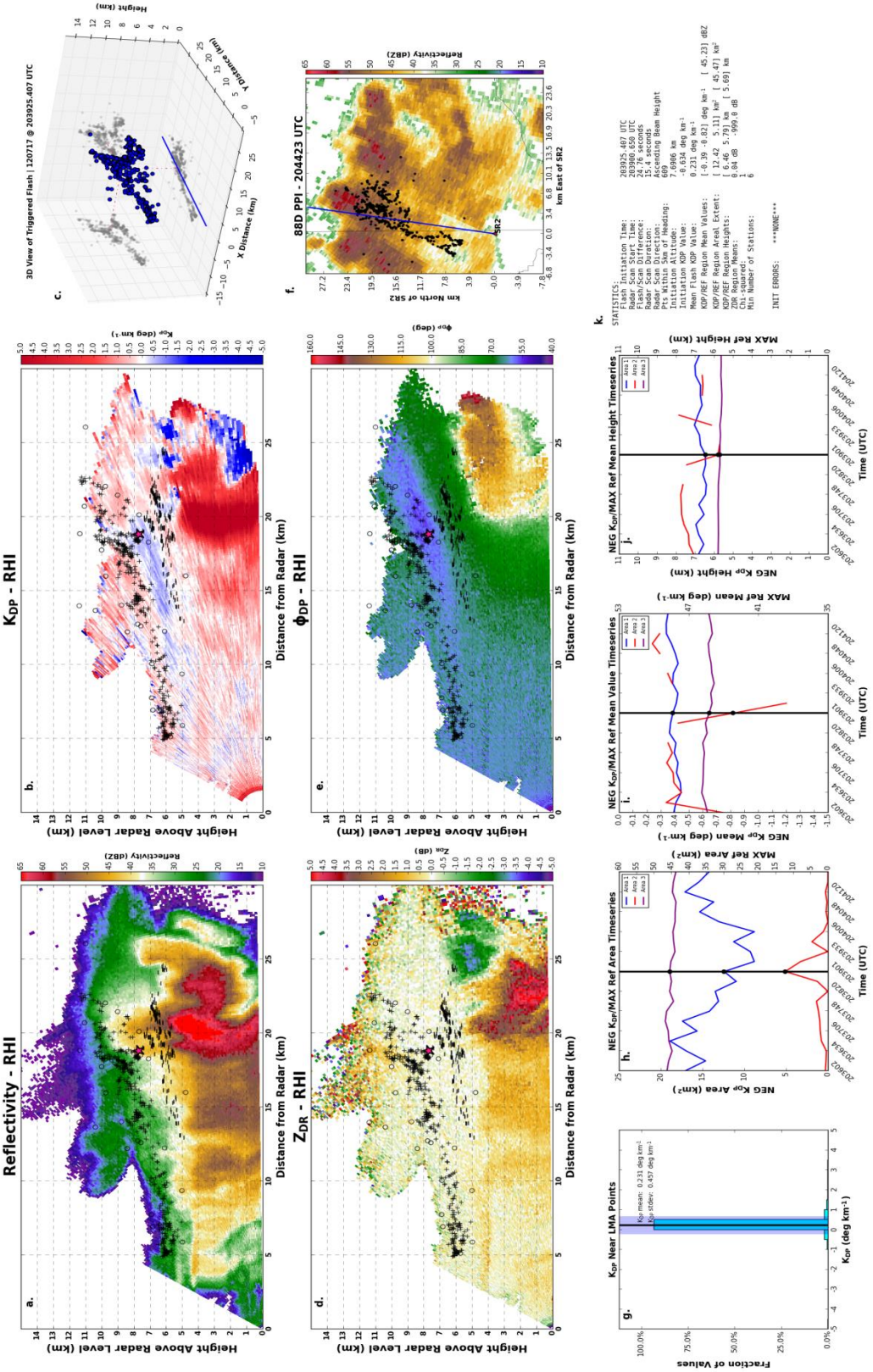

Figure A - 33: Flash 203925.407 UTC

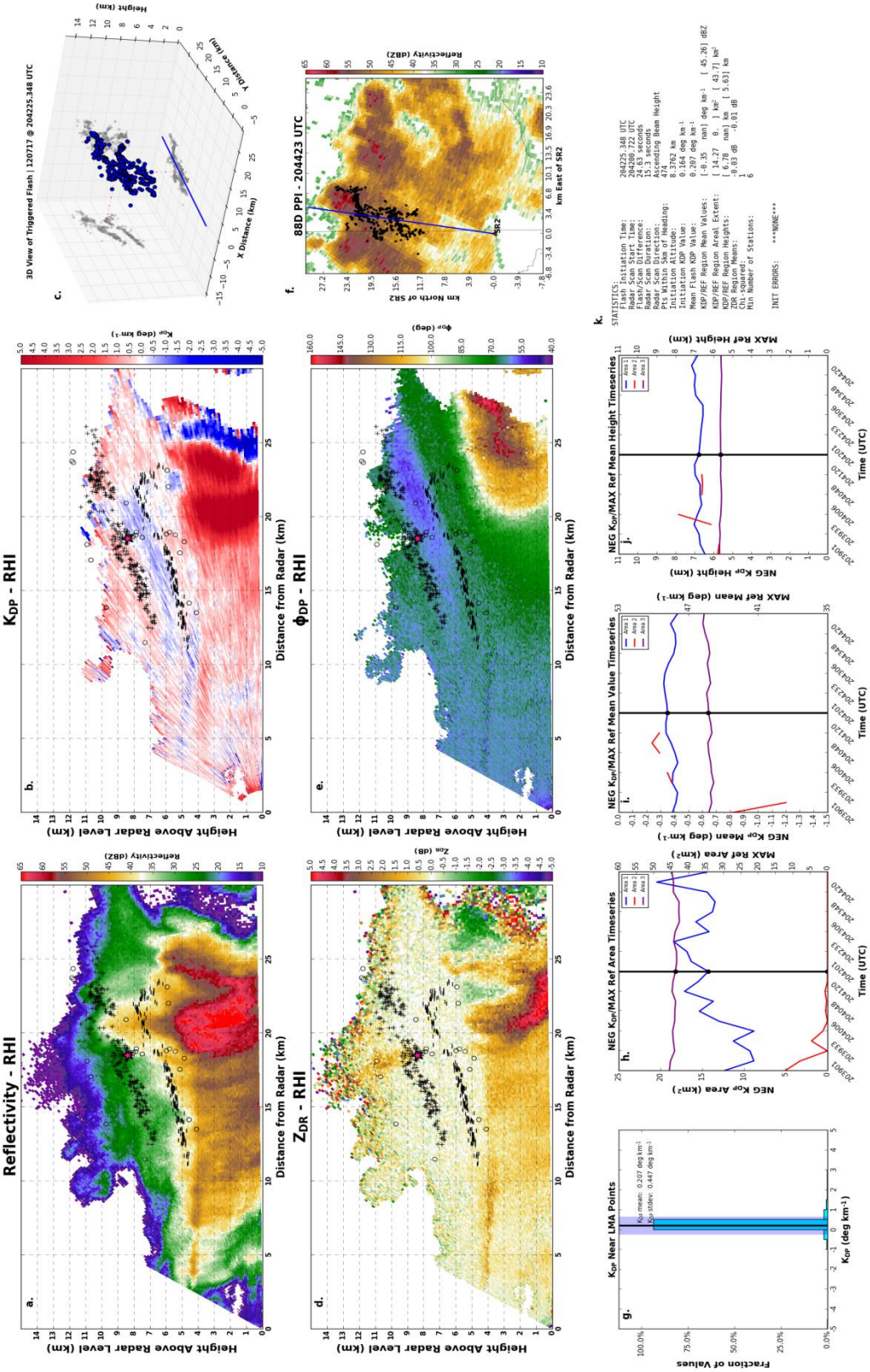

Figure A - 34: Flash 204225.348 UTC

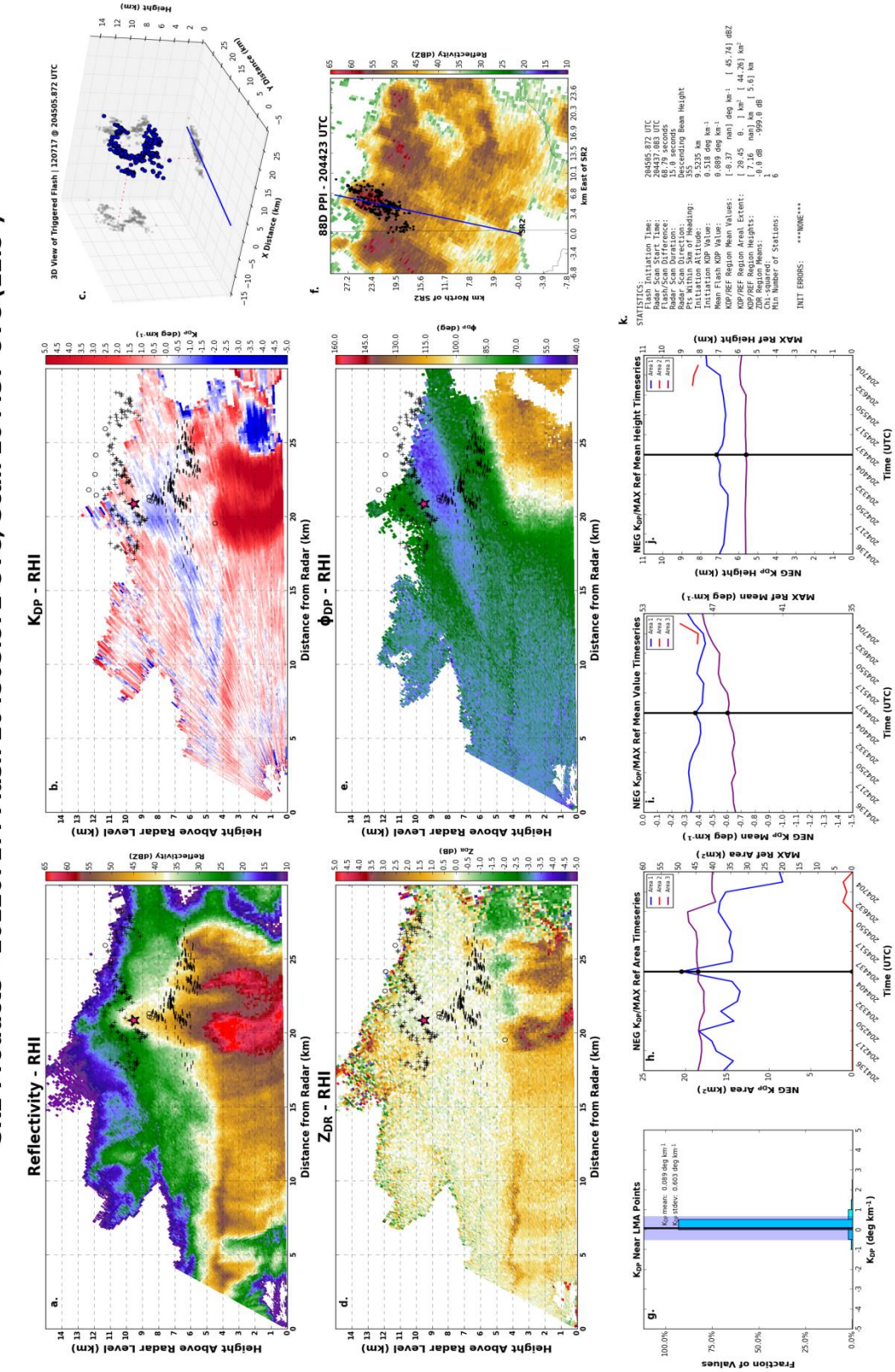

Figure A - 35: Flash 204505.872 UTC

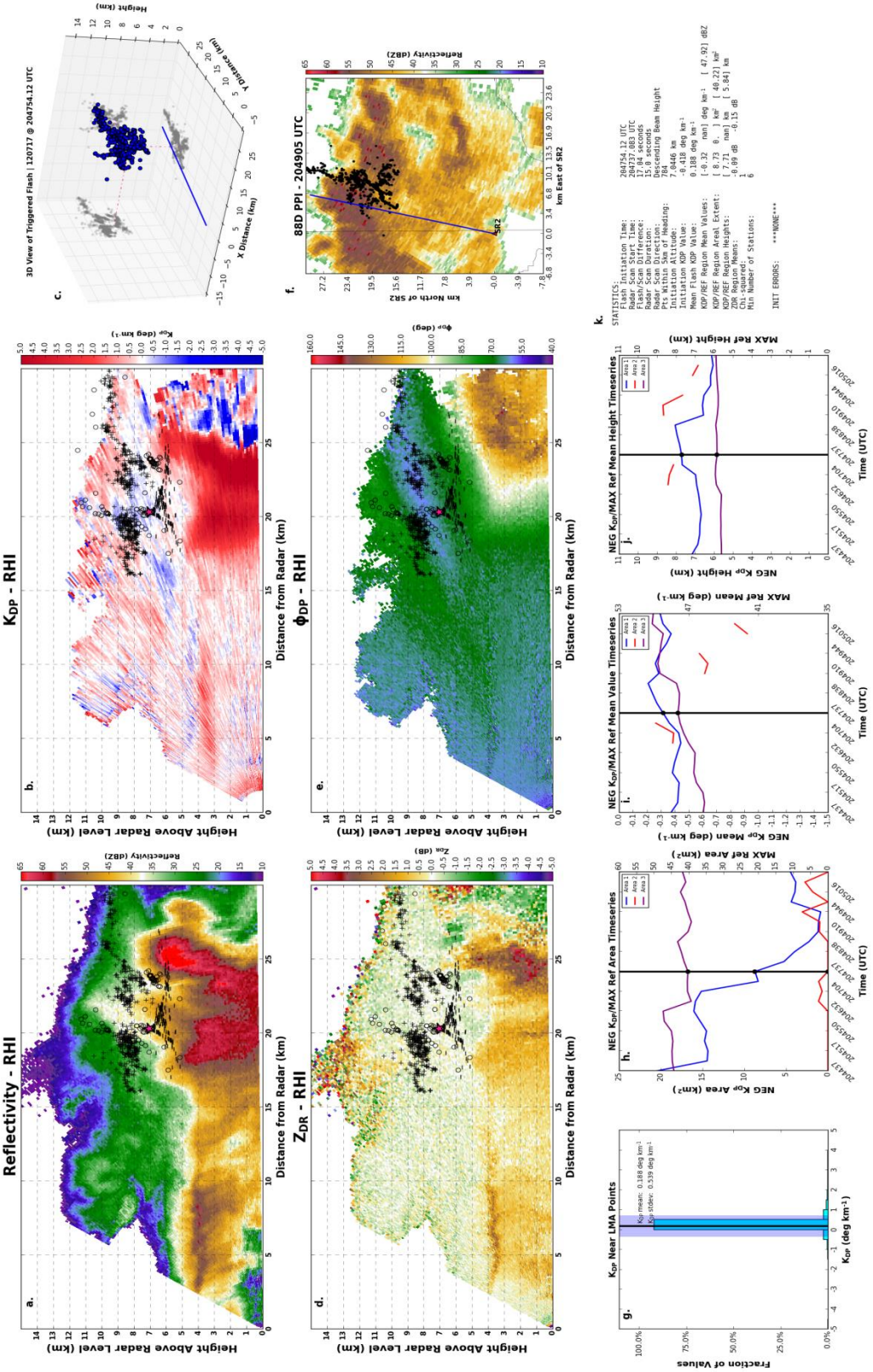

Figure A - 36: Flash 204754.12 UTC

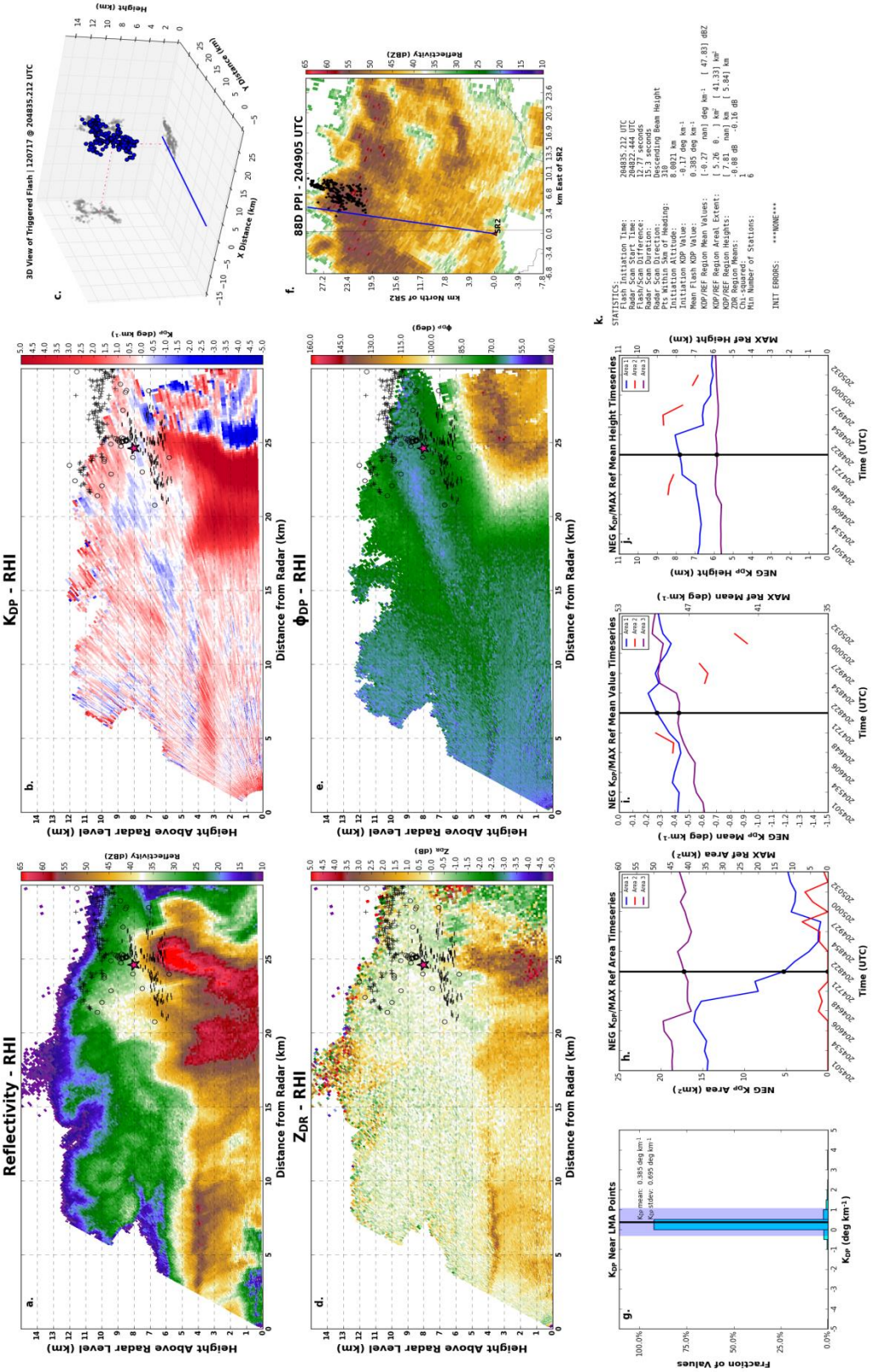

Figure A - 37: Flash 204835.212 UTC

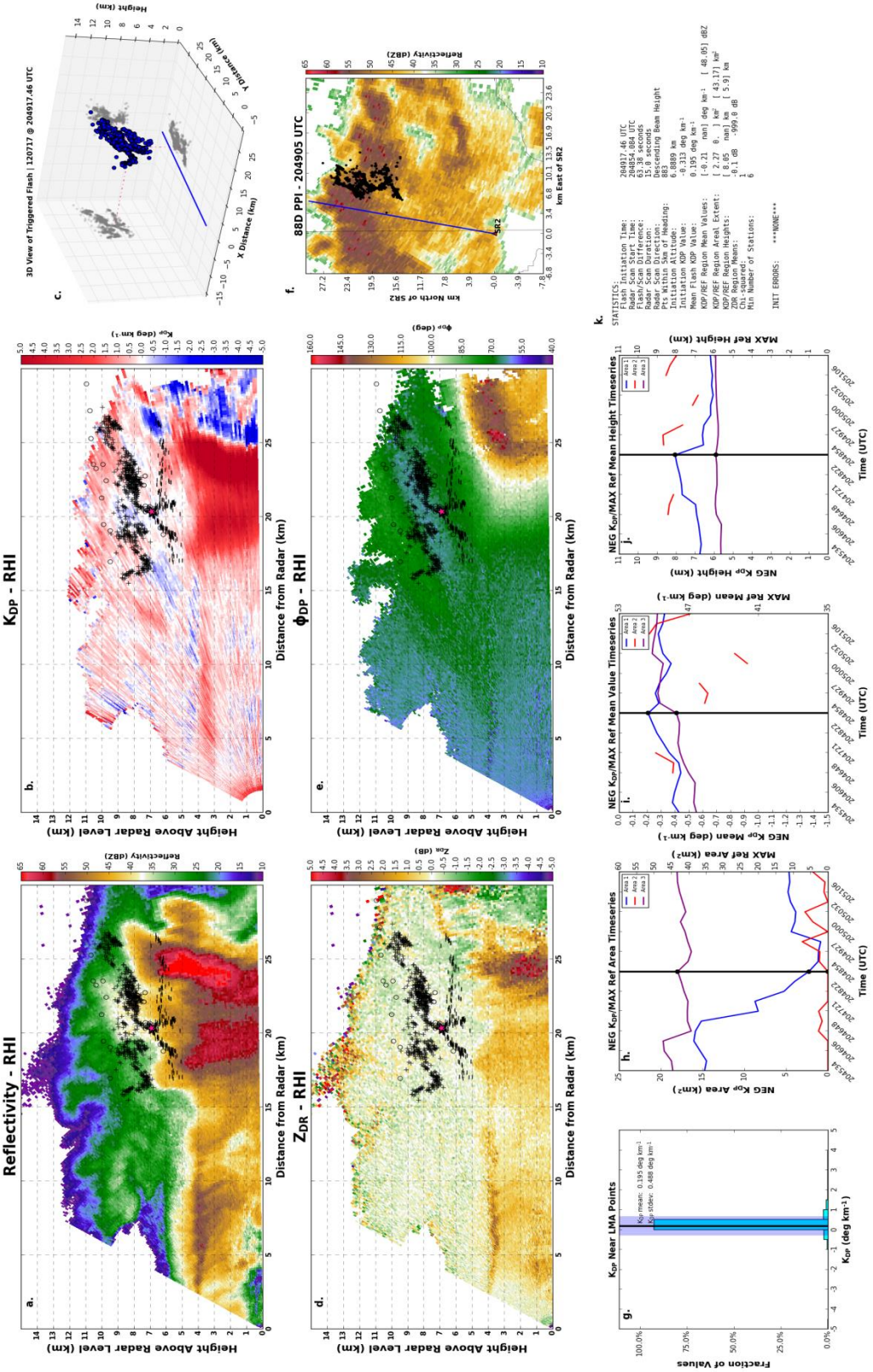

Figure A - 38: Flash 204917.46 UTC

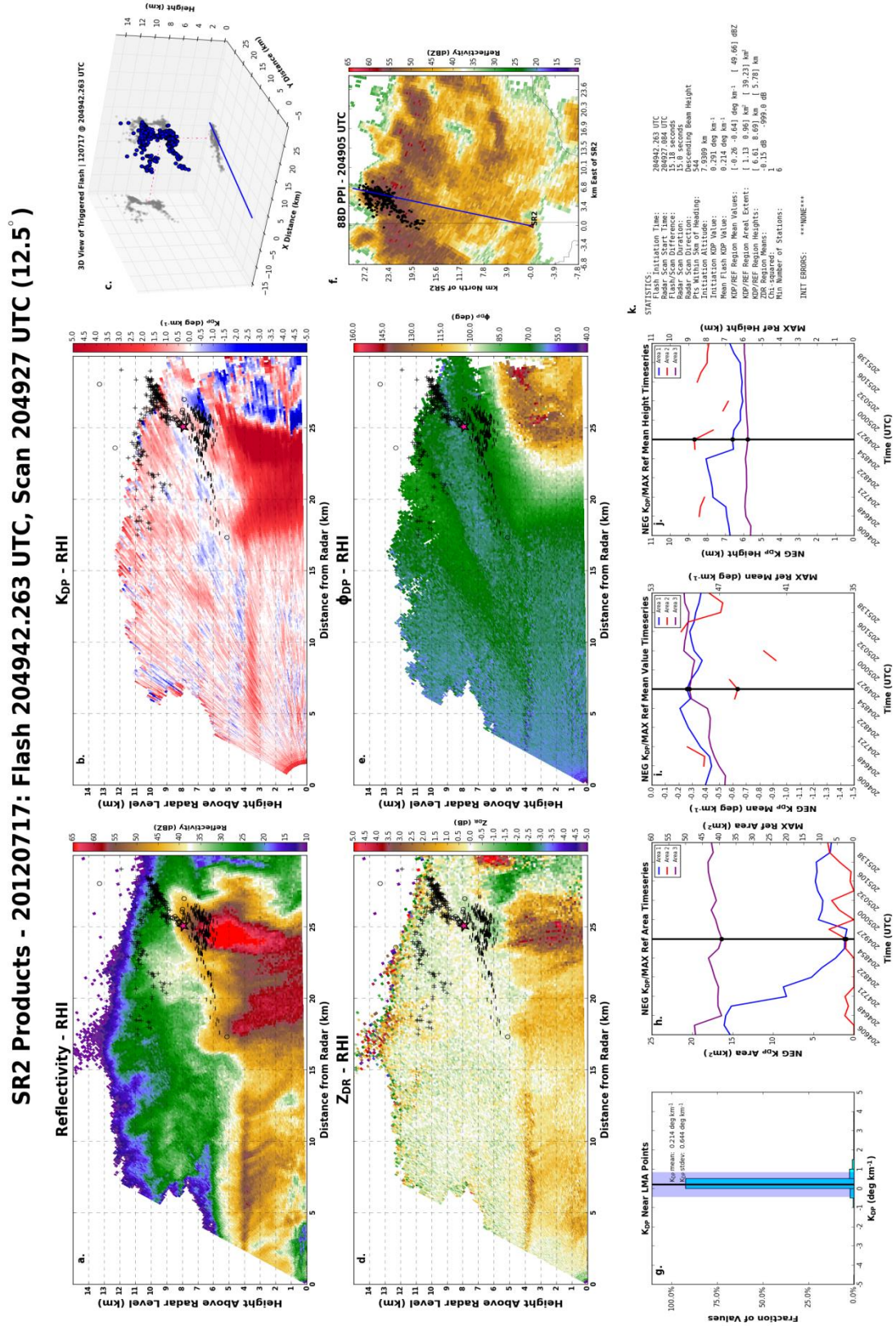

Figure A - 39: Flash 204942.263 UTC

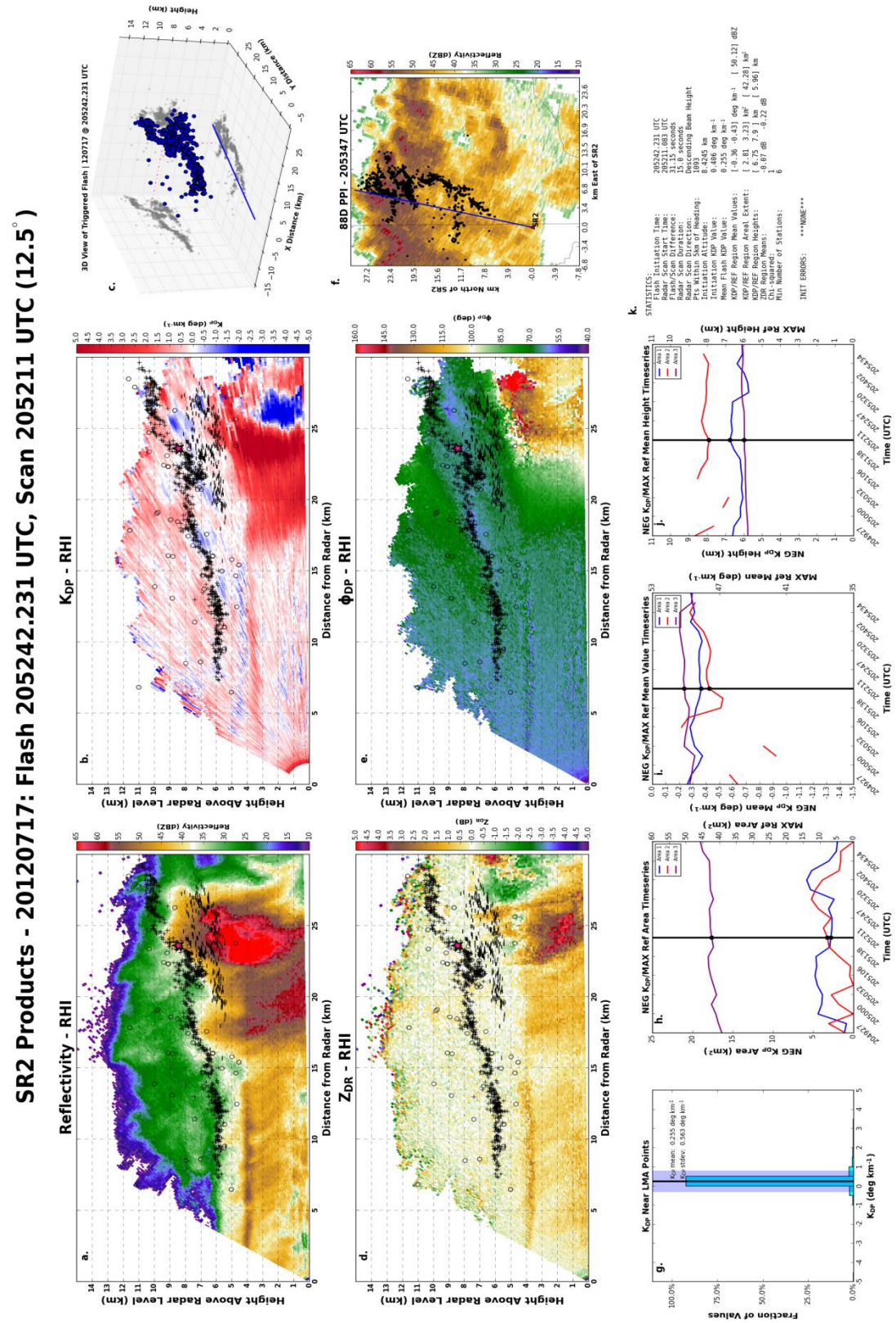

Figure A - 40: Flash 205242.231 UTC

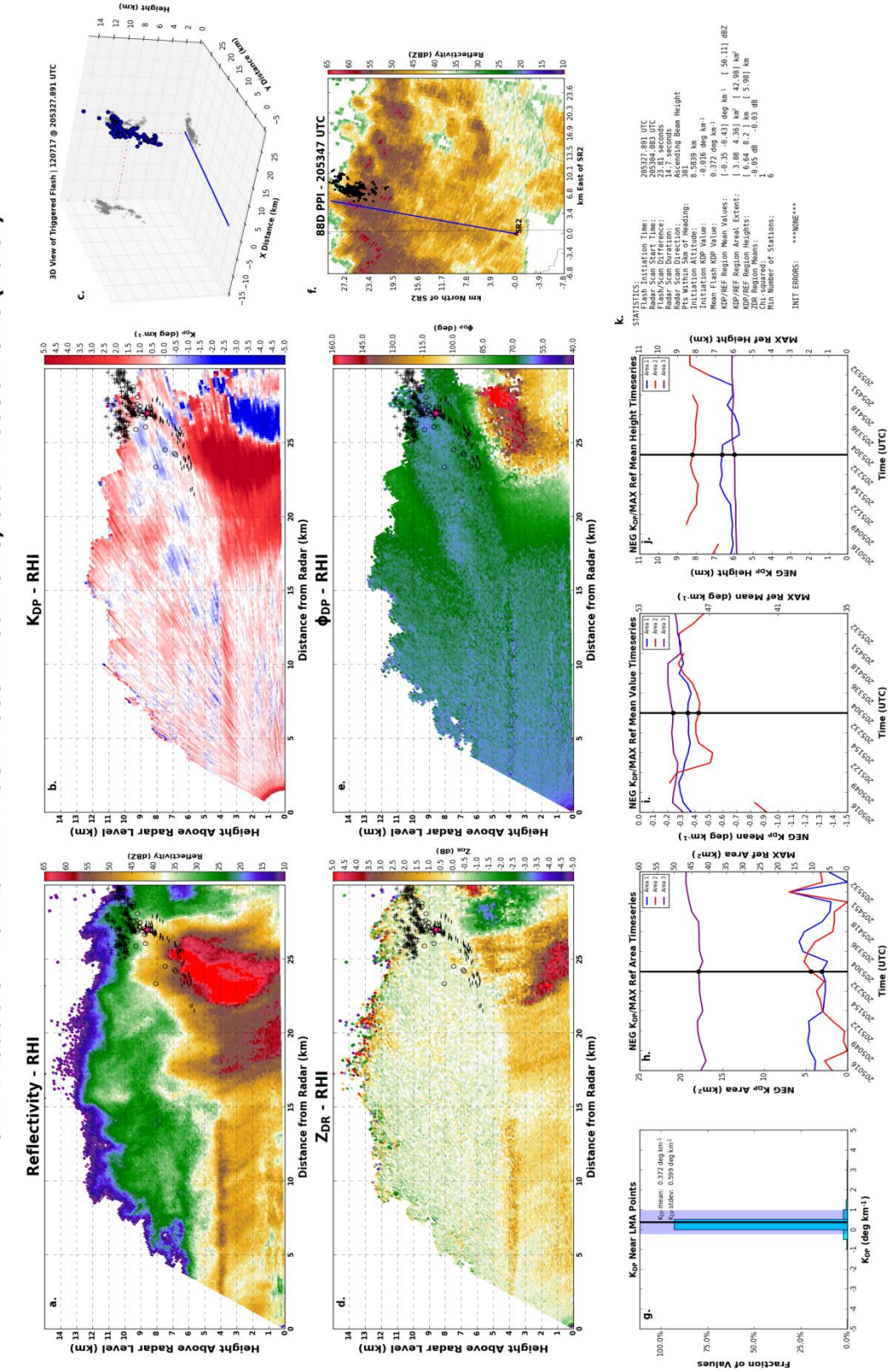

Figure A - 41: Flash 194827.331 UTC

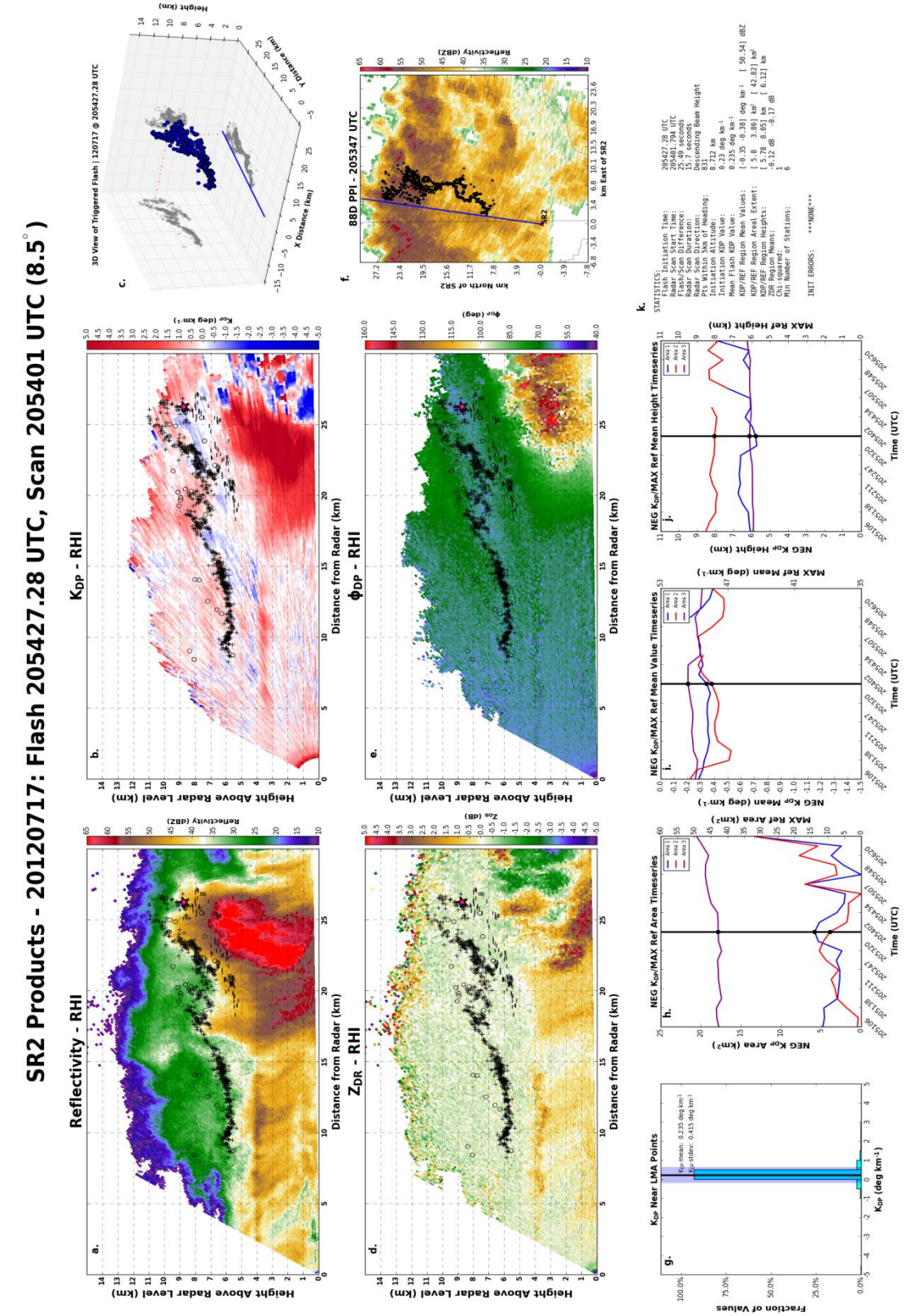

Figure A - 42: Flash 205427.28 UTC

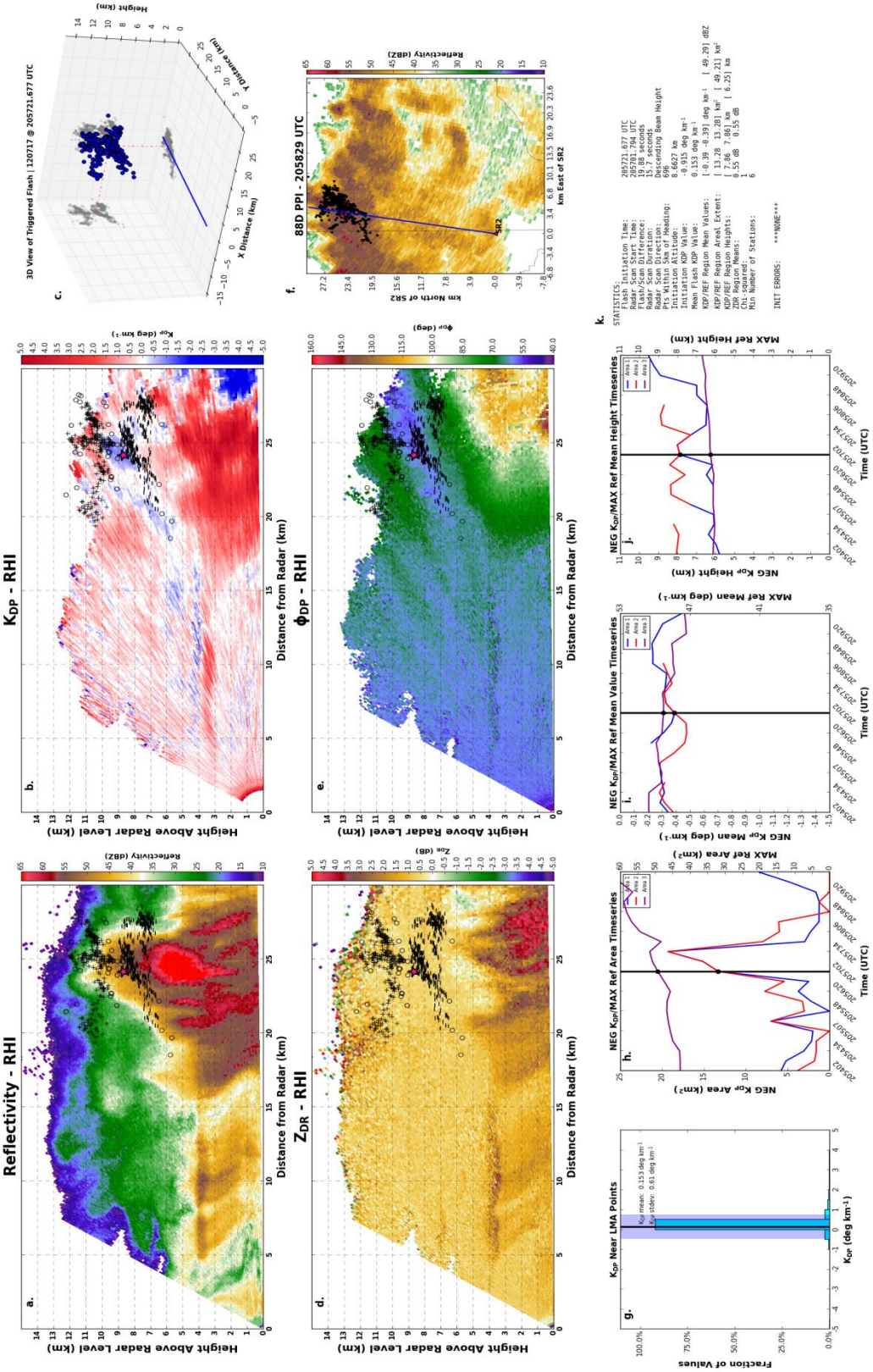

Figure A - 43: Flash 205721.677 UTC

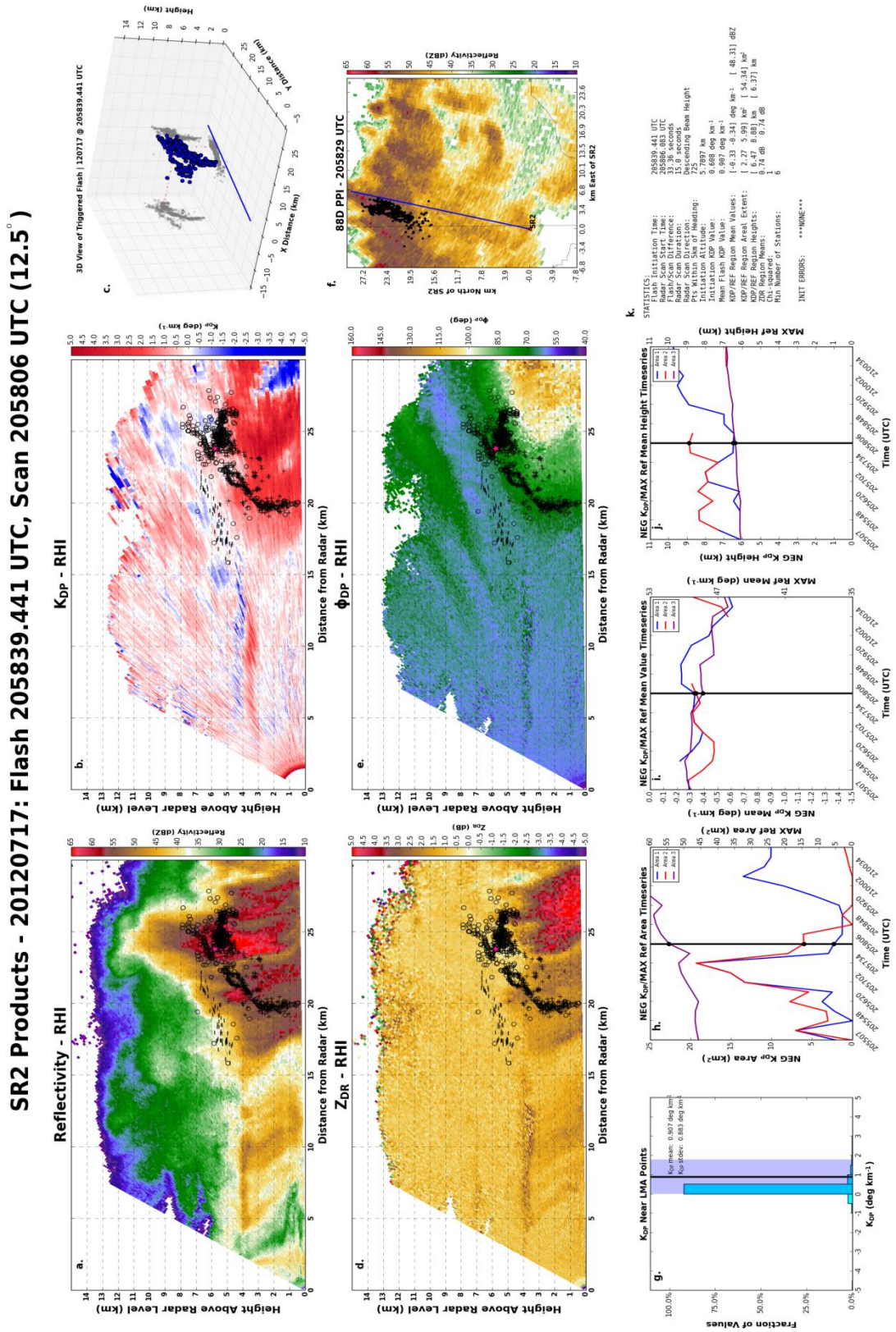

Figure A - 44: Flash 205839.441 UTC

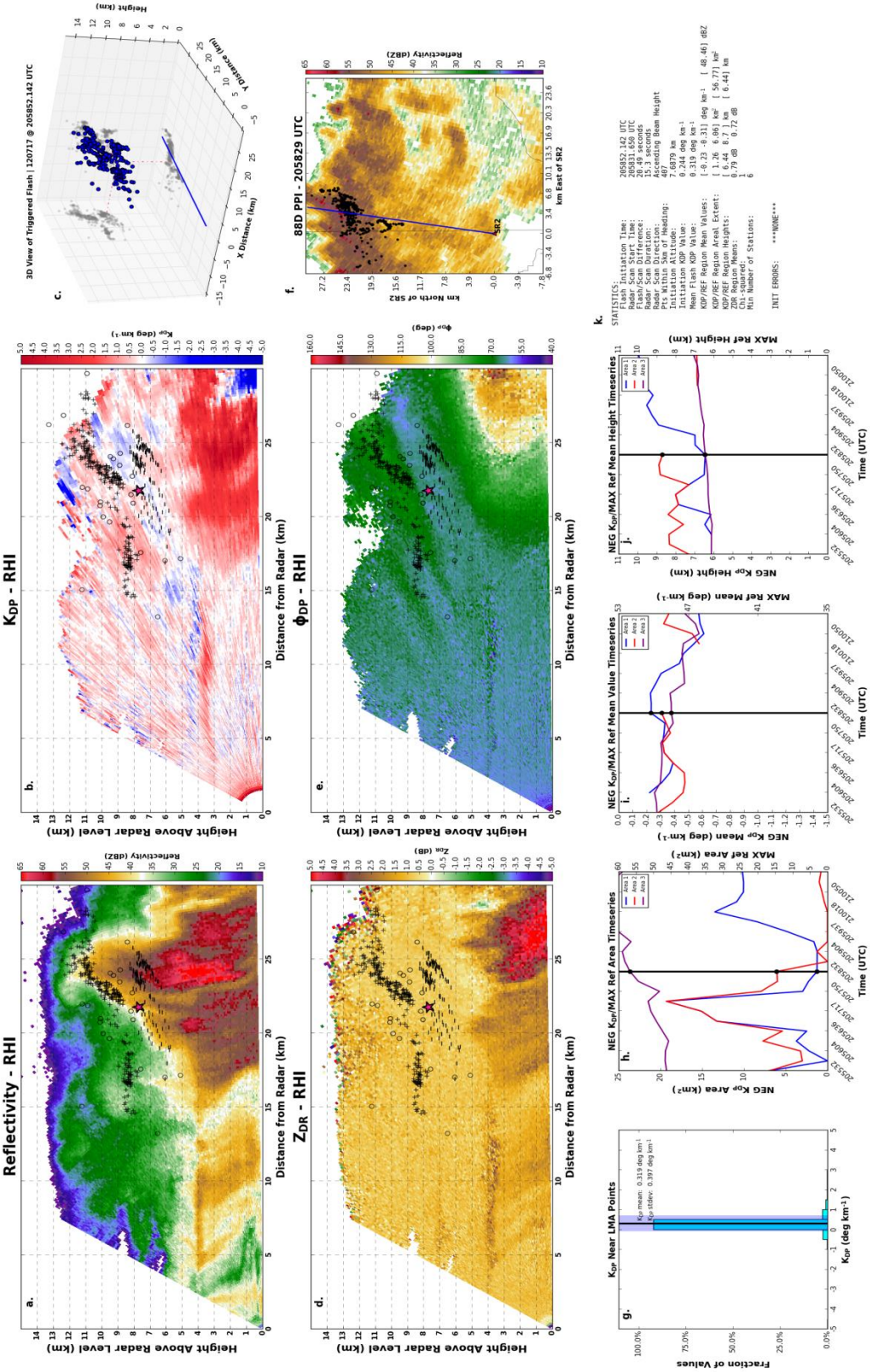

Figure A - 45: Flash 205852.142 UTC

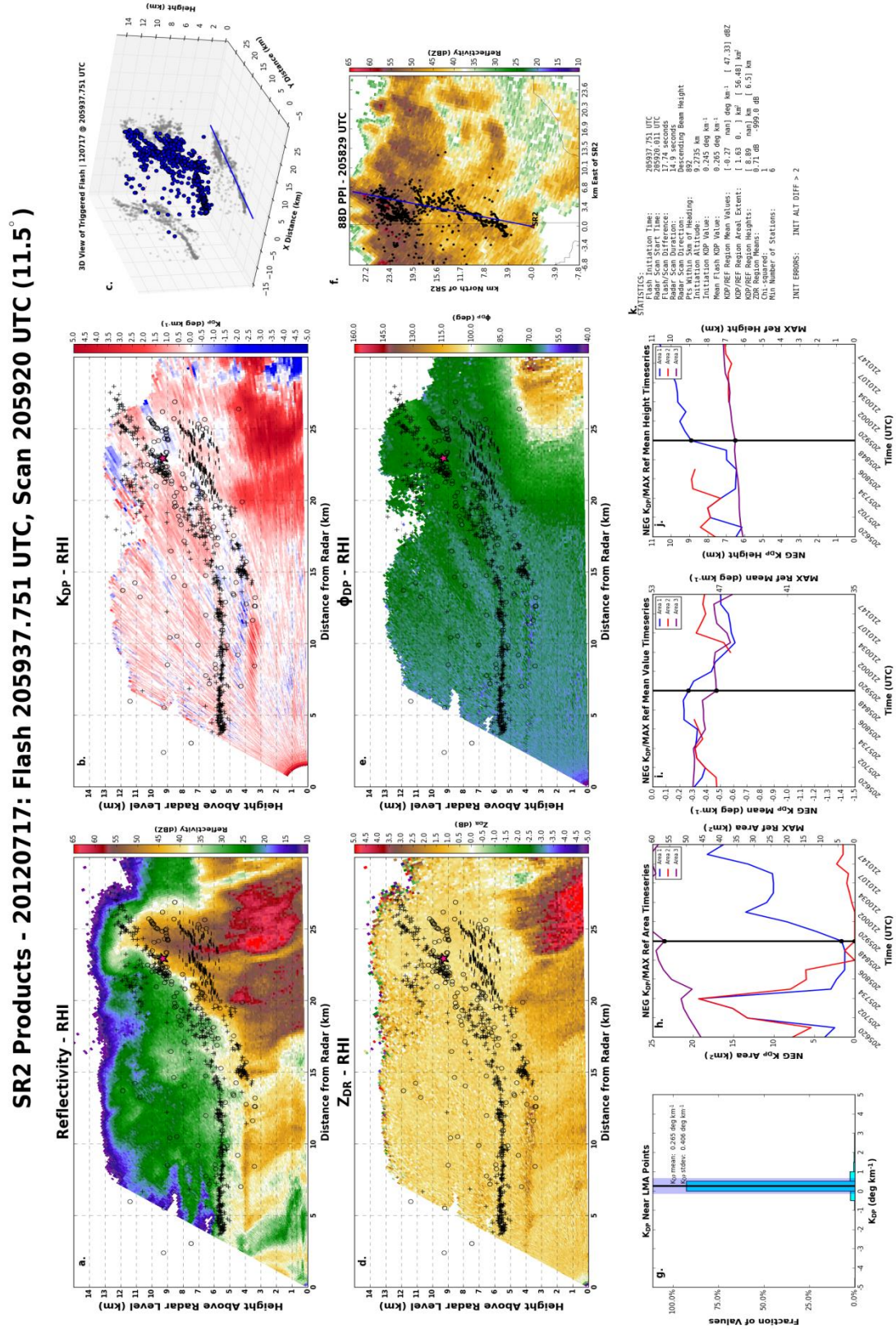

Figure A - 46: Flash 205937.751 UTC